THÈSE

En vue de l'obtention du

DOCTORAT DE L'UNIVERSITÉ DE TOULOUSE

Délivré par : *l'Université Toulouse 3 Paul Sabatier (UT3 Paul Sabatier)*

Présentée et soutenue le *20/10/2015* **par :**

Sara MARCATILI

Multi-scale dosimetry for Targeted Radionuclide Therapy optimisation

JURY

Isabelle BERRY	Professeur d'Université	Présidente du Jury
Glenn FLUX	Directeur de Recherche	Rapporteur
Gérard MONTAROU	Directeur de Recherche	Rapporteur
Frédéric COURBON	Professeur d'Université	Examinateur
David SARRUT	Directeur de Recherche	Examinateur
Jean-Philippe VUILLEZ	Professeur d'Université	Examinateur
Manuel Bardiès	Directeur de Recherche	Directeur

École doctorale et spécialité :
GEET : Radio-physique et Imagerie Médicale
Unité de Recherche :
Centre de Recherche en Cancérologie de Toulouse (UMR 1037)
Directeur(s) de Thèse :
Manuel BARDIÈS
Rapporteurs :
Glenn FLUX et *Gérard MONTAROU*

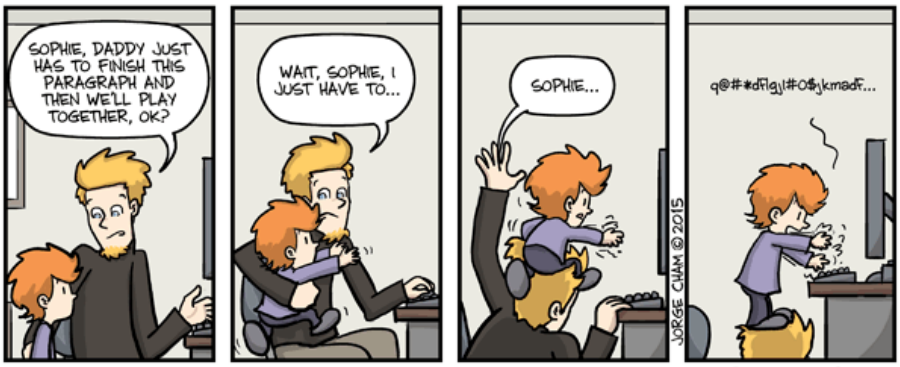

WWW.PHDCOMICS.COM

Contents

List of Figures

List of Tables

List of abbreviations

BREP	Boundary REPresentation
CEA	Anti-Carcinoembryonic Antigen
CERN	Conseil Européen pour la Recherche Nucléaire
CCD	Charge-Coupled Devices
CPM	Counts Per Minute
CRCT	Centre de Recherche en Cancérologie de Toulouse
CSDA	Continuous Slowing Down Approximation
CSG	Constructive Solid Geometry
CT	Computed Tomography
DAR	Digital Autoradiography
DNA	DeoxyriboNucleic Acid
DPK	Dose Point Kernel
DTC	Differentiated Thyroid Cancer
DVK	Dose Voxel Kernel
DVH	Dose Volume Histogram
dDVH	differential Dose Volume Histogram
EBRT	External Beam RadioTherapy
EDTMP	ethylenediaminetetramethylenephosphonic acid
FORE	FOurier REbinning
GE	General Electrics
HER2	Human Epidermal Receptor type 2
HES	Hematoxylin Erythrosine Saffron
HR	High Resolution
HR–MS	High Resolution Multi Scale
HR–SS	High Resolution Single Scale

IC	Isolated Cells
ICRP	International Commission on Radiological Protection
ICRU	International Commission on Radiation Units & Measurements
IRCM	Institut de Recherche en Cancérologie de Montpellier
LLI	Lower Large Intestine
LLNL	Lawrence Livermore National Laboratory
LR	Low Resolution
LR–SS	Low Resolution Single Scale
mAb	monoclonal Antibody
MC	Monte Carlo
MIBG	meta-iodobenzylguanidine
MIRD	Medical Internal Radiation Dose committee
MR	Magnetic Resonance
MRI	Magnetic Resonance Imaging
MRT	Molecular RadioTherapy
NHL	Non-Hodgkin Lymphoma
NURBS	Non-Uniform Rational B-Spline
ORNL	Oak Ridge National Laboratory
PA	PAtient
pbs	phosphate buffered saline
PET	Positron Emission Tomography
PRRT	Peptide Receptor Radionuclide Therapy
RIT	RadioImmunoTherapy
ROI	Region Of Interest
RPI	Rensselaer Polytechnic Institute
SC	Surrounding Clusters
SI	Small Intestine
SPECT	Single Photon Emission Computed Tomography
TC	Target Cluster
TEP	Tomographie par Emission de Positons
TDM	TomoDensitoMétrie
TRT	Targeted Radionuclide Therapy
UF	University of Florida

ULI	Upper Large Intestine
VDK	Voxel Dose Kernel
VHP	Visible Human Project
VOI	Volume Of Interest
2D	two-dimension, two-dimensional
3D	three-dimension, three-dimensional
4D	four-dimension, four-dimensional

Résumé

La Radiothérapie Interne Vectorisée (RIV) consiste à détruire des cibles tumorales en utilisant des vecteurs radiomarqués (radiopharmaceutiques) qui se lient sélectivement à des cellules tumorales. Dans un contexte d'optimisation de la RIV, une meilleure détermination du dépôt d'énergie dans les tissues biologiques est primordiale pour la définition d'une relation dose absorbée - effet biologique et pour l'optimisation des traitement du cancer. Cela nécessite une évaluation quantitative de la distribution de l'activité (avec la technique d'imagerie moléculaire la plus appropriée) et d'effectuer le transport du rayonnement à l'échelle à laquelle se produisent les phénomènes biologiques pertinents. Les méthodologies à appliquer et les problématiques à établir dépendent strictement de l'échelle (cellule, tissu, organe) de l'application considérée, et du type de rayonnement en cause (photons, électrons, particules alpha). Mon travail de recherche a consisté à développer des techniques dosimétriques dédiées (dosimétrie mono-échelle) et innovantes, capables de prendre en compte la particularité de différents scénarios expérimentaux (cellulaire, pré-clinique, RIV clinique). Les méthodes mises en œuvres au cours de cette thèse (dans le cadre d'application dosimétrique réelles) sont :

- Le développement et la validation d'un modèle cellulaire 3D qui ont permis une meilleure compréhension des processus radiatifs et non radiatifs associés à la mort cellulaire dans le cadre d'expériences de survie clonogénique avec des émetteurs bêta.

- Une application Monte-Carlo pour le calcul des distributions de dose absorbée dans les tumeurs de souris ex vivo qui a permis d'établir une relation dose absorbée - effet pour trois anticorps différents marqués par un émetteur alpha (^{212}Pb).

- Une comparaison des différents algorithmes de calcul de dose absorbée dans un contexte de diagnostic qui a mis en évidence les limites potentielles des approches dosimétriques standards actuellement utilisées en clinique.

- Une approche de résolution adaptative pour la dosimétrie clinique (dosimétrie multi-échelle) également proposée afin d'augmenter la précision sur la dose absorbée dans de petits organes radiosensibles.

Mots-clés : Radiothérapie interne vectorisée - dosimétrie cellulaire - dosimétrie préclinique - dosimétrie clinique - modélisation Monte Carlo - dosimétrie multi-échelle.

Introduction

La Radiothérapie Interne Vectorisée (RIV) consiste à détruire des cibles tumorales en utilisant des vecteurs radiomarqués (radiopharmaceutiques) qui se lient sélectivement à des cellules tumorales. Comme la radiothérapie externe, la RIV a l'avantage de délivrer une très haute dose absorbée à une cible spécifique, mais, elle a en plus en commun avec la chimiothérapie, la capacité de fournir un traitement systémique en attaquant des sites multiples dans le corps. Cependant, alors que la radiothérapie externe est une technique déjà standardisée pour laquelle des procédures strictes sont suivies en amont de la thérapie pour la planification de la dose absorbée au patient, en RIV la thérapie est les plus souvent administrée par des quantités fixes de radioactivité. La principale limite de cette approche est de négliger l'existence des différences métaboliques d'un patient à l'autre, compromettant ainsi l'efficacité du traitement. Dans la mesure où la réponse métabolique à un radiopharmaceutique donné est spécifique à chaque individu, une même activité injectée peut résulter en une dose absorbée très différente sur une population des patients. Si la dose absorbée par la tumeur est insuffisante, le risque de récidive devient plus important. En revanche, si la dose absorbée par les organes radiosensisibles sains est trop importante, le traitement peut avoir des effets toxiques délétères.

L'optimisation de la RIV passe donc par la mise en place de traitements thérapeutiques personnalisés, incluant le fractionnement et/ou l'augmentation de l'activité administrée, qui permettront de gagner en efficacité et de limiter la toxicité pour les organes sains (Pouget et al. 2011). Afin d'atteindre une efficacité thérapeutique maximale, les doses absorbées par la tumeur et les organes à risque doivent être évaluées avant le traitement, à travers une mesure personnalisée de la biodistribution *in vivo* de la radioactivité, à la fois dans l'espace et dans le temps, après l'injection d'une quantité réduite de radiopharmaceutique. Le rôle de la dosimétrie est d'interpréter ces mesures pour établir la quantité de radioactivité optimale qui devrait être administrée. Aujourd'hui, de plus

en plus d'éléments indiquent que la réalisation d'une dosimétrie personnalisée en pré-traitement est nécessaire, et améliorerait considérablement la qualité et les résultats de la RIV. Les bénéfices cliniques de la dosimétrie pour la RIV ont déjà été démontrées pour le traitement des maladies bénignes et malignes de la thyroïde (à la fois pour la toxicité et pour l'efficacité), pour l'utilisation de peptides radiomarquées à l'yttrium 90 (pour la toxicité rénale, et partiellement pour l'efficacité), pour l'utilisation d'anticorps radiomarqués à l'iode 131 dans le traitement des hémopathies malignes (efficacité), et pour l'utilisation de microsphères dans le traitement du cancer du foie (toxicité et efficacité) (Strigari et al. 2014). Néanmoins, l'optimisation de la RIV clinique doit aussi s'appuyer sur une meilleure évaluation de la relation dose absorbée-effet, via des expériences pré-cliniques dont le but est de déterminer l'efficacité et la toxicité propre des radiopharmaceutiques. Les connaissances acquises lors de ces expériences pourraient en effet fournir de nouvelles stratégies plus efficaces pour l'administration des traitements en RIV. En ce sens, tout effort cherchant à faire progresser la RIV devrait considérer à la fois une meilleure détermination de la dose absorbée dans un contexte clinique, et le développement de la dosimétrie cellulaire et du petit animal.

La dosimétrie à l'échelle cellulaire a pour but de mieux comprendre l'action de la radiation ionisante sur le matériel biologique. Les connaissances actuelles en radiobiologie proviennent pour l'essentiel de la radiothérapie externe, pour laquelle les doses absorbées et les débits de dose absorbée sont parfaitement connus. Cependant, en RIV, les distributions de vecteurs radiomarqués sont très hétérogènes (même à l'échelle cellulaire), et l'émission radiative est isotrope, de différents types et à diverses énergies. L'effet biologique est en outre modulé en présence d'un débit de dose absorbé faible et variable (Wheldon et al. 1990). La détermination de nouveaux paramètres de référence radiobiologiques est réalisée par des expériences de survie sur des colonies de cellules. Dans une même colonie, les cellules peuvent avoir différentes tailles, différents niveaux d'internalisation de la radioactivité et différentes distributions intracellulaires d'activité : ce grand niveau d'hétérogénéité reflète celui observé dans les tissus biologiques *in vivo*. Des travaux ont déjà montré que l'hétérogénéité des paramètres des cultures cellulaires ont un impact significatif sur la forme des courbes de survie cellulaire (Howell et al. 2012, Uusijarvi et al. 2008).

A l'échelle du petit animal, la dosimétrie est nécessaire pour établir la relation entre la dose absorbée et l'effet biologique en RIV pré-clinique, pour caractériser tant l'efficacité

que la toxicité des radiopharmaceutiques. Les études de dosimétrie pré-clinique sont, en générale, basées sur des modèles de calcul très simplifiés (i.e. des sphères pour simuler la dose auto-absorbée à la tumeur), et faisant l'hypothèse d'une absorption homogène de la radioactivité par les organes et la tumeur. Cette simplification est directement liée aux techniques employées pour déterminer l'absorption de la radioactivité par les différents tissus biologiques du petit animal. En effet, les études conventionnelles de biodistribution de la radioactivité sont réalisées par l'échantillonnage des tissus après le sacrifice de l'animal, tissus dont on mesure ensuite l'activité moyenne à l'aide de compteurs gamma. Ceci implique que toute étude des effets liés à l'hétérogénéité de la biodistribution est généralement négligée.

Si l'on considère maintenant l'optimisation de la RIV dans son ensemble, une dosimétrie précise implique la modélisation de l'interaction entre la radiation et le tissu vivant à l'échelle caractéristique des phénomènes biologiques d'intérêt : un paramètre important à prendre en compte est alors la dimension relative du milieu de propagation (cellule, tissu, corps) par rapport à la longueur d'interaction dans le tissu de la radiation considérée (particules α ou β, électrons Auger...). De ce fait, le caractère pénétrant ou non de la radiation ne doit pas être considéré comme une propriété intrinsèque mais plutôt comme une propriété contextuelle, fonction des dimensions caractéristiques du système biologique étudié. En conséquence, on remarquera que l'implémentation d'un modèle dosimétrique réaliste et détaillé de très haut niveau n'est pas forcément la meilleure des solutions dans toutes les circonstances. Par exemple, alors que la modélisation de la dose absorbée dû au feu croisé des cellules est cruciale en présence d'un émetteur β à courte longueur d'interaction tel que le lutétium 177 (^{177}Lu), il est correct de faire l'hypothèse simple d'une absorption complète dans l'organe source lorsque ce même radionucléide est utilisé en clinique et que seule la dose moyenne absorbée par l'organe est d'intérêt. De façon similaire, pour le calcul de la dose absorbée par la tumeur sur le petit animal, l'hétérogénéité de l'absorption de la radioactivité dans la tumeur peut, ou non, être un paramètre important selon que l'on utilise des radionucléides émetteurs α (courte longueur d'interaction) ou β (grande longueur d'interaction).

Ce travail de recherche a consisté à développer des méthodes de calcul dosimétrique dédiées (dosimétrie mono-échelle) et innovantes, capables de prendre en compte la particularité de différents scénarios expérimentaux (RIV cellulaire, pré-clinique et clinique).

Les méthodes mises en œuvres au cours de cette thèse on été vérifiées dans le cadre d'applications dosimétriques réelles.

Le premier chapitre est une revue des techniques et modèles les plus souvent utilisés pour la dosimétrie cellulaire, animal et clinique. Les points forts et faibles de chaque méthode sont détaillés en fonction des conditions expérimentales de manière à identifier des possibles stratégies pour l'optimisation de la dosimétrie pour la RIV à différentes échelles.

Le chapitre 2 est consacré au développement et à la validation d'un modèle dosimétrique cellulaire 3D *in silico*. Sur la base de paramètres obtenus expérimentalement, le modèle génère une géométrie réaliste de la culture cellulaire en prenant en compte la tendance des cellules à s'agréger en amas de différentes tailles. Dans une même colonie virtuelle, les cellules peuvent avoir différents rayons, niveaux de radioactivité internalisé et différentes distributions d'activité intracellulaire. Ce modèle générique a été utilisé pour dériver les courbes de survie de cultures de lymphocytes B traités avec des anticorps monoclonaux marqué au lutétium 177. L'impact important de l'irradiation par tirs croisés en rapport à l'irradiation par auto-absorption a montré que la modélisation complète et détaillée de la géométrie de la culture cellulaire est nécessaire pour réussir une analyse dosimétrique réaliste à l'échelle cellulaire dans le cas des émetteurs β. Plus généralement, le modèle permet une meilleure compréhension des processus radiatifs et non-radiatifs associés à la mort cellulaire dans le cas d'une expérience de survie clonogénique impliquant des émetteurs β.

Dans le chapitre 3, il est démontré qu'un calcul dosimétrique approximatif sur une tumeur peut masquer l'existence de la corrélation dose absorbée-effet, si l'on est en présence d'une grande hétérogénéité de l'absorption de la radioactivité. Trois anticorps monoclonaux différents, marqués au plomb 212 (^{212}Pb), ont été évalués lors d'une expérience préclinique de radioimmunothérapie menée sur des souris ayant des carcinoses péritonéales de volume réduit. La dose absorbée moyenne, estimée par comptage des gamma sur des tumeurs disséquées, n'était pas corrélée aux courbes de survie des souris, mesurées au cour d'une expérience précédente. En effet, des images de coupes cryogéniques de tumeurs, obtenues par autoradiographie digitale, ont permis de mettre en évidence des distributions de la radioactivité très différentes pour les trois anticorps : en particulier, l'un d'eux n'était

pas internalisé, la radioactivité restant distribuée à la surface de la tumeur. Seule une prise en compte précise de la distribution de la dose absorbée, via une méthode dosimétrique basée sur des simulations Monte-Carlo, a permis de prédire correctement l'efficacité des divers anticorps.

Dans le chapitre 4, il est montré que le choix de l'algorithme pour le calcul de la dose absorbée, et l'utilisation de modèles anatomiques approximatifs, peuvent introduire des biais à l'échelle clinique, en particulier lorsque la radiation gamma est importante (Marcatili et al. 2015). Comme étape préliminaire pour la compréhension des avantages et/ou des limites des méthodes dosimétriques existantes en RIV clinique, un jeu de données constitué de scans séquentiels TEP/TDM de 6 patients auxquels a été injecté du ^{18}F-Flutemetamol (General Electrics), a été analysé en suivant trois différentes approches : dosimétrie basée sur les fantômes (logiciel OLINDA/EXM), dosimétrie basée sur des *Voxel Dose Kernels* (VDK) (logiciel STRATOS), et dosimétrie basée sur des simulations Monte-Carlo (application Gate dédiée). Le choix d'évaluer ces techniques dans le contexte d'une dosimétrie à visée diagnostique, a permis d'étudier dans un même cadre les effets sur la dose absorbée d'émissions à courte (positron) et à grande (gamma de 511 keV) longueurs d'interaction. Si, dans un contexte diagnostique, les approches dosimétriques basées sur des fantômes et VDK se sont montrées rapides et adéquates, un regard plus général sur le problème suggère que l'utilisation de ces méthodes dans un cadre clinique ne permettrait pas d'obtenir une dosimétrie précise.

Actuellement, la méthode la plus précise pour la réalisation d'une dosimétrie personnalisée consiste à exploiter les informations morphologiques obtenues à l'échelle du voxel par les techniques d'imagerie 3D, afin de réaliser le transport direct de la radiation émise par le radiopharmaceutique considéré via des simulations Monte-Carlo. Cependant, le problème principal de cette méthode est son manque de réalisme pour les petites structures radiosensibles (i.e. moelle osseuse, œil...), structures pour lesquelles la dose absorbée est généralement celle qui limite l'activité maximale administrée lors du traitement. Le chapitre 5 présente une solution permettant de surmonter ce problème par l'implémentation d'une technique de résolution adaptative appliquée à l'échelle clinique (dosimétrie multi-échelle). Cette méthode permet en particulier d'améliorer la précision de l'estimation de la dose absorbée dans les organes radiosensibles de petite dimension

(Marcatili et al. 2014). Les descriptions voxelisées et analytiques de la géométrie sont combinées afin de profiter à la fois du haut niveau de personnalisation de l'imagerie 3D et du réalisme anatomique des méthodes analytiques (dosimétrie multi-résolution). En outre, dans la mesure où la simulation de la distribution de la dose absorbée pour un corps entier décrit par une géométrie au maillage très fin est difficilement réalisable, on démontrera que cette nouvelle approche permet d'obtenir une dosimétrie précise dans les structures choisies, tout en limitant le temps de calcul total. Comme preuve de principe, l'exemple d'une vessie contenant une distribution homogène d'iode 131 (^{131}I) a été mis à l'étude : l'estimation de la dose maximale absorbée par la paroi de la vessie est quatre fois plus importante lorsque l'on utilise un modèle haute résolution, révélant ainsi un problème potentiel de toxicité que le modèle basse résolution, approximatif par nature, ne peut mettre en évidence.

Introduction

In Targeted Radionuclide Therapy (TRT), a radioactive isotope is usually attached to a biological vector (to form a radiopharmaceutical) that selectively seeks out tumour cells. As with External Beam RadioTherapy (EBRT), TRT offers the advantage of delivering high absorbed doses to specific targets, but in common with chemotherapy, it can deliver treatment systemically, attacking multiple sites throughout the body. However, while EBRT treatment delivery is highly standardised and specific procedures are established for the evaluation of patient absorbed dose before therapy, in TRT, treatments are most often administered according to fixed amount of radioactivity. The main limitation of this approach is to neglect the existing inter-patient variability, thus compromising the efficacy of the treatment. Since the metabolic response to a given radiopharmaceutical is different for each individual, the same administered activity may result in very different absorbed doses in a population of patients. At one extreme, the absorbed dose to the tumour may be too low, causing the occurrence of relapses; at the other, absorbed dose to radiosensitive healthy organs may be too high inducing toxic effects.

Optimisation of TRT relies on personalized therapeutic schedules, with fractionation and/or intensification of administered activity in order to increase efficacy, while maintaining acceptable toxicity (Pouget et al. 2011). In order to attain the therapeutic efficacy, absorbed dose to tumour(s) and organs at risk should be estimated before the treatment, evaluating patient-specific biodistribution *in vivo* (both in space and time) after the injection of a reduced amount of radiopharmaceutical. The role of dosimetry is interpreting this knowledge to establish the amount of radioactivity that should be administered. Today, there is increasing evidence that personalised pre-treatment dosimetry is necessary and would improve the quality and outcome of TRT. Clinical benefit of dosimetry in TRT has already been demonstrated in the treatment of benign and malignant thyroid disease (for toxicity and efficacy); for the use of ^{90}Y-labelled radiopeptides (for renal toxicity and, par-

tially, efficacy); for the use of ^{131}I- labelled antibodies in the treatment of haematological malignancies (efficacy); and for the use of microspheres in the treatment of liver cancers (toxicity and efficacy) (Strigari et al. 2014). Nevertheless, clinical TRT optimisation also relies in a better evaluation of the absorbed dose-effect relationship in pre-clinical experiments aiming to assess efficacy and toxicity of radiopharmaceuticals. The knowledge derived from these investigations may in fact provide novel and more effective strategies for TRT treatment delivery. In this sense, any effort for the advancement of TRT should consider, not only a better determination of the absorbed dose in a clinical settings, but also the development of cellular and small animal dosimetry.

The goal of cell scale dosimetry is to better understand the action of ionizing radiation on biological material. Most of the current radiobiology knowledge derives from external beam radiotherapy, where absorbed doses and absorbed dose rate are completely characterized. However, TRT results in heterogeneous distribution of radiolabelled vectors, even at the cellular scale, with an isotropic emission of radiations of different type and energy. In addition, the biologic effect is impacted by a low and varying absorbed dose rate (Wheldon et al. 1990). The derivation of new radiobiological parameters is performed through survival experiments in cell colonies. Within the same colony, cells may have different sizes, different levels of radioactivity internalization and different intracellular activity distributions: this reflects the high level of heterogeneity displayed by a tissue *in vivo*. Previous works have demonstrated that heterogeneity of cell culture parameters produces significant effects on the shape of survival curves (Howell et al. 2012, Uusijarvi et al. 2008).

On the other hand, small animal dosimetry is necessary to establish the relationship between absorbed dose and biological effects during preclinical TRT, both in terms of efficacy and toxicity. Preclinical dosimetric studies are in general based on simplistic computing models (i.e. spheres that simulates the self-absorbed dose for a tumour) and on the assumption of homogeneous organ/tumour uptake; this directly depends on the techniques employed to determine animal uptake of radioactivity in different tissues. A conventional biodistribution study will in fact rely on tissue sampling after animal sacrifice and average activity concentration determination on gamma counters. This means that any investigation of the heterogeneity-related effects is usually neglected.

Considering the optimisation of TRT as a whole, accurate dosimetry implies modelling the interaction between radiation and the living tissue at the scale at which biologically

relevant phenomena occur: an important parameter to account for is the relative dimension of the propagating medium (cell, tissue, body) with respect to the range in tissue of the considered radiation (α- or β-particles, Augers electrons...). In this regard, the penetrating or non-penetrating quality of the radiation should not be interpreted as an intrinsic property but rather considered with respect to the characteristic sizes of the biological system of interest. This implies that implementing the most realistic and detailed dosimetric model is not necessarily the best solution in all circumstances. For example, while modelling the cross-irradiation absorbed dose in a cell culture treated with a short range β-emitter (i.e. ^{177}Lu) is crucial to achieve realistic dosimetry, complete self-absorption within the source organ may be safely assumed when the same radionuclide is used in the clinics and the average organ absorbed dose is of interest. At the same time, for the calculation of tumour absorbed dose in small animal experiments, the heterogeneity of radioactivity uptake within the tumour may, or may not, be a relevant parameter depending on whether α- or β-emitting radionuclides are employed.

This research work consisted in developing dedicated computational dosimetric approaches (single-scale dosimetry) capable of taking into account the peculiarity of different experimental scenarios (cellular, preclinical, clinical TRT). All methods developed were tested in the framework of actual research applications and experiments.

The first chapter provides a review of the most common techniques and models currently available for cellular, animal and clinical dosimetry. Their strengths and weakness are analysed in different experimental conditions in order to identify possible strategies for TRT dosimetry optimisation at different scales.

In chapter 2, the development and validation of a 3D cellular dosimetric model (*in silico*) is reported. On the basis of experimentally determined parameters, the model generates realistic culture geometries taking into account cell tendency to aggregate into clusters of different sizes. Within the same virtual colony, cells may have different radii, different levels of radioactivity internalization and different intracellular activity distributions. This general-purpose model was applied to the establishment of clonogenic survival curves for in-vitro lymphocyte B cell colonies treated with ^{177}Lu-labeled monoclonal antibodies (mAbs). The high impact of cross-irradiation with respect to self-absorption demonstrated that a full modelling of cell culture geometry is necessary to achieve realistic dosimetry in the case of β-emitters, at the cellular level. More generally, the model

allowed a better understanding of the radiative and non-radiative processes associated to cellular death in the case of clonogenic survival experiments involving β-emitters.

An example of how approximate tumour dosimetry could mask an existing absorbed dose-effect correlation in the case of heterogeneous radioactivity uptake, is discussed in chapter 3. Three different mAbs labelled with ^{212}Pb, were evaluated in a preclinical radioimmunotherapy (α-RIT) experiment involving mice with small volume peritoneal carcinomatosis. Average absorbed doses based on gamma counting of dissected tumours did not correlate with mice survival curves assessed in previous experiments. Indeed, Digital AutoRadiography (DAR) images of tumour cryosections highlighted a very different radioactivity distribution for the tree mAbs: in particular, one of them did not internalise, with all the radioactivity remaining at tumour surface. For this reason, the actual efficacy of the three labelled-mAbs could only be predicted by considering their absorbed dose distribution (obtained by Monte Carlo dosimetry).

In chapter 4, it was demonstrated that the choice of the absorbed dose calculation algorithm and the implementation of approximate anatomical models may introduce a bias, at the clinical scale, especially when gamma radiations are of importance (Marcatili et al. 2015). As a necessary step to understand the advantages and/or limits of currently available dosimetric methods in clinical TRT, the same dataset, consisting of sequential PET/CT scans of 6 patients injected with ^{18}F-Flutemetamol (General Electrics), was analysed with three different approaches: phantom-based dosimetry (OLINDA/EXM software), Dose Voxel Kernel (DVK) dosimetry (STRATOS software), and Monte Carlo dosimetry (Gate custom application). The choice of evaluating these techniques in a diagnostic context has allowed to consider, at the same time, the impact of both short (positron) and long (511 keV gammas) range emissions on the absorbed dose calculation algorithm. While in a context of diagnostic dosimetry, the phantom-based and the DVK approaches resulted to be fast and adequate, a more general look at the problem suggested that the use of these approaches in a therapeutic setting, could prevent the achievement of accurate dosimetry.

Currently, the most accurate approach for the assessment of personalised dosimetry, consists on exploiting morphological information obtained at the voxel level through 3D imaging, to directly transport radiations emitted by the radiopharmaceutical considered (Monte Carlo method). However, the main drawback of this approach is its lack of anatomical realism for small radiosensitive structures (i.e. bone marrow, eye...) whose absorbed

dose ultimately limits the maximum tolerated activity for the treatment. In order to overcome this issue, in chapter 5, an adaptive resolution approach to clinical dosimetry (multi-scale dosimetry) is also proposed to increase the accuracy of absorbed dose delivery in small radiosensitive organs (Marcatili et al. 2014). Voxelised and analytical geometry descriptions are combined in order to bring together the level of personalisation achieved through 3D imaging, and the anatomical realism of the analytical method (multi-resolution dosimetry). Since the simulation of very finely sampled, whole body absorbed dose distributions is not computationally feasible, this approach will allow to achieve accurate dosimetry in selected structures, while keeping computation time low. In a proof of principle example consisting of a bladder homogeneously filled with ^{131}I, the maximum absorbed dose to the bladder wall was four times higher when implementing a high resolution model, thus predicting potential toxicities that are hidden by the approximate nature of a low resolution model.

Chapter 1

Computational methods for Targeted Radionuclide Therapy

1.1 Targeted Radionuclide Therapy

Surgical resection, either alone or in combination with External Beam RadioTherapy (EBRT), is nowadays the most widely employed therapeutic strategy for the treatment of locoregional tumours. In the case of diffuse systemic cancers, however, a surgical approach is not feasible, and the applicability of EBRT is limited. In this context, chemotherapy is, at present, the technique of choice, even if its administration results in high morbidity and important side effects.

Targeted Radionuclide Therapy (TRT), also called Molecular RadioTherapy (MRT), consists in the administration of radiolabelled vectors that specifically binds to tumour cells and produce radiation-induced cytotoxic effects. TRT offers the advantage of target selectivity achievable in EBRT treatments, while being systemic as chemotherapy. In addition, its toxicity is generally limited to the haematopoietic tissue, and few side-effects are observed (Chatal and Hoefnagel 1999). According to the biochemical pathway selected, and to the physical characteristics of the tumour, different vectors and radionuclides can be used for a variety of therapeutic applications. Separate branches of TRT are usually identified depending on the targeting mechanisms employed (Dash et al. 2013). These include cellular metabolic processess for accumulation of radioactive iodine in thyroid cancer cells, the use of specific cell surface receptors for accumulating radiolabelled peptides (Peptide Receptor Radionuclide Therapy, PRRT) and cell surface antigens to target monoclonal antibodies (Radioimmunotherapy, RIT).

Treatment of differentiated thyroid cancer (DTC), both papillary and follicular, with ^{131}I is by far the most common and established procedure in TRT. It takes advantage of the naturally occurring iodine uptake mediated by thyroid cells for the synthesis of thyroid hormones. On this basis, radioactive iodine treatments are dispensed to ablate remnant thyroid tissue after surgery in order to reduce the recurrence rate, and to treat iodine-avid metastases. Available data show a remarkable efficacy of this therapy, with a 5-year relative survival rates between 83 and 98% for patients with iodine-avid DTC, while the survival drops to 66% in the case of non-avid DTC (Worden 2014).

In PRRT tumour cells are targeted with radiolabelled peptides. Peptides are molecules consisting of two or more aminoacids linked together with peptide bond, and that regulates many physiological processes in the human body, acting at some sites as endocrine or paracrine signals and, at others, as neurotransmitters or growth factors (Santos 2012). Peptides usually display favorable pharmacokinetics characterised by high concentration in the target tissue and rapid clearance from the blood and non-target tissues. However, high uptake in the kidneys is sometimes a concern as it may cause potential nephrotoxicity. PRRT is mainly used for the treatment of endocrine tumour as most of them over-express receptors that binds to somatostatin, a peptide hormone that regulates the endocrine system. Octreotide and octreotate are somatostatin analogues that binds to somatostatin receptors on neuroendocrine tumours. In PRRT they are usually combined with ^{90}Y, ^{177}Lu or ^{111}In to deliver a lethal absorbed dose to the tumour.

Antibodies are integral agents of our immune system, primarily used to identify and aid in the clearing of foreign pathogens. In RIT, radiolabelled monoclonal antibodies (antibodies with monovalent affinity) are used to target specific antigens that are over-expressed in cancer cells and under-expressed in normal cells. The concept of RIT was initially proposed, more than a century ago by Ehrlich (Ehrlich 1899). However, his work had a limited success due to the unavailability of specific tumour antibodies at the time. In 1976, with the development of the hybridoma technique (Breedveld 2000), the production of monoclonal antibodies (mAbs) was made possible, increasing the scientific community interest in RIT. Nowadays, RIT is primarily used for the treatment of haematological malignancies such as non-Hodgkin's lymphoma (NHL). Antibody therapy with Rituximab is commonly administered to NHL patients (immunotherapy); the use of radioimmunoconjugates augments the effectiveness of the cold mAbs, producing lethal effects also to cancerous cells not expressing the targeted antigen. Currently, two commercial radiola-

belled antibodies are available for treatment of follicular NHL, ^{90}Y-ibritumomab tiuxetan (Zevalin) and ^{131}I-tositumomab (Bexxar). Both of them target the CD20 antigen expressed at the surface of pre–B lymphocytes, mature B lymphocytes and more than 90% of B-cell NHL (Ersahin et al. 2007); the antibodies recognise epitopes in the extracellular domain of the CD20 antigen, and form antibody-antigen immune complexes, which induce apoptosis, complement-dependent cytotoxicity, and antibody-dependent cytotoxicity. RIT is usually administered along with sufficient unlabelled antibody to saturate the non-tumour antibody binding sites, and to potentially increase tumour to background ratio. Efficacy of RIT was demonstrated for patients who are refractory to unlabelled anti-CD20 immunotherapy and chemotherapy, or have relapsed after these therapies (Goldsmith 2010).

Other forms of TRT include treatments of neuroendocrine tumours with I-131-meta-iodobenzylguanidine (MIBG) and metastatic bone pain palliation.

MIBG structurally resembles norepinephrine and hence, it enters neuroendocrine cells by an active uptake mechanism and is stored in the neurosecretory granules. On this basis, ^{131}I-mIBG is mainly used to image and treat symptomatic medulla neoplasms, such as neuroblastoma and pheochromocytoma, but also for the treatment of medullary thyroid cancer, and carcinoid tumours.

Pain palliation with bone-seeking radiopharmaceuticals is a common practice in patients with skeletal metastases especially from advanced breast and prostate cancers, for which more than 50% of patients develop bone metastases (Dash 2013). While the use of radiopharmaceuticals in tumour therapy involves their binding to the tumour cells, bone therapy targets the reactive osteoblastic reaction in the normal bone directly adjacent to the metastasis, which is generally the cause of pain. Bone pain palliation therapy is administered either with natural boneseekers radionuclides acting as calcium analogues, or with radionuclides chelated to organic phosphates. Traditionally, beta emitting radionuclides are selected for this kind of treatments: ^{89}Sr-chloride (Metastron®) and ^{153}Sm-EDTMP (Quadramet®) are the most commonly employed radiopharmaceuticals for bone pain palliation. More recently, an alpha-emitter, ^{223}Ra-dichloride (Xofigo®) has been also approved for clinical use. Xofigo is especially promising because in addition to providing pain palliation, it was shown to extend overall survival of men with metastatic prostate cancer (Parker et al. 2013).

Like any therapy involving ionising radiation, TRT's goal is to achieve the highest efficacy delivering the highest possible absorbed dose to the tumour, while sparing healthy

tissues. In order to achieve this objective, the choice of a highly specific vector, must be combined to a careful selection of the most appropriate radionuclide according to its decay properties and emissions.

1.1.1 Radionuclides for TRT

In TRT the radiations of primary interest are particle emissions (α, β and Auger) causing non-reparable damage to nuclear DNA strands by radiation-induced processes as ionisation. The choice of the most appropriate radionuclide for a given therapeutic application depends on its chemical and physical characteristics, that should be consistent with the selected administration pathway and the type and size of tumour being treated.

Regarding its chemical properties, the radionuclide selected is expected to produce a stable radionuclide-vector bond; to have high specific activity (i.e. the number of labels per molecule obtainable); to be available with high purity (radionuclidic, radiochemical, and elemental purity) and free from trace metal contamination.

For what concerns its physical characteristics, most importantly, the radionuclide half life should be compatible with the *in-vivo* pharmacokinetics of the targeting molecule. A too short half life, in fact, may produce a high number of disintegrations before radiopharmaceutical binding to the target, thus leading to a significant non-specific irradiation and potential toxicity for the healthy tissues. Conversely, a too long period may lead, to very low absorbed dose rate irradiations that would limit the treatment efficacy for tumour control. At the same time, the consequently long radiopharmaceutical excretion time would cause serious radioprotection issues associated to patient care and radioactive waste disposal.

Another important parameter to consider is obviously the type of radiation emitted by the radionuclide, with particular attention to its its Linear Energy Transfer (LET). The LET is defined as the amount of energy deposited by the ionising radiation per unit length of path, and it is usually expressed in keV/μm. This property depends on the type of particle and plays an important role on radiobiological effects. In TRT applications, radionuclides should be carefully selected on the basis of emitted particles LET, taking into account tumour size and radiopharmaceutical internalisation properties.

Finally, the availability of a gamma emission component is a desirable characteristic as it allows monitoring the radiopharmaceutical distributions *in vivo* both for pre-treatment dosimetry and therapeutic response. Ideally, gamma radiation should be of low abundance

to minimize the contribution to non-target organs, and low energy (100-200 keV) to provide effective gamma camera imaging.

In the next paragraphs, the physical properties of the particle emissions of interest for TRT application will be described in more detail. Table 1.1 provides a summary of their main physical characteristics.

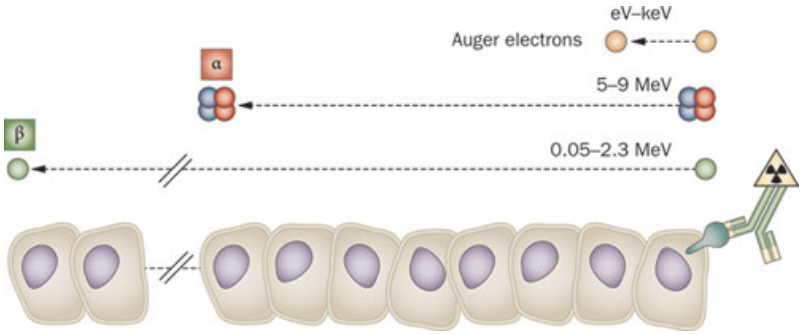

Figure 1.1: Schematic representation of Auger, α- and β-particles range in tissue, at the cellular scale. Source: Pouget et al. 2011.

1.1.1.1 Beta emitters

Beta particles are electrons released through beta decay in combination with an antineutrino. Since the decay energy is shared between these two particles, the electron presents a continuous energy spectrum between 0 and E_{max}, with E_{max} being the energy of the transition. Typically, E_{max} goes from tenths to hundreds of keV, corresponding to a maximum electron range in water of several millimeters. Among the radionuclides employed in TRT, ^{90}Y is the most energetic, with a maximum range in water of 1.1 cm, even if 90% of its energy is deposited within the first few mm (Roeske et al. 2008).

Relatively low energy electrons, as β-particles, mainly deposit their energy through collisional losses involving excitation and ionisation of the atoms in the medium. Since their interactions are mainly with particles of the same mass (orbital electrons in the medium), these can result in large scattering angles. As a consequence, electrons follow a very tortuous path. Figure 1.2(a) shows a schematic view of a typical β-particle trajectory in the biological tissue at the cellular scale: beta range can cover hundreds of cell diameters (cross-irradiation). The linear energy transfer for β-particles is low (0.2 - 4 keV/μm) in

comparison to that of α-particles and Auger electrons.

All these characteristics make β-particles effective for the treatment of medium-large size tumours (of the order of 1cm radius or less). Their range, in fact, is short enough to keep irradiation within the neighborhood of the emission point. At the same time, the cross-fire effect at the cellular level reduces the need of targeting each single tumour cell in order to achieve an effective treatment. Currently, ^{131}I, ^{90}Y and ^{177}Lu are among the most widely employed β-emitters in TRT.

1.1.1.2 Alpha emitters

Alpha particles are positively charged (+2), mono-energetic helium nuclei ($^4_2$He) with typical energies ranging from 3 to 9 MeV (Roeske et al. 2008). Alphas primarily interact through Coulomb forces between their positive charge and the negative charge of orbital electrons within the absorber atoms, causing atom ionisation and excitation. Given their large mass ($\sim$ 4 MeV) with respect to that of electrons ($\sim$ 0.5 MeV), they are basically undeviated by the interaction, and therefore follow a very straight path in tissue. Their LET is of the order of 80 keV/μm at the beginning of their track, and increases approximately to 300 keV/μm at the end, due to electron pick-up that reduces α-particles' charge. Their consequent short range in tissue, varying between 5 and 10 cell diameters (50-100 μm), results in a significant amount of energy deposited near the point of emission. Figure 1.2(b) shows the typical track of α-particles in tissue at the cellular scale, compared to that of β-particles. In figure 1.1, their range is compared to those of beta and Auger electrons.

Alpha particles short range makes them suitable for the treatment of micrometastases and very small tumours, allowing for localised irradiation of target cells with minimal radiotoxicity for the sourrounding normal cells. At the same time, given the lack of cross-fire effect, a uniform cell labelling should be achieved for the treatment to be effective. Because of their high LET, α-particles are of great interest from a radiobiological point of view. It has been shown, in fact, that as few as 1-3 tracks across the nucleus may result in cell death (Roeske et al. 2008). In addition, their killing effect is independent of dose rate, oxygenation level, and cell cycle state (Sofou 2008). However, only a handful of α-emitters have suitable characteristics for clinical use. Many progenitors, in fact, present a short half-life that severely limits radionuclide shipment from the site of production. At the same time, the absence of stable daughters in most decay chains involving emissions of

α-particles, makes it very difficult to fully characterise the radiolabelled compounds being developed and poses important radioprotection issues. At present, ^{223}Ra, ^{211}At, ^{212}Bi, ^{212}Pb,, ^{213}Bi and ^{225}Ac are the most commonly used α-particles emitters in TRT.

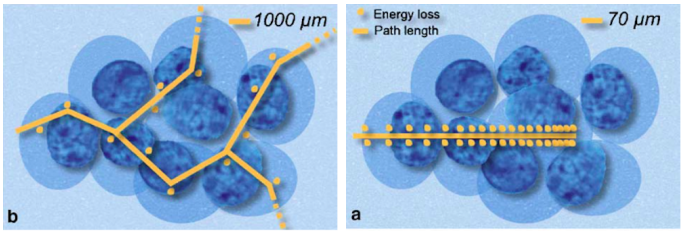

Figure 1.2: Schematic representation of β- and α-particles tracks at the cellular scale. Source: Couturier et al. 2005.

1.1.1.3 Auger emitters

Auger electrons are low energy, orbital electrons whose emission is usually the result of two nuclear processess: electron capture (EC) and internal conversion (IC). In both cases, the spectrum of the emitted electrons presents several mono-energetic emissions going from few eV to tenths of keV. When travelling across biological material, Auger electrons undergo the same physical processes that characterise β-particle interactions. However, given their lower energies, they exhibit significantly higher LET (4 - 26 keV/μm) and much shorter range (several nanometers). While α- and β-particles deposit their energy at the cellular scale, (see figure 1.1), the energy deposition of Auger electron is confined within the labelled cell. For this reason, Auger electrons are only effective when bound to carriers molecules that can cross cell membrane and reach the nucleus to cause damage to the DNA. If, on one side, their short range minimises toxicity to normal cells, on the other, it may negatively impact on therapeutic efficacy. The application of Auger emitters to TRT, still remains an area of research (Sofou 2008).

1.1.1.4 The role of dosimetry in TRT

Optimisation of TRT treatments relies on personalized therapeutic schedules, with fractionation and/or intensification of administered activity, in order to increase efficacy while maintaining acceptable toxicity (Pouget et al. 2011). An essential prerequisite to TRT

Characteristic	Beta	Alpha	Auger
Energy	0.05 – 2.5 MeV	3 – 10 MeV	10 eV – 10 keV
Range	0.2 – 11 mm	50 – 100 μm	10 nm
LET	0.2 – 4 keV/μ	m 80 – 300 keV/μm	4 – 26 keV/μm
Path track	Tortuous	Straight	Contorted
Mechanism	Cross fire effect	Traversed path length in cell nuclei	Breaks in DNA strands
Requisite	Close to target/ cell surface	Binding to cancer cells	Incorporation into nucleus
Cross-fire effect	Yes	No	No

Table 1.1: Summary of beta, alpha and Auger emissions characteristics. Adapted from Dash et al. 2013.

optimization is dosimetry. Its role, in a clinical context, is to establish the amount of radioactivity to administer, on the basis of patient biokinetics data, available from nuclear medicine imaging. The value of dosimetry in assessing therapeutic outcome and toxicities has already been demonstrated in several clinical applications (Strigari et al. 2014). In preclinical experiments (both at the animal and and the cellular scale) establishing treatment efficacy is also crucial for the evaluation and comparison of novel radiopharmaceuticals before Phase I studies on humans. Nevertheless, while the implementation of dosimetry in EBRT is well established and has seen continuous improvements and standardisation in the past decades, dosimetry in TRT is far from reaching the same level of advancement. Todays, TRT treatments are typically delivered with fixed level of activities, neglecting inter-patient variability in terms of radiopharmaceutical uptake and metabolic response. The choice of the administered activity is often made conservatively in order to avoid potential toxicities, and on the basis of dose-limits inferred from a population of patients (cohort-based treatment planning). This approach most commonly leads to the delivering of sub-therapeutic treatments, eventually causing the occurrence of relapses. On the other hand, some individuals may still develop radiation-induced toxicities because of longer than average radiopharmaceutical retention (Glatting et al. 2013). In addition, even when pre-therapy dosimetry is performed to optimise treatment delivery, the current situation is that of a wide heterogeneity of implemented dosimetric approaches, which

ultimately limits the development of patient-specific TRT (Lassmann et al. 2011). The following sections introduce a critical review of the most commonly employed computational dosimetric methods and models in TRT. Their main advantages and drawbacks are also identified and commented.

1.2 The MIRD schema for the calculation of the absorbed dose

The absorbed dose (D) is defined as the energy (E) deposited in a given tissue per unit of mass (M), and it is expressed in gray (1 Gy = 1 J/kg):

$$D(Gy) = \frac{E(J)}{M(kg)} \tag{1.2.1}$$

In targeted radionuclide therapy, according to standard, time-independent MIRD formulation (Bolch et al. 2009), the absorbed dose to a target region r_T can be expressed as the sum of the contribution from all source regions r_S:

$$D(r_T) = \sum_{r_S} \tilde{A}(r_S, T_D) S(r_T \leftarrow r_S) \tag{1.2.2}$$

where $\tilde{A}(r_S, T_D)$ is the time-integrated activity (also called cumulated activity in Loevinger et al. 1991) in the source region r_S over the absorbed dose-integration period T_D, and $S(r_T \leftarrow r_S)$ is the absorbed dose in the target per disintegration in the source (also called S value). In the particular case source and target regions coincide, equation 1.2.2 only includes the term for $r_S = r_T$, and the absorbed dose is generally referred to as self-absorbed. At the same time, the absorbed dose due to the radioactivity in source regions other than the target ($r_S \neq r_T$), is identified as cross-irradiation absorbed dose.
In this section and in the following, the terms "source"and "target"are used generically without further specifications. Indeed, despite its remarkably simple formulation, the MIRD schema can be applied to a wide range of scenarios. Source and target regions can hence be identified as organs, tissue subregions, voxelized tissues or organ structures, cellular compartments and so on.

1.2.1 Time-integrated activity

The first term of equation 1.2.2, $\tilde{A}(r_S, T_D)$, expressed in units of Bq s, represents the number of disintegrations occurring in a source regions r_S during treatment time T_D, and depends on the half life of the radionuclide and its spatial and temporal distribution in the source. These properties are specific of each radiopharmaceutical and depend, in turns, on the metabolism of the source, its uptake (defined as the fraction of injected activity absorbed in the region of interest) and its clearance. The amount of activity contained in a source region changes with time. If the time-activity curve is known, the cumulated activity for a source organ is obtained by measuring the area under this curve. Mathematically, the time-activity curve can generally be modeled as:

$$A(r_S, t) = A_0 \; f_S(t) \; e^{-(\lambda_p + \lambda_b)t} \tag{1.2.3}$$

where A_0 is the injected activity at time $t = 0$, f_S is the fractional uptake in source r_S, and λ_p and λ_b are the physical and biological decay constants of the radiopharmaceutical. The cumulated activity can be calculated integrating equation 1.2.3:

$$\tilde{A}(r_S, T_D) = A_0 \int_0^{T_D} f_S(t) \; e^{-(\lambda_p + \lambda_b)t} \tag{1.2.4}$$

In clinica TRT dosimetry, T_D is usually set to infinite as the radiopharmaceutical acts in the patient body until its complete biological excretion and/or physical decay. For pre-clinical applications, as for examples cell cultures incubated with radioactivity, T_D is limited to the time frame the radiopharmaceutical interacts with the biological system considered.

1.2.2 Absorbed dose per unit activity

The second term of equation 1.2.2, $S(r_T \leftarrow r_S)$, is a radionuclide-specific quantity that represents the mean absorbed dose to the target region, per disintegration in the source

region, and it is expressed in units of Gy/Bq s. The S value can be written as:

$$S(r_T \leftarrow r_S) = \frac{1}{M_{r_T}} \sum_i \Delta_i \; \phi(r_T \leftarrow r_S, E_i) \tag{1.2.5}$$

where Δ_i is the mean energy of the i^{th} transition per nuclear transformation, and $\phi(r_T \leftarrow r_S, E_i)$ is the absorbed fraction, defined as the fraction of emitted energy E_i that is absorbed in the target region of mass M_{r_T}. The energy emitted per disintegration Δ_i only depends on the radionuclide considered and can be derived from standard physics or dosimetry tables (Eckerman and Endo 2008, Browne and Firestone 1986). Conversely, the absorbed fraction accounts for the emission type, the energy, and the geometry of source and target tissues. Given the impossibility of directly measuring the absorbed fraction, this is most often determined *una-tantum* by Monte Carlo simulations of particle propagation in virtual geometries presenting the same shape and composition of the tissue modelled. In the case of simple geometries, S values have also been calculated analytically through the integration of absorbed dose kernels over target volume. Depending on the spatial accuracy of the geometry selected, the determination of the S values may take place at the macroscopic level, neglecting tissue and radioactivity heterogeneity within the selected region (region-based dosimetry), or with a more refined spatial resolution that allows modelling sub-region heterogeneities (voxel dosimetry). In any case, the establishment of a virtual model of the biological system considered is a prerequisite for the calculation of S values. In the next paragraphs, the principal models and methods developed for region- or voxel-based dosimetry in clinical, pre-clinical and cellular contexts are presented.

1.3 Digital models for region-based dosimetry

For region-based TRT dosimetry, the use of digital models allows calculating region S values for any radionuclide of interest and a large number of target-source combinations (depending on the spatial resolution and realism of the model adopted). The primary advantage of this approach is that the S values obtained can be stored for later use, thus avoiding the need to perform time-consuming Monte Carlo simulation for each dosimetric calculation.

In the last 60 years, research groups worldwide have developed virtual models of any

kind to make it possible the generation of S values at the clinical, animal and cellular scales.

1.3.1 Anthropomorphic models

In clinical TRT dosimetry, anthropomorphic models of different kinds are often employed to establish organ S values that, in combination with patient-specific pharmacokinetic information, can be used to calculate the absorbed dose delivered to the patient. However, this strategy clearly implies that the model used is representative of patient anatomy.

The concept of Reference Man was proposed by the International Commission on Radiological Protection (ICRP) after the end of the Second World War for use in radiological protection. The Reference Man[1] is an individual with a physiology and organs of size, mass and composition representative of a given population. The use of a dosimetric model issued from Reference Man characteristics, however, does not guarantee that the model matches patient morphology. Because of this, tabulated S values are primarily used for diagnostic applications where the absorbed doses are low, so that the inherent inaccuracies in modelling a given patient are of no practical concern and largely balanced by traceability and possible comparison of different radiopharmaceuticals. In principle, it would be inappropriate to use a reference model in TRT planning, as the resulting errors can lead to the deliver of inadequate absorbed dose to the tumour or to excess irradiation of normal healthy tissue. However, in the absence of an approach of easy implementation, model-based dosimetry is nowadays largely employed also for radiotherapy applications.

In the last 60 years, researcher worldwide have put considerable effort in generating human models for the calculation of internal radiation dose. Most of them were developed for the assessment of population-based risk of internal exposure, while others were conceived for medical imaging and radiotherapy (both EBRT and TRT) applications. The very first human model was proposed by ICRP in 1959 (ICRP 1960). It represented the total body as a 30 cm sphere, and each organ as a sphere with different "effective radii". The radionuclide of interest was assumed to be located at the center, for the calculation of the "effective absorbed energy".

Since then, model development has seen a continous improvement, with the genera-

[1]Here "man "is used in its generic sense and includes the female and the child.

tion of models with increasing level of anatomical detail. Among them, three main types of models can be identified (Xu 2014) on the basis of their topological characteristics and the mathematical techniques employed for their definition: stylised, voxel-based and Boundary REPresentation (BREP) models. This categorisation is also chronological, as each type of model was mainly developed in a specific time frame, and goes on pair with the advance of available computational resources at the time. Regardless of their mathematical representations, these models have been used to generate S values at the organ level, assuming uniform radioactivity distribution within the organs, and thus neglecting potential intra-organ heterogeneities of the absorbed dose.

Next sections provide a quick review of the principal models that have been employed for TRT dosimetry. For each category, models representing adult men and women (including pregnant women), and children of different ages, have been proposed for a better description of actual patient anatomy. Here, the discussion will focus on adult models.

1.3.2 Stylised models

The so-called stylised or mathematical models are generated using Constructive Solid Geometry (CSG). This techniques consists in creating solid objects using Boolean operators to combine very simple shapes called primitives, in order to build organ models. Examples of these primitives include cuboids, cylinders, prisms, pyramids, spheres, cones and ellipsoids surfaces that are easily described by quadric equations. In figure 1.3a and 1.3b, a CSG model of the left lung obtained from the subtraction of two ellipsoides is shown as an example (Xu et al. 2007). The main advantage of this approach is of being very computationally efficient, as most Monte Carlo codes provide fast methods for particle propagation through surface-equations-based geometries. Also, the use of CSG allows, in principle, the modelling of any structure of interest, even the smallest, without imposing limits on the model spatial resolution. Thus, currently available stylised phantoms, typically include Monte Carlo efficient models of the skin, the red marrow, hollow organs walls, and other small size structures that are hard to implement in voxel-based and BREP models.

Since these models were originally developed to perform radioprotection calculations, their geometry is defined on the basis of population averaged characteristics (height, body and organ weights). In some way, this feature represents both the strength and the weakness of anthropomorphic stylised models, when considering their use for clinical TRT dosimetry. On one hand, in fact, a preliminary determination of S values to be used

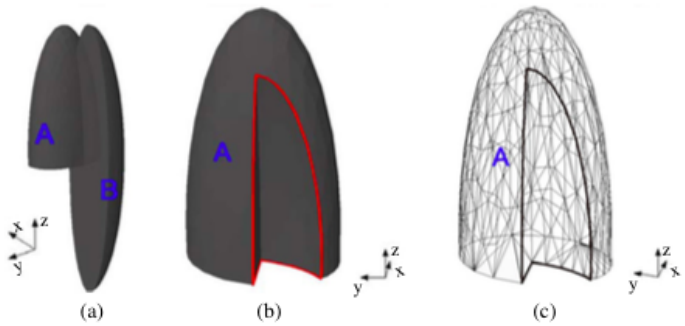

Figure 1.3: A model of the left lung defined by different modeling methods. (a) The CSG-type modeling before the Boolean operation (subtraction) is performed involving two ellipsoids A and B. (b) After the subtraction of B from A. (c) A BREP type of modeling of the same lung using a polygon mesh. Source: Xu et al. 2007

with any patient only makes sense if the model represents a wide range of anatomies. On the other, however, the use of a fixed geometry does not take into account inter-patient anatomical variability, and may significantly bias the absorbed doses obtained for some organs.

In addition, one of the main problem of CSG geometries, is that organs are well separated (see figures 1.4b and 1.4c as an example), while in reality they touch one another. As a result, the source organ sees the target organs under solid angles that differ significantly from those of actual patient anatomy, especially for larger source-target distances. Several authors (Lamart et al. 2011, Marcatili et al. 2015) have demonstrated that this difference may cause a relevant underestimation of the absorbed dose obtained from stylised models.

The early models developed were geometrically simplistic as necessitated by the limited computing power available at the time (1950 - 1960). In the sixties, Fisher and Snyder (Fisher and Snyder 1966, Fisher and Snyder 1967) who worked at Oak Ridge National Laboratory (ORNL), proposed one of the first humanoid model (in figure 1.4a, the adult phantom) composed of three main regions: the head and neck, the trunk including the arms, and the legs. About 120 sub-regions were defined in the model, which were used to assign approximate values of the absorbed dose to organs located within specific regions. The model was assumed to have homogenous tissue composition, and hence did not include any model of lungs and bones.

The first heterogeneous, hermaphroditic adult model was developed by Snyder and

colleagues in 1969 (Snyder et al. 1969). It was made up of three tissue types (skeletal, lung, and soft) and its organ masses were selected to match those of the Reference Man as described by ICRP Publication 23 (ICRP 1975). In 1978, an improved version of the Snyder model (see figure 1.4b), including more than 20 organs and more detailed anatomical features, was used to calculate absorbed dose fractions that appeared in the MIRD Pamphlet No. 5, Revised (Snyder et al. 1978). Because of its adoption by the MIRD Committee, the Snyder model is frequently referred to as the MIRD phantom.

More recently, the work of Cristy and Eckerman marked the beginning of the contemporary stylized models. The Cristy–Eckerman phantom family (Cristy and Eckerman 1987) is the series in most common use in current nuclear medicine dosimetry calculations. It consists of six models: the adult male and five pediatric examples (newborn, 1-, 5-, 10-, and 15-year old). The 15-year-old model was taken to be representative of the adult female. The adult male (see figure 1.4c), which is actually hermaphroditic, was very similar to the Fisher-Snyder model, with some minor modifications, and included some organs that the Fisher-Snyder model did not. Absorbed dose factors for this family of phantoms have been calculated for a large number of radionuclides, and are currently implemented in the software OLINDA/EXM (Stabin et al. 2005) which is intended for diagnostic dosimetry.

1.3.2.1 Voxel models

With the advent of medical imaging techniques such as CT and MRI, researchers could, for the first time, visualize the internal structures of the body in 3D and store the images in versatile digital formats. Medical image data could hence be converted to voxel geometry that provides a direct way of realistically describing the human anatomy. The model derived is made up of individual voxels which can then be segmented and grouped to isolate specific organs or suborgan structures as source and target regions. A specific material can in principle be assigned to each voxel in order to reproduce tissue heterogeneity encountered in the human body.

All voxel-based models developed from the 80's are either based on CT (Computed Tomography) and/or Magnetic Resonance (MR) images of living subjects, or on cross-sectional photographs of cadavers. Once the image data have been acquired, organs and tissues are consequently identified and tissue types and compositions assigned to segmented organs. For large, macroscopically-visible tissues, this segmentation, despite being

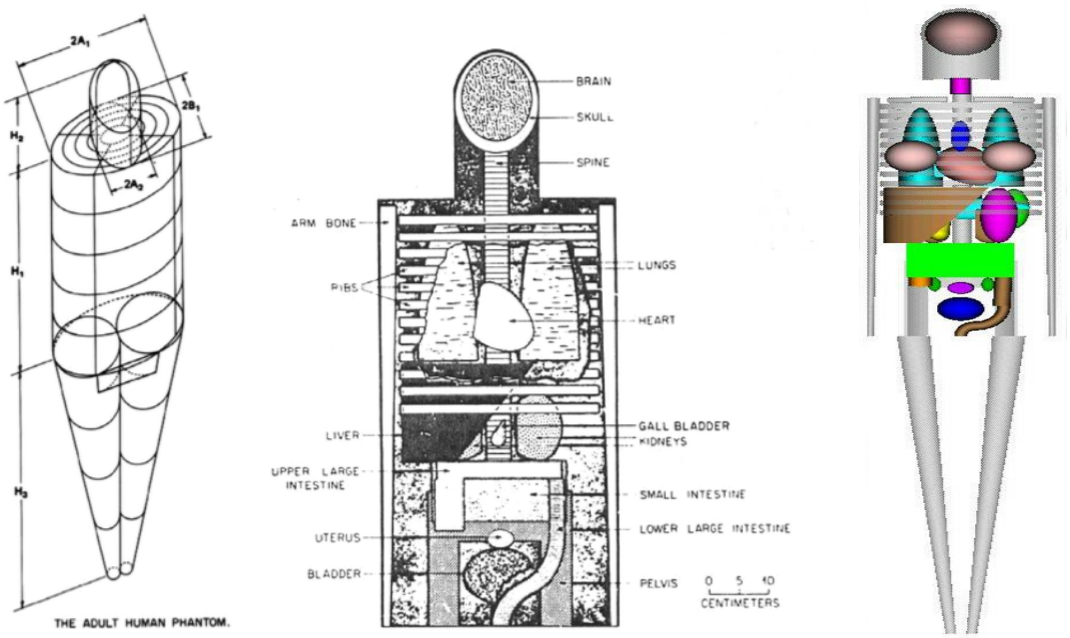

Figure 1.4: Examples of stylised models showing a different degree of anatomical detail. From left to right, the Snyder (Snyder et al. 1969), the MIRD (Snyder et al. 1978) and the OLINDA (Stabin et al. 2005) models are shown.

time-consuming, is relatively easy to implement. However, for tissues with spatial dimensions comparable to, or smaller than the image sampling (i.e. voxel dimension), special interventions are required in order to model the tissue. This problem has led, so far, to artificial solutions for the modelling of such structures. For example, the skin is often represented by adding a single voxel layer at body surface, however, the size of voxels is typically larger than skin actual thickness.

Indeed, the limited spatial sampling achievable is one of the main disadvantages of voxellised models dosimetry. The spatial sampling adopted ultimately depends on the spatial resolution of the imaging technique used to acquire the anatomical data. CT and MR tomographic images are composed of many slices, each constituted by a 2-dimensional pixel map of the anatomy. The typical pixel size is of the order of 1 mm^2, providing a quite accurate description of the transverse plane anatomy. However, along the longitudinal axis, image slices are generally acquired at higher sampling ($\sim$ 3-6 mm) in order to keep patient absorbed dose from X-rays as low as possible in the case of CT scans, or to reduce acquisition time in the case of MR imaging. The direct consequence of the low longitudinal resolution is the presence of stair-stepped artefacts in modeled organs, as

those shown in figure 1.6a (Lee et al. 2007). A possible approach to obtain improved resolution data, is to acquire tomographic 3D images or optical photographic cryosections from cadavers as was done in the Visible Human Project (VHP) (Xu et al. 2000). However, even if producing very-high-spatial-sampling whole body digital models is not inherently impossible, it should be remarked that such datasets would consist of billions of labelled voxels. Therefore, they would be hardly manageable by standard computers because of the required memory, and certainly nearly impossible to handle for any Monte Carlo code currently available.

Another aspect that should be considered when using voxel-based models, is that they are usually based on the anatomy of a single man or woman: this is the case, for example, of VoxelMan (Zubal et al. 1994), MAX (Male Adult voXel) and FAX (Female Adult voXel) models (Kramer et al. 2003, 2004). The generation of phantoms families that covers a wider range of anatomical characteristics, as the GSF (German National Research Centre for Environment and Health Gesellschaft für Strahlenforschung) phantom series (Williams et al. 1986, Zankl et al. 1988, Smith et al. 2000, Petoussi-Henss et al. 2002, Zankl et al. 2002, Fill. et al 2004, Becker. et al 2007, Zankl et al. 2005), only partially address the problem. A more effective solution consists in the development of voxel models based on the Reference Man anatomy. The earliest effort in this sense, was made by Kramer et al. (2006) who adjusted MAX and FAX models to Reference Man height and organ masses listed in ICRP Publication 89 (ICRP 2002). In 2009, the ICRP released to the public the Reference Male and the Reference Female (ICRP 2009) models adapted from the male and female models of the GSF serie and based on CT images of individuals close to the Reference Man and Woman. Body weight and height, and individual organs were adjusted to reference values by adding and subtracting voxels: these processes were extremely time-consuming as the voxel data format is difficult to deform, and the deformation generally produces several artificial holes. Tissues densities and compositions were those of ICRP Publication 89. In figure 1.5, the ICRP 110 female and male models are shown. They present different spatial samplings: a $1.775 \times 1.775 \times 4.84$ mm^3 voxel size was used for the women, and a $2.137 \times 2.137 \times 8.00$ mm^3 size for the man.

1.3.2.2 BREP models

The stylized and the voxel-based models represent two extremes. Clearly, the first is simplistic and representative of a defined Reference Man. The second, on the other hand,

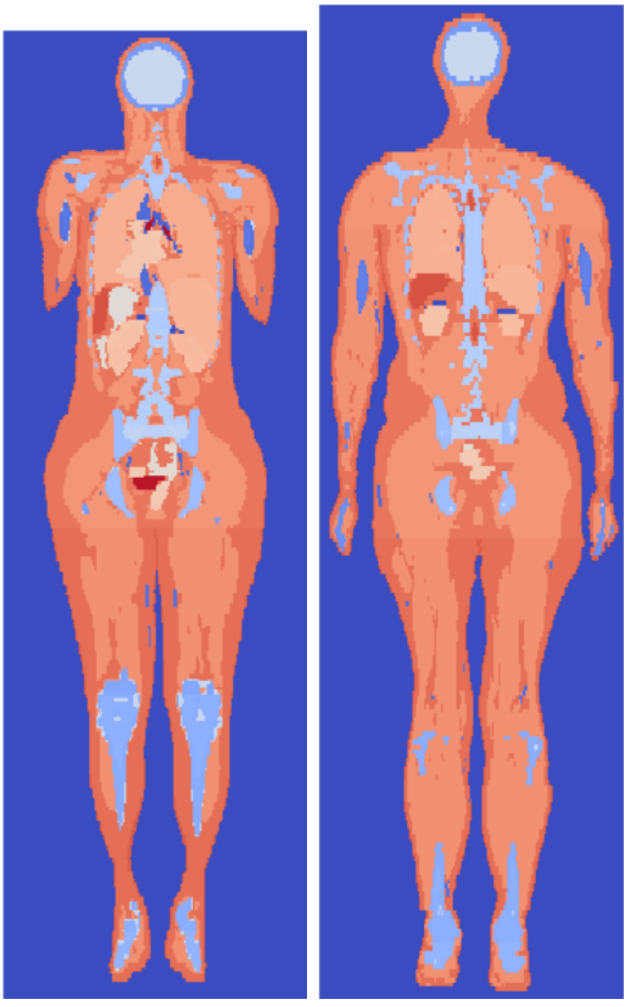

Figure 1.5: Female and male reference models from ICRP Publication no. 110 (ICRP 2009).

is far more realistic a representation of the anatomy and allows more comprehensive measures of the internal radiation dosimetry, despite being representative of the anatomy of a single individual (with few exceptions). The recent developments of boundary representations models (Leyton 2001, Stroud 2006) seeks to preserve both the anatomic realism of voxel phantoms and the mathematical flexibility of stylized phantoms creating models applicable to any individual. The most common technique to create a BREP-based model involves the surface contour extraction of each organ from a tomographic image dataset, followed by the integration of individual organs into a whole body assembly. In essence, the contours convert the voxels into Non Uniform Rational B Splines (NURBS) or polygonal mesh surfaces that are smooth and anatomically realistic. NURBS geometries are flexible and computationally efficient, but fine details may be lost on certain organs that have complex topology. On the other hand, polygonal models can be used to create very smooth surfaces with impressive anatomical detail, by paying the price of having a large number of vertices. As a results, NURBS are typically more efficient for real-time applications, as the representation of cardiac and respiratory motion. Nevertheless, both NURBS and polygonal meshes allow, through the use of mathematical transformations, to easily model variations in anatomy and differences in organ size and morphology. Thus, with respect to voxel-based models, they also permit a much easier construction of models whose anatomy approaches that of a given patient.

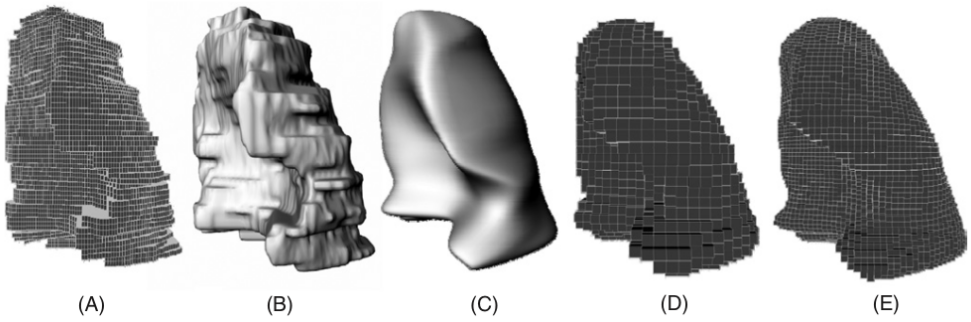

Figure 1.6: Example of the construction and voxelization of a BREP model, starting with (A) the original voxel model of newborn left lung, (B) its polygon mesh model, (C) its NURBS surface model and (D), (E) voxelized models at two different isotropic voxel sampling (2 mm and 1 mm, respectively). Source: Lee et al. 2007.

In figure 1.6, Lee et al. (2007) show the necessary steps to build a BREP model using the left lung as an example. Starting from a tomographic voxel dataset (A), they first build the polygonal mesh model (B). A mesh model would be based on structures of this type that undergo further manipulations as smoothing, to reduce the stairs-stepped artifacts, and volume scaling to adjust each organ to the desired mass value. Alternatively, the polygonal mesh model can be used to generate a NURBS surface model (C), providing a smoother, more realistic representation of the organ. However, as highlighted by Lee example, in both cases, the Monte Carlo simulation of BREP models requires their transformation into 3D voxel models (D,E), thus sacrificing the spatial resolution of the model itself.

Despite most modern Monte Carlo codes accepts the definition of BREP volumes, particle tracking through this kind of geometry is still extremely inefficient. In principle, anatomical realism could be preserved by resampling the BREP model into a high resolution voxel dataset; however, the number of voxels a Monte Carlo toolkit can handle is limited, and a too fine sampling easily results in memory faults and/or unreasonably long computational times.

Still, the BREP approach represents the most efficient strategy to generate families of phantoms (in figure 1.7, the RPI phantom serie) that fit the anatomical characteristics of a wide range of individuals. It should also be noted, that the voxelization of a BREP model allows, at least, having a uniform sampling in the three directions, thus reducing the spatial resolution problems typical of voxel-based models along the longitudinal axis. For these reasons, BREP models could be the ideal compromise between the need of precalculated S values, and the need for patient specificity. For the end user, the dosimetric assessment process remains simple to implement, while allowing a more personalised treatment planning.

Since 2000, many research groups have started the development of BREP models, and up to now, a total of about 200 models was reported (Xu 2014). Among the pioneers in this filed, Segars developed the well known NCAT model (Segars 2001) originated from the Visible Human CT dataset. The model was later extended (Segars et al. 2009) to include cardiac and respiratory motions using tagged MRI data from a living patient (4D-NCAT). More recently, the characteristics of the NCAT model were updated, and a family of 47 4D models representing the cardiac and repiratory motions of multiple patients was developed.

Figure 1.7: The RPI Adult Male (top) and Adult Female (bottom) models representing the 5th, 25th, 50th, 75th, and 95th weight percentiles (from left to right). Source: Na et al. 2010.

The male and female model of this family are based on the high resolution Visible Male and Female anatomical datasets. Despite these models were mainly conceived and used for medical imaging applications, absorbed dose fractions for ^{177}Lu and three individual voxel models from the XCAT population were recently calculated at Lund University (Brolin et al. 2015).

Between the many research groups involved in BREP models development, two of them are particularly prolific.

At RPI (Rensselaer Polytechnic Institute, Troy, New York, USA), Xu et al. generated a pair of models called RPI Adult Male and Adult Female (Zhang et al 2009), with more than 70 organs and 45 bones adjusted to match ICRP 89 reference values. In a subsequent work, the RPI Adult Male and Adult Female models (shown in figure 1.7) were extended into weight-specific models representing the 5^{th}, 25^{th}, 50^{th}, 75^{th}, and 95^{th} weight percentiles (Na et al 2010), and to describe overweight and obese patients (Ding et al 2012). At RPI, they also developed a set of female models at the end of three gestational periods (3, 6 and 9 months) called RPI-P3, RPI-P6 and RPI-P9 (Xu et al 2007).

Bolch and colleagues at University of California, proposed a family of phantoms, known as the UF family, of both genders and children of various ages (Lee et al 2007, 2008, 2010; Bolch et al 2010), and also including fetal models (Maynard et al 2011). In 2008, ICRP established that its future reference models for pediatric individuals would be based upon the UF series. Recently, Zaidi and colleagues, have used the UF models for a number of nuclear medicine absorbed dose calculations (Xie et al 2013, Xie and Zaidi 2014).

1.3.3 Small animal models

Absorbed dose assessment in rodents is a mandatory step for the evaluation of toxicity and efficacy of novel radiopharmaceuticals before their test on humans. In the last 20 years, following the developments in human model research, several digital models have been proposed for the calculation of organ absorbed dose in mouse and rats. Most of these models are in the form of stylised (Hui et al. 1994, Flynn et al. 2001, Hindorf et al. 2004) or voxel-based models (Stabin, Dogdas et al. 2007, Bitar et al. 2007), obtained either from MR/CT tomographic images, or from photographic acquisitions of mice cryosections. As their anthropomorphic counterparts, the first suffer of a poor anatomical realism, while the second are usually derived from a specific subject of a given specie, and hence their range of applicability remains limited. Using mathematical, stylized models, Hindorf et

al. (2004) showed a notable effect on mouse dosimetry when geometric differences such as organ mass, organ shape, and the relative locations of organs to one another are considered. This effect is particularly pronounced for high energy β-emitters, whose particle range is comparable to the size of mice anatomical structures.

In 2004, following the conceptual design of the human model NCAT, Segars et al. developed the first mouse (MOBY) and rat (ROBY) 4D digital models based on NURBS (Segars et al. 2004, Segars and Tsui 2007, Segars et al. 2010a). These models are available through a computer program that allows deforming mouse/rat body as a whole, or each organ separately. A 3D voxel image is then generated for its Monte Carlo implementation. Originally conceived for imaging applications, these models have been used by several authors to calculate organs S values for TRT dosimetry (Larsson et al. 2007, Keenan et al. 2010, Xie and Zaidi 2013).

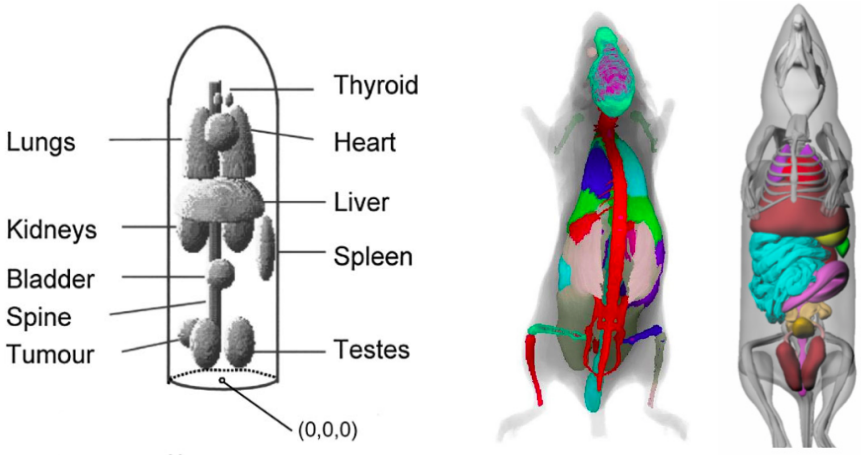

Figure 1.8: Examples of stylised (Hindorf et al. 2004), voxel-based (Bitar et al. 2007) and NURBS (Segars et al. 2004) mouse models.

1.3.4 Cellular models

In a context of cellular dosimetry, cell geometry is typically represented by two concentric homogeneous spheres of density 1 g/cm^3, with the radii of the whole cell and of the nucleus designated as R_c and R_n respectively (see figure 1.9). The radionuclide is assumed to be uniformly distributed in one of the cellular compartment: the nucleus, the cytoplasm, or the cell surface. This very simple model can take into account variations of cell and

nucleus size, but neglects radioactivity distribution heterogeneity within a compartment, and asymmetries in cellular shape. For the calculation of cross-irradiation absorbed dose in multi-cellular systems, replicas of the single cell model are usually arranged according to the selected spatial distribution.

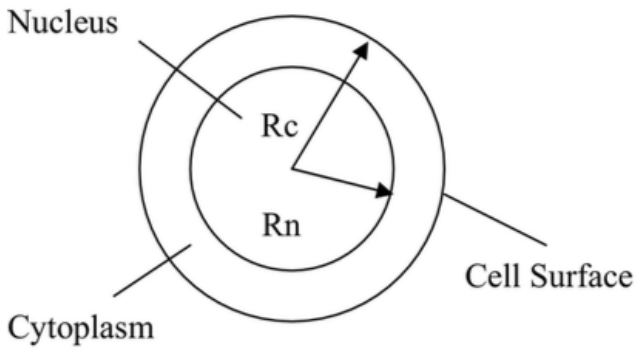

Figure 1.9: Spherical symmetric model of cell geometry. R_n and R_c indicate nucleus and cell radii respectively. Source: Roeske et al. 2008

The symmetric cellular model has been used extensively for the generation of cellular S values. Some authors (Goddu. et al 1997, Vaziri et al. 2014, Emfietzoglou et al 2008) implemented an analytical approach integrating particle stopping powers over cell geometries and radionuclide energy spectrum. Typically, experimentally determined relationship between electron energy and range have been used for electrons (Cole 1969, Howell 1989), and tabulated stopping power for α-particles (ICRU 1993). Photons and secondary electrons were usually neglected in the analytical calculation. Other authors, made use of pre-calculated Dose Point Kernels (see section 1.4.2) (Bardiès and Chatal 1994, Bardiès et al. 1990, Faraggi et al. 1998, Hartman et al. 2000) or direct Monte Carlo radiation transport (Cai et al. 2010, Bousis et al. 2010).

The work of Goddu. et al (1997) is of particular importance in this area of research, as they generated cellular S values for different compartments and different cell/nucleus radii, and 287 radionuclides. In the same publications, they also showed the effect of cell model geometry on the absorbed dose to various compartments. Performing Monte Carlo simulations of mono-energetic electron sources in ellipsoidal cells, they demonstrated that asymmetries in the geometry may significantly impact nucleus absorbed doses, in

particular for low energies electrons (5 keV) and for source distributed at cell surface. For other source-target compartments, the differences between S values calculated in the spherical and in the elliptical configurations resulted of minor importance. More recently, a similar work by Amato et al. (2011), showed the necessity of applying geometrical corrective factors for cell shapes that differ significantly from a sphere.

1.4 Computational methods for voxel dosimetry

While reference models are valuable for defining idealized exposures conditions and for calculating S values for radiological protection, they are of much more limited use in assigning organ absorbed doses for TRT treatments, especially when the individual patient has a body morphometry far from the 50^{th} height/weight percentile. In addition, model based dosimetry neglects, by its own nature, heterogeneities in tissue compositions and radioactivity distributions. The same considerations hold for small animal dosimetry. In the specific case of cellular dosimetry, on the other hand, considering all cells as spherical and symmetric, is the equivalent of using a Reference Man for clinical dosimetry. Also, non-uniform radiopharmaceutical uptake within a cellular compartment may considerably impact cell absorbed dose in the case of high LET emitters (α, Auger), in the same way β-emitter heterogeneity can impact dosimetry at the human scale.

In order to provide means for a more accurate absorbed dose assessment in TRT applications, different computational methods have been proposed that take into account realistic activity distributions and/or actual tissue composition with different levels of accuracy. These techniques, valid at cellular, tissue or human scale, are based on the availability of imaging tools capable of quantifying activity distribution and tissue density in a given biological system. The resulting datasets are usually in the form of 2D or 3D voxel maps. In the case of clinical dosimetry, PET or SPECT images are generally employed to assess personalised 3D radiopharmaceutical distributions, while CT is used to produce maps of tissue compositions. For cellular and *ex-vivo* mouse dosimetry, digital autoradiography (DAR) is most often used for the determination of activity uptake distributions. In the case of *in-vivo* small animal dosimetry, dedicate PET, SPECT or CT scanner can also be used in analogy with the techniques implemented in the clinic.

Even if voxel-based computational methods are very attractive, as they allow in principle a higher deegree of accuracy in the determination of the absorbed dose for a specific

system, still, they all present the same weakness. These approaches demand, in fact, the establishment of cumulated activities at the voxel level; this requires the co-registration, with sub-voxel precision, of PET, SPECT or DAR images taken at different times. As a matter of fact, sophisticated co-registration software that is not generally available to the general user, would be needed to achieve this task.

1.4.1 Analytical approach

Under the assumption of homogenous propagating medium, the absorbed dose at a given point only depends on its distance from the radiation emission point. In these conditions, the function describing the energy deposition in a target point can be expressed analytically and subsequently integrated over the target volume in order to obtain its average absorbed dose.

Historically, analytical methods were the first developed for the calculation of the internal absorbed dose. In principle, they allow taking into account activity heterogeneity in the source region, and to score the absorbed dose in complex geometries. However, their practical implementation is mathematically challenging in most cases, with the exception of their application to simple geometrical shapes as spheres. For this reason, with the development of the Dose Point Kernel and the Monte Carlo approaches (see next paragraphs), analytical methods were progressively abandoned. However, their implementation in cellular dosimetry remains relevant and cellular S values calculated with this approach are still used nowadays (Goddu et al. 1997).

In this case, given the reduced size of cells, photon emissions can be neglected and the calculation of cellular absorbed dose can be restrained to the integration of particle stopping powers over cell geometry. Mathematically, the absorbed fraction $\phi(r_T \leftarrow r_S, E_i)$ defined in paragraph 1.2.2, can be expressed, for the i^{th} mono-energetic particle, as:

$$\phi_i(r_T \leftarrow r_S, E_i) = \int_0^{\infty} \Psi_{r_T \leftarrow r_S}(x) \frac{1}{E_i} \frac{\mathrm{d}E}{\mathrm{d}X}\bigg|_{X(E_i)-x} \mathrm{d}x \tag{1.4.6}$$

where E_i is the initial energy of the i^{th} particle, $\Psi_{r_T \leftarrow r_S}(x)$ is the geometric reduction factor, and $\mathrm{d}E/\mathrm{d}X|_{X(E_i)-x}$ is the stopping power evaluated at $X(E_i) - x$, the residual range of particle with initial energy E_i, after passing a distance of x through the medium. The geometric reduction factor represent the mean probability that a randomly directed

vector of length x, starting from a random point in the source region r_S, ends within the target region r_T. Its value depends on source and target geometries; explicit functions for $\Psi_{r_T \leftarrow r_S}(x)$ have been derived by several authors for cellular dosimetry in self- and cross-irradiation conditions (Howell et al. 1990, Goddu et al. 1994a, 1994b).

For electron dosimetry, the implementation of equation 1.4.6 usually reposes on the analytical fit of stopping powers data (Cole 1969); for alpha particles, tabulated stopping powers in water are typically used (ICRU 1993). In the case of radionuclides, equation 1.4.6 should be integrated over the radionuclide spectrum, considering both mono-energetic and beta-particle emissions.

1.4.2 Dose point kernel approach

A Dose Point Kernel (DPK) is defined as the radial distribution of absorbed dose around an isotropic point source in an infinite homogeneous propagation medium (Bardiès et al. 2003). DPKs can be calculated analytically in the Continuous Slowing Down Approximation approximation[2] (CSDA) (Prestwich et al. 1989a, Berger 1971) or using the Monte Carlo technique (Berger 1973, Papadimitroulas et al. 2012, Furhang et al. 1996, Botta 2011); in both cases, a punctual source (mono-energetic photons, electrons sources or the whole spectrum of a radionuclide) is modelled, and its energy scored in concentric spherical shells. The absorbed dose in a point located at distance r from the source, is then obtained by dividing the absorbed dose scored in the shell by the shell volume. Shell thickness must be negligible with respect to the CSDA range of the simulated particle, in order to avoid sampling errors.

DPKs can be used to produce 3D absorbed dose distributions from cumulated activity maps. This requires the integration of kernels over the voxel geometry defined by the cumulated activity map available. A simpler approach consists in assuming the source located at the center of the source voxel, and to calculate the absorbed dose at the target voxel center. For increased accuracy, the activity may be considered uniformly distributed in the source voxel, to perform a volume integration over both source and target voxels.

The use of point kernel methods, however, is restricted to homogenous tissue regions. Indeed, the shape of DPKs is significantly affected in the presence of tissue heterogeneities,

[2]In the CSDA regime, charged particles are assumed to lose their energy continuously at a rate given by the stopping power. No secondary electrons (delta rays) or photons (bremsstrahlung radiation) are considered in this approximation.

especially at tissue interfaces (Pérez et al. 2011).

1.4.3 Dose voxel kernel approach

The MIRD schema described in section 1.2 for region-averaged dosimetry, can be extended to take into account variations of the cumulated activity at the voxel level (Bolch et al. 1999). The absorbed dose to a target voxel v_T due to the cumulated activities in source voxels v_S can be expressed as:

$$D(v_T) = \sum_{S=0}^{N} \tilde{A}(v_S) S(v_T \leftarrow v_S) \tag{1.4.7}$$

where the sum is extended to all source voxels. The voxel S value is defined as the absorbed dose to the target voxel per unit decay in the source voxel, when they both are contained in an infinite homogeneous medium.

According to this definition, Dose Voxel Kernels (DVK) can be obtained by Monte Carlo simulation of voxel geometries representing an infinite medium of uniform composition; the radionuclide source is placed at the center of this geometry, and the absorbed dose is scored in surrounding voxels. The mathematical convolution of pre-calculated DVKs with a cumulated activity map provides the absorbed dose distribution for the biological system considered.

A necessary condition for the application of this method, is for the DVK sampling to match the cumulated activity image voxel size. This requires the generation of dedicate kernels, not only for each radionuclide of interest, but also for any possible sampling. However, in clinical TRT dosimetry for example, the variability of voxel sizes selected for SPECT and PET images can be remarkable. Not to mention the many different voxel sizes needed to cover dosimetric applications at the cellular, animal and clinical scales.

Several groups (Bolch et al 1999, Lanconelli et al. 2012, Amato et al. 2013) have published DVKs for most radionuclides commonly used in TRT, and a few voxel sizes that are supposed to reasonably cover the needs of clinical dosimetry. More recently, some authors (Dieudonné et al. 2010, Fernández et al. 2013) proposed analytical methods to scale DVKs simulated for a determined geometry sampling to the desired voxel size. Amato et al. (2012), generalised this approach to obtain an analytical formulation of DVKs for any radionuclide.

An inherent limitation of the DVK approach is that, in principle, heterogeneities in the propagation medium cannot be accounted for. Thus, its implementation in anatomical areas including bone and lung tissue is not recommendable, as the resulting absorbed dose could be significantly biased. On the other hand, their use in regions containing organs with density and composition that can be assimilated to soft tissue, is generally not problematic. In the specific case of cellular dosimetry, the biological systems considered are usually assigned unit density compositions anyway, and a DVK approach is hence appropriate. Still, a simple way to correct, although in part, for tissue heterogeneity has been proposed and tested in a clinical application involving dosimetric calculations in the abdomen (Dieudonné et al. 2013). With this approach, the dose voxel kernel $D(v_T)$ in a target voxel v_T is scaled by the voxel actual tissue density ρ_T:

$$D(v_T, \rho_T) = D(v_T)\frac{\rho}{\rho_T} \tag{1.4.8}$$

where ρ is the material density implemented in the MC simulation of the non-corrected kernels. Obviously this method does not account for tissue heterogeneities that are encountered by the particle along its track. Its applicability to highly heterogeneous anatomical regions is hence questionable.

1.4.4 Monte Carlo based dosimetry

Direct Monte Carlo radiation transport in voxel geometries is considered nowadays the most accurate approach to TRT dosimetry at any scale, as it allows taking into account both tissue density and radioactivity heterogeneity. This kind of calculations, in fact, is based on the acquisition of 3D voxel images describing tissue compositions (typically CT or MR for *in-vivo* dosimetry) and activity distribution (PET or SPECT for *in-vivo* dosimetry, DAR for *ex-vivo* dosimetry of tissue samples and cells) of the biological system considered. Typically, the radioactivity distribution is assessed at different times (after the injection of a limited amount of radioactivity in the case of clinical TRT) in order to obtain time-activity curves (either at the voxel or at the organ level) that are employed to build a cumulated activity voxel image. This image acts as an emission probability chart for the definition of virtual voxel sources in the Monte Carlo simulation: homogeneously distributed, isotropic radioactive sources are hence created in each voxel. For each radio-

nuclide decay, the emitted radiation is typically tracked in a voxel geometry defined from the morphological image acquired: a different tag, corresponding to a specific material, may in principle be assigned to each voxel. The interaction between radionuclide emissions and the tissue can hence be modelled taking into account all the different materials crossed by the particle along its track.

A number of MC codes have been developed for 3D patient-specific absorbed dose calculation in clinical TRT, implementing different approaches. Most of these codes assume homogeneous activity distributions inside organs and lesions (Lehmann et al 2005, Yoriyaz et al 2001), or use a partition-level approach (Song et al 2006, Yoriyaz et al 2001), while others fully model patient's functional and morphological images (Dewaraja et al 2005, Dewaraja et al 2010, Hobbs et al 2009, Chiavassa et al 2006, Marcatili et al. 2013). Figure 1.10 shows the typical output of a Monte Carlo based dosimetric application. Nevertheless,

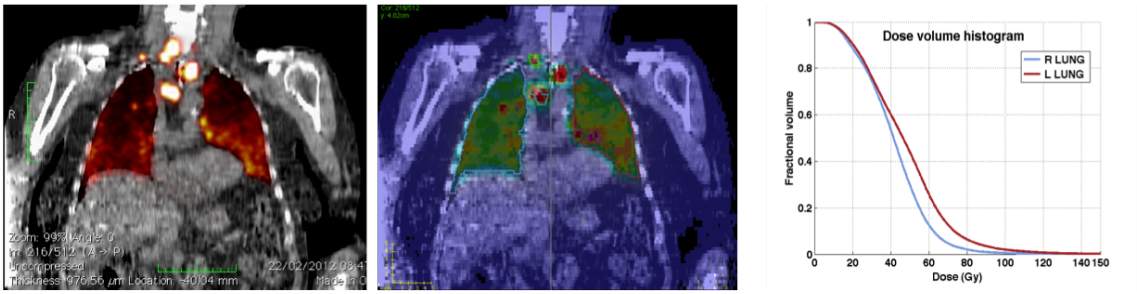

Figure 1.10: Patient-specific dosimetry obtained with the RAYDOSE software (Marcatili et al. 2013) for a ^{124}I/^{131}I matched-pair TRT treatment. From left to right: ^{124}I PET/CT images at 24 hours post injection, ^{131}I absorbed dose 3D image, and Dose Volume Histrograms in the lungs.

despite being highly promising and desirable, the direct Monte Carlo approach is still far from being introduced in day-to-day clinical practice, and is more likely to be used for research purposes. This lack of success depends on different factors. The main limitation lies in the need for highly-processed input datas. The generation of the cumulated activity map requires, in fact, a carefull co-registration of the functional images acquired with a sub-voxel level of accuracy. Not only this process can be very time-consuming, but also, the achievement of a viable result is not always guaranteed as the main sources of image misalignment (patient movement and breathing) are not easily corrected via software. Another difficulty to overcome is the resistance of patients and the medical staff to the

acquisition of multiple SPECT or PET images for routine treatments, using the tracer amount of activity needed to adequately characterize the dosimetry. Finally, the long computation times needed to obtain a personalised absorbed dose distribution are often incompatible with the tight organisation of a Nuclear Medicine department.

The Monte Carlo may, in principle, be applied to small animal *in-vivo* dosimetry. The availability of dedicated PET, SPECT, CT and MRI scanners, makes it possible to acquire sequential images of the same mouse and hence to implement Monte Carlo based voxel dosimetry. However, this is not usually done. On one hand, in fact, the assessment of the average absorbed dose after mouse sacrifice and biopsy is much quicker and easier. On the other, the lack of dedicated quantitative reconstruction algorithms for preclinical scanners, and the impossibility to implement user-defined data reconstruction on commercial systems, results in a very approximate determination of organ uptake which diminishes the relevance of sophisticated dosimetric calculation.

A few examples of Monte Carlo cellular dosimetry have also been reported. Despite the need for tissue heterogeneity modelling is limited in this context, as cells are generally assumed to be homogeneously composed by water, this approach is useful to take into account uptake heterogeneity within the cell, or for a group of cells. Arnaud (2013) calculated the absorbed dose distribution for a realistic cell geometry and source distribution issued from immunofluorescence microscopy, in the case of Auger electrons from ^{125}I. His work demonstrated that, in the case of high LET radiations, the nucleus absorbed dose obtained in realistic conditions may be significantly different from that obtained with a spherical symmetric cellular model. The Monte Carlo approach was also used to model complex multi-cellular systems (Malaroda et al. 2003, Rajon et al. 2011).

In the last decades, many different Monte Carlo toolkits have been employed for TRT dosimetry. Traditionally, codes as EGS, with its modern version EGSnrc (Kawrakow and Rogers 2003), and MCNPx (Briesmeister 2000), have been considered the reference for the simulation of radiotherapy experiments involving electron-photon transport at low energies (down to 1 keV). More recently, the work undertaken by the "low energy electromagnetic physics"work group, has made the Monte Carlo code Geant4 a most valuable tool for the simulation of electromagnetic interactions of photons, electrons, hadrons and ions with matter, down to very low energies (eV scale). In 2004 Gate, a user-friendly MC toolkit based on Geant4 and dedicated to medical physics applications, was developed. Since

then, Geant4 and Gate are being increasingly used and trusted by the medical physics community.

1.4.4.1 Geant4

Geant4 (Geometry and tracking) is a general-purpose, open-source Monte Carlo toolkit originally developed at CERN (European Organization for Nuclear Research) for the simulation of high energy physics experiments (Agostinelli et al. 2003). Nowadays, it is also used for nuclear and accelerator physics, as well as studies in medical and space science. Geant4 allows modelling complex geometries and particle source characteristics to virtually reproduce any possible experimental condition. The user can build his/her own application on the basis of predefined `C++` classes that handle geometry and source definition, and particle tracking and interaction at a lower level. Geant4 also offers numerous physics models to describe the interaction of radiation with matter in different energy ranges. Of particular interest for radiotherapy applications, are the Livermore models (Chauvie et al 2004) for the simulation of electromagnetic interactions down to 250 eV. These models are based on the evaluated tables from LLNL (Lawrence Livermore National Laboratory): EPDL97 (Cullen et al 1997), EEDL (Perkins et al 1991a) and EADL (Perkins et al 1991b), and they have already been validated by several authors for TRT applications (Maigne et al 2011, Papadimitroulas et al 2012, Amato et al 2013, Mauxion et al 2013). More recently, the Geant-4 DNA collaboration also developed physics models for the simulation of early biological damage induced by ionising radiation at the DNA scale (Chauvie et al. 2006).

1.4.4.2 Gate

The MC toolkit Gate (Geant4 Application for Emission Tomography) is an open source code originally dedicated to nuclear medicine imaging, and based on the Geant4 generic MC toolkit (Jan et al. 2004). It currently supports modelling of Emission Tomography (PET and SPECT) and Computed Tomography (CT). Since version 6.0 it also allows scoring absorbed doses in defined volumes or voxels for radiotherapy applications. In particular, Gate permits an accurate description of time-dependent phenomena that are not possible to include in a single Geant4 simulation.

Gate is conceived as a layer of `C++` classes built on top of the Genat4 core, in order to allow a more straightforward description of medical physics experiments (both for imaging

and radiotherapy applications). The same physics models available in Geant4 are hence maintained, while the definition of source and geometry is made easier for the end user. Unlike Geant4, the use of Gate does not require any particular coding skill, since the simulation can be set up by simple macro scripting.

1.5 TRT dosimetry optimisation at different scales

Depending on the size of the source and target regions identified, and depending on the particles range in tissue for the radionuclide selected, the dosimetric model adopted may rely on different hypotheses/approximations. Next sections provide a quick review of the peculiarities of TRT dosimetry in different experimental contexts. The most common issues encountered at the cellular, animal and clinical scales, and their possible solutions are analysed, providing means for TRT optimisation.

1.5.1 Cellular dosimetry

The derivation of new radiobiological parameters is performed through survival experiments in cell colonies. Survival curves are usually expressed in terms of administered activity. However, establishing cell survival in terms of absorbed dose is crucial to investigate the absorbed dose-effect relationship, especially at very low doses: the lack of correlation could, for example, indicate the presence of bystander effect (Chouin et al. 2009). To a first approximation, cell absorbed dose can be calculated, on the basis of MIRD schema, summing up the contribution of cell self-absorption and cross-irradiation, plus the contribution of radioactivity in the culture medium, when relevant. However, this approach only offers an absorbed dose estimation of limited accuracy. Within the same colony, cells may have different sizes, different levels of radioactivity internalisation and different intracellular activity distributions: this reflects the high level of heterogeneity displayed by a tissue *in vivo*. Therefore, depending on the type of emissions involved, the dosimetric calculation should attain different levels of "realism". So, while for β-emitters it is usually not essential to model cellular uptake heterogeneity and actual cell shape/size, in the case of alpha and Augers this is crucial in order to obtain sound dosimetric results (Arnaud 2013, Roeske 2008). Conversely, β-emitters dosimetry requires a special attention to the calculation of the cross-irradiation absorbed dose, since this may be significantly higher than self-absorbed dose, especially for large colonies or clusters of cells (Goddu et

al. 1994b). Moreover, since the cross-irradiation strictly depends on the spatial distribution of cells within the culture, realistic modelling of the experimental conditions are generally required, as demonstrated in chapter 2.

Another aspect to consider for dosimetry at the cellular scale, is also the stochastic nature of energy deposition. Use of the average absorbed dose to an individual cell, in fact, assumes that equilibrium conditions are satisfied with respect to the number and type of particles entering and exiting a given calculation volume. For low LET radiation, this condition is generally verified, as a large number of decays is required to deposit a considerable dose. However, this assumption may not be valid when there is a very inhomogeneous cellular uptake or the cellular absorbed dose is low. In the case of α-particles, for which only a few cellular decays are required to cause radiation-induced effects (Roeske 2008), this assumption may also not be appropriate. In these cases, stochastic dosimetric methods (micro-dosimetry) may be required (Bardiès and Pihet 2000).

1.5.2 Small animal dosimetry

Small animal absorbed dose assessment is required during radiopharmaceuticals development to document and compare the risks associated with the use of unsealed sources of radiations. In addition, small animal dosimetry may be necessary to establish the relationship between absorbed dose and biological effect during preclinical TRT. Conventional pharmacokinetics assessment is usually performed by counting radioactivity present in tissues samples after animal sacrifice, at various time points after the administration of the radiopharmaceutical. Organ S values obtained from Monte Carlo mouse models are then used to obtain the organ absorbed dose. For tumours, in analogy with model-based clinical dosimetry, water sphere S values are employed.

However, this approach is limited (but simple to implement) as it only provides mean activity concentration in a given sample, thus restraining absorbed dose determination to whole organs or tumours (activity heterogeneity within the tissue/organ is not taken into account). In addition, the radiopharmaceutical kinetics is extracted from different mice at different time points: this technique is not ideal as inter-subjects variability could possibly bias the shape of the biodistribution. Even if each point of the time-activity curve is generally averaged over kinetic data from a few mice, the resulting curve is not necessarily the same one would obtain averaging mouse-specific biodistributions (as it is usually done in Phase I human studies).

A possibly more rigorous method would consist in performing longitudinal mouse imaging studies employing small animal PET or SPECT scanner. However, the technical difficulties associated to small animal scanner calibration for quantitative imaging, makes this approach difficult to implement for non-experts.

As described in section 1.2, the absorbed dose to an organ is computed as the sum of the contributions of radioactivity in the organ itself (self-absorbed dose) and in surrounding structures (cross-absorbed dose). In clinical applications, the cross-absorbed dose mainly depends on photon irradiation: as a consequence, for most radionuclides employed in therapy, its values is low compared to the self-absorbed component. On the contrary, for small animals, whose organ's size is of the same order of the range of particles involved, the cross-irradiation may be substantial, especially for long range β-emitters. As the cross-absorbed dose depends on the shape and size of organs, as well as on their relative placement in the virtual model adopted for the simulation, any approximation introduce at this level may remarkably impact the dosimetry (Boutaleb et al. 2009, Hindorf et al. 2004). The higher level of organ cross-irradiation, also produces indirect consequences to the absorbed dose extrapolated to humans, for experiments aiming at evaluating novel radiopharmaceuticals: the preclical study, in fact, may potentially predict higher toxicities for non-source organs, that are not going to be observed in the Phase I study.

At the same time, given the relative dimensions of organ size and β-particle range, the self-absorption approximation generally adopted in preclinical experiments, is not always appropriate, as demonstrated by Konijnenberg et al. (2007) for energetic β-particles from ^{90}Y. Irradiation from surrounding tissue can, in fact, play a relevant role in tumour absorbed dose, making the use of mice models including tumour models recommendable (Larsson et al. 2011). On the other hand, however, the impact of heterogeneous distributions of β-emitting radiopharmaceuticals can generally be neglected, as long range particles contribute to the irradiation of tumours areas where the pharmaceutical is not directly bound, thus producing smooth absorbed dose distributions.

This is not necessarily true for high LET radiations (Auger electrons, α-particles) that deposits their energy locally. The particle range is, in fact, much shorter than typical tumour sizes encountered in mice experiments. As a consequence, any heterogeneity evidenced in the radioactivity distribution persist in the absorbed dose distribution. Tumour dosimetry based on average activity determination (i.e. through gamma counting) may lead, in this case, to a wrong interpretation of the efficacy of the radiopharmaceutical

under investigation, as shown in chapter 3.

1.5.3 Clinical dosimetry

In a typical clinical scenario, 2D (planar scintigraphy) or 3D (SPECT or PET) patient images acquired at different times after radiopharmaceutical injection, are used to build time-activity curves for the organs of interest and the tumour(s), and to calculate the corresponding cumulated activities. Generally, a uniform uptake within each Volume Of Interest (VOI) is assumed. Then, the absorbed dose to each VOI is computed from the MIRD formula (equation 1.2.2) using tabulated organ S values. For tumour dosimetry, water spheres S values are typically employed.

In the case of organ dosimetry, S values are often calculated by Monte Carlo simulation of anthropomorphic models. For these calculations, radionuclide emissions are usually categorised in two groups according to their absorption properties: α, β and Auger emissions are usually assumed to release all their energy within the tissue of origin; photons, depending on their energy, are absorbed in both source organ and surrounding tissues. While the self-absorption hypothesis is certainly valid, at the human scale, for Auger and α-emissions having a range in tissue from nanometers to $\sim$100 μm, for β-particles this is not necessarily true. High energy β-particles, as those from ^{90}Y, can have ranges up to a cm, and hence produce a measurable absorbed dose in adjacent organs. Nevertheless, because of their limited range, their irradiation may only affect a restricted area of the target organs. Also, the probability of an energetic beta particle escaping the source organ remains low, thus leading to very slow statistical convergence of the MC simulation. Under these conditions, the calculation of the average beta absorbed dose to the target organ may be critical, and the relevance of averaging the absorbed dose over the whole volume may be questionable. As a consequence, considering the small absorbed doses involved, beta cross-irradiation is usually neglected.

Another approximation that is often adopted, is to neglect the effect of bremsstrahlung radiation on the cross-dose. However, as demonstrated by Stabin et al. (1994), although the bremsstrahlung-related absorbed dose can be much smaller than that due to the β-particles themselves (e.g., by a factor of 1,000 at a distance of 1 mm from the source in soft tissue), the absorbed doses of both mechanisms equate at distances of about 1 cm for ^{90}Y. Hence, depending upon the β-particle kinetic energy spectrum and the amount of activity of the β-emitting radionuclide, energy deposition to surrounding organs due to

bremsstrahlung may not be negligible (Williams et al. 1989). Since the bremsstrahlung cross section scales as m^{-2}, where m is the charged particle's mass, the radiation emitted by a decelerating α-particle at the energies typical of a decay, may be safely neglected. On the other hand, positrons emit bremsstrahlung, but their radiative yield becomes comparable to those of electrons only at kinetic energies exceeding about 75 keV (McParland 2010).

As seen in section 1.4.4, a more personalised approach to clinical dosimetry can be achieved through direct radiation transport in voxel geometries representing patient-specific tissue compositions and activity distributions. Monte Carlo simulation can easily be configured to take into account all physical processes of interest, without the need of making approximations on the radionuclide emission spectrum and particles penetration. Still, the use of MC dosimetry in clinical routine is limited for the reasons previously discussed.

1.5.3.1 Multi-resolution dosimetry

One of the limiting factors to the achievement of accurate personalised dosimetry is the use of low resolution anatomical models either coming from patient-specific imaging or anthropomorphic models. In the first case the spatial sampling is limited by the intrinsic resolution of the imaging technique used to assess tissue ($\sim$ 1 mm) and activity ($\sim$ 1 cm) distributions *in vivo*. In the case of virtual models, even when they are highly anatomically realistic in their NURBS form, when used in their voxel form they present the same limitations as patient images. The ultimate problem is, in fact, that currently available Monte Carlo codes, are not optimised for the simulation of BREP geometries, thus requiring the implementation of voxel geometries. At the same time, only a limited number of voxels can be defined within a single simulation in order to keep computation times reasonably low and mostly to avoid saturating the computer memory. Even if these constraints are not impedimental in the vast majority of clinical applications, they pose obvious difficulties in the determination of the absorbed dose to small (with respect to the spatial sampling of the model adopted) anatomical structures. This is particularly true for a small radiosensitive organ as the red marrow, but also for the eye, the skin, and hollow organ walls in general. In chapter 5, a multi-resolution approach is proposed, to obtain high resolution absorbed dose distributions in selected organs of interest, while keeping simulation time and memory consumption low. This method is based on the use of voxels of different

sizes to represent regions of different anatomical interest, and was validated as a proof of principle example involving beta dosimetry to the bladder wall.

1.6 Conclusions

Several approaches are currently available for the calculation of the internal absorbed dose in different TRT applications. Some of them are quite approximate as they only allow establishing average absorbed doses to macroscopic regions on the basis of pre-defined virtual geometries (model-based dosimetry), but offer the advantage of being of easy and fast implementation. Other methods allow increasing dosimetric accuracy at different levels, offering the possibility to take into account activity and/or tissue density heterogeneities (voxel-based dosimetry), and actual geometry of the biological system considered. Nevertheless, all dosimetric strategies described in this chapter are in principle equally valid and it would be incorrect to establish a priori which method is the best, without contextualising its application. Indeed, the pertinence of a given dosimetric approach is strictly related to the penetrating or non-penetrating character of the radiation involved, with respect to the characteristic size of the propagating medium considered. In this sense, TRT dosimetry optimisation implies choosing the most appropriate approach for the particular experimental conditions analysed.

In this thesis, different dosimetric procedures are investigated in the context of cellular (chapter 2), small animal (chapter 3) and clinical (chapter 4) targeted radionuclide therapy applications, involving α- and β-emitting radionuclides. Considering the peculiarities of each experiment, it is shown that different levels of accuracy are required to reach sound dosimetric results. In the last chapter, an original multi-resolution approach is also proposed to optimise Monte Carlo based absorbed dose calculations in small anatomical structures.

Chapter 2

Realistic multi-cellular dosimetry for ^{177}Lu labelled antibodies: model and application

2.1 Introduction

Radiopharmaceutical development is a growing research field: new molecules for the treatment of cancer through TRT are regularly proposed and tested (clinical, preclinical experiments). Cellular behaviour of administered radiopharmaceuticals is commonly studied using in vitro radiobiological experiments. Correct absorbed dose quantification is required for the evaluation of observed radiobiological effects and to predict or compare the therapeutic efficacy of different radiopharmaceuticals. Absorbed dose calculations are also needed to establish the absorbed dose-effect relationship (or the lack thereof) in clonogenic survival experiments and to better understand cell death mechanism.

Following the MIRD schema (Bolch et al. 2009), the *in-vitro* absorbed dose to a given cell depends on the radioactivity internalised by the target cell itself (self-absorbed dose) and the surrounding cells (cross-absorbed dose), and by the radioactivity in the culture medium (non-specific absorbed dose). Traditional MIRD dosimetry applied at the clinical scale, generally assumes uniform distribution of radioactivity within the source organ. However, within the same colony, cells may have different sizes, different levels of radioactivity internalization and different intracellular activity distributions. All these variables, that in turns reflect the high level of heterogeneity displayed by a tissue *in*

vivo, can make it difficult to predict the response of cell populations to a given radiopharmaceutical. Nevertheless, previous works demonstrated that heterogeneity of cell culture parameters produces significant effects on the shape of survival curves (Howell et al. 2012, Uusijärvi et al. 2008).

In addition, in clinical dosimetry, α, Auger and β-particles are usually considered as non-penetrating radiations, and their contribution to the absorbed dose of non-source organs is often neglected. However, considering the cell-to-cell distances typical of *in-vitro* experiments (from a few to few hundreds of um), and the particle range in water for this type of radiations (from few um to few mm), this assumption no longer holds true, and the relevant cross-dose should be calculated for the specific geometry and radiation considered. In the last decades, many researchers have developed digital models for the calculation of cellular absorbed dose for *in-vitro* experiments using both Monte Carlo and analytical methods. Most of these works focuses on the study of α and Auger emitters and therefore considers cell culture geometries of limited sizes: typically, cell clusters in closed packed geometry are generated for the calculation of the cell cross absorbed dose (Faraggi et al. 1998, Cai et al. 2010). Goddu et al. 1994b, calculated the self-dose-to-cross-dose ratios to cell nucleus for different cluster sizes (up to 400 um) considering α, Auger and β-emitters: for β-emitters they demonstrated that the cross-absorbed dose is important irrespectivly of cluster size and sub-cellular source distribution, and increases as the cluster size increases. Other authors, performed cellular dosimetry for more realistic geometries in the case of β-emitters (Freudenberg et al. 2011) and mono-energetic electrons up to 1 MeV (Rajon et al. 2011). In most of these works, however, the contribution of the non-specific irradiation is usually disregarded since they focus on *in-vivo* applications.

Despite the great research interest in cellular dosimetry, still, the availability of pre-calculated cellular S values is limited to the self-absorption contribution (Goddu et al. 1997). The only exception is represented by the MIRDcell software (Vaziri er al. 2014) that is freely available online and allows the user to predict cell survival curves for many radionuclides and mono-energetic radiations of different types. Unfortunately, only few specific geometrical configurations (single clusters of cells and cell monolayers in closed packed geometry) are implemented in MIRDcell: as a consequence, the complexity of certain in vitro experiments cannot be appropriately modelled.

This chapter reports the development of an in-silico model for the determination of the average cell absorbed dose in 3D colonies. On the basis of experimentally determined

parameters (cell density, cluster density, average cluster size, cell cumulated activity), the model generates realistic, randomised culture geometries taking into account cell tendency to aggregate into isolated clusters of different sizes. Within the same virtual colony, cells may have different radii, different levels of radioactivity internalization and different intracellular activity distributions. The physical size of the modelled experiment is not limited in order to cover the range in water of β-emitters. A mixture of Monte Carlo and analytical approach was applied to achieve as accurate as possible results while reducing calculation time. This general-purpose cellular model was applied to the *in-vitro* dosimetry of lymphocyte B cells (Ramos and DOHH2 cells) treated with ^{177}Lu-labelled monoclonal Antibodies (mAbs). The aim was to investigate the therapeutic efficacy of a novel radiopharmaceutical (^{177}Lu-HH1, also called Betalutin^{TM}) in human lymphoma cells and to compare it with those of ^{177}Lu-Rituximab and of the irrelevant ^{177}Lu-IgG, namely ^{177}Lu-Erbitux, that targets epidermal growth factor receptors (EGFR). In the next sections, the application of the dosimetric model developed to these experiments is discussed in details.

2.2 Materials and Methods

2.2.1 Experiments

All cell experiments listed in this section were performed by colleagues at "Institut de Recherche en Cancérologie de Montpellier"(IRCM), U1194 INSERM, Montpellier, France.

2.2.1.1 Cell lines and radiolabelled monoclonal antibodies

Ramos and DOHH2 cell line were obtained from American Tissue Culture Collection. Cells were grown at 37°C in a humidified atmosphere of 95% air/5% CO_2 in RPMI (Life technologies) medium supplemented with 10% heat-inactivated fetal bovine serum, 1% Geneticin, 100 g/ml L-glutamine and antibiotics (0.1 U/ml penicillin and 100 g/ml streptomycin). Cell diameter and area were determined after propidium iodide staining and observation under a fluorescence microscope.

Ramos and DOHH2 cells, both expressing CD20 and CD37 cell surface receptors were targeted with Rituximab or HH1 mAbs. Rituximab is a chimeric antibody established from the murine monoclonal antibody (mAb), namely ibritumomab, targeting CD20 receptors expressed by B cells lymphoma. HH1 is a murine mAb targeting CD37 receptors also

expressed by B cells lymphoma. Cetuximab (or Erbitux, using its commercial name) is a chimeric antibody directed against type I human epidermal receptor (HER1) which is not expressed by lymphoma cells. It was used as non-specific mAb for control purposes. All mAbs were conjugated with p-SCN-benzyl-DOTA and radiolabelled with ^{177}Lu at a concentration of 10 mg/mL (1 mL). They were radiolabelled with $^{177}LuCl_3$ (Perkin Elmer, Boston) at specific activity of 200 MBq/mg. Radiochemical purity was $> 97\%$, with radionuclidic purity $> 99.94\%$.

2.2.1.2 Determination of time-activity curves

The uptake of radioactivity was determined in Ramos and DOHH2 cells exposed to ^{177}Lu-HH1 (Betalutin^{TM}), ^{177}Lu-Rituximab or ^{177}Lu-Erbitux. Typically, 10^6 cells/mL of culture medium were incubated for 18 hours with increasing activities (0, 0.5, 1, 2, 4 and 6 MBq/mL) of ^{177}Lu-labelled mAbs. Then, cells were washed twice and seeded in 12 micro-well plates containing 1 mL of culture medium at a concentration of 200 10^3 cells/mL. At different times (2h, 24h, 48h, 72h and 144h), cells were collected, washed twice with phosphate buffered saline (pbs), and re-suspended in 1 mL pbs. An aliquot fraction (8 μL) was used for cells numbering using a cell counter (Muse, Merck Millipore), while the radioactivity of the remaining volume was determined using a gamma counter (Hewlett Packard, Palo Alto, CA). The activity per cell (Bq/cell) was next obtained for each time point. The total average cell cumulated activity was obtained from the integration of the time-activity curves in the relevant time range. For all cell lines and each mAb, experiments were done in triplicates and repeated at least three times, allowing for the extrapolation of a statistical error on the average cellular cumulated activities. Figure 2.1 shows a schematic representation of the protocol used for determining cell activity.

2.2.1.3 Clonogenic survival experiments

Therapeutic efficacy of radiolabelled and unlabelled mAbs was assessed using clonogenic assay. A concentration of 10^6 cells/mL was grown in 12 micro-well plates containing 1 mL of RPMI medium before being incubated for 18 h at 37°C/5% CO_2: a) with increasing test activities (0, 0.5, 1, 2, 4 and 6 MBq/mL) of ^{177}Lu-mAbs (^{177}Lu-HH1, ^{177}Lu-Rituximab and ^{177}Lu-Erbitux) or b) with increasing test concentrations (0, 5, 10, 15, 25, 40 μg/mL) of unlabelled mAbs (HH1, Rituximab and Erbitux). Next, cells were collected, centrifuged and washed twice, before being suspended in 5 mL of RPMI medium and counted. 1500

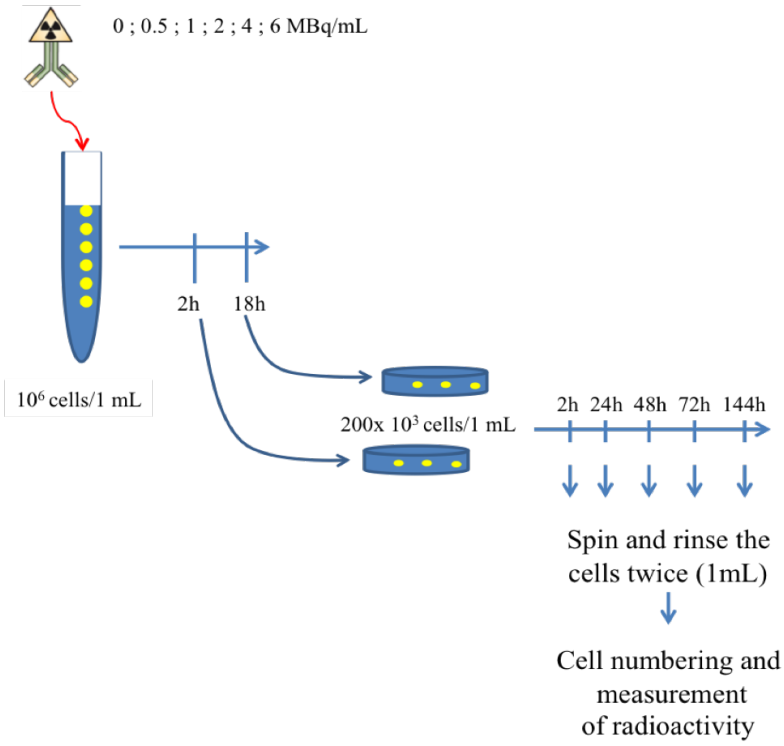

Figure 2.1: Schematic representation of the protocol used for determining the cellular uptake of radioactivity. Courtesy of A. Pichard and JP. Pouget.

cells were mixed with 4.5 mL of MethoCult® (Stem cell Technologies) medium and seeded at increasing concentrations for increasing test activities (500 – 10000 cells/petri dish containing 1.5 mL medium). Petri dishes were next kept for 12 to 16 days for determining the number of colonies. Colonies containing 50 or more cells were scored and the surviving fraction was calculated. All the experiments were repeated at least three times in triplicate. Figure 2.2 shows a schematic representation of the protocol used for clonogenic survival experiments.

Survival curves issued from experiments with labelled mAbs were corrected for antibody toxicity in order to identify purely radiative effects. The activity concentration in the medium (MBq/mL) used in the experiments with the labelled mAbs was expressed in terms of antibody concentration (ug/mL). Then, cell survival curves, supposedly including only radiative effects (CS_{rad}), were obtained by subtracting survival curves obtained with labelled mAbs (CS), from survival curves obtained with cold mAbs (CS_{cold})

$$CS_{rad} = 100 - (CS_{cold} - CS) \tag{2.2.1}$$

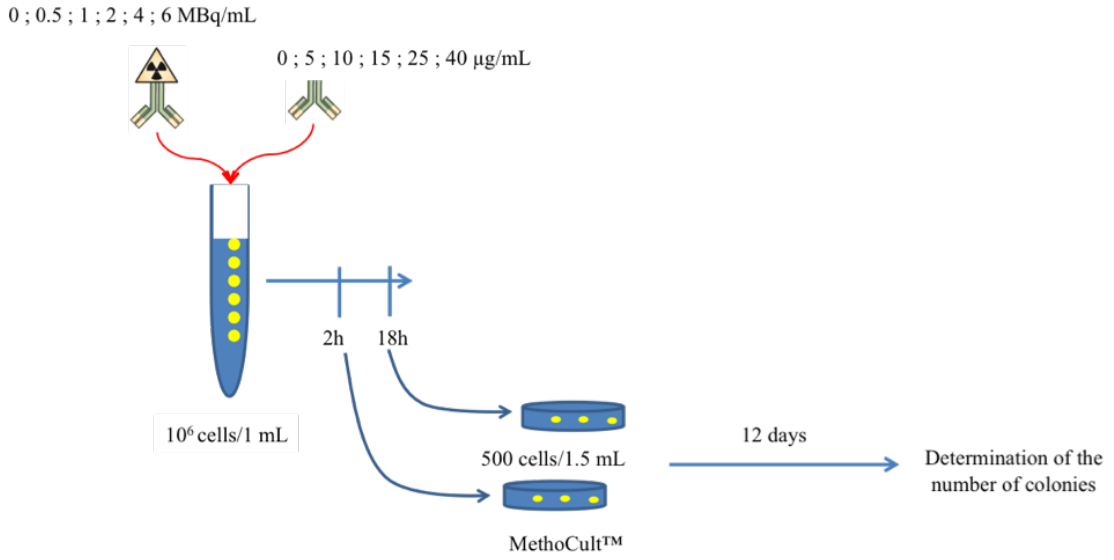

Figure 2.2: Schematic representation of the protocol used for clonogenic survival experiments. Courtesy of A. Pichard and JP. Pouget.

under the assumption that radiative and non-radiative cell death mechanisms are independent phenomena.

2.2.1.4 Determination of culture cell geometry

During incubation (between 0 and 18 hours), Ramos and DOHH2 cells showed the tendency to accumulate at the centre of the culture well: within this macro-aggregate they mainly formed clusters of different sizes with some cell remaining isolated. Cell spatial distribution was highly heterogeneous and cell were organised in few layers in suspension. Since the average absorbed dose to the cell strictly depends on the geometrical configuration of the cell culture, a preliminary determination of the relevant geometrical parameters was performed on the basis of pictures acquired by optical microscopy. Four sets of pictures were acquired, corresponding to Ramos and DOHH2 cells treated with ^{177}Lu-HH1 and ^{177}Lu-Rituximab. Three concentric regions were identified in the cylindrical culture well of radius r_w= 3.4 cm as shown in figure 2.3: centre (a cylindrical region of radius r_c), halfway (a cylindrical shell with $r_c < r < r_h$) and edge (a cylindrical shell with $r_h < r < r_w$). For each region, cell line and for both antibodies, two planar pictures were taken at ×5 and ×20 magnifications, in order to measure the cell density in each area. In figure 2.4, the ×20 pictures acquired for Ramos cells treated with Betalutin and Rituximab are shown as an example. For each picture acquired, the following parameters

were extracted: density of isolated cells (cell/cm^2); clusters density (clusters/cm^2); average cluster radius in μm and its relative standard deviation. Culture thickness of three, two and one cell diameters was assumed for the central, halfway-through and edge regions respectively. The extracted parameters were used to estimate the total number of cells in each region. The size of the central region (r_c) was determined directly segmenting the cell macro-aggregate (visible by eye) which laid approximately at the centre of the culture well. The outer radius of the halfway region (r_h) was tuned in order to obtain an overall number of cells in the culture of the order of the nominal value (4 millions of cells). Microscope observation of culture suspensions in flasks did not reveal any significant difference in geometrical arrangement according to whether cells were exposed to ^{177}Lu-Erbitux, ^{177}Lu-HH1 or ^{177}Lu-Rituximab. Hence, for further modelling of cell suspension analysis, the parameters obtained with ^{177}Lu-HH1 were arbitrarily used for ^{177}Lu-Erbitux.

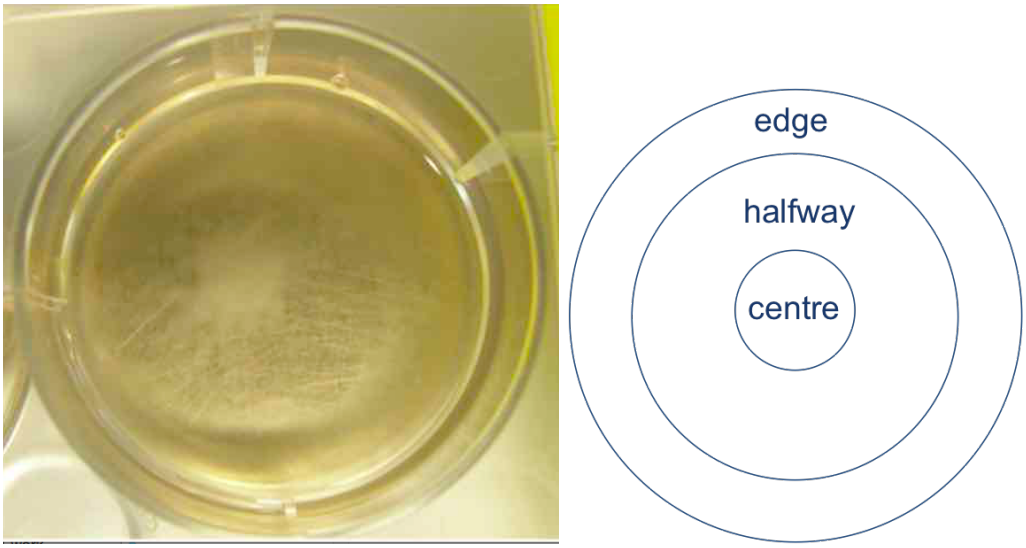

Figure 2.3: Left: picture of the culture well (3.4 cm radius) for Ramos cells treated with ^{177}Lu-HH1. At the centre a cell macro-aggregate is visible by eye. Right: schematic representation of the three regions identified in the culture well.

After 18 hours of incubation in radioactive medium, between 500 and 10000 cells were seeded in petri dishes containing 1.5 mL medium. Under this conditions, cells exhibited an approximately uniform and isotropic spatial distribution. A maximum density of 6667 cells/cm^3 was found for DOOH2 cells treated with ^{177}Lu-Rituximab.

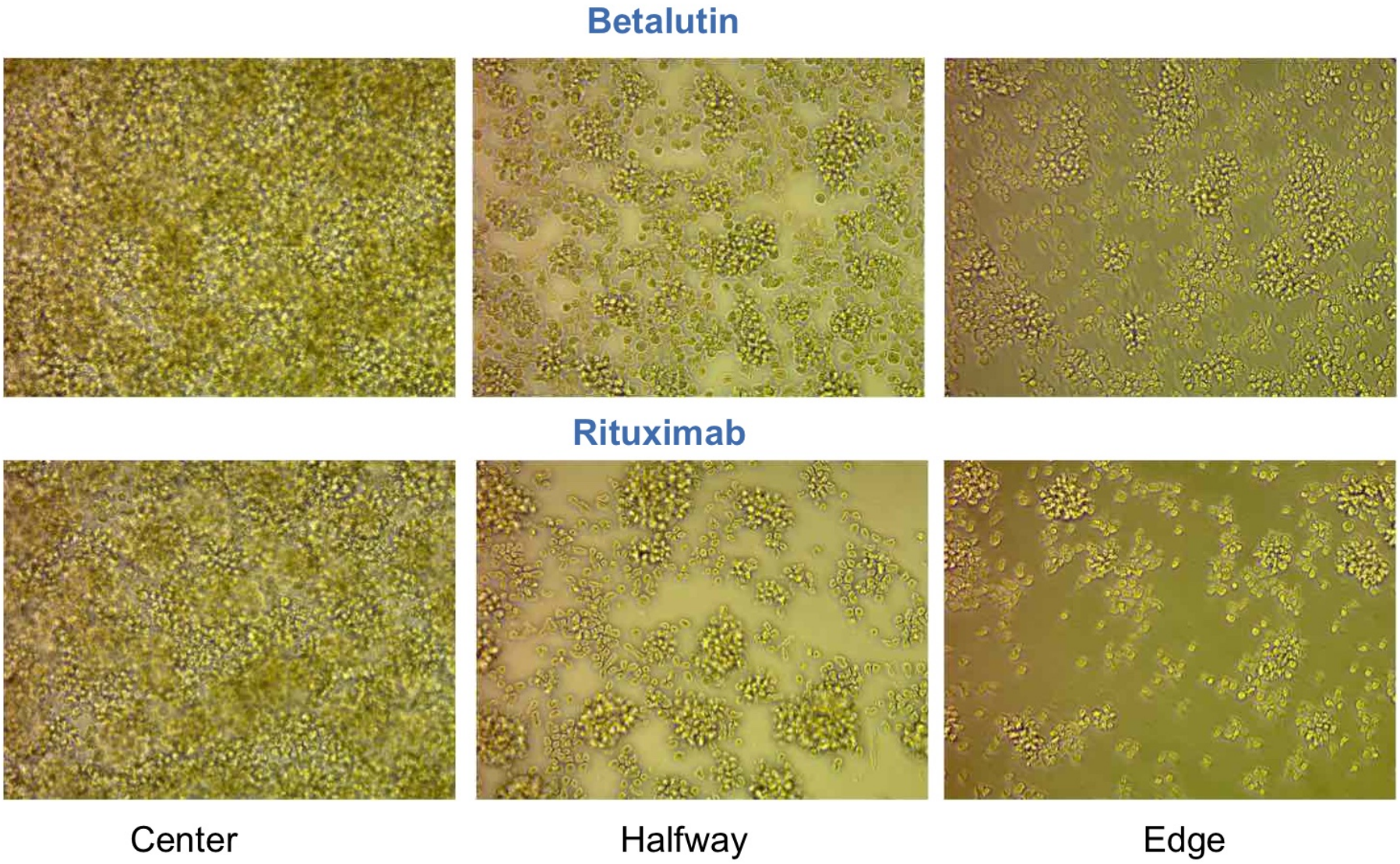

Figure 2.4: Optical microscopy images of Ramos cell colony acquired at ×20 magnification. Cells treated with ^{177}Lu-HH1 are shown on top and those treated with ^{177}Lu-Rituximab in the bottom pictures. From left to right, the pictures refer to the central, halfway-through and edge regions respectively.

2.3 Dosimetric model

According to the standard MIRD schema (Bolch et al. 2009), the absorbed dose to a target cell (D_t) can be obtained summing up the contribution of the activity in the target cell (D_{self}) itself, in the cells other than the target (D_{cross}) and in the culture medium (D_m):

$$D_t = D_{self} + D_{cross} + D_m \tag{2.3.2}$$

Each of these components can be calculated as the product of the S value corresponding to the appropriate source/target combination ($S_{t \leftarrow s}$), and the cumulated activity in the source:

$$D_t = \tilde{A}_t \; S_{t \leftarrow t} + \sum_{s}^{N-1} \tilde{A}_s \; S_{t \leftarrow s}(d_s) + \tilde{A}_m \; S_{t \leftarrow m} \tag{2.3.3}$$

In equation 2.3.3, $\tilde{A}_t$, $\tilde{A}_s$ and $\tilde{A}_m$ respectively indicate the cumulated activities in the target cell, in the s^{th} source cell and in the culture medium.

In next paragraphs, the techniques implemented for the calculation of self-absorption, cross-irradiation and non-specific irradiation S values are described. S values are obtained via Monte Carlo simulation and then used for the calculation of the average cell absorbed dose according to equation 2.3.2.

2.3.1 Self-irradiation absorbed dose

Cell geometry was modelled with two concentric homogeneous unit density spheres representing the cell and the nucleus. Each cell was hence composed by three compartments: cell nucleus (N), cell cytoplasm (Cy) and cell surface (CS) (see picture 1.9 in chapter 1). Cell sizes were defined according to experimentally determined cell (R_C = 5.1 um) and nucleus (R_N = 4.0 um) radii. The cell model was implemented in Geant4.9.6 patch 04 (Agostinelli et al. 2003) in order to calculate cell S values for different hypotheses of antibody internalisation and different target regions. For this and all MC simulation performed for this work, the whole ^{177}Lu spectrum was considered as defined in the MIRD

radionuclide data and decay schemes (Eckerman and Endo 2008). The Livermore physics list was selected as it allows tracking particle down to an energy of 250 eV: this corresponds to a cut in range of 10 nm, which is adequate for energy deposition in cells of few microns. 10^6 primary particles were generated for the simulation of each self-irradiation S value, in order to obtain a statistical uncertainty below 1%.

The self-irradiation absorbed dose factor (S_{self}) assumes different values depending on the localization of the labelled mAbs within the cell. Here, absorbed dose in the whole cell, the nucleus and the cytoplasm was scored for two different radioactivity distribution hypotheses: 100% of the source uniformly distributed in the cytoplasm (internalising antibody) and 100% of the source uniformly distributed in the cell membrane (non-internalising antibody). In general, for any target compartment considered (nucleus, cytoplasm or the whole cell), if A_{Cy} and A_C are the activities in the cytoplasm and in the whole cell at a given time of measurement, S_{self} can be expressed as a function of the S values corresponding to a source in the cytoplasm (S_{Cy}) and to a source at cell surface (S_{CS}):

$$S_{self} = \frac{A_{Cy}}{A_C} S_{Cy} + (1 - \frac{A_{Cy}}{A_C}) S_{CS} \tag{2.3.4}$$

Sub-cellular localisation of radioactivity in Ramos and DOHH2 cells was experimentally determined from immunofluorescence images. On this basis, a 50% CS + 50% Cy radioactivity distribution was assumed for ^{177}Lu-HH1, and a 100% CS distribution for ^{177}Lu-Rituximab and ^{177}Lu-Erbitux. Equation 2.3.4 was used to derive S_{self} for Ramos cell treated with ^{177}Lu-HH1. Subsequently, the experimentally determined cell cumulated activities were multiplied by the corresponding S values, in order to obtain the absolute cell absorbed dose due to self-irradiation. The error associated to the self-absorbed dose was obtained propagating the standard deviations of cell cumulated activities applying conventional error propagation rules.

2.3.2 Cross-irradiation absorbed dose

In principle, the most accurate approach for the calculation of cross-irradiation cellular S values consists in the direct MC simulation of a couple of source and target cells, since it allows taking into account the contribution of all secondary electrons. Even if this is feasible for short cell-to-cell distances (with respect to cell radius), at larger distances the

simulation may not converge for ballistic reasons.

Beta particles emitted by ^{177}Lu have a maximum range in tissue of 1.76 mm (Berger et al. 2009), hence, for the calculation of the absorbed dose to a cell in the culture, the contribution of all source cells placed at distances between two cell radii and at least 1.76 mm should be taken into account. This requires the knowledge of cross-irradiation S values up to a cell-to-cell distance of 1.76 mm or larger, that are impossible to obtain via direct MC simulation.

In this work, three different approaches for the calculation of cross-irradiation S values were implemented: direct MC simulation at short cell-to-cell distances, the use of MIRDcell software, and the generation of S values from DPKs (Dose Point Kernels). The comparison of results obtained with these three approaches served as a validation benchmark.

2.3.2.1 Generation of cross-irradiation S values

Monte Carlo simulation of cross-irradiation S values. The same simulation set-up implemented for the generation of self-irradiation S values was used for the generation of cross-irradiation S values. In this case, however, the absorbed dose was scored in the nucleus, the cytoplasm and the whole volume of a target cell placed at a variable surface-to-surface distance from the source cell (0.0, 5.1, 10.2, 15.3, 20.4 and 51.75 um). Ramos cell experimentally determined nucleus and cell sizes were considered (R_C = 5.1 um and R_N = 4.0 um).

MIRDcell software for the generation of cross-irradiation S values. The "Cell Source/Target tab"of the MIRDcell applet (Vaziri et al. 2014) was used for the calculation of cross-irradiation S values for two cells placed at a variable centre-to-centre distance ranging from 10 (adjacent cells) to 1578 um. The upper limit roughly corresponds to the Continuous Slowing Down Approximation (CSDA) range of ^{177}Lu β-particles in water and is set by the software. 5 um radius cells with a 4 um radius nucleus were considered for both cell lines, as in MIRDcell, cell radii can only be defined as integers. In MIRDcell, the ^{177}Lu beta spectrum is defined according to MIRD radionuclide data and decay schemes as in the MC simulations implemented for this study. The absorbed dose is calculated analytically in the CSDA.

Generation of cross-irradiation S values from DPKs. ^{177}Lu Dose Point Kernels (DPKs)

were simulated using MCNPX (Briesmeister 2000): the energy deposited by a punctual ^{177}Lu source (spectrum defined according to Eckerman and Endo 2008) was scored in concentric spherical shells. MNCPX is the natural choice for the generation of DPKs as it easily allows scoring the deposited energy in concentric spherical shells through macro scripting. On the contrary, the implementation of the same geometry in Geant4 would require the development of user-defined `C++` classes. A shell thickness of 17.6 um was used to generate DPKs between 17.6 and 2552 um, simulating 800 millions of primary particles. 800 millions additional particles were also generated for the simulation of DPK between 17.6 and 228.8 um on a shell thickness of 8.8 um, in order to increase DPK sampling accuracy in the steepest region of the curve at low distances from the source. The DPKs obtained were subsequently used to calculate the absorbed dose (S values) to a target sphere (representing the cell) placed at variable distance from the source. For this calculation the source and the target cells were assumed to be punctual, so the DPKs and the S values basically coincide except for a change in units (MeV cm^{-3}/Bq s versus Gy/Bq s). This approximation is easily verified for cell-to-cell distances much greater than cell size. At shorter distances, a validation of S values obtained from DPK is required: the DPK S values were hence compared to cross-irradiation S values obtained with direct Monte Carlo simulation and with MIRDcell.

2.3.2.2 Generation of multi-cellular geometries

The cross-irradiation S value ($S_{t\leftarrow s}(d_s)$) allows calculating the contribution to the absorbed dose of a single source cell located at a fixed distance (d_s) from the target cell. In a culture well containing N labelled cells, the average cross-absorbed dose to a given cell (D_{cross}) is obtained summing up all the contributions from the N-1 source cells having a cumulated activity $\tilde{A}_s$ (c.f. the second term of equation 2.3.3). In order to calculate D_{cross}, the knowledge of the 3D spatial distribution of cells in the culture is required for the determination of d_s and hence $S_{t\leftarrow s}(d_s)$. According to cell incubation experiments (0<t<18 hours), in each region of the culture well, both isolated cells and cell clusters of different sizes may be present during the incubation time. The calculation of the cross-absorbed dose to a given target cell was hence separated into three contributions:

- the absorbed dose due to the activity in isolated cells (D_{IC}, Dose from Isolated Cells);

- the absorbed dose due to the activity in cells of the cluster the target cell belongs to (D_{TC}, Dose from Target Cluster);
- the absorbed dose due to the activity in cells of surrounding clusters (D_{SC}, Dose from Surrounding Clusters).

Since the experiments indicated that Ramos and DOHH2 cells tend to aggregate, the target cell was arbitrarily assumed to belong to a cluster. Three separate models for the description of cell culture geometry were developed in order to allow the calculation of D_{IC}, D_{TC} and D_{SC}. Since the maximum range in water of ^{177}Lu β-particles is 1.76 mm, the contribution of cells located at much larger distances was neglected. Moreover, considering that cells are arranged in few layers along the vertical axis (Z) of the culture well, the geometrical models were restricted to cylindrical volumes (from here on called Model Volume) having radius of 2550 um (= 500 Ramos cell radii) and height corresponding to the number of observed cell layers (N_{Layers}) times cell diameter ($2R_C$) expressed in microns. The Model Volume is arbitrarily determined so that its radius in the XY plane is larger than the maximum beta range in water, to include also Bremsstrahlung contribution; this volume is small enough to fit into all well regions defined in this study. In this volume, random distributions of non-overlapping isolated cells and clusters were generated with a series of `C++` classes implemented in ROOT[1] (Brun and Rademakers 1997).

For the calculation of cross-irradiation absorbed dose after 18 hours, only isolated cells contribution was modelled. In this case, the Model Volume was a cylinder of radius 2550 um and height 1.6 mm, corresponding to the full height of culture medium in the Petri dishes.

3D model of isolated cells. Randomly distributed, non-overlapping, isolated cells were modelled. The minimum allowed distance between two cells was equal to two cell radii. The software takes as input cell density (cell/cm^2) and computes the number of cells to be placed in the Model Volume. Then, it generates random X, Y, and Z coordinates (cell centres) within the established limits: if the current cell does not overlap to any other previously created cell, its coordinates are stored. The output of this piece of software is a list (in txt format) of distances (d_s) between source cells and the target cell arbitrarily placed at the barycentre of the Model Volume. Even if, in principle, the model can be

[1] https://root.cern.ch

used to calculate the absorbed dose to a cell placed anywhere in the Model Volume, the calculation was restricted to the central cell. The resulting error in the final absorbed dose is expected to be negligible since most of cells in any culture well region can be inscribed into a circle having a 2.5 mm radius.

Different isolated cell models were generated for each antibody/cell line combination and for each region of the culture well where the presence of isolated cells was experimentally detected. For example, in the case of Ramos cells treated with ^{177}Lu-HH1, isolated cells were not detected in the central region and this case was hence not included in the model. In addition, for each eligible configuration of antibody, cell line and region, 50 different geometrical arrangements of isolated cells were created running the software with different random seeds.

3D model of target cell cluster. In analogy with the 3D isolated cell model, cell clusters of different sizes were modelled in ROOT. Fifty clusters were generated in order to establish an average absorbed dose (and the corresponding standard deviation) that does not depend on the specific geometrical configuration modelled. Clusters radii (on the XY plane) were randomly sampled according to a Gaussian distribution having the mean and the standard deviation equal to the experimentally determined values. The maximum cluster thickness was set to $N_{Layers} \times 2R_C$. Assuming a packing factor of 0.74 (typical of hexagonal close packing lattices), randomly distributed, non-overlapping cells were generated to cover the cluster volume. In figure 2.5, a 17.6 um radius and a 35.4 um radius clusters are represented as an example.

Subsequently, within each cluster generated, the relative distances between each cell and the others was computed and stored in a txt file. This approach allowed obtaining an average cell absorbed dose independent from the specific position of the target cell. This was felt necessary as, at short cell-to-cell distances, the difference between the absorbed doses of two cells placed at the centre or at the edge of the cluster may, in principle, be significant.

3D model of surrounding cell clusters. The many clusters present in the Model Volume were modelled as non-overlapping cylinders with a thickness of $N_{Layers} \times 2R_C$, and a randomly selected radius obtained from the sampling of a Gaussian distribution having a mean and a standard deviation equal to the experimentally measured values. The number

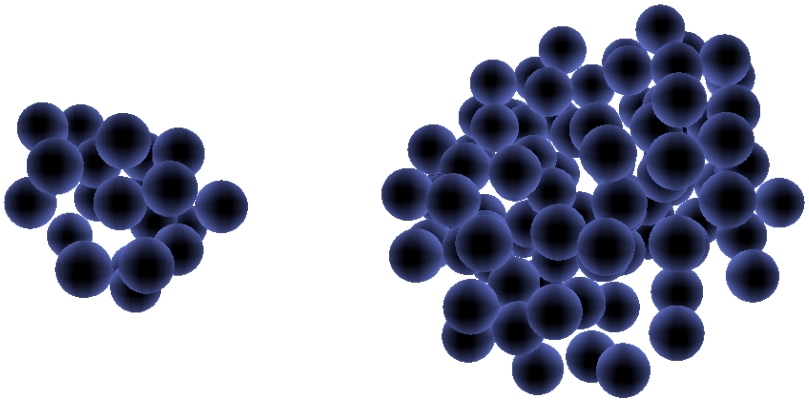

Figure 2.5: Graphical representations of a 17.6 um radius (left) and a 35.4 um (right) radius cell clusters. Cell positions and radii are shown in a realistic scale.

of clusters to be generated was determined according to the experimental cluster density (cluster/cm^2). The number of cells (N_{cells}) comprised in each cluster was calculated as the ratio of the given cluster volume ($V_{cluster}$) and the cell volume (V_{cell}), and assuming a packing factor (PF) of 0.74:

$$N_{cells} = \frac{V_{cluster}}{V_{cell}} PF \tag{2.3.5}$$

The target cell was placed at the barycentre of the volume model and included in a cluster of random size. For each cluster, its distance to the target cell (calculated from the cluster barycentre to the Model Volume barycentre), its radius and the number of cells included, are stored for the subsequent calculation of cell absorbed dose. For each cell line, antibody and well region combination, 50 geometrical configurations of multiple clusters were generated to obtain average absorbed doses independent from the specific geometry modelled.

2.3.2.3 Cell cumulated activities

The cumulated activity $\tilde{A}_s$ for the s^{th} source cell (c.f. the second term of equation 2.3.3) was randomly assigned sampling a Lognormal distribution of the form:

$$L(\tilde{A}_s) = \frac{1}{\sqrt{2\pi}\, lnk} \frac{1}{\tilde{A}_s} \exp(-\frac{(ln(\tilde{A}_s/\mu))^2}{2(lnk)^2}) \tag{2.3.6}$$

with $k = (\sigma/m) + 1$ and $\mu = m$ (Cousins 2010), where m and σ are the experimentally determined average cell cumulated activities (in the time frame of interest) and standard deviations.

The Lognormal distribution represents a random variable whose logarithm follows a normal distribution. It is typically used to model the errors of a process involving many small multiplicative errors (Limpert et al. 2001). Here, it was used alternatively to a Gaussian distribution in order to avoid selecting negative cumulated activities (the Lognormal distribution is defined for $x > 0$). Nevertheless, when the measured standard deviations are small, the choice made for μ and k parameters (equations 2.3.6) allows approximately reproducing the shape of a Gaussian distribution having a mean equal to m and a standard deviation equal to σ. In figure 2.6, the Lognormal and the Gaussian distributions corresponding to m=1041.49 and σ=230.25 and to m=1795.09 and σ=1312.90 are shown as an example.

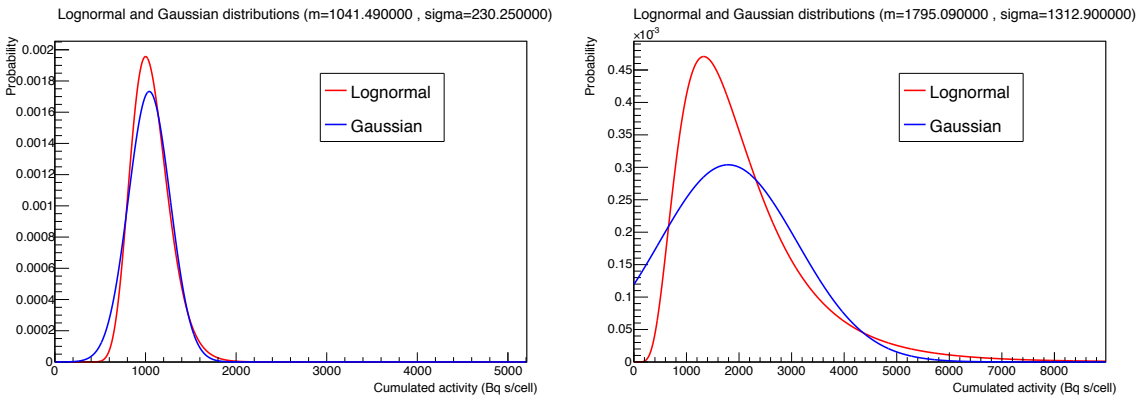

Figure 2.6: Lognormal (red) and Gaussian (blue) distributions corresponding to different average cumulated activities and standard deviations. For smaller standard deviations, the shape of the Lognormal distribution approaches that of the Gaussian distribution.

2.3.2.4 Calculation of cross-irradiation absorbed dose between 0 and 18 hours

In order to obtain the average cell absorbed dose for the whole cell culture, absorbed doses obtained for each region were first computed separately and then summed up, using the total number of cells belonging to each region (estimated from experiments) as weights.

The cross-irradiation absorbed dose was calculated according to the second term of

equation 2.3.3. Cell cumulated activities ($\tilde{A}_s$) between 0 and 18 hours were randomly sampled according to equation 2.3.6. The cross-irradiation S value ($S_{t\leftarrow s}(d_s)$) was evaluated for each source-to-target distance d_s, linearly interpolating the merged S values data obtained from the DPKs and the direct MC simulation at very short distances.

For the calculation of the absorbed dose from surrounding clusters (D_{SC}), the $S_{t\leftarrow s}(d_s)$ term was assumed to slowly vary within a given cluster. The cross-irradiation absorbed dose to the target cell (D_{cross}) can hence be written as:

$$D_{cross} = \sum_{s}^{N-1} \tilde{A}_s \; S_{t\leftarrow s}(d_s) \approx S_{t\leftarrow cluster}(d_{cluster}) \sum_{i}^{N_c-1} \tilde{A}_{cluster} \tag{2.3.7}$$

where $S_{t\leftarrow cluster}(d_{cluster})$ is the cross-irradiation S value estimated at the centre of the cluster, and $\tilde{A}_{cluster}$ is the total cumulated activity in the cluster between 0 and 18 hours; $\tilde{A}_{cluster}$ was directly generated randomly sampling the Lognormal distribution in equation 2.3.6. In the first part of equation 2.3.7 the sum is extended to all cells (N) from all clusters, while in the second part, it is extended to the number of clusters generated (N_c).

The three contributions to the cross-irradiation absorbed dose D_{IC}, D_{TC} and D_{SC} were averaged over the 50 geometrical configurations generated for each model. The absorbed dose calculated for the target cluster (D_{TC}) is also averaged over the possibility of each cell of the cluster being the target. It was hence possible to associate a standard deviation to the average absorbed doses obtained for each well region, which reflects the variability introduced by the geometrical model, and which takes into account the different labelling of the various cells. The average cross-irradiation absorbed doses D_{IC}, D_{TC} and D_{SC} for any cell in the culture, were subsequently calculated summing up the values obtained at the edge, halfway-trough and at the centre of the culture well, and weighting for the total number of cells in each region. Then, the average cross-irradiation absorbed dose was calculated summing up the contributions of isolated cells, target cluster and surrounding clusters. At each stage, the standard deviation for the absorbed dose was obtained according to standard error propagation rules.

2.3.2.5 Calculation of cross-irradiation absorbed dose between 18 hours and 14 days

The calculation of the cross-irradiation absorbed dose for cells seeded in Petri dishes after 18 hours was much more straightforward as the cells were uniformly distributed throughout the dish volume. Ten different geometrical configurations of isolated cells were generated to model the conditions of maximum cell density (6667 cells/cm^3), for which the highest cross-absorbed dose was expected. The stored isolated cell positions were subsequently used to calculate the cross-absorbed dose according to the second term of equation 2.3.3. A lognormal cumulated activity distribution was also assumed: average cumulated activities and standard deviations were obtained from the integration of cells time-activity curves between the time of cell rinsing (18 hours) and the time of cell counting (on average 14 days = 336 hours). Since the cross-irradiation absorbed dose found for the maximum cell density conditions was irrelevant (4.38 10^{-5} $\pm$ 5.16 10^{-6} Gy), the cross-absorbed dose after 18 hours was neglected for all cell line/mAb combinations.

2.3.3 Non-specific irradiation absorbed dose

2.3.3.1 Generation of non-specific S values

Given ^{177}Lu β-particles range in water, all radioactivity incorporated in a spherical volume of 1.76 mm radius surrounding the target cells, potentially contributes to its absorbed dose. Therefore, the non-specific irradiation S value was simulated with Geant4, modelling a homogeneous spherical water medium of 2.55 mm radius uniformly filled with ^{177}Lu and surrounding the target cell. Sphere's radius was arbitrarily selected larger than 1.76 mm in order to account for Bremsstrahlung radiation. The presence of cells other than the target was not modelled since the volume they occupy is negligible with respect to the total culture volume (1 million Ramos cells per mL corresponds to 0.007% of the culture volume occupied by cells). The same source and physics parameters used for the generation of cellular S values, were also adopted for this simulation. The absorbed dose was scored in three regions of the target cell: the whole cell having a radius of 5.1 um (Ramos cell), the nucleus (radius=4.0 um) and the cytoplasm. 3.7 10^9 events were simulated to achieve a statistical uncertainty below 5%. Simulation time was about three weeks on a single CPU (3.1 GHz Intel Core i5).

In order to validate the results obtained, the MIRDcell software was employed as well

to calculate the non-specific irradiation S value, using the tool for the calculation of the self-irradiation S value. Despite MIRDcell has not been conceived for the implementation of this kind of geometry, the option for the calculation of the nucleus S value for a source distributed in the cytoplasm ($S_{Cy \leftarrow N}$) can be adapted to the calculation of cell S value for a source located in a spherical shell of any size (2.55 mm in this case). In fact, these two configurations present the same geometry: it is sufficient to identify the nucleus as the whole cell, and the cytoplasm as the medium. Since the MIRDcell program only accepts integers for the definition of cell dimensions, two cells of 4 and 5 um radii were considered.

2.3.3.2 Calculation of non-specific absorbed dose

The nominal cumulated activity concentration in the culture medium was calculated integrating the initial activity concentrations (0.5, 1, 2, 4, 6 MBq/mL) over the incubation time (18 hours). Multiplying this value by the total volume non occupied by cells, the nominal cumulated activity in the medium was obtained. The volume occupied by cells was calculated for Ramos and DOHH2 cells treated with the three antibodies, taking into account experimentally determined cell and cluster densities in each well region. In order to obtain the actual cumulated activity in the medium, the total cumulated activity in the cells at 18 hours was subtracted from the nominal cumulated activity, for each region separately.

Subsequently, for each combination of cell line, antibody and well region, the medium cumulated activities were multiplied for the non-specific irradiation S value issued from the MC simulation, in order to obtain the absorbed dose to the whole cell and to the nucleus. The three absorbed dose values obtained for each cell line/antibody combination in each region, were summed up using the total number of cells in each region as weights. Standard error propagation was applied throughout the calculation.

2.3.4 Total absorbed dose and clonogenic survival

For each combination of cell line and mAbs, the average absorbed dose to a target cell placed at the centre of the Model Volume was calculated as the sum of three contributions: i) the self-absorbed dose, ii) the non-specific absorbed dose and iii) the cross-irradiation absorbed dose. Table 2.1 provides a summary of the models used and the integration times considered for the determination of each contribution. As in cellular dosimetry it is generally recognized that radiosensitive sites are associated to DNA (Humm et al. 1994),

Abs. dose contribution	Incubation time $0 < t < 18$ h	Clonogenic experiments $0 < t < 336$ h	Dosimetric model
Self			Symmetric sphere
Cross			IC, TC, SC (3 regions)
		negligible	IC
Non-specific			Uniform sphere (3 regions)

Table 2.1: Summary table of the dosimetric models adopted for the calculation of the self-, cross- and non-specific irradiation cross absorbed doses. Gray cells visually highlight the integration time considered for the assessment of each contribution.

when the absorbed dose to other compartments was available, the nucleus was selected as the target region for the construction of cell survival curves. The squared error on the total absorbed dose was computed as the squared sum of the errors of the single components. The dosimetric results obtained for Ramos and DOHH2 cells treated with ^{177}Lu-HH1, ^{177}Lu-Rituximab and ^{177}Lu-Erbitux, were applied to clonogenic survival curves in order to express cell survival in terms of the average nucleus absorbed dose.

2.4 Results

2.4.1 Experiments

2.4.1.1 Determination of cell cumulated activities

Time activity curves obtained for Ramos and DOHH2 cells exposed to ^{177}Lu-HH1, ^{177}Lu-Rituximab and ^{177}Lu-Erbitux (initial activity concentration ranging from 0 to 6 MBq) are reported in figure 2.7 and in the first graphs of figures 2.8 and 2.9. Between 0 and 18 hours, they describe the uptake of radioactivity within the cells; after 18 hours, when cell are rinsed, the radioactivity begins to fade, following a simple mono-exponential decay that depends on both ^{177}Lu physical half life and biological wash-out. In order to assess cell cumulated activities, time-activity curves should be integrated over the experiment time (0 - 336 hours), however, when their shape is not know, this process may not be straightforward. A possible solution would be to integrate the curves using the parallelogram rule. However, in this particular case, the result may be significantly biased by the limited number of time points available (only 2 for the uptake phase). In particular, the

lack of an experimental data point at 18 hours, immediately before cell rinsing, makes it very difficult to extrapolate the time of maximum uptake.

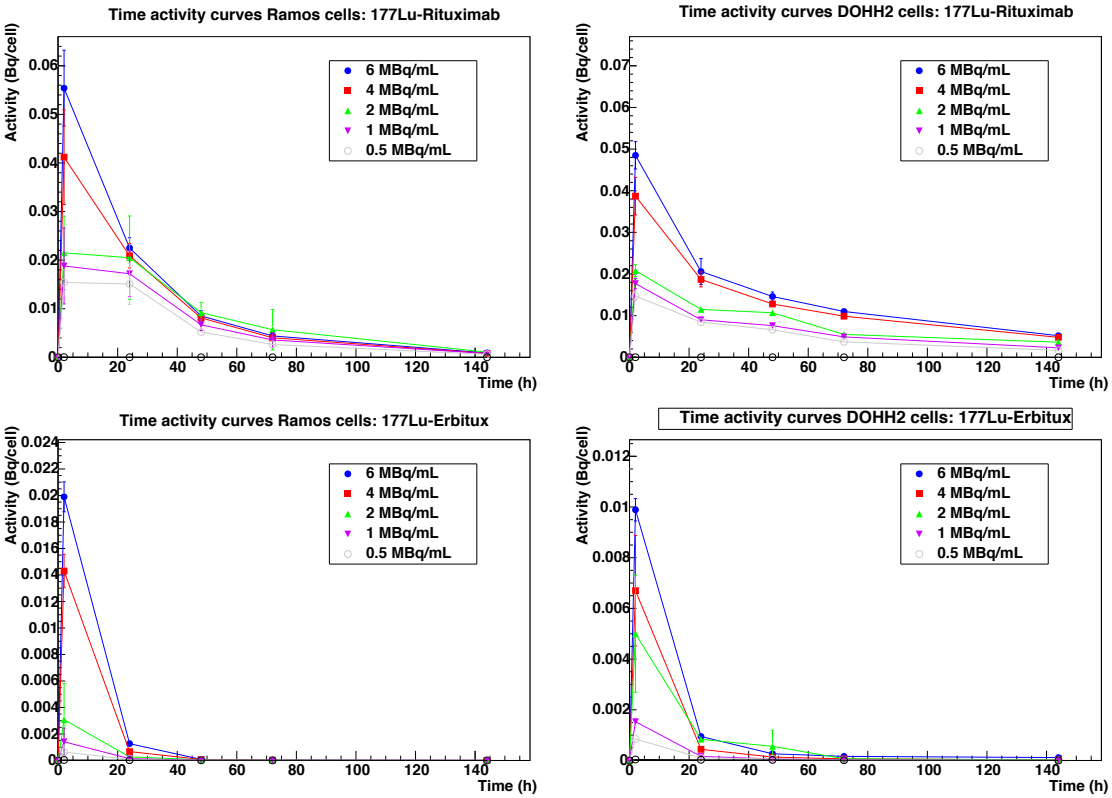

Figure 2.7: Time-activity curves for Ramos (left) and DOHH2 (right) cells treated with ^{177}Lu-Rituximab (top) and ^{177}Lu-Erbitux (bottom). Each plot contains the data relative to different initial activity concentrations in the medium (from 0.5 to 6 MBq/mL).

To make the most out of the available points, time-activity curves were fitted using two separate functions for the incubation and wash-out phases. For the latter, a mono-exponential function was used to fit the 4 time points (24, 48, 72, 144 h) at t > 18 hours, allowing the extrapolation of cell activity at t = 18 hours. This point was subsequently added to the curve and included in the fit for t $\leq$ 18 hours. In principle, in fact, only the radioactivity present in the culture medium is removed when cells are rinsed, while the labelled mAbs bound to cell receptors are not eliminated. In other words, cell activity versus time is expected to be described by a continous function. For both cell lines and all mAbs, all the activities extrapolated at t = 18 resulted inferior to activities measured at t = 2 hours. Thus, assuming that maximum uptake took place between before 18 hours,

the incubation phase was modelled with a function describing un uptake phase followed by a mono-exponential decay phase. In summary, time activity curves were fitted with the following equations:

$$A(t) = A_1\ (e^{-\lambda_a t} - e^{-\lambda_b t}) \qquad \text{for } 0 < t < 18 \text{ h} \tag{2.4.8}$$

$$A(t) = A_2\ e^{-\lambda_c t} \qquad \text{for } 18 < t < 336 \text{ h} \tag{2.4.9}$$

Figures 2.8 and 2.9 show fit results for Ramos and DOHH2 cells treated with ^{177}Lu-HH1; time-activity curves are plotted in the same vertical scale to facilitate the comparison. Curves shapes obtained for the other mAbs were very similar; for most experiments, the maximum uptake resulted between 5 and 10 hours. In the case of cells treated with ^{177}Lu-Erbitux, for which cell activity was very low, most of fits performed at t < 18 hours did not converge. For those curves, cumulated activity before 18 hours was estimated using the parallelogram rule, while for t > 18 hours, the mono-exponential fitted function was integrated. For all experiments, the error on cumulated activity was obtained propagating the fit parameters errors using the dedicate function in ROOT.

Average cumulated activities obtained in Ramos cells exposed to ^{177}Lu-HH1, ^{177}Lu-Rituximab and ^{177}Lu-Erbitux are reported in figure 2.10 for the different activity concentrations introduced in the culture medium. The large error bars are due to the fact that the number of parameters for the fit equals the number of experimental points, and thus the fit cannot bit well constrained. Cumulated activities in cells treated with ^{177}Lu-Rituximab are always significantly higher than those obtained for ^{177}Lu-HH1, which is most probably explained by the highest number of CD20 receptors, compared with CD37 receptors at the surface of Ramos and DOHH2 cells. As expected, cells treated with the non-specific mAb ^{177}Lu-Erbitux exhibited the lower level of internalisation: except for the highest medium activity concentrations tested, their cumulated activities were almost negligible from a dosimetric point of view.

2.4.1.2 Clonogenic survival experiments

Ramos cell survival curves obtained with the radiolabelled mAbs and expressed as a function of the activity concentration in the medium are reported in figure 2.11. For the same test activity, ^{177}Lu-Rituximab resulted in the highest therapeutic efficacy, ^{177}Lu-Erbitux

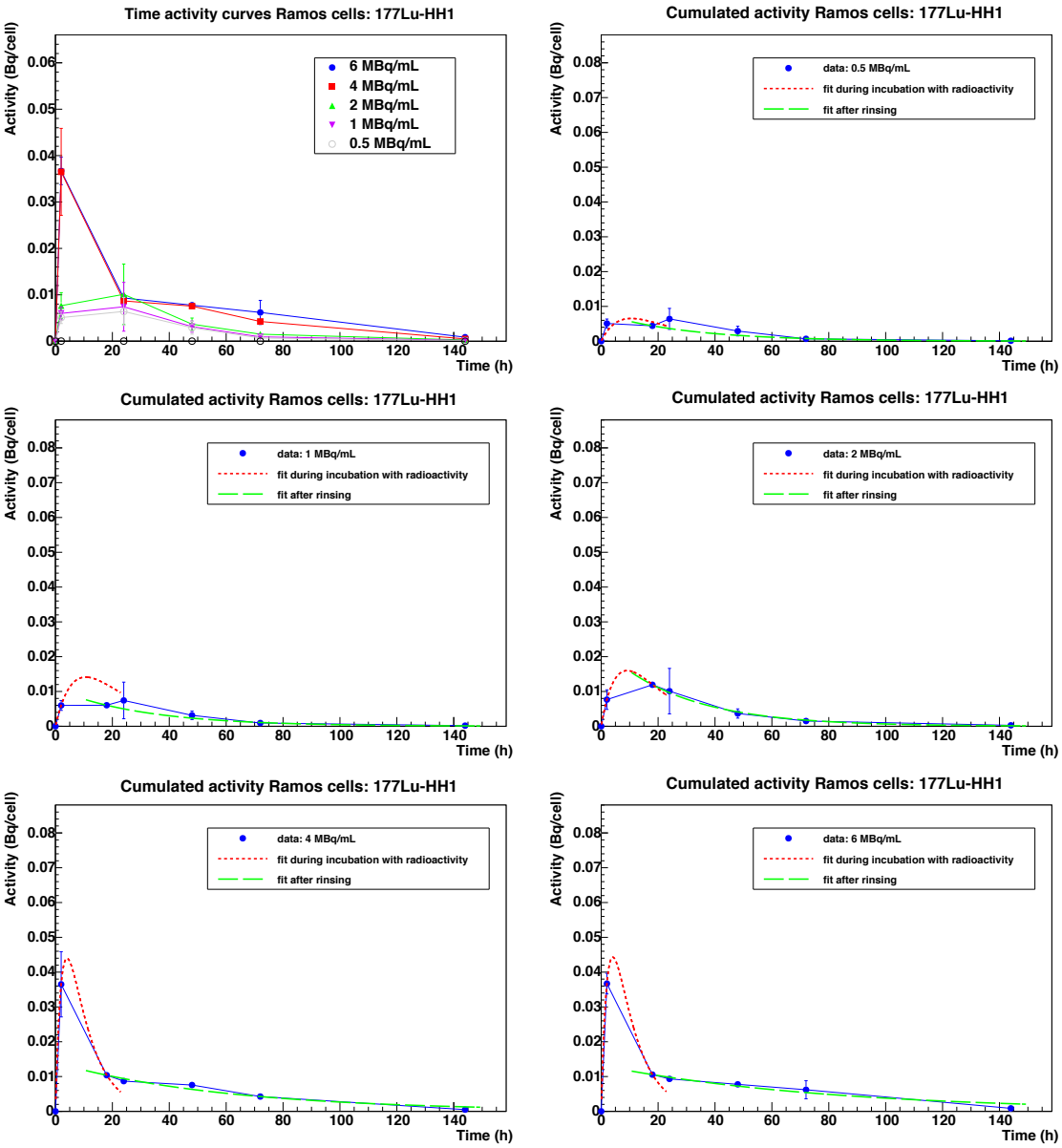

Figure 2.8: Top left: time activity curves obtained for Ramos cells treated with ^{177}Lu-HH1, and for the five different initial activity concentrations in the culture medium. In the other plots, each single time-activity curves is fitted with equations 2.4.8.

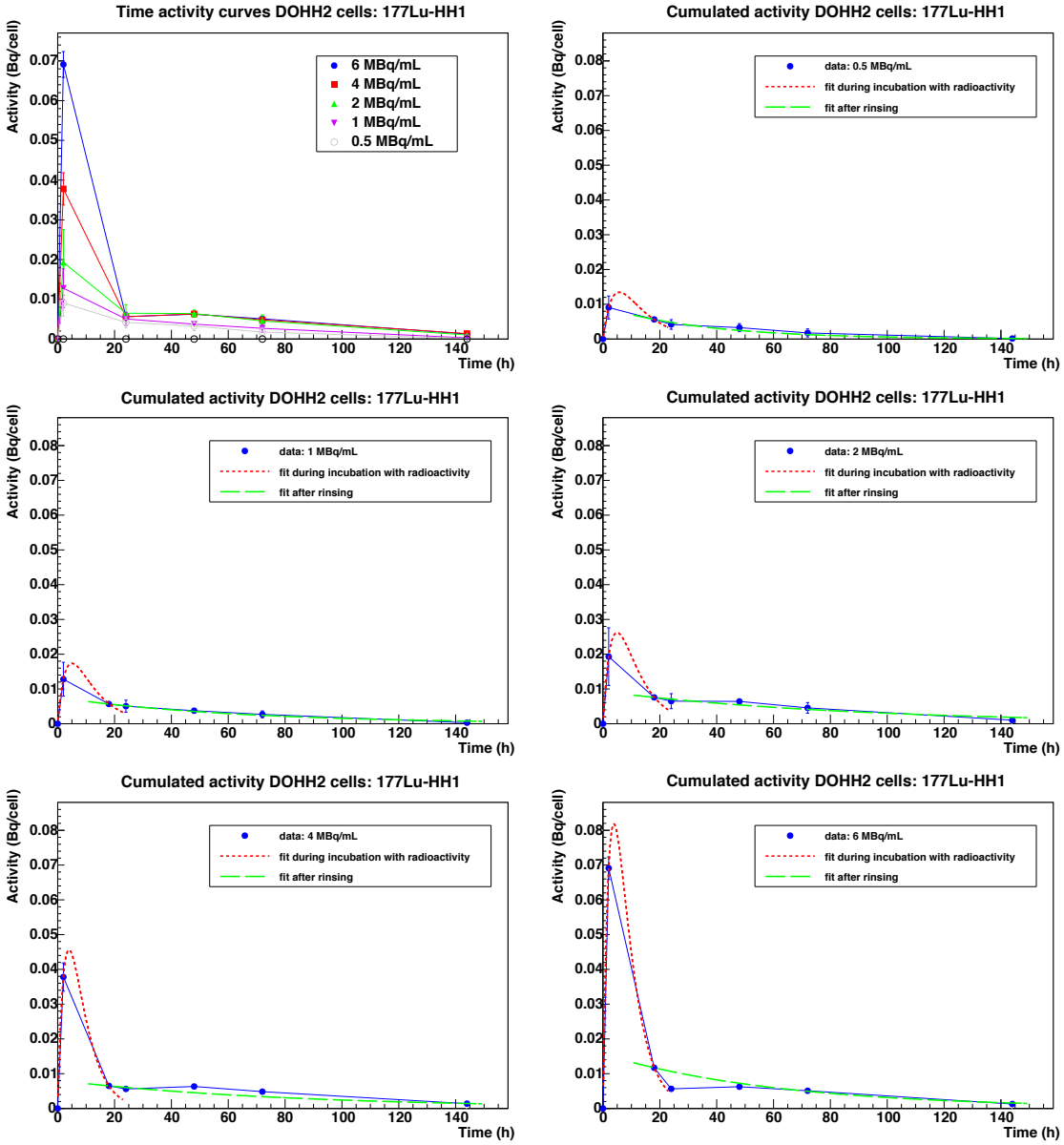

Figure 2.9: Top left: time activity curves obtained for DOHH2 cells treated with ^{177}Lu-HH1, and for the five different initial activity concentrations in the culture medium. In the other plots, each single time-activity curves is fitted with equations 2.4.8. In this figure and in figure 2.8, the same vertical scale was selected in order to facilitate the comparison.

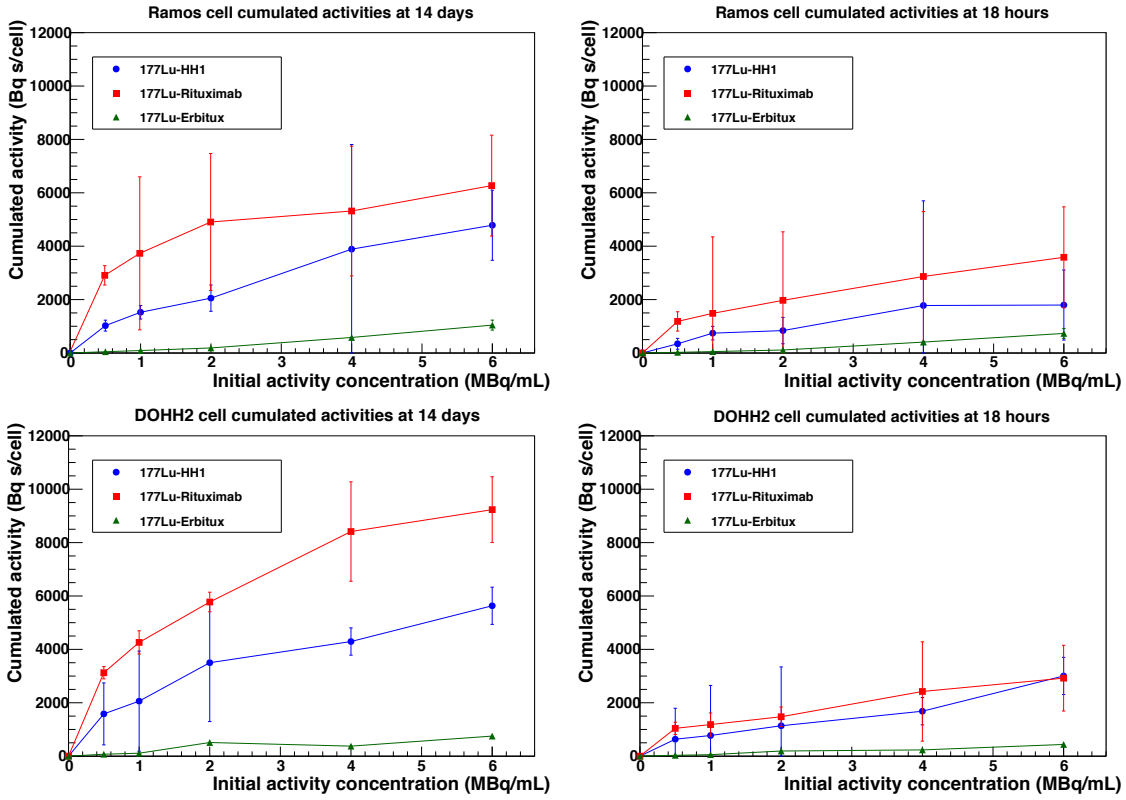

Figure 2.10: Ramos (top) and DOHH2 (bottom) cells cumulated activity as a function of the initial activity concentration in the medium (MBq/mL) for the three mAbs. The plots on the left correspond to time-activity curves integrated between 0 and 336 hours. For plots on the right, the integration was performed between 0 and 18 hours.

in the lowest while ^{177}Lu-HH1 was in between. It must be kept in mind that Erbitux does not bind to the cells. In figure 2.12, survival curves obtained with the labelled and the unlabelled version of HH1 and Rituximab are expressed in terms of mAb concentration (ug/mL) in the medium for direct comparison. The high cytotoxicity of Rituximab is evidenced in figure 2.12, right, where approximately half of the cell population is killed by the treatment. On the contrary, HH1 (figure 2.12, left) showed a lower (although not negligible) cytotoxicity with only 10% of cells killed.

2.4.1.3 Determination of culture cell geometry

The relevant parameters describing Ramos and DOHH2 cells cultures geometry are reported in tables 2.2 and 2.3 for the three regions considered. They were obtained from cells treated with ^{177}Lu-HH1 and ^{177}Lu-Rituximab, and they were subsequently used as input to the dosimetric model. As expected, the values found for cluster size and cell/cluster

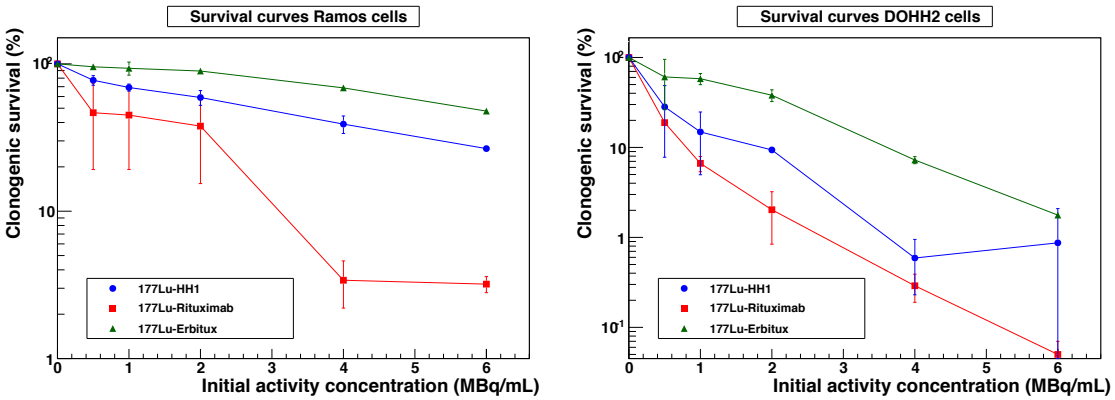

Figure 2.11: Ramos (left) and DOHH2 (right) cells clonogenic survivals as a function of the initial activity concentration in the medium (MBq/mL).

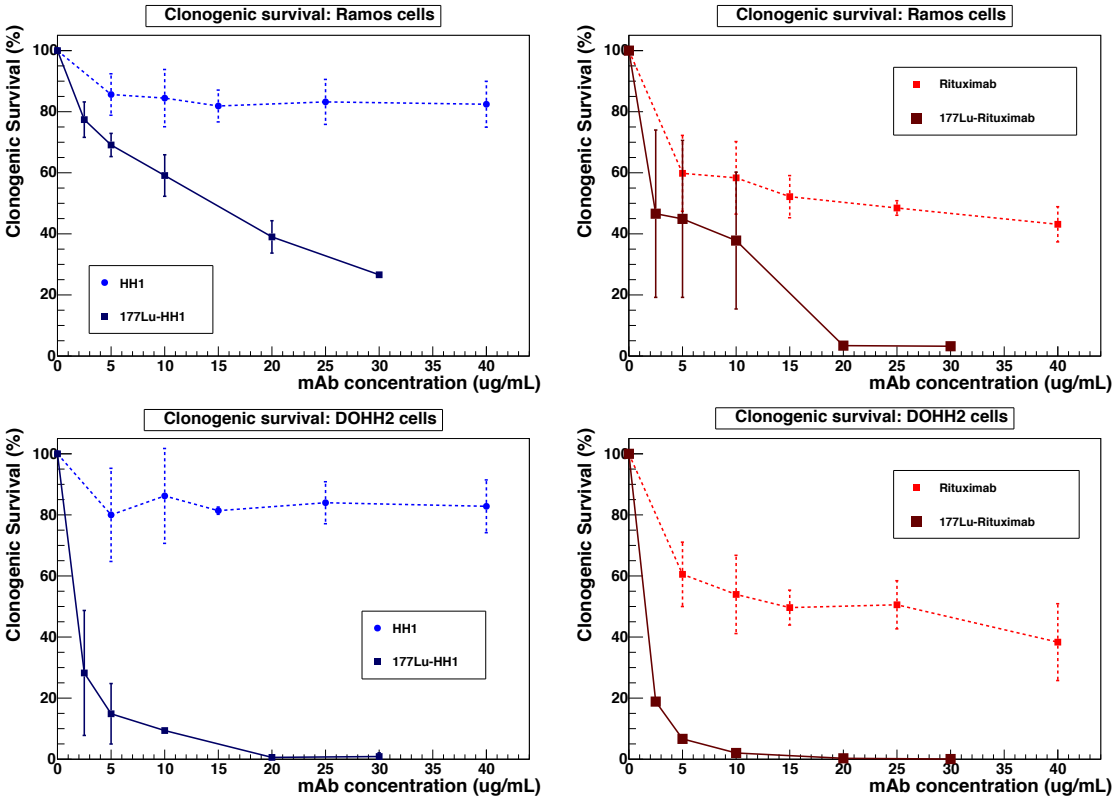

Figure 2.12: Ramos (top) and DOHH2 (bottom) cells clonogenic survivals as a function of the initial mAb concentration (ug/mL) in the medium. Cell survivals on the left are obtained with the labelled and unlabelled versions of HH1, and those on the right with the labelled and unlabelled versions of Rituximab.

density do not differ significantly for the two mAbs.

Ramos cells					
Region	Cluster radius (um)	St. Dev.(um)	Isolated cell/cm^2	Clusters/cm^2	N_{layers}
^{177}Lu-HH1					
centre	23.87	4.88	none	2.72 10^4	3
halfway	21.46	6.50	negligible	2.31 10^4	2
edge	21.62	9.90	1.20 10^5	2.17 10^4	1
^{177}Lu-Rituximab					
centre	28.52	4.03	none	2.29 10^4	3
halfway	28.31	10.06	1.09 10^5	1.10 10^4	2
edge	21.64	7.75	5.89 10^4	1.06 10^4	1

Table 2.2: Geometrical parameters derived from Ramos in-vitro experiments.

DOHH2 cells					
Region	Cluster radius (um)	St. Dev.(um)	Isolated cell/cm^2	Clusters/cm^2	N_{layers}
^{177}Lu-HH1					
centre	24.91	4.59	none	3.36 10^4	3
halfway	32.35	15.32	negligible	6.12 10^3	2
edge	14.08	1.11	2.52 10^4	1.02 10^3	1
^{177}Lu-Rituximab					
centre	26.85	3.87	none	2.35 10^4	3
halfway	23.08	9.28	9.78 10^4	9.15 10^3	2
edge	19.28	6.43	5.13 10^4	6.35 10^3	1

Table 2.3: Geometrical parameters derived from DOHH2 in-vitro experiments.

2.4.2 Dosimetry

2.4.2.1 Self-irradiation

Self-irradiation S values are reported in table 2.4 for the three different target regions and the three source distributions considered. S values corresponding to 50% of radioactivity in the cytoplasm and 50% in the cell surface were calculated using equation 2.3.4. These results were compared to MIRD cellular S values (Goddu et al. 1997) for validation

purposes. MIRD S values are calculated analytically using electron stopping powers in the CSDA, and neglecting photon contribution. Percentage differences of few percents were found, which are most probably due to the fact that secondary electrons and photons are not considered in the analytical calculations.

Self-irradiation S values (Gy/Bq s)			
Ramos cells			
		Source	
Target	100% CS	100% Cy	50% Cy + 50% CS
Cell	$6.51\ 10^{-4}$	$9.32\ 10^{-4}$	$7.91\ 10^{-4}$
Cytoplasm	$9.07\ 10^{-4}$	$1.28\ 10^{-3}$	$1.09\ 10^{-3}$
Nucleus	$3.75\ 10^{-4}$	$5.61\ 10^{-4}$	$4.68\ 10^{-4}$
DOHH2 cells			
		Source	
Target	100% CS	100% Cy	50% Cy + 50% CS
Cell	$6.19\ 10^{-4}$	$8.25\ 10^{-4}$	$7.22\ 10^{-4}$
Cytoplasm	$1.11\ 10^{-3}$	$1.50\ 10^{-3}$	$1.30\ 10^{-3}$
Nucleus	$4.02\ 10^{-4}$	$5.26\ 10^{-4}$	$4.64\ 10^{-4}$

Table 2.4: Self-irradiation S values for Ramos and DOHH2 cells.

Variations on cell and nucleus size have the highest impact when the absorbed dose is scored in the cytoplasm: percentage differences between Ramos and DOHH2 cells S values are in this case 22% and 17% for a 100% CS and a 100% Cy source respectively. The influence of source localisation is rather pronounced for all target regions considered and both cell lines: percentage difference of 45% and 33% are found for Ramos and DOHH2 cells respectively, when the source is localised in the cytoplasm or on the cell surface.

2.4.2.2 Cross-irradiation

In figure 2.13, cross-irradiation S values obtained from direct MC simulation are reported as a function of the cell-to-cell distance calculated at cell surface, for the three target regions (Nucleus, Cytoplasm and the whole cell from left to right). In each plot, results for

the three source distributions considered are presented. The cross-irradiation contribution is about one order of magnitude lower than self-irradiation when the cells are in contact. At 4 radii distance (surface-to-surface distance of 20.4 um) the ratio between self- and cross-irradiation S values for the whole cell is of the order of 100.

The radioactivity localisation in the source cell has not a significant impact on the absorbed dose to the target cell: the highest discrepancy (∼7%) is found between a 100% CS and a 100% Cy source distributions in the case of contiguous cells and when considering the cytoplasm as target volume. Under the same conditions, the percentage difference between S values for two cells placed at 4 radii distance is about 0.5%. These results justify the use, at higher cell-to-cell distances, of cross-irradiation S values not taking into consideration the radioactivity heterogeneity within the cell.

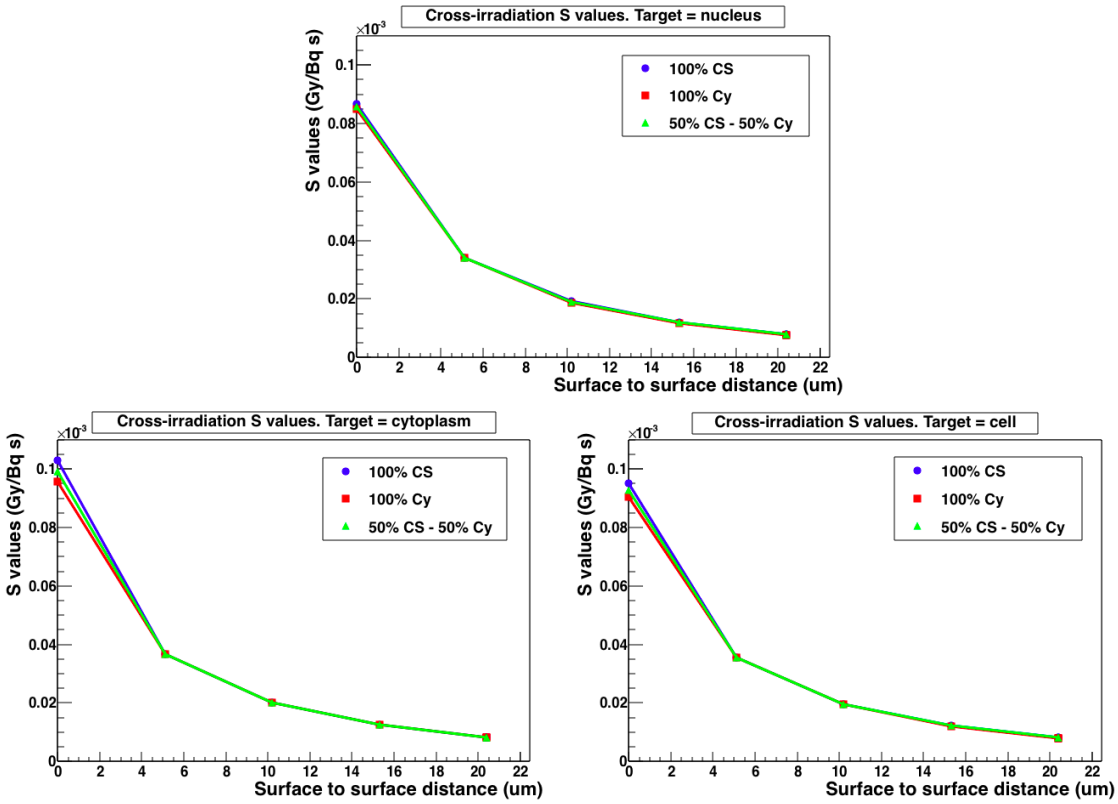

Figure 2.13: Cross-irradiation S values obtained from direct MC simulation for three different targets (nucleus, cytoplasm and whole cell). In each plot, S values are reported for different cell-to-cell distances, and for difference radioactivity internalisation hypotheses.

In figure 2.14 (left), cross-irradiation S values derived from ^{177}Lu DPKs are represented

by a blue dashed line, together with those calculated with MIRDcell (continuous red line). Data points (green) represent ^{177}Lu cross-irradiation S values obtained via direct MC simulation. The direct MC approach is assumed to produce the most accurate absorbed doses with respect to MIRDcell, for which secondary electrons are neglected, and the DPK approach based on a punctual source and target approximation. In the range 22.0 – 61.95 um, where three of the simulated S values superpose the DPK S values, the percentage difference between the two datasets is below 5% (c.f. figure 2.14, triangular points). Their agreement at short cell-to-cell distances validates the assumption of punctual target and source made for the generation of DPK S values. At the same time, at rather short cell-to-cell distances, MIRDcell and DPK data visually show the same behaviour. However, MIRDcell S values display an artificial periodicity that increases with cell-to-cell distance, and that most probably depends on a bug in the MIRDcell applet. Even in the range 22.0 – 120 um, where the MIRDcell periodic response is less evident, the percentage differences between the DPK and the MIRDcell datasets (DPK - MIRDcell)x100/MIRDcell) are quite high: a maximum and an average percentage difference of 28.8% and 20.0% are observed respectively (see figure 2.14, circular points).

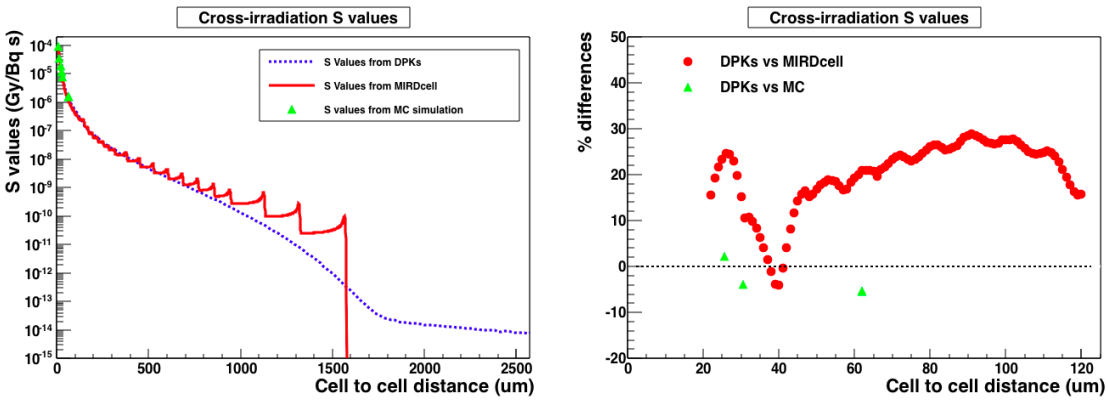

Figure 2.14: On the left plot: cross-irradiation S values obtained from MIRDcell (red), from DPKs (blue), and via direct MC simulation (green). On the right: percentage differences between MIRDcell and MC data with respect to S values derived from DPKs.

Calculation of cross-irradiation absorbed dose.

Cross-irradiation average absorbed doses obtained from isolated cells (D_{IC}), single tar-

get cluster (D_{TC}) and surrounding multiple clusters models (D_{SC}) in each region of the counter well, were summed up using the total numbers of cells in each region as weights. For each combination of cell line and antibody considered in this study, a specific average cross-irradiation absorbed dose values was found. The separate contributions of D_{IC}, D_{TC} and D_{SC} are shown in figure 2.15 in the case of Ramos (top) and DOHH2 (bottom) cells treated with the two specific antibodies (^{177}Lu-HH1 and ^{177}Lu-Rituximab). In all experiments, the highest absorbed dose comes from radioactivity in the cluster the target cell belongs to; D_{TC} is about two times D_{SC}. On the other hand, the impact of radioactivity in isolated cells is low but generally not negligible (of the order of 0.5 Gy for Ramos cell treated with ^{177}Lu-Rituximab), with the exception of DOHH2 cells treated with ^{177}Lu-HH1 for which it is almost null. The higher absorbed doses obtained for cells treated with ^{177}Lu-Rituximab are mostly due the highest measured cumulated activity per cell. Cross-irradiation absorbed doses for cell treated with the non-specific antibody (^{177}Lu-Erbitux) resulted negligible with respect to ^{177}Lu-HH1 and ^{177}Lu-Rituximab absorbed doses: at 6 MBq/mL, ^{177}Lu-HH1 cross-irradiation absorbed dose is about 3 and 7 times higher for Ramos and DOHH2 cell respectively, while ^{177}Lu-Rituximab absorbed dose is 7 times higher for both cell lines.

For all mAbs and both cell lines considered, the relative standard deviation on the total cross-irradiation absorbed dose was on average 24%. This value directly depends on the randomisation of cellular uptake of radioactivity and geometrical configurations implemented in the dosimetric model; in turn, it provides a measure of the great heterogeneity of parameters characterising a cellular systems both *in vitro* and *in vivo*.

2.4.2.3 Non-specific irradiation

Non-specific irradiation S values obtained from direct MC simulation of a single Ramos cell (5.1 um cell radius and 4.0 um nucleus radius) are reported in table 2.5 for the three target regions considered. In the same table, S values calculated with MIRDcell for a 4 and 5 um radius cells, are also shown.

The non-specific irradiation cell S value obtained for the 4 um radius cell in MIRDcell could be approximately considered as the nucleus S value if assuming that the medium activity included (or missing) in the spherical shell between 4 and 5 um does not have a significant contribution to the nucleus/cell absorbed dose. In these conditions it is possible to compare nucleus S values obtained with MIRDcell and the direct MC simulation, for

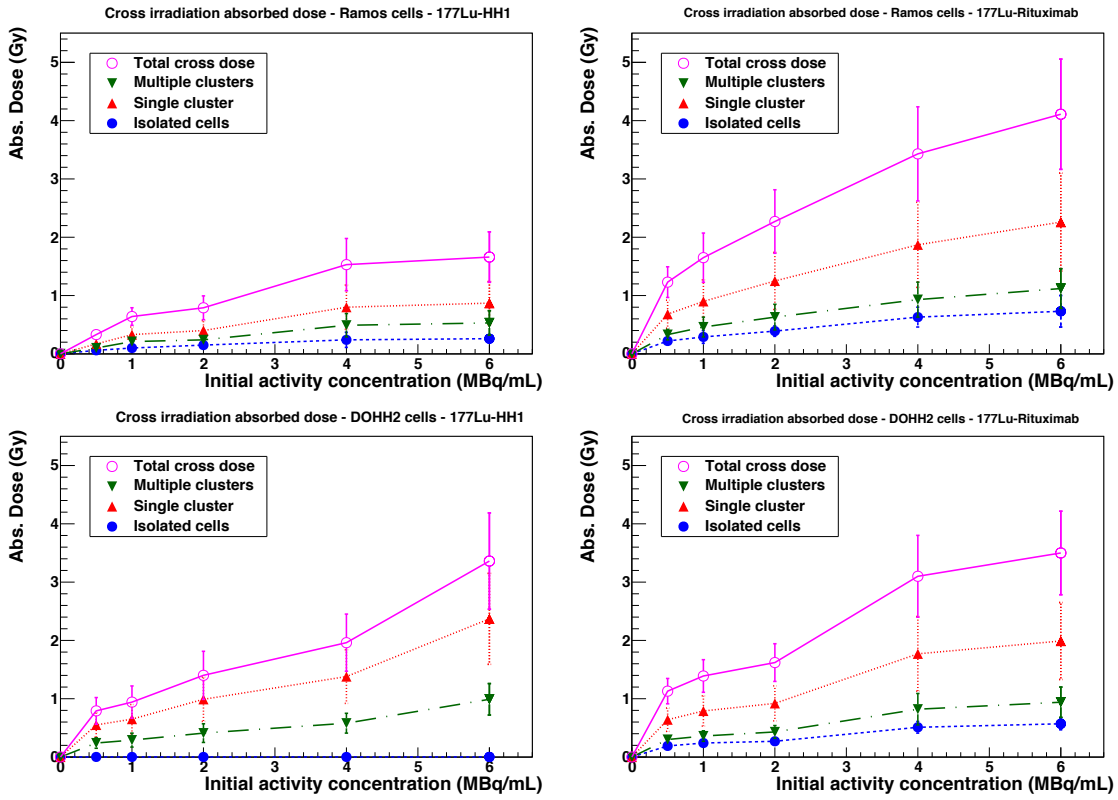

Figure 2.15: The different contributions of D_{IC}, D_{SC} and D_{MC} are shown for the two specific mAbs (^{177}Lu-HH1 on the left and ^{177}Lu-Rituximab on the right) and the two cell lines (Ramos on top, DOHH2 at bottom.)

Non-specific irradiation S values			
Target	Cell	Cytoplasm	Nucleus
MC (Ramos cell)	$3.10\ 10^{-10}$	$3.19\ 10^{-10}$	$3.01\ 10^{-10}$
MIRDcell (4 um radius cell)	$3.44\ 10^{-10}$	-	-
MIRDcell (5 um radius cell)	$3.43\ 10^{-10}$	-	-

Table 2.5: Non-specific irradiation S values obtained via direct MC simulation and from MIRDcell.

which a 14% difference was found. At the same time, the percentage difference between nucleus and cell S values obtained with Geant4 was 3%, while a 0.3% differences was found between S values calculated with MIRDcell for cells of 4 and 5 um radius. Besides, the difference between the S values obtained with MIRDcell and the direct simulation is about 10% for the 5 um radius cell. The direct MC simulation is a priori more realistic and provides in principle the more accurate result. For this reason, in this work, the non-specific irradiation nucleus S value issued from the MC simulation was used for the calculation of the total absorbed dose. However, considering the huge spare of time allowed by the analytical approach, the use of MIRDcell or another equivalent method is recommended for future applications.

2.4.2.4 Total absorbed dose

In figure 2.16, self-, cross- and non-specific absorbed doses to the nucleus are reported as a function of the initial activity concentration in the medium, for Ramos and DOHH2 cells treated with ^{177}Lu-HH1, ^{177}Lu-Rituximab and ^{177}Lu-Erbitux. In general, most of the absorbed dose to the target cell is due to non-specific irradiation. For both cell lines treated with the non-specific mAb (^{177}Lu-Erbitux), the non-specific absorbed dose augments with increasing activity concentration in the medium, at approximately constant rate. A quite similar behaviour is also observed for Ramos cells treated with the two specific mAbs. In the case of DOHH2 cells, instead, at high initial activities, non-specific irradiation is lower (for ^{177}Lu-HH1) or of the same order (for ^{177}Lu-Rituximab) of the cross-irradiation contribution. This effect is a direct consequence of the higher cumulated activities found for DOHH2 cells. Indeed, if more labelled mAb is internalised in the cells, the activity in the medium, and hence the corresponding absorbed dose, is reduced

accordingly. Furthermore, at low activity concentrations, for which cellular receptors are not saturated, the cross- and the self-irradiation absorbed doses are higher than the non-specific absorbed dose, for both cell lines treated with ^{177}Lu-Rituximab. Conversely, for cells treated with ^{177}Lu-HH1, the non-specific irradiation becomes dominant at quite low initial activities (> 1 MBq/mL).

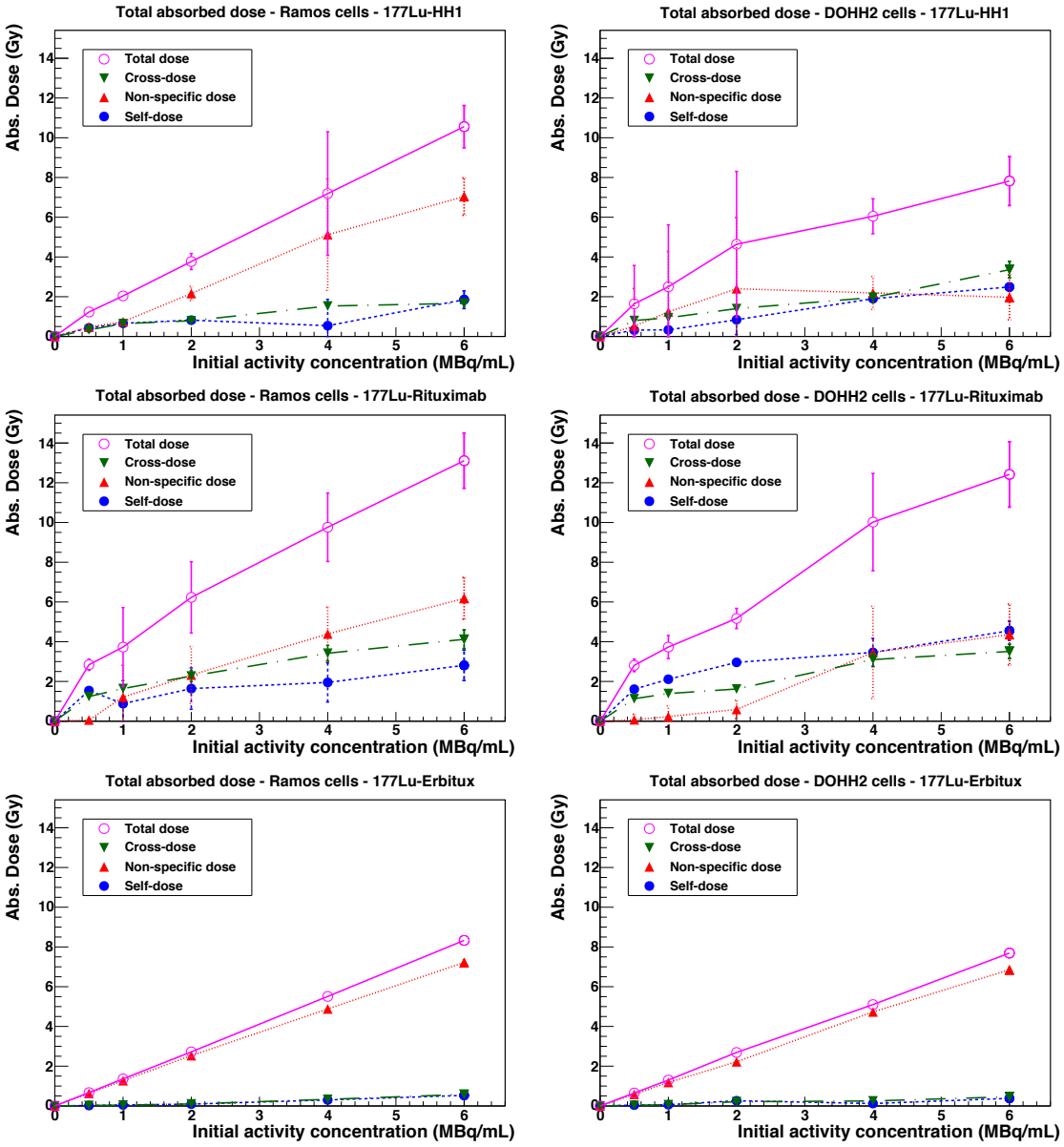

Figure 2.16: The Different contributions of self-, cross- and non-specific irradiation absorbed doses are shown for the three mAbs and the two cell lines (Ramos on the left, DOHH2 on the right).

Despite the self-absorbed dose is calculated over a larger temporal frame with respect to the cross-absorbed dose (336 hours vs. 18 hours), its contribution is, on average, the smallest. However, for DOHH2 cells treated with ^{177}Lu-Rituximab, the self-absorbed dose is higher than the cross-absorbed dose, most probably because of the high mAb uptake for this configuration. The results here presented correspond to specific internalisation hypotheses for the three antibodies (50% CS + 50% Cy for ^{177}Lu-HH1, and a 100% CS for ^{177}Lu-Rituximab and ^{177}Lu-Erbitux). Other possibilities have been explored, reaching compatible absorbed dose values, since in the dosimetric model implemented the internalisation only impacts the self-irradiation absorbed dose.

2.4.3 Clonogenic survival

In figures 2.17 and 2.18, Ramos and DOHH2 survivals are presented as a function of nucleus absorbed dose for the three ^{177}Lu-mAbs considered, before (top) and after (bottom) correction for mAb toxicity. A Linear Quadratic (LQ) model (Dale 1985) was considered for the fit of all datasets. Errors on both axes were considered, using a generalised version of the χ^2 method (effective variance method) as implemented in ROOT. Fit results are displayed in each plot: the parameter p0 and p1 correspond to the α and β parameters of the LQ model.

For Ramos cells, ^{177}Lu-HH1 data not corrected for toxicity showed a linear behaviour ($\beta = 0$), while for ^{177}Lu-Rituximab and ^{177}Lu-Erbitux, β was different from zero. According to these results, the combination of radiation damages and biological toxicity was more effective for ^{177}Lu-Rituximab than for the non specific ^{177}Lu-mAb (^{177}Lu-Erbitux), with ^{177}Lu-HH1 being in between. After correction for antibody toxicity, both ^{177}Lu-HH1 and ^{177}Lu-Rituximab displayed a linear behaviour, with β compatible to zero. The effect of the correction on ^{177}Lu-HH1 survival curves was to approximately double the D_{37} value (the absorbed dose required to achieve 37% survival) from 7.2 Gy to 12.9 Gy without directly impacting on the shape of the curve. Conversely, ^{177}Lu-Rituximab survival was shifted from a LQ response with a $D_{37} = 4.6$ Gy, to a linear response with D_{37} =18.3 Gy. For the non-specific antibody, which was supposed non-cytotoxic, survival curves followed the LQ model with a $D_{37} = 9.9$ Gy and $\alpha/\beta = 3.7$ Gy.

An interesting effect of toxicity correction is that survival curves of the three mAbs get closer: in particular at low absorbed doses, where the experimental errors are relatively low, the three curves almost perfectly superpose. If the hypothesis that cell deaths by

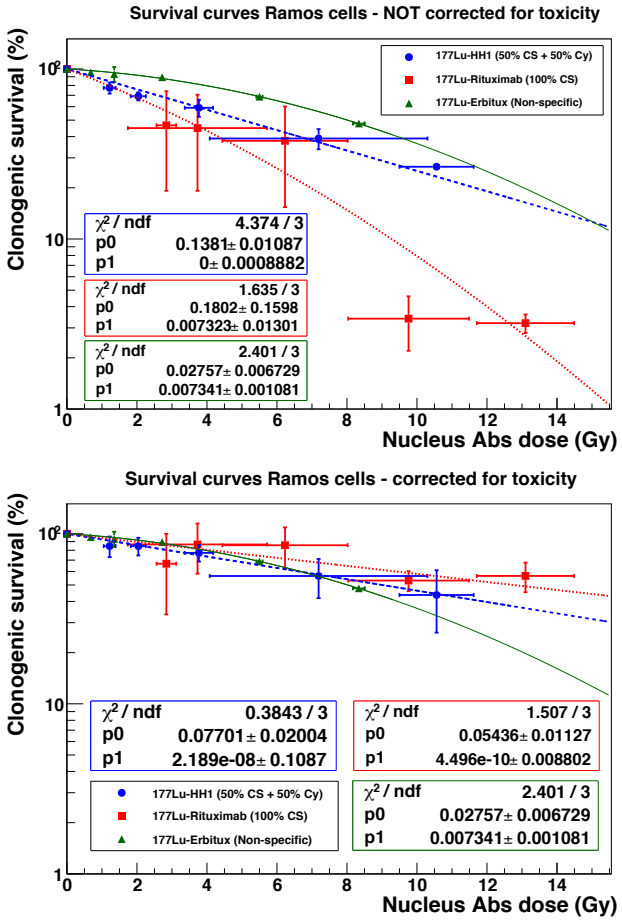

Figure 2.17: Ramos cells clonogenic survival as a function of nucleus absorbed dose.Survival curves on top include both cytotoxic and radiative effect, while those at bottom are corrected for antibody toxicity.

radiation and by cytotoxicity are additive phenomena is correct, the curves at bottom of figures 2.17 and 2.18 only account for radiative effects, hence, a similar absorbed dose-response relationship is expected for the three ^{177}Lu-mAbs. In order to determine if the treatment has a significant effect on the curve shape, the three corrected survivals have been compared with an F-test (Motulsky and Christopoulos 2005), which is appropriate for nested data. For each couple of datasets, the null hypothesis is that the same curve fits both data points and the difference is purely due to chance. The high p-value (0.27) found for the couple ^{177}Lu-Rituximab/^{177}Lu-HH1 demonstrated that, given the errors introduced by the experiments and the absorbed dose model, it is not possible to reject the null hypothesis. A similar conclusion can be drawn for the couple ^{177}Lu-HH1/^{177}Lu-Erbitux, for which the p-value was 0.28. Conversely, the non-specific antibody survival

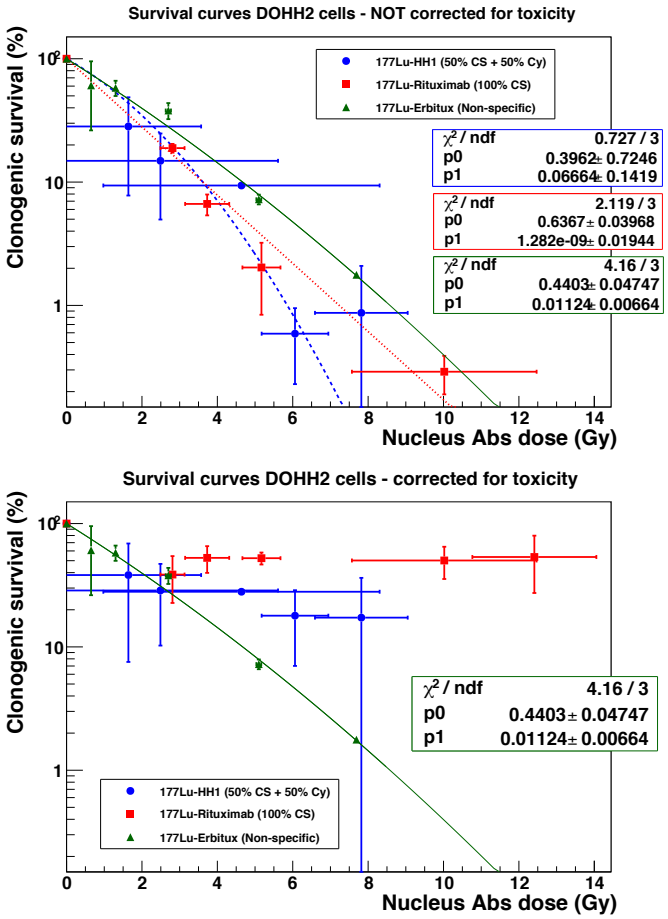

Figure 2.18: DOHH2 cells clonogenic survival as a function of nucleus absorbed dose. Survival curves on top include both cytotoxic and radiative effect, while those at bottom are corrected for antibody toxicity.

resulted significantly different from ^{177}Lu-Rituximab survival (p-value = 0.03), if considering a 5% significance.

For DOHH2 cells, the overall efficacies of ^{177}Lu-HH1 and ^{177}Lu-Rituximab seemed to be comparable when both cytotoxic and radiative effects were taken into account. The two specific antibody also showed a higher efficacy than ^{177}Lu-Erbitux's. Both ^{177}Lu-HH1 and ^{177}Lu-Erbitux curves could be fitted with a LQ model, obtaining D_{37} values of 1.9 and 2.1 Gy respectively. At the same time, an α/β ratio of 39.2 Gy was found for cells treated with ^{177}Lu-Erbitux, which confirmed the higher radiosensitivity of DOHH2 cells with respect to Ramos. Conversely, ^{177}Lu-HH1, showed a linear behaviour with D_{37} = 1.6 Gy. After correction for antibody toxicity, ^{177}Lu-HH1 and ^{177}Lu-Rituximab survival

curves displayed a saturation effect even at low absorbed doses. In both cases, it was not possible to fit the data neither with a linear nor with a LQ model. According to figure 2.18 (bottom), DOHH2 cell treatment with ^{177}Lu-HH1 resulted more effective than with ^{177}Lu-Rituximab, when considering only radiation effects.

2.5 Discussion

Paradigm of radiobiology is that radiation-induced biological effects are proportional to the delivered absorbed dose. Therefore in conventional External Beam RadioTherapy (EBRT) linear or linear quadratic response is generally established for survival of cells exposed to radiation. However, such an assumption is not straightforward in targeted radionuclide therapy (TRT) in particular because cell irradiation between EBRT and TRT differs in many ways. In TRT, cells are irradiated at low absorbed dose rate (< 1 Gy h^{-1} in the experiment here described) and therefore, they have more time to repair; irradiation may be highly heterogeneous at the cellular level; and finally the contribution of the unlabelled cytotoxicity associated with the radiopharmaceutical needs to be considered to extract purely radiative effects and thus establish an absorbed dose-effect relationship. Clonogenic assay is the reference technique for investigating biological effects of radiation on cells: the relationship between clonogenic survival and nucleus absorbed dose allows comparing differences in efficacy of various treatments. Calculating nucleus absorbed dose in TRT is much more complex than in EBRT. Many variables can affect the absorbed dose to a given cell in a colony *in vitro*: sub-cellular and intra-cellular radioactivity distribution, cell spatial distribution, cell size. Taking into account this level of variability can make the dosimetry a challenge, especially for what concerns the calculation of the cross-absorbed dose. In particular, when considering beta emitting radiopharmaceuticals with a range in water of few millimetres, the average cell cross-absorbed dose depends on the heterogeneous characteristics of a large number of cells.

2.5.1 Dosimetric model

The dosimetric model developed allows calculating the average cell absorbed dose for *in-vitro* experiments taking into consideration realistic culture characteristics (cell size, isolated cell/cluster density, cluster size, average cell cumulated activity). Intracellular variability of these parameters is further taken into account randomising the geometrical

properties of the modelled colony, and calculating a standard deviation for the resulting cell absorbed dose. The approach used is generic and can be applied to any type of radiation, provided that the relevant self-absorbed dose S values and DPKs are known. The firsts are easily found in the literature for most common radionuclides (Goddu et al. 1997), while the seconds are available for some β-emitters (Papadimitroulas et al. 2012, Prestwich et al. 1989b) and mono-energetic electrons (Cross et al. 1982).

In this work, the model was applied to the dosimetry of two different cell lines treated with three monoclonal antibodies (mAbs) radiolabelled with a β-emitter (^{177}Lu). For this particular scenario, the highest contribution to cell absorbed dose was in general due to non-specific irradiation associated to the radioactivity in the culture medium (with the exception of DOHH2 cells treated with ^{177}Lu-Rituximab). Clearly, this outcome is specific of *in-vitro* experiments where cells and cell clusters are well spaced and most of the culture volume is occupied by the incubation medium. *In vivo*, cells are closers and the non-specific activity is expected to contribute less. Disregarding non-specific irradiation, most of cell absorbed dose was associated to cross-irradiation from cells other than the target. Cross-absorbed dose contribution from the cluster the target cell belongs to, was about two times the cross-absorbed dose due to other clusters (of the order of 2 Gy for Ramos and DOHH2 cells treated with ^{177}Lu-Rituximab, at 6 MBq/mL of medium activity). At the same time, cross-absorbed dose contribution from isolated cells was the lowest but, in some cases, not negligible (i.e. $\sim$0.7 Gy and $\sim$0.6 Gy for Ramos and DOHH2 cells treated with ^{177}Lu-Rituximab, at 6 MBq/mL of medium activity). Both contributions of cell clusters and isolated cells are large enough to produce measurable modification of survival curves if neglected, which proves the necessity of modelling the whole culture geometry when β-emitters are involved. On average, cross- and self-irradiation absorbed doses were of the same order.

Results obtained also evidenced a little dependence of the total absorbed dose on cell size and sub-cellular radioactivity distribution in the case of ^{177}Lu. In fact, both these variables, are only included in the calculation of the self-absorbed dose, which only partly contributes to the total cell absorbed dose. At the same time, ^{177}Lu cross-irradiation S values have been demonstrated to be independent on sub-cellular uptake for cell-to-cell distances larger than 20.4 um (4 cells radii). Moreover, cross-irradiation S values calculated in the punctual approximation were able to well reproduce (within 5%) the S values obtained via direct Monte Carlo simulation and taking into account actual cell size.

In order to avoid even this level of approximation, the use of MIRDcell cross-irradiation S values was initially considered, but this path was abandoned because of the artificial periodicity found in MIRDcell data. Even if the 20% difference found between cross-irradiation S values calculated in this study and MIRDcell's may seem inconsequential considering the small absolute values of the data involved, it should be noted that, summed up over thousands cells the difference may become considerable.

The aim of this approach was to generate a multi-cellular model as realistic as possible. Still, some approximations had to be made in order to keep it reasonably simple. The main assumption was to consider constant the number of cells in the colony during the 18h-incubation time with radioactivity, while proliferation may occur with a direct impact on cell/cluster density and cluster size. Also, the computation of the cross-absorbed dose was limited to a target cell placed at the centre of the Model Volume. This restriction was considered appropriate since the Model Volume (whose size is of the order of ^{177}Lu beta range in water) is much smaller than the culture well volume. As a consequence, most of cells in the colony can be safely considered as "central": many Model Volumes can, in fact, be inscribed in the well volume.

Furthermore, a non-conventional approach was used to take into account cell labelling heterogeneity. While in many works (Rajon et al. 2011, Vaziri et al. 2014) only a fixed fraction of cells is assumed to be labelled, and hence considered in the dosimetric calculation, here all modelled cells were included in the dosimetry. In this work, in fact, the experimental determination of cell cumulated activity (and its standard deviation), is performed on samples of about 8000 cells; in principle, within these cells, different levels of radioactivity uptakes are achieved, with some cells being unlabelled. Therefore, randomly sampling cell cumulated activity on the basis of these variables, indirectly guarantees to adequately model cell labelling heterogeneity.

Nevertheless, the establishment of cell cumulated activities remains the main weakness of this work. The limited number of experimental points available for the cells time-activity curves made it very difficult to determine the time of maximum uptake. A two-function-fit approach was hence proposed to estimate the shape of the curve during incubation. However, the consequent need to fit a three parameters function on three data points, made the convergence of the fit very unstable, and the errors associated to the cumulated activities considerably large. In addition, for most experiments, a maximum uptake time between 5 and 10 hours was found, which is earlier than expected. Further measurements

(already scheduled) of cells activity, including several data points between 2 and 18 hours, will be able to confirm or contradict this result. A better sampling of the time-activity curve is also expected to provide more accurate estimations of cell cumulated activities.

2.5.2 Interpretation of survival curves

Despite the experimental errors involved and the approximation introduced by the dosimetric model, we have been able to establish curves expressing clonogenic survival as a function of the nucleus absorbed dose. It was showed that, correcting clonogenic survival response for unlabelled mAb toxicity, modified the shape of absorbed dose-effect relationship, with curves getting closer in the case of Ramos cells: this effect suggested a certain degree of absorbed dose-effect correlation. Under this hypothesis, the rather similar Ramos cells survivals obtained for the specific (^{177}Lu-Rituximab and ^{177}Lu-HH1) and the non-specific (^{177}Lu-Erbitux) antibodies, may be interpreted as an indirect validation of the dosimetric model. This is particularly true for the simplest of the three models, consisting of Ramos cells exposed to ^{177}Lu-Erbitux. In this case, in fact, nucleus absorbed dose almost exclusively depends on the radioactivity accumulated in the culture medium. The dosimetric model is therefore extremely simple and hence more reliable (the model depends on fewer *a priori* assumptions). Besides, in the case of ^{177}Lu-Erbitux, the cell killing mechanism is by definition purely radiative since Erbitux does not bind to cells (or at least not significantly). At the same time, adding the complexity of the cross-absorbed dose calculation (c.f. ^{177}Lu-Rituximab and ^{177}Lu-HH1) produces survival curves close to those of ^{177}Lu-Erbitux, which is the expected effect in case of absorbed dose-effect correlation.

In order to determine the presence (or the lack thereof) of a absorbed dose-effect correlation in Ramos cells experiments, survival curves were fitted with LQ model as it is generally done in EBRT for low-LET radiation. The idea was to compare the LQ curves and determine if the three mAbs survivals could be described by a single absorbed dose-effect relationship. It was found that the differences between ^{177}Lu-Rituximab and ^{177}Lu-HH1 curves, and between ^{177}Lu-HH1 and ^{177}Lu-Erbitux curves were not significative (5% confidence level), while ^{177}Lu-Erbitux curves were significantly different from ^{177}Lu-Rituximab survival even after correction for cytotoxicity. In addition, according to survival curves corrected for toxicity (figure 2.17, bottom), ^{177}Lu-Erbitux seems to have a higher therapeutic efficacy than the specific antibodies. This result clearly indicates that

something is still missing in the model (a possible over-estimation of the cross-absorbed dose) or in the biological interpretation of the data. Certainly, a better estimation of cell cumulated activities could contribute, in the future, to reduce the uncertainties in the absorbed dose calculation.

The same effect was found for DOHH2 cell lines. DOHH2 cells survival curves including both cytotoxic and radiation induced effects indicated that the two specific ^{177}Lu-mAbs had approximately the same therapeutic efficacy, with ^{177}Lu-Erbitux being less effective. However, after correction, ^{177}Lu-Erbitux presented a higher therapeutic efficaciy. This outcome is somehow unexpected, as ^{177}Lu-Erbitux is non-specific and hence it is not significantly internalised by lymphocyte B cells.

A plausible explanation to this phenomenon is that lymphoma cells contain two sub-populations with different sensitivities: a first population is sensitive to the genotoxic effects of the treatment (indifferently of either mAb or ^{177}Lu) and dies first, while a second population is constituted of more resistant cells. Therefore, the greater the efficacy of the mAb alone, the lower the effect of radiation per Gy. This would suggest that biological effects of unlabelled mAbs (HH1 and Rituximab) occur before the effects of radiation are detectable. The plateaux observed after correction for cytotoxicity for DOHH2 cells treated with ^{177}Lu-Rituximab and ^{177}Lu-HH1 further corroborates this hypothesis. In the case of DOHH2 cells, the increased efficacy of the non-specific antibody is even more evident because of the higher sensitivity of these cell lines (α/β ratio was 29.7 Gy for DOHH2 cell and 3.4 Gy for Ramos cells when considering ^{177}Lu-Erbitux survivals). Further experiments are currently ongoing in order to verify this assumption.

Another possible explanation of ^{177}Lu-mAbs results would be the involvement of bystander effects. This phenomenon consists in the death of cells that have not been directly crossed by particles but are in proximity of irradiated cells. In this context, a higher than expected cytotoxicity may be observed at low cell absorbed doses, while a saturation effect may occur at higher absorbed doses.

All these data highlight the complexity of establishing absorbed dose-effect relation in TRT. In particular, the nature of interactions between pure mAb-induced and pure radiation-induced biological effects is unknown; it was thus showed that ^{177}Lu-Erbitux was more efficient per Gy in killing cells than ^{177}Lu-HH1 or ^{177}Lu-Rituximab. These conclusions would not be different if synergy (instead of additivity) between mAb efficacy and radiation effects was considered.

2.6 Conclusions

In a context of clonogenic survival experiments for the evaluation of novel radiopharmaceuticals, an accurate assessment of cell absorbed dose is crucial to better understand cell death mechanisms, and to evaluate the therapeutic efficacy *in vitro*. The calculation of the absorbed dose in TRT is intrinsically more complex than in EBRT since it depends on many variables. Especially when β-emitters are involved, particular attention should be paid to the calculation of the cross-irradiation absorbed dose.

A realistic multi-cellular dosimetric model was developed for the calculation of average cell absorbed dose on the basis of experimentally determined parameters (cell size, isolated cell/cluster density, cluster size, average cell cumulated activity). The model was applied to the study of a novel ^{177}Lu-labelled radiopharmaceutical targeting CD37 receptors expressed by lymphoma B cells. This approach is generic and it can be useful for the determination of the average cell absorbed dose in clonogenic survival experiments involving any type of radiation.

Chapter 3

Tumour dosimetry in α-particles radioimmunotherapy

3.1 Introduction

Animal studies are a pre-requisite for the application of new drugs in human clinical trials. This requirement is established by law in both Europe and USA. In preclinical studies aiming at the evaluation of radiopharmaceuticals (radioactive agents), an accurate dosimetry is essential for the observation of an absorbed dose-effect correlation, both for efficacy and toxicity assessment. These need has been acknowledged by several scientists working in this field (Pouget et al. 2011, Konijnenberg et al. 2011, Behr et al. 2000, Konijnenberg et al. 2007).

Nevertheless, pre-clinical dosimetric models usually do not take into account tissue and activity heterogeneity within organs and tumours. This goes usually on pair with the way activity is determined. Conventional pharmacokinetics assessment is typically performed by counting radioactivity (gamma counters) present in collected organs after animal sacrifice, at various time points after the administration of the radiopharmaceutical. This approach is limited (but simple to implement) as it only provides mean activity concentration in a given sample, thus limiting absorbed dose determination to whole organs or tumours (activity heterogeneity within the tissue/organ is not taken into account).

Other factors that may impair the reliability of the absorbed dose estimate are the employment of incomplete pharmacokinetic models, and the imprecise measurement of tumour volumes. In general, absorbed dose uncertainties of 20% or more can be observed in these studies, and this can make the difference between establishing or not an absorbed

dose-effect correlation (Konijnenberg et al. 2011).

Especially in the case of short range radiations (α-particles, Auger electron), the average absorbed dose delivered to the tumour is not necessarily a relevant parameter for the evaluation of novel radiopharmaceuticals in terms of efficacy. In this case, in fact, if the size of the organ/tumour considered is significantly larger than particle range in tissue, the energy released by the radiopharmaceutical is deposited locally and the resulting absorbed dose distribution is almost as heterogeneous as the radioactivity distribution. In this chapter, average and voxel-based tumour dosimetries are compared in the framework of a *alpha*-particle radioimmunotherapy experiment.

In radioimmunotherapy (RIT), diffuse or metastatic cancer cells are killed by using radiolabelled monoclonal antibodies (mAbs) against tumour-associated antigens. Several studies in humans and animals have shown a potential indication of intraperitoneal radioimmunotherapy for the treatment of peritoneal carcinomatosis (2-3 mm in size) as an adjuvant treatment after cytoreductive surgery in combination with or in replacement of Hyperthermic IntraPEritoneal Chemotherapy (HIPEC) (Aarts et al. 2007, Koppe et al. 2005, Santoro et al. 2009, Boudousq et al. 2010). However, the only phase III clinical trial to evaluate intraperitoneal RIT for ovarian cancer using ^{90}Y-HMFG1 mAb was rather unsatisfactory (Verheijen et al. 2006). A possible explanation is the use of long range (10.1 mm in water) and low Linear Energy Transfer (LET = 0.2 keV/um) β particles. These characteristics, combined to the reduced size of tumours treated, resulted in a too low absorbed dose to the tumours (Oei et al. 2007). The use of α-particles, is therefore a promising alternative: their short range (50 - 100 um) and high LET (80 - 300 keV/um) make them much more deleterious locally than conventional β-emitters.

Recently, Boudousq et al. (2013) evidenced a lack of absorbed dose-effect correlation in animal alpha-radioimmunotherapy (α-RIT) experiments of small volume peritoneal carcinomatosis, when only the average tumour absorbed dose was taken into account. Most of preclinical studies on RIT with ^{212}Pb (Milenic et al. 2005, Milenic et al. 2007, Horak et al. 1997, Tan et al. 2012, Milenic et al. 2008) have targeted the Human Epidermal growth factor Receptor 2 (HER2). As anti-HER2 mAbs are internalized in the cytoplasm after receptor binding (Hudis 2007), ^{212}Pb-mAb internalization could contribute to both RIT efficacy and toxicity. Their objective was hence to compare the efficacy and toxicity of non-internalizing ^{212}Pb-35A7 (anti-carcinoembryonic antigen, CEA) monoclonal antibody,

which mostly remains at cell surface, and of internalizing ^{212}Pb-trastuzumab (anti-HER2) mAb, in RIT of small volume peritoneal tumours that express CEA and HER2 receptors. They injected (intraperitoneally) three groups of swiss nude mice bearing 2-3 mm tumour xenograft, with 1.48 MBq of ^{212}Pb labelled mAbs: ^{212}Pb-35A7, ^{212}Pb-trastuzumab plus a non-specific mAb (^{212}Pb-PX) as a control. Subsequently, they built Mice Survival (MS) curves over a period of 130 days (see figure 3.1) and calculated the Kaplan-Meier survival estimates (Goel et al. 2010) for the three groups, plus a group of mice treated with NaCl for control. A mediam MS of 94 days was found for mice treated with ^{212}Pb-35A7, while the median MS was not even reached for mice treated with ^{212}Pb-trastuzumab, indicating a higher therapeutic efficacy of the internalising mAb. Nonetheless, tumour dosimetry, performed under the assumption of spherical tumour shape and homogeneous radioactivity uptake (measured with a gamma counter after mice sacrifice), resulted in a higher absorbed dose for the non-internalising mAb.

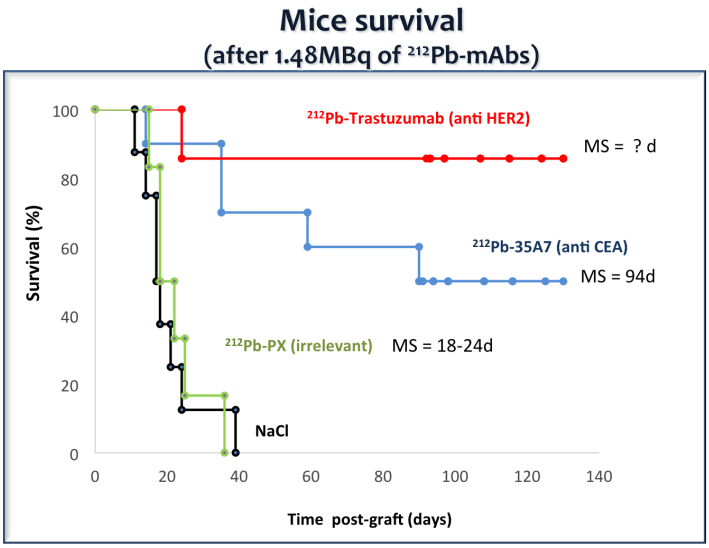

Figure 3.1: Survival curves obtained by Boudousq et al. (2013), for mice treated with ^{212}Pb-trastuzumab,^{212}Pb-35A7, ^{212}Pb-PX (irrelevant), and NaCl (for control).

The aim of this work is to apply more refined absorbed dose assessment techniques to animal experiments carried out at IRCM (Institut de Recherche en Cancérologie de Montpellier) under the same conditions of those described in Boudousq et al. (2013). In order to better understand the uptake mechanism of the three mAbs, the assessment of

activity distribution heterogeneities at tumour level was carried out using beta imaging to determine receptors distributions *in vivo* through autoradiography. tumour absorbed dose distributions calculated on the basis of these images were in agreement with mice survival curves determined in the previous work, confirming that the lack of absorbed dose-effect correlation found by Boudousq et al. was due to approximate dosimetry.

3.2 Experiments

Experiments described in this section were performed by the Radiobiology and Targeted Radiotherapy group at "Institut de Recherche en Cancérologie de Montpellier"(IRCM), U1194 INSERM, Montpellier, France.

3.2.1 Labelled antibodies

Trastuzumab (Herceptin, Genentech Incorporated, San Francisco CA, USA) is a humanized IgG1k internalizing mAb against the Human Epidermal Receptor type 2 (HER2) expressed in vulvar squamous carcinoma A-431 cells. The non-internalizing murine IgG1k mAb 35A7, specific for the CEA Gold 2 epitope (Pouget et al. 2008) was obtained from hybridoma, kindly provided by Dr J-P Mach, Lausanne, Switzerland (Hammarstrom et al. 1989). Affinity of 35A7 for CEA is 9.76 10^{-8} M (Robert et al. 1996) while affinity of trastuzumab for HER2 is 0.16 10^{-9} M (Baselga et al. 1998). The non-targeting IgG1 mAb PX was purified from the ATCC mouse hybridoma P3X63Ag8 (Kohler et al. 1976) and was used for control experiments. A summary of the properties of the three mAbs used is reported in table 3.1.

antibody	targeted antigen	receptor binding
Trastuzumab	HER2	internalising
IgG1k 35A7	CEA	non-internalising
IgG1 PX	-	non-specific

Table 3.1: List of mAbs employed in this study and their characteristics.

Trastuzumab, 37A7 or PX were conjugated with TCMC (Macrocyclics, Dallas, TX,

USA) using a 12-fold molar excess of ligand to mAb, as described in Milenic et al. (2005). The $^{224}Ra/^{212}Pb$ generators were provided by AREVA Med SAS (Bessines-sur-Gartempes, Haute-Vienne, France) and radiolabelling with ^{212}Pb was performed as described by Tan et al. (2012). Then, 1 mg mAb-TCMC was incubated with 37 MBq ^{212}Pb at 37 ^oC for 1 hour and the reaction quenched with 4 mL, 0.1 M EDTA (Ethylenediaminetetraacetic Acid Disodium Salt) solution. Specific activities were about 37 MBq/mg for the three mAbs. The labeling yield (ratio $^{212}Pb/^{212}Pb$-mAbs) was generally $< 2\%$.

3.2.2 Animal experiments

Swiss nude mice (7 weeks old females) from Charles River were acclimated for 1 week before experimental use. Subsequently, they were intraperitoneally (ip) grafted with 0.7 10^6 HER-2 positive vulvar squamous carcinoma A-431 cells, suspended in 0.3 mL DMEM (Dulbecco's Modified Eagle Medium), and transfected with CEA and luciferase genes. Three days post-graft, tumour growth was determined by bioluminescence imaging to separate mice in three homogeneous groups. The following day, mice received a single ip injection of ^{212}Pb-35A7 (anti-CEA), ^{212}Pb-trastuzumab (anti-HER2) or ^{212}Pb-PX (non-specific) mAbs with an activity of 1.48 MBq (37 MBq/mg). The following nomenclature was adopted for the three mice groups:

- G1: 6 mice treated with ^{212}Pb-trastuzumab;
- G2: 5 mice treated with ^{212}Pb-35A7;
- G3: 3 mice treated with ^{212}Pb-PX;

Mice were eventually sacrificed at 4, 17 and 24 hours post-injection and tumours were resected. Tumour mass (of the order of a few mg) was distributed among 6.2 $\pm$ 4.5 nodules/mouse. In figure 3.2, a typical tumour set extracted from a single mouse is shown.

3.2.3 Tumour imaging

For each mouse, all resected tumours were quickly frozen in liquid nitrogen using a single slide, for a total of 14 slides. Each slide was then cut in half along the longitudinal axis in order to approximately access the central plane of the tumours. Two adjacent 10 um thick cryosections were selected for DAR (Digital AutoRadiography) imaging and histopathology analysis.

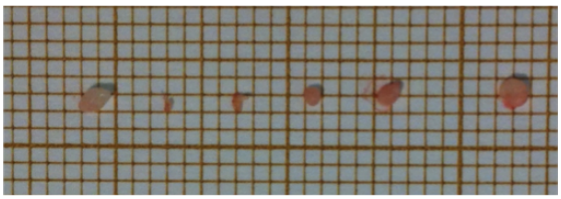

Figure 3.2: Typical tumour samples resected from a single mouse of this study. Courtesy of JP. Pouget.

The BetaIMAGER^{TM}dFine (Biospace Lab) was used to determine the spatial distribution of ^{212}Pb-mAbs with a spatial resolution of 10 – 25 um. The sample was covered with a scintillating foil to convert electrons emitted by ^{212}Pb, ^{212}Bi and ^{208}Tl into photons that are detected by an intensified CCD (Charge-Coupled Devices) camera. Images were acquired for a minimum time of 30 minutes for the early time points (4h) to a maximum time of 2 hours for the latest (24 h), in order to account for count loss due to decay. Imaging times were arbitrarily chosen to make it possible the scan of all cryosections within the working day. Final data were stored in the form of binary images ($20 \times 20 \times 10$ um^3 voxel size) of the Counts Per Minute (CPM) registered.

Adjacent tumour sections were also stained with Hematoxylin Erythrosine Saffron (HES) and the general morphology was analyzed under a standard transillumination microscope. With this technique, both tumour areas with and without radioactivity uptake were stained. In figure 3.3 and 3.4, DAR (left) and HES (right) images obtained for two adjacent sections of tumours treated with ^{212}Pb-Trastuzumab and ^{212}Pb-35A7 are shown as an example. Ten and eleven larger tumours can be identified in the ^{212}Pb-Trastuzumab and ^{212}Pb-35A7 images respectively. On average, in the case of ^{212}Pb-35A7 treatment, the radioactivity was mainly present at tumour surface, while for ^{212}Pb-Trastuzumab and the non-specific antibody (not shown here) a quite homogeneous radioactivity distribution was found. Necrosis did not occur in any of the nodules shown.

3.3 ^{212}Pb-mAbs pharmacokinetics

3.3.1 ^{212}Pb source

^{212}Pb beta-decays into ^{212}Bi that in turns decays into ^{208}Tl and ^{212}Po. In ^{212}Pb-mAbs radioimmunotherapy, the main α-particles emitted by ^{212}Bi (6.09 MeV) and ^{212}Po (8.78 MeV) are employed to deliver a short-range, lethal absorbed dose to tumour cells. The

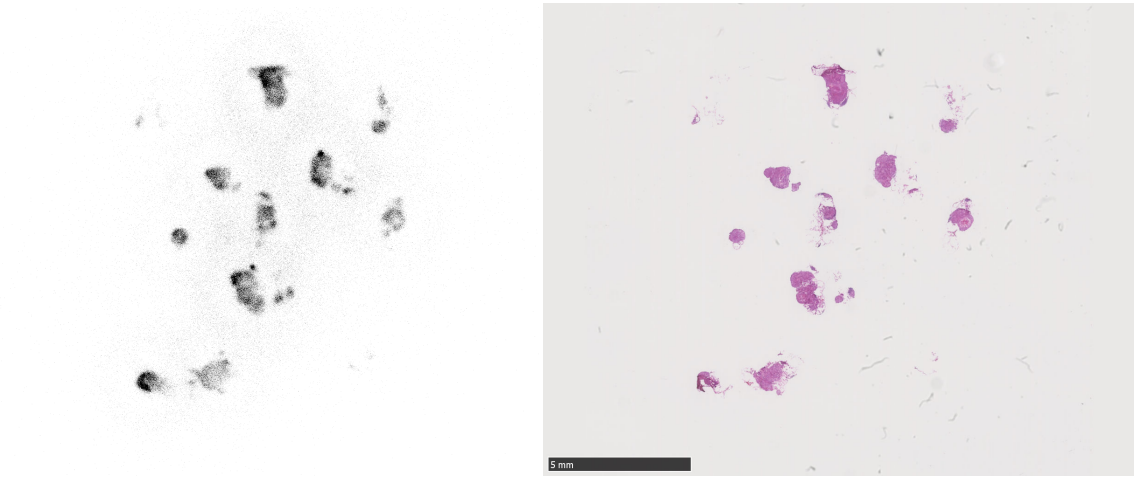

Figure 3.3: Example of DAR (left) and HES images (right) for tumours treated with ^{212}Pb-Trastuzumab (G1).

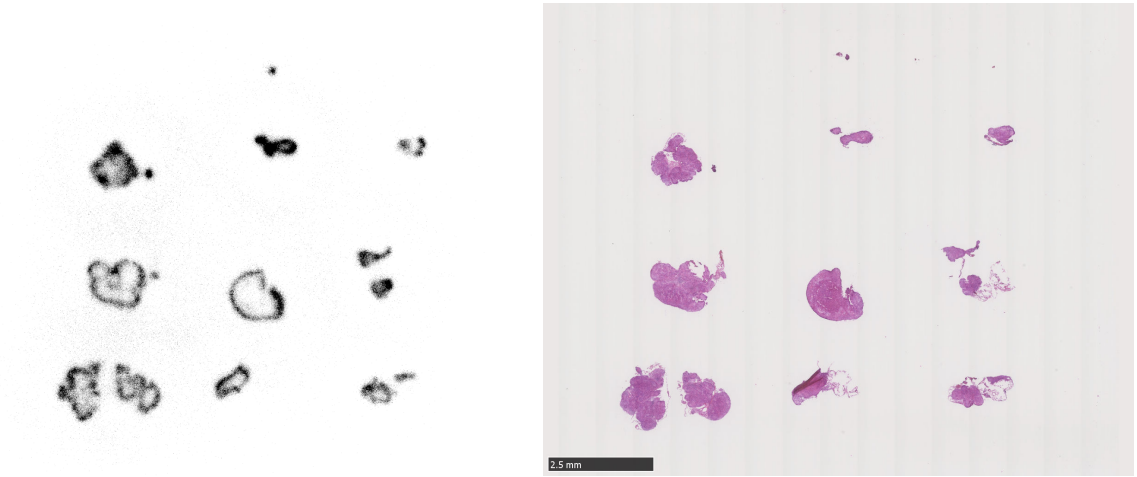

Figure 3.4: Example of DAR (left) and HES images (right) for tumours treated with ^{212}Pb-35A7 (G2).

radioactive decay scheme for ^{212}Pb is shown in figure 3.5. It includes α- and β-particles with energies going from a few hundred keV up to 8.78 MeV, corresponding to ranges in tissue from micrometers to centimeters. The physical half-life of ^{212}Pb is 10.64 h, while

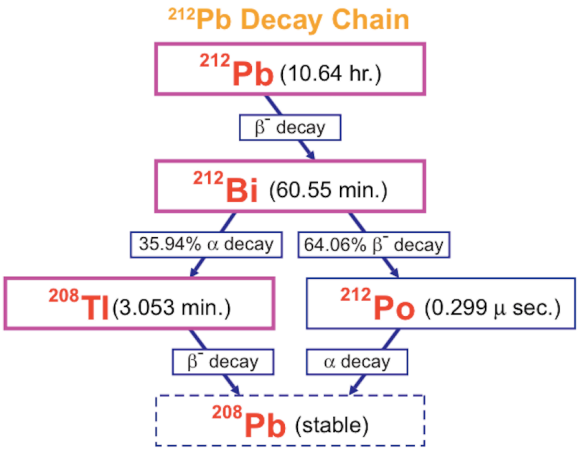

Figure 3.5: ^{212}Pb decay chain.

the half-lives of its daughters are 60 minutes or less, so the decay products are in transient equilibrium with the parent radionuclide (Maiello and Hoover 2010). In figure 3.6 (left) the decay curves of ^{212}Pb and its daughters is obtained from the solution of Bateman equations (McParland 2010) generalised to a decay chain of the form $X_1 \rightarrow X_2 \rightarrow X_3, X_4$:

$$A_1(t) = A_{1,0}\, e^{-\lambda_1 t} \tag{3.3.1}$$

$$A_2(t) = A_{1,0}\Big(\frac{\lambda_2}{\lambda_2 - \lambda_1}\Big)\Big(e^{-\lambda_1 t} - e^{-\lambda_2 t}\Big) \tag{3.3.2}$$

$$\begin{aligned} A_i(t) &= BR_i\; A_{1,0}\Big(\frac{\lambda_{2,i}\lambda_i}{(\lambda_{2,i} - \lambda_1)(\lambda_i - \lambda_1)(\lambda_i - \lambda_{2,i})}\Big) \\ &\times \Big((\lambda_i - \lambda_{2,i})e^{-\lambda_1 t} - (\lambda_i - \lambda_1)e^{-\lambda_{2,i} t} + (\lambda_{2,i} - \lambda_1)e^{-\lambda_i t}\Big) \end{aligned} \tag{3.3.3}$$

In equations 3.3.1, 3.3.2 and 3.3.3, λ_1 and λ_2 are respectively the decay constants of ^{212}Pb (λ_{Pb}) and ^{212}Bi (λ_{Bi}). At the same time, $\lambda_{2,i}$ and BR_i are the ^{212}Bi decay constant and the branching ratio for either the ^{208}Tl ($i = 3$) or the ^{212}Po ($i = 4$) channel, depending on the decay chain the equation is applied to. Similarly, λ_i is the decay constant of either

^{208}Tl or ^{212}Po to ^{208}Pb. $\lambda_{2,1}$ and BR_i satisfy the relations:

$$\lambda_{2,3} = \lambda_{Bi \to Tl} = BR_{Bi \to Tl}\ \lambda_{Bi} \tag{3.3.4}$$

$$\lambda_{2,4} = \lambda_{Bi \to Po} = BR_{Bi \to Po}\ \lambda_{Bi} \tag{3.3.5}$$

with:

$$\lambda_2 = \lambda_{Bi} = \lambda_{Bi \to Tl} + \lambda_{Bi \to Po} \tag{3.3.6}$$

In figure 3.6 (right) the daughter–parent activity ratios for the three daughters of ^{212}Pb show that a transient equilibrium (constant ratios) is reached approximately at 10 hours for ^{212}Bi and ^{212}Po, while for ^{208}Tl it takes approximately 24 hours. Despite many authors (Baidoo et al. 2013, Howell et al. 1994, Boudousq et al. 2013) assume the transient equilibrium is reached within 4-5 hours, at 5 hours, the ratio of ^{212}Bi, ^{208}Tl and ^{212}Po activities with respect to ^{212}Pb activity is still 4%, 40% and 15% less than their ratio at equilibrium. Therefore, any radioactivity measurement performed before 24 hours should be interpreted with great care.

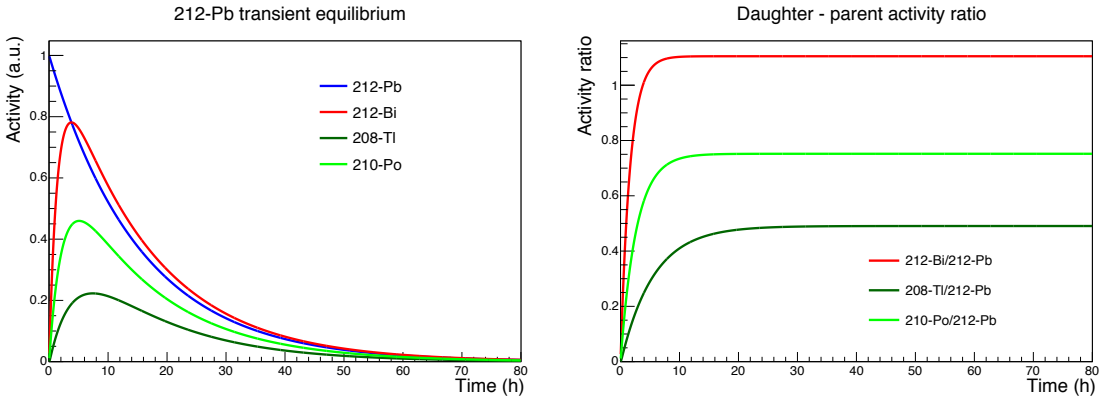

Figure 3.6: Left: radioactive decay of ^{212}Pb and its daughters. Daughters activity is normalised to the the activity of the progenitor. Right: daughter/parent activity ratios. The transient equilibrium is reached at approximately 24 hours.

3.3.2 DAR imager calibration

The absolute ^{212}Pb activity in 8/14 tumour slides was determined immediately after mouse sacrifice and tumour sectioning. Using a previously calibrated gamma counter and selecting the 238.632 keV gamma of ^{212}Pb, activities ranging from 2.87 to 45.38 Bq were found. Since ^{212}Pb activity is measured directly, without contamination from its daughters, the values obtained are free from possible biases even for the earlier time points, when the equilibrium is not reached.

The same plates were subsequently scanned with the BetaIMAGER$^{\text{TM}}$dFine in order to establish a calibration factor for the DAR images. The beta imager, mainly measures β-particles from ^{212}Bi and ^{208}Tl. However, it should be noted that, for tumour slides corresponding to mice sacrificed at 4 hours, transient equilibrium was not reached, especially for ^{208}Tl. For the 17 hours time point, on the other hand, the ratio between ^{208}Tl and ^{212}Pb activity is only 3% lower than the same ratio at equilibrium.

Given the low radioactivity in the slides and the low acquisition times, the DAR images obtained were quite noisy (see for example figures 3.3 and 3.4, left) with only few counts per voxel, on average. Therefore, DAR images were first smoothed by averaging voxel content over a 2 voxels radius, and then, all voxels outside tumour volume having less than 2 counts per minute were arbitrarily put to zero applying a mask. In this way, it was possible to suppress the background counts producing artificial halos around each tumours. In figure 3.7, the processed DAR image corresponding to the tumour set of figure 3.3 (left) is shown as an example.

^{212}Pb and electron activities obtained from the two sets of measurements, were compared to obtain a calibration curve for the DAR images. Since both measurements were performed within approximately 1 hours after mouse sacrifice, the data were not corrected for the physical decay of ^{212}Pb in this time frame. In figure 3.9, the ^{212}Pb activity of the whole tumour section is plotted against DAR counts per minute (CPM_{DAR}). Poisson errors were considered for CPM_{DAR}; error bars fall within the point size. Assuming a linear response without offset, the following calibration factor (k_{DAR}) could be inferred:

$$k_{DAR} = \frac{A(Bq)}{CPM_{DAR}} = 1.432\ 10^{-4} \tag{3.3.7}$$

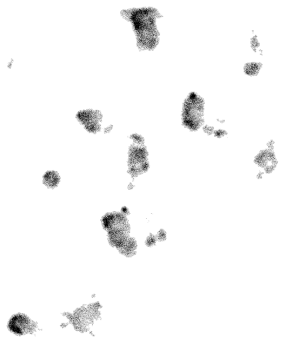

Figure 3.7: DAR image corresponding to the tumour set of figure 3.3 (G1), post-processed for activity determination.

3.3.3 Time activity curves

Single tumours in each DAR image were segmented by thresholding, in order to obtain the total number of tumour voxels N_t in the slide. In most tumours treated with anti-CEA, many voxels in the central region, did not present any uptake of radioactivity. In order to include all tumour voxels in the segmentation, the "fill holes" function of the ImageJ software[1] was applied to the thresholded images. In both cases, the corresponding HES image was used as a reference to visually validate the segmentation.

For each mouse, the specific activity A_t (Bq/g) in the tumour mass (including all nodules) was calculated as

$$A_t = \frac{CPM_{total}\ k}{N_t\ M_{voxel}} \tag{3.3.8}$$

where CPM_{total} are the total DAR counts in the nodule segmented image and M_{voxel} is the voxel mass in grams. When multiple mice were available for a single data point (c.f. G1 and G2), their specific activities were averaged. The resulting average specific activities and standard deviations were hence employed to build time–activity curves for each ^{212}Pb-mAbs (see figure 3.9). Time activity curves were subsequently fitted assuming a mono-exponential decay to extract the cumulated activities ($\tilde{A}_t$) for the three groups.

[1] http://imagej.nih.gov/ij/

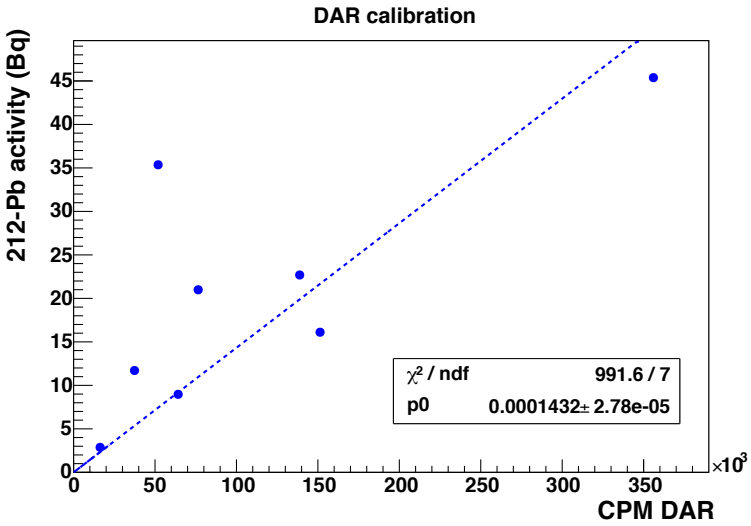

Figure 3.8: DAR calibration curve.

Results are reported in table 3.4.

3.4 Tumour dosimetry

Two different techniques were used for the calculation of tumour absorbed dose on the basis of DAR imaging. To a first approximation, average tumour absorbed dose was calculated assuming a spherical shape and a homogeneous radiopharmaceutical distribution, while in the second instance, radioactivity heterogeneity was taken into account to obtain tumour absorbed dose distribution at the voxel level. With both approaches, only the self-absorbed tumour dose was considered since the short range of ^{212}Pb α-particles prevent the irradiation from surrounding tissues. In both cases, the Monte Carlo technique was applied using the GATE toolkit.

3.4.1 Simulation of ^{212}Pb source

The Monte Carlo simulation of a radioactive source in Gate requires the definition of all emitted radiations in terms of energy and emission probability. For convenience, the emissions are usually categorised per particle type (mono-energetic electrons, mono-energetic photons, β- and α-particles) to define separate macro-sources with different probabilities of emission. At run time, the probability of an event coming from macro-source i, is given by the sum of the emission probabilities (particles/Bq s) of all radiations included

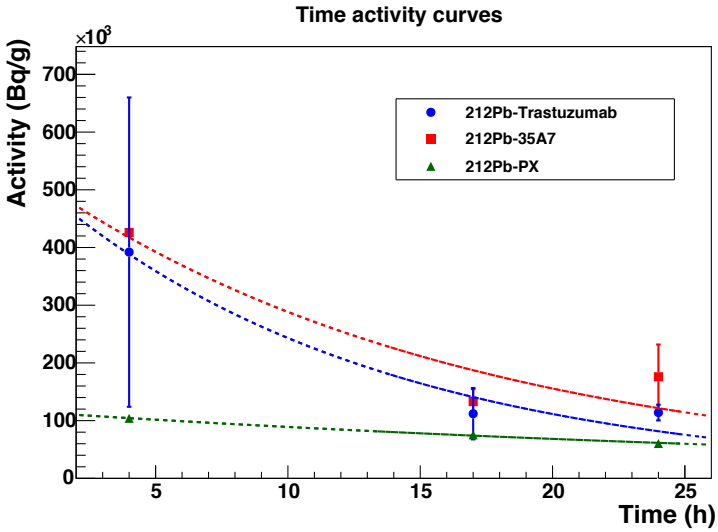

Figure 3.9: Time-activity curves obtained from DAR images of tumours treated with the three ^{212}Pb-mAbs.

in the given macro-source. These probabilities, calculated using the decay data listed in Eckerman and Endo 2008, are reported in table 3.2.

For the simulation of a radioactive decay chain as in the case of ^{212}Pb, the relative branching ratios (BR) of parent and daughter radionuclides should be taken into account. Eleven separate macro-source were hence defined to include all type of emissions from the 4 radionuclides of the ^{212}Pb decay chain. Their relative emission probability was calculated as the product of the particle/Bq s emitted (as listed in Eckerman and Endo 2008) and the BR (reported in table 3.2) of each macro-source. Recoil energy associated with the ^{212}Bi and ^{212}Po decays is ignored (Goddu et al. 1994).

3.4.2 Average tumour absorbed dose

Tumour nodules in the DAR images were analysed one-by-one to calculate their average absorbed dose. Nodule masses were estimated under the assumption that i) they had a spherical shape and that ii) the DAR image was taken at the tumour central slice. Their radius was hence calculated as $(A/\pi)^{1/3}$ where A is the tumour area in mm^2 calculated from DAR images. Average nodule masses were 0.6, 0.7 and 0.5 mg for G1, G2 and G3 respectively.

The Gate Monte Carlo toolkit was used to generate ^{212}Pb S values for water spheres of selected radii (from 0.1 to 1.0 mm). The standard hadron physics list (*hadrontherapyStand-*

Particle/Bq s emitted by the ^{212}Pb decay chain				
Particle type	^{212}Pb	^{212}Bi	^{208}Tl	^{212}Po
photons	6.566219	4.268342	3.635647	0.000000
electrons	5.561768	4.013696	1.224487	0.000000
beta	1.000001	0.640600	1.000001	0.000000
alpha	0.000000	0.359400	0.000000	1.000000
BR	1.000000	1.000000	0.359400	0.640600

Table 3.2: Particles per Bq s emitted by ^{212}Pb and its daughters: the values are given for each type of emission. In the last line, the branching ratios (BR) of each radionuclide is also reported.

ardPhys.mac) available in the "example/example_PhysicsLists "folder of the Gate code was used. The *hMultipleScattering* process was added to take into account α-particles multiple scattering. A range cut of 1.0 μm was selected. Five millions primary particles were generated in order to obtain a negligible statistical uncertainty on the average absorbed dose ($< 0.1\%$). Resulting S values are shown in figure 3.10 as a function of sphere radius.

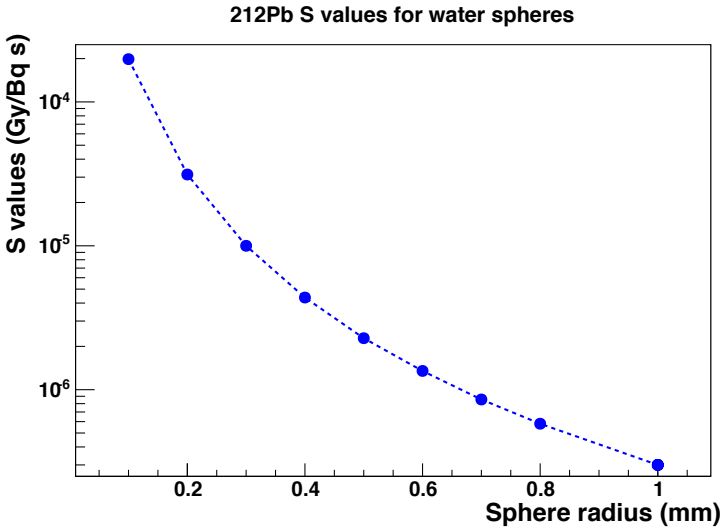

Figure 3.10: Water sphere S values for ^{212}Pb.

S values for any sphere size (ranging from the minimum to the maximum tumour radius) were extrapolated by linear interpolation of simulated data, and then used to

calculate the absorbed dose to each nodule taking into account its specific size (estimated mass) and the specific cumulated activities (Bq s/g) obtained for the three groups. The average tumour absorbed dose and the standard deviation obtained for each group is reported in table 3.3.

		Tumour-specific dosimetry		Self-absorption approximation
Group	Average mass (g)	Abs. Dose (Gy)	Std Dev (Gy)	Abs. Dose (Gy)
G1	6.91 10^{-4}	28.12	2.15	34.14
G2	8.39 10^{-4}	36.16	2.66	43.48
G3	6.45 10^{-4}	17.74	1.34	22.02

Table 3.3: Average tumour absorbed doses for the three groups, obtained using tumour-specific S values (tumour-specific dosimetry) and assuming that all energy emitted by ^{212}Pb is absorbed within the tumour (self-absorption approximation). In the first case, the absorbed dose standard deviation is calculated from the absorbed doses of all tumours resected. For the self-absorption approximation, a unique absorbed dose, independent of tumour mass was achieved. Average tumour mass estimated from 2D DAR images is also reported.

A priori, the hypotheses made to extract nodule masses from 2D DAR images may lead to the use of the wrong S value for a given tumour: this may introduce a certain level of error in the calculation of the absorbed dose. For this reason, an alternative approach that does not take into account tumour mass was also considered (Boudousq et al. 2013). The absorbed dose D_t was calculated assuming that all energy emitted in the tumour (E_{dep}=8.7 MeV/Bq s) is deposited within the tumour itself (self-absorption approximation):

$$D_t(Gy) = \frac{E_{dep}(J)}{mass(g)\ 10^{-3}}\ \tilde{A}_t(s/g)\ mass(g) \tag{3.4.9}$$

The resulting total absorbed doses are shown in table 3.3 for the three groups. Considering the tumour masses in this study, tumour absorbed dose calculated in the self-absorption approximation was overestimated from 10% to 50%. As a matter of fact, for tumours masses of about 0.5 g, the self-absorption hypothesis does not hold true.

3.4.3 Voxel dosimetry

DAR images for the three groups showed heterogeneous radiopharmaceutical distributions for most tumours, especially for what concerns those treated with anti-CEA mAb. The calculation of the absorbed dose at the voxel level is therefore required if this heterogeneity has to be be taken into account.

A representative tumour for each group dataset was selected and used as input for the simulation of the voxel absorbed dose. In picture 3.11, from left to right, HES (top) and DAR (bottom) images of selected tumours for the G1 (^{212}Pb-Trastuzumab), G2 (^{212}Pb-antiCEA) and G3 (^{212}Pb-PX) groups are shown.

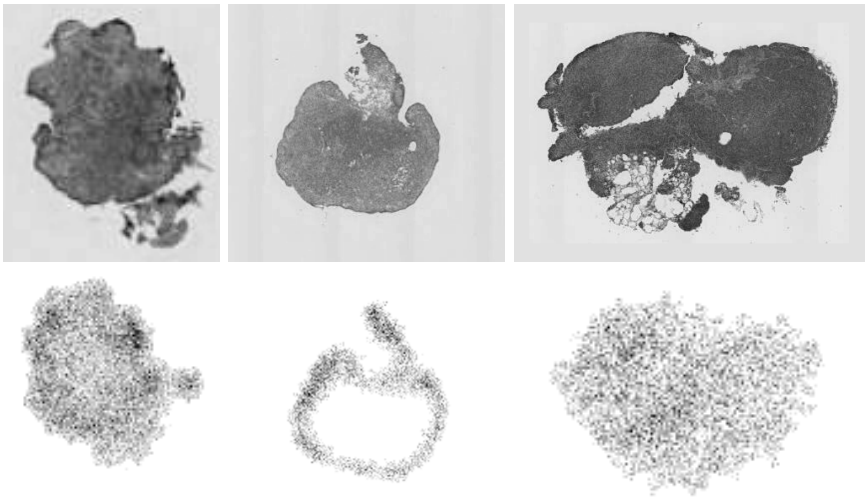

Figure 3.11: HES (top) and DAR (bottom) images of G1, G2 and G3 (from left to right) tumours selected for voxel dosimetry.

The obvious issue for the calculation of tumour absorbed dose from DAR images is to extrapolate the 3D absorbed dose distribution on the basis of a 2D activity distribution. This problem was overcome by performing two different MC simulations. In the first (2D model) the tumour was modelled as bi-dimensional (XY plane) in order to assess the penetration of ^{212}Pb emissions in the third dimension (Z) . In the second, this information was used to build a fictitious 3D model of the tumour (semi-infinite model). This approach allowed taking into account, not only the absorbed dose due to the activity in the tumour slice considered, but also the absorbed dose due to the activity in contiguous slices. For both simulations, the same physics list settings adopted for the generation of the S values

was employed. Nevertheless, a custom maximum step of 0.1 um was used instead of the default value of 20.0 um. In a voxel geometry, in fact, this parameter (and the range cut) should be set to values lower than the voxel size, in order to avoid artefacts in the energy distribution. As a general rule of thumb, a maximum step equal to 1/20 of the voxel pitch is generally considered appropriate. For each simulation, 5 milions primary events allowed a voxel statistical uncertainty $< 1\%$ for all voxels considered.

3.4.3.1 2D model

A 2D ^{212}Pb voxel source was simulated according to the activity distribution reported in the DAR image selected. The thickness of the simulated source was 20 um. The absorbed dose was scored in the XY plane defined by the image (at Z=0), as well as along the Z axis, from -110 um to 110 um. The goal of this simulation was to assess the penetration of ^{212}Pb emissions. In figure 3.12 (left), the absorbed dose along the Z axis, normalised to the absorbed dose at Z=0, is reported in the case of the tumour treated with ^{212}Pb-Trastuzumab. The red line represents the absorbed dose due to α-particles, while the blue line represents the absorbed dose due to all emissions but alphas. In green, the total absorbed dose is also reported. Equivalent results were obtained for the other two tumours (G2 and G3). Since most of the absorbed dose is due to α-particles emitted by ^{212}Bi and ^{212}Po, the penetration in tissue of the ^{212}Pb source is limited. This preliminary simulation allowed demonstrating that the energy emitted in the central slice is almost completely deposited within 105 um from the source.

3.4.3.2 Semi-infinite model

For each group, the 20 um tumour slice defined from the selected DAR image, was replicated 11 times along the Z axis (from -110 um to 110 um) in order to model a fictitious 3D activity distribution. In this geometry, the absorbed dose in the central slice is supposed to account for all energy emitted in the 3D tumour volume. Obviously, edge effects due to tumour radioactivity at top and bottom extremities are neglected in this approximation. Nevertheless, this was considered the most accurate approach in the lack of experimental data concerning the actual 3D activity distribution in the tumour.

In figure 3.12 (right), the total absorbed dose (green points) along the Z axis, normalised to the absorbed dose at Z=0, is reported in the case of the tumour treated with ^{212}Pb-Trastuzumab, together with the alpha (red points) and non-alpha contributions

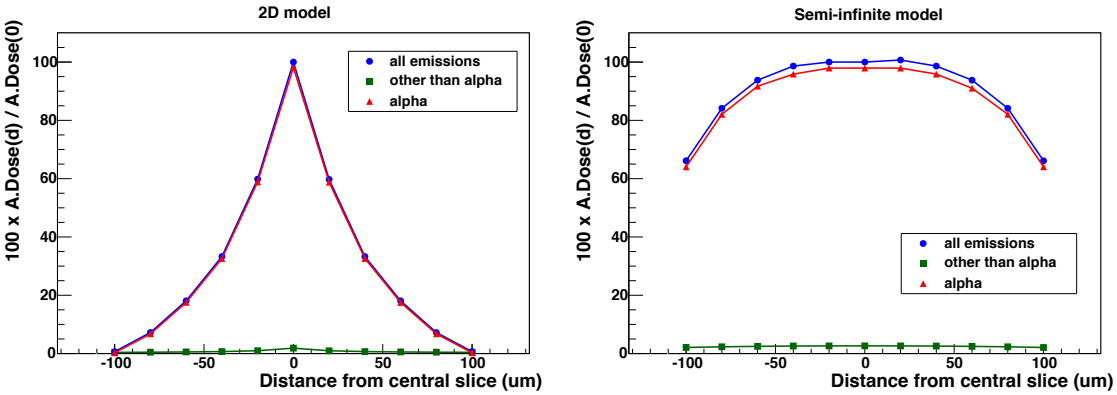

Figure 3.12: Absorbed dose in the axis perpendicular to DAR images (Z), normalised to the absorbed dose at Z=0, obtained for a tumour of G1, in the case of 2D (left) and semi-infinite models (right). The separate contributions of α-particles and other emissions are shown in red and green respectively. Total absorbed dose is reported in blue.

(blue points). Obviously, the absorbed dose attains its maximum value in the central slice; the other slices, in fact, are only reached by a fraction of α-particles emitted within the semi-infinite tumour. In figure 3.13, the absorbed dose maps in the central slice, obtained for the selected tumours of G1, G2 and G3 are shown on the same intensity scale and with realistic relative sizes. As expected, the energy deposition for ^{212}Pb is mainly localised in the emission voxels. As a results, the spatial distributions of radiopharmaceutical activity (DAR images) and absorbed dose were very similar, with the smoother look of absorbed dose maps due to α-particle range in tissue. In figure 3.14, the Dose Volume Histograms (DVHs) for the three groups, calculated in the central tumour slice, shows that 30% of the tumour treated with anti-CEA receives a null absorbed dose, justifying the lower therapeutic efficacy found in the previous study (Boudousq et al 2013).

Average absorbed doses for the three tumours considered, were established restricting the calculation to the the central slice of the simulated absorbed dose distributions. Results are reported in table 3.4 together with the estimated tumour massess and the relevant cumulated activities. Water sphere S values corresponding to the three tumour masses are also reported for validation: the difference between the average absorbed doses calculated with the average and the voxel dosimetry approaches was below 4% for the three groups. The average absorbed dose obtained via voxel dosimetry are also in agreement with those found considering all tumours of this study (c.f. 3.3).

Figure 3.13: Absorbed dose distributions obtained for the selected tumours of G1, G2 and G3 (from left to right).

Group	Tumour S value (Gy/Bq s)	Mass (g)	Sphere S value (Gy/Bq s)	$\tilde{A}_t$ (Bq s/g)	$\tilde{A}_t$ (Bq s)	Tumour Abs. Dose (Gy)
G1	$8.61\ 10^{-7}$	$1.45\ 10^{-3}$	$8.60\ 10^{-7}$	$2.45\ 10^{10}$	$3.55\ 10^{7}$	30.54
G2	$6.22\ 10^{-7}$	$1.97\ 10^{-3}$	$6.43\ 10^{-7}$	$3.12\ 10^{10}$	$6.15\ 10^{7}$	38.23
G3	$5.16\ 10^{-7}$	$2.38\ 10^{-3}$	$5.37\ 10^{-7}$	$1.58\ 10^{10}$	$3.77\ 10^{7}$	19.44

Table 3.4: S values and average absorbed doses (Gy/Bq s and Gy) obtained for the G1, G2 and G3 tumours selected for voxel dosimetry. S values for water spheres of the same mass of tumours considered is reported for comparison. Tumour cumulated activities (expressed in Bq s/g and Bq s) for the three groups are also listed.

3.5 Discussion and conclusions

The average absorbed dose delivered to the tumour is not necessarily a relevant parameter for the evaluation of novel radiopharmaceuticals in terms of efficacy, as demonstrated by previous experiments carried out at IRCM. In Boudousq et al. (2013), they established survival curves for athymic nude mice bearing intraperitoneal tumour xenografts and treated with ^{212}Pb labeled anti-HER2 (internalizing) and anti-CEA (non-internalising) mAbs. Their results demonstrated a higher efficacy of anti-HER2 mAbs with respect to anti-CEA mAbs (figure 3.1). However, the higher average absorbed dose found for tumours treated with anti-CEA seemed to indicate a lack of correlation between absorbed dose and effect. Analysis of tumour slices at Digital AutoRadiography (DAR) evidenced a non-uniform distribution of radioactivity in tumours treated with anti-CEA (figure 3.4). Dosimetry performed on the basis of these images confirmed the higher average absorbed dose for tumours treated with ^{212}Pb-35A7, with values in agreement with the previous

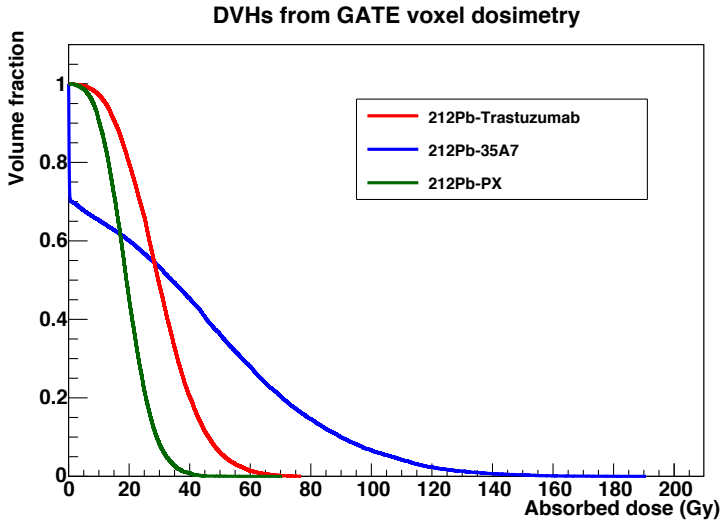

Figure 3.14: Dose volume histograms for the selected tumours treated with ^{212}Pb-Trastuzumab (red), ^{212}Pb-35A7 (blue) and ^{212}Pb-PX (green). About 30% of G2 tumour receives a null absorbed dose.

study (28.12 Gy and 36.16 Gy, on average, for G1 and G2 tumours in this study, versus 27.6 and 35.5 Gy found in the previous study). Nevertheless, the absorbed dose distributions obtained for two representative tumours of G1 and G2 indicate that, despite the anti-CEA mAb exhibits a higher average absorbed dose, a high fraction of tumour volume (30%) receives an absorbed dose compatible to zero (figure 3.14).

The heterogenous irradiation achieved with ^{212}Pb-35A7 mAb perfectly justifies its lower therapeutic efficacy. For the G2 tumour considered, in fact, a large portion of tumour cell is overkilled, with few voxels receiving an absorbed dose up to 180 Gy. On the other hand, in the 30% of tumour volume not receiving any irradiation, tumour cells are allowed to proliferate undisturbed. Clearly, this outcome is determined by the short range of α-particles whose emitted energy is deposited locally: the same antibody (35A7) labelled with a β-emitter, would have produced a rather uniform absorbed dose distribution in the tumour (for the tumour size considered), but also a more important irradiation to surrounding healthy tissues.

This work clearly demonstrates why dosimetry must be carried out at the scale at which biologically relevant phenomena occurs. The implementation of inadequate dosimetry with predictive purposes could, for example, bias the conclusions of a preclinical study, as in the case highlighted. As part of the optimisation of TRT in preclinical exper-

iments, the evaluation of spatial heterogeneity may be crucial for the establishment of an absorbed dose-effect correlation, depending on the pharmaceutical and the radionuclide involved.

Here, the use of DAR imaging was chosen to derive both radiopharmaceutical pharmacokinetics and distribution *in vitro*. However, for ^{212}Pb, this approach is still not optimal considering the rather long time needed for the transient equilibrium to be reached. In most works on ^{212}Pb dosimetry (Baidoo et al. 2013, Howell et al. 1994, Boudousq et al. 2013), it is generally assumed that the equilibrium is reached within 4–5 hours: this hypothesis, however, is not strictly verified for all ^{212}Pb daughters, with ^{208}Tl employing about 24 hours to achieve a constant activity ratio with respect to its progenitor. On the other hand, this is not necessarily a problem when measuring ^{212}Pb-mAbs radioactivity using a gamma counter. In this case, ^{212}Pb activity is evaluated directly, with only gammas from ^{212}Pb taken into account (typically using an energy window centered on the 238.632 keV emission); as a result, the measurement does not depend on the achievement of the equilibrium condition.

On the contrary, in this work, radiopharmaceutical activity was assessed through beta counting. As a matter of fact, β-particles from both the parent (^{212}Pb) and two of its daughters (^{212}Bi and ^{208}Tl) contributed to DAR signal: ^{212}Pb activity was hence inferred indirectly, through cross-calibration of the DAR imager and the gamma counter. While this approach could lead to accurate activity determination when the relative contribution of the three radionuclides is constant, its implementation should be avoided when the transient equilibrium is not reached. For the DAR images collected 4 hours post injection, in fact, ^{212}Bi and ^{208}Tl activities were still changing at different rates during the acquisition, providing a possible explanation for the scattered calibration points obtained. For images acquired at 17 hours, instead, the ratio between ^{208}Tl and ^{212}Pb activity was only 3% lower than the ratio at equilibrium.

If, on one hand, this may have biased the time-activity curves obtained, on the other, the similarity of average absorbed doses obtained in this and in the previous experiment leads to conclude that the error introduced is not so important to compromise the outcome of the study. Also, it should be stressed that the conclusions drawn from the comparison of 12Pb-Trastuzumab and ^{212}Pb-35A7 DVHs, still hold in the case of an incorrect determination of the cumulated activity. Any error introduced in the measurement of ^{212}Pb activity

at 4 hours post-injection, in fact, equally impacts the dosimetry of the three antibodies.

Obviously, it would not have been reasonable to procrastinate the acquisition of the first image to wait for equilibrium: time-activity curve should, in fact, be sampled at biologically relevant time points. However, a more rigorous approach would have consisted of measuring all tumour slides at the gamma counter (and not only some of them) to extract ^{212}Pb-mAbs pharmacokinetics, and using DAR as a non-quantitative tool to assess relative radiopharmaceutical distributions.

Chapter 4

Model-based versus specific dosimetry in diagnostic context: comparison of three dosimetric approaches.

The importance of accurate radiopharmaceutical dosimetry in targeted radionuclide therapy is nowadays generally acknowledged. In addition to being a legal requirement in most countries, patient-specific clinical dosimetry enables TRT optimization. Several approaches have been proposed to better assess absorbed doses delivered during therapy, and absorbed dose-effect correlations have been evidenced in a clinical context for several applications (Buckley et al. 2009, Flux et al. 2010, Barone et al. 2005, Garin et al. 2012, Ferrer et al. 2012, Strigari et al. 2014). On the other hand, diagnostic radiotracer dosimetry is usually performed to assess the effective dose, in a context where irradiation delivered to the patient is not inducing deterministic effects. According to ICRP recommendations, absorbed doses should be determined for models rather than for an actual patient. In this sense, the population-based approach accepts a certain degree of approximation (the model never faithfully represents the actual patient), a price to pay to be able to compare different tracers and diagnostic procedures. In ICRP 60 (ICRP 1991), ORNL models (Cristy and Eckerman 1987, Cristy 1980) were recommended: it is generally accepted that the models and results presented in OLINDA/EXM (Stabin et al. 2005) are equivalent to those recommended in the ICRP 60. Since ICRP 103 (ICRP

2007), new computing models were introduced in ICRP 110 (ICRP 2009). On principle, current reference dosimetry for diagnostic radiotracers should therefore be performed using the formalism introduced in ICRP 103 (separation of the absorbed dose computation between male and female patients, use of new organ weighting factors) and models from ICRP 110. However, neither absorbed fractions nor S Factors are currently available for the ICRP 110 model. At this stage (and even though the situation is likely to evolve in the future), the evaluation of the dosimetry for new radiopharmaceuticals should implement ICRP 60 recommendations (through the use of OLINDA/EXM for example). Nevertheless, performing patient specific dosimetry with tools available from the TRT experience is appealing since this may give an idea of the distance between population-based and specific dosimetry.

The first aim of this study is to establish whether current dosimetric models are capable to provide realistic absorbed dose estimations in Nuclear Medicine diagnostics with respect to a more personalised approach to dosimetry. In the second instance, a more general goal is to establish the impact of the calculation method on the patient's absorbed dose and to understand how much each step involved in the absorbed dose assessment chain can affect the final result. In order to achieve these tasks, a comparison of the absorbed doses to various organs computed with different dosimetric techniques, was performed for a cohort of 6 patients administered with a novel PET radiotracer, Flutemetamol (18F) Injection.

Currently, there are three main approaches to the calculation of absorbed doses from internalized radiopharmaceuticals: phantom based dosimetry, Dose Voxel Kernel dosimetry and Monte Carlo dosimetry.

Phantom based dosimetry is usually built on the widely acknowledged formalism proposed by the Medical Internal Radiation Dose (MIRD) committee of the Society of Nuclear Medicine (Bolch et al. 2009). At the organ scale, this formalism is based on the computation of the S value ($S_{r_T \leftarrow r_S}$), which is the mean absorbed dose to the target organ (r_T), per unit of nuclear transition of the radionuclide of interest in the source region (r_S) considered (in Gy Bq^{-1} s^{-1}). The S value is then multiplied to the total number of disintegrations in the source region (cumulated activity $\tilde{A}$ in Bq s) in order to obtain the absorbed dose (Gy) to the target.

In the Dose Voxel Kernel (DVK) approach (Bolch et al. 1998, Dieudonné et al. 2010, Amato et al. 2012, Fernandez et al. 2013) a 3D cumulated activity map is convolved with pre-calculated absorbed dose kernels for the radionuclide of interest in order to obtain

3D absorbed dose distributions. The DVKs are generated una tantum via Monte Carlo simulation by considering a radionuclide voxel source and scoring the absorbed dose in a voxellized homogeneous medium made of water or soft tissue.

In principle, the most accurate dosimetry can be obtained by performing a full MC simulation considering patient-specific anatomy and radiopharmaceutical distribution on the basis of morphological and functional 3D images.

In this work, the dosimetry obtained with a custom application based on the Gate MC toolkit (Jan et al. 2011) was compared to those obtained with two commercially available software applications based on the MIRD formalism at the organ level (OLINDA/EXM) and on DVKs (STRATOS by Philips).

4.1 Materials and Methods

4.1.1 Patient data

In order to compare the three dosimetric approaches described, a pre-existing dataset provided by GE Healthcare Ltd, was employed. In this paragraph, the data acquisition and post-processing protocol implemented by GE is described.

Six healthy Caucasian patients have been enrolled in a Phase I study to assess the toxicity of a novel PET radiotracer, Flutemetamol (^{18}F) Injection, with the intent to detect amyloid deposits in early Alzheimer disease. The study was approved by the local Ethics Committee, and it was performed in accordance with the Declaration of Helsinki and the International Conference of Harmonisation ICH-6 E6-Good Clinical Practice. All subjects provided written informed consent before the study started. Flutemetamol (^{18}F) Injection is currently not approved in the EU.

The patients (5 male and 1 female, age range 51-74 y) were injected with an average ^{18}F activity of 121.3 MBq (ranging from 95.8 MBq to 146.5 MBq). Patient demography, including masses for the organs considered in this study, is summarized in table 4.1. ORNL and ICRP 110 phantom data are reported for comparison. Each patient underwent from 8 to 10 whole body PET/CT scans in 3D acquisition mode with FORE (FOurier REbinning) histogramming (Defrise et al. 1997), on a Biograph 16 by Siemens. PET images were composed of 128 $\times$ 128 voxels of 3.81 $\times$ 3.81 mm^2 size; slice thickness was 3.0 mm. The first 8 PET scans were acquired dynamically starting immediately after the injection (up to 1.3 hours a.i. on average), with the patients remaining on the bed in order to avoid

image co-registration issues as much as possible. The remaining scans were acquired at approximately 150 and 260 minutes post injection. PET images were iteratively reconstructed using 8 subsets and correcting for random coincidences (delayed window method), scatter (model based) and dead time. The attenuation correction was performed using the CT image corresponding to each acquired PET series (one CT corresponding to the first 8 dynamic images, one for each of the 150 and 260 minutes scans). All CT images were obtained with a 80 kVp tube potential and a variable pitch between 1 and 2. The tube current (mAs) and the effective mAs were adjusted (according to body weight) in order to give an estimated effective dose of 0.5 mSv. A trained physician manually segmented eleven Regions Of Interest (ROI) (bladder, brain, gallbladder, heart, intestines, kidneys, liver, lungs, spine, spleen, thyroid and injection arm) on the first PET scan of each patient. Six organs displayed specific radiotracer uptake (bladder, gallbladder, intestines, kidneys liver, and in minor part the brain), while the others can be considered as target organs.

					Organ mass (g)					
	Age (y)	Sex	Weight (kg)	Height (cm)	Brain	Kidneys	Liver	Lungs	Spleen	Thyroid
PA1	74	M	63.0	165	1835	493	1889	757	229	26
PA2	71	F	58.0	153	1812	430	1570	515	129	18
PA3	73	M	71.0	160	1829	531	1972	888	231	10
PA4	51	M	69.5	172	2219	502	1779	872	192	26
PA5	56	M	81.0	188	2185	473	2246	1029	405	13
PA6	63	M	80.0	174	1966	459	2244	1044	409	37
ORNL	-	M	73.7	167	1420	299	1910	1000	183	21
	-	F	56.8	-	1200	275	1400	800	150	17
ICRP	-	M	73.0	176	1450	310	1800	1208	150	20
	-	F	60.0	163	1300	275	1400	950	130	17

Table 4.1: Demographic data for the 6 patients of the cohort, the ORNL hermaphrodite phantom and the ICRP 110 model. The masses of the 6 organs considered in this study, are also included.

4.1.2 Absorbed dose calculations

The GE dataset was analyzed applying a model-based approach through the software OLINDA/EXM (Stabin et al. 2005), a Dose Voxel Kernel (DVK) approach as implemented in the commercial software STRATOS (version 3.0) by Philips, and performing a full MC simulation for each patient on the basis of a custom application developed with the MC toolkit Gate (version 6.2).

In order to highlight the differences associated to the absorbed dose calculation algorithm, the same cumulated activities were used as input data for the three approaches. Since in STRATOS it is not possible to import cumulated activity maps produced with third party software, the use of maps as processed by STRATOS for the three dosimetric approaches was unavoidable. This introduces an obvious bias, but it was felt to be the most sensible way to evaluate differences induced by the absorbed dose computation algorithm.

STRATOS

STRATOS has been recently validated on phantom and patient data, against OLINDA/EXM and a home-made software based on DVKs, in the case of ^{177}Lu dosimetry (Grassi et al. 2014). STRATOS can read repeated PET (or SPECT) scans of a single patient to determine patient specific pharmacokinetics at the voxel level. It also offers several co-registration tools to align functional images before cumulated activity calculation. For this study, the rigid co-registration tool was used to align the 9^{th} and the 10^{th} PET scans to the first CT. No co-registration was necessary for the first 8 dynamically acquired PET scans. Cumulated activity in each voxel was obtained by applying the parallelogram rule up to the last imaging time point, and then extrapolating the curve to infinity assuming a simple physical decay, as this is the only procedure implemented in STRATOS 3.0. Before calculating the cumulated activity maps, STRATOS resamples the PET images to a 4.42 $\times$ 4.42 $\times$ 4.42 mm^3 voxel size by default. The 3D cumulated activity maps were then convolved with pre-calculated water DVKs for the radionuclide of interest, to obtain 3D absorbed dose maps for each patient under the assumption of uniform propagating medium. In figure 4.1, a typical SRTATOS output is shown as an example. In the case of ^{18}F, the DVK provided by Philips were initially in a format of a 7 $\times$ 7 $\times$ 7 voxels matrix with a 4.42 mm pitch, corresponding to a cube of 3.1 $\times$ 3.1 $\times$ 3.1 cm^3. They were generated by Philips from DPKs (Dose Point Kernels) computed at our institution using the MCNPX MC

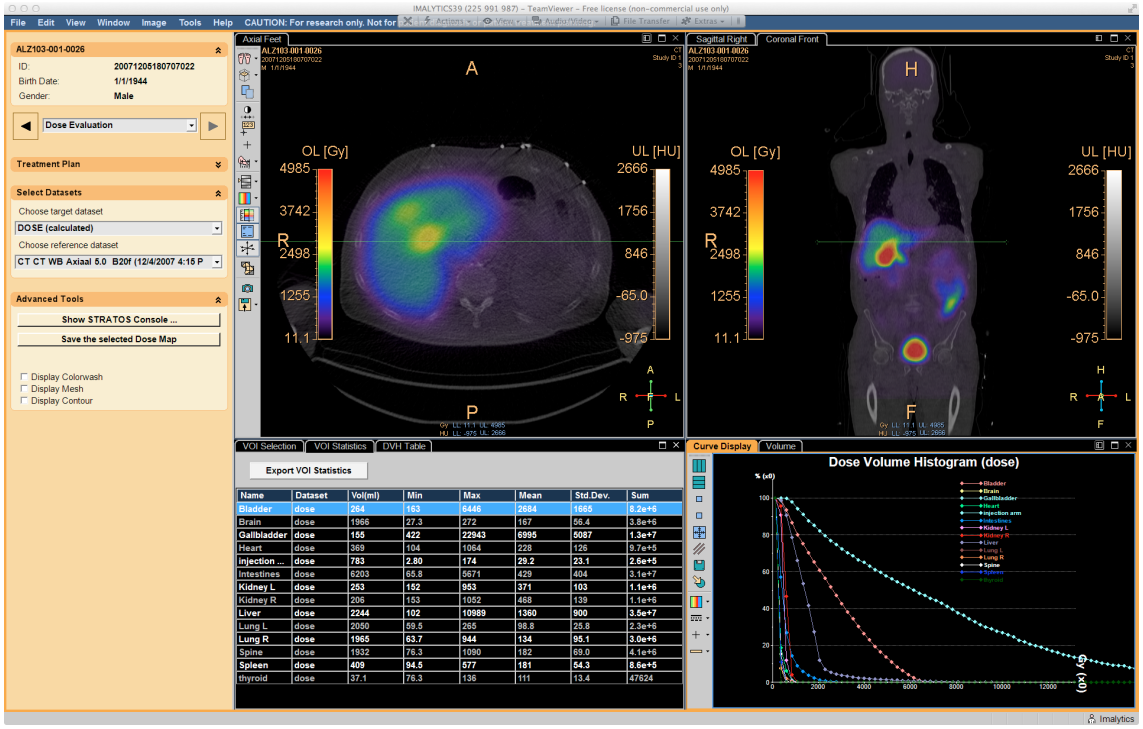

Figure 4.1: STRATOS output window.

code: the energy was scored in 50 microns concentric shells around a point source under the assumption of a uniform water medium. The deposited energy relative uncertainties in each shell were below 1%.

In addition, a supplementary absorbed dose calculation was performed for one patient (PA6) using a DVK matrix of 15 × 15 × 15 voxels (on a 4.42 mm pitch), to study the impact of the DVK matrix size on dosimetry. The 15 × 15 × 15 DVKs were computed in house with Gate and then implemented in STRATOS. The simulation assumed uniform water propagating medium and a ^{18}F source placed in the central voxel. The maximum statistical uncertainty was below 1.2 % for the farthest voxels from the source; a statistical uncertainty of 0.7 % was obtained averaging over all voxels.

The relative percentage difference between the STRATOS DVKs and the 7 × 7 × 7 central voxels of the 15 × 15 × 15 DVKs generated with Gate was 0.6% on average (the highest percentage difference of 8.8% was found for the farthest voxels) proving that the two datasets are in good agreement. For both kernel sizes, the convolution of DVK and cumulated activity took less than a minute for the whole body. The Regions Of Interest (ROIs) provided with the GE dataset were adapted to STRATOS proprietary format through a series of python scripts developed for the purpose. ROIs were subsequently

imported in STRATOS and used to derive average absorbed doses in each organ and the corresponding Dose Volume Histograms (DVH).

OLINDA/EXM

OLINDA/EXM allows mean absorbed doses computation to various organs on the basis of predetermined S values calculated from the Cristy and Eckerman adult male phantom (Cristy and Eckerman 1987) and the adult female phantom by Stabin et al. 1995 (see figure 1.4 in chapter 1). The user is required to input average cumulated activities normalised for the injected activity (residence time) for each source organ; for this study, these values were extracted from STRATOS. Differences in the segmentation of the ORNL model and the GE patients required making some approximations when entering the cumulated activities for some organs in OLINDA. In the case of the heart, that in OLINDA is split between wall and content, it was not possible to achieve the same level of segmentation from the PET images because of the limited spatial resolution of the imaging technique. Hence, the cumulated activity in each component (wall and content) was calculated by weighting the total cumulated activity in the whole organ with the mass of each component according to ICRP 89 values (ICRP 2002). Similarly, the intestine region as segmented in the GE dataset corresponded to the Lower Large Intestine (LLI), Small Intestine (SI), Upper Large Intestine (ULI) and stomach content of the OLINDA/EXM phantom. Hence, under the assumption of uniform activity distribution in this macro-region, the cumulated activity in each sub-region was extrapolated by weighting with the ICRP 89 mass of each component. For the other source organs, the average cumulated activity on the corresponding GE region of interest was used. The segmented regions not matching any OLINDA/EXM organ were included in the remainder of the body.

For the calculation of the absorbed dose, since the percentage differences of actual patient organ masses (from CT images) and ORNL model ranged from -121% to +48% (-23% on average), OLINDA organ masses were scaled to the actual patient organ masses using the specific option in OLINDA. This option includes a linear term to scale the beta absorbed dose in source = target configurations, and two non-linear terms to take into account the effect of photon self- and cross-irradiation (Stabin et al. 2005). A calculation using the original ORNL model masses was also performed, in order to establish the impact of mass scaling on OLINDA dosimetry results.

Gate

A custom application was developed to perform patient-specific internal dosimetry with Gate. Gate is a simulation platform based on the Geant4 MC toolkit (Agostinelli et al. 2003) and dedicated to the modelling of medical imaging devices and radiotherapy experiments: Gate version 6.2 is based on Geant4.9.6 patch03. The use of Gate for radiopharmaceutical dosimetry applications was validated by several authors (Mauxion et al. 2013, Papadimitroulas et al. 2012, Maigne et al. 2011) however, this is the first time it is used to implement whole body patient dosimetry. The application developed can read a CT image of a patient in order to define the geometry for the MC simulation. Four materials were implemented (soft tissue, lung, bone, air) according to Cristy and Eckerman classification (Cristy and Eckerman 1987). STRATOS cumulated activity maps (voxel size of $4.42 \times 4.42 \times 4.42$ mm^3) were used to define the spatial distribution of the radiotracer in the simulation, and to obtain patient-specific 3D absorbed dose maps for each patient. ^{18}F spectrum was defined according to (Eckerman and Endo 2008). With the generation of 6 10^8 primary particles per patient, corresponding to 2 hours of simulation time when using 100 cores the available cluster (20 MacPro multi-processor, Intel Xeon at 2.66 GHz and with 16 Gb of RAM), a statistical uncertainty below 3.5% was achieved in each voxel including voxels from non-source organs.

Moreover, in order to estimate, through an example, the impact of model geometry on cross irradiation, the Gate application was used to calculate the $S_{thyroid \leftarrow liver}$ values (where the liver is considered the source and the thyroid is the target) according to the real anatomy of the 6 patients.

4.2 Results

4.2.1 Flutemetamol biodistribution

In table 4.2, residence times obtained for the 6 patients of the cohort are reported as they were entered in the software OLINDA. They were obtained averaging at the organ level the voxel cumulated activities calculated by STRATOS and adapting the GE segmentation to the ORNL phantom geometry as specified in the materials and methods section. For PA2, the gallbladder was not segmented in the original dataset and was hence not included in the dosimetry. In figure 4.7a the time activity curves for the main source organs of PA6 are presented to provide a representative example of Flutemetamol biodistribution in vivo.

In figure 4.2, the cumulated activity map obtained with STRATOS for the same patient is also reported.

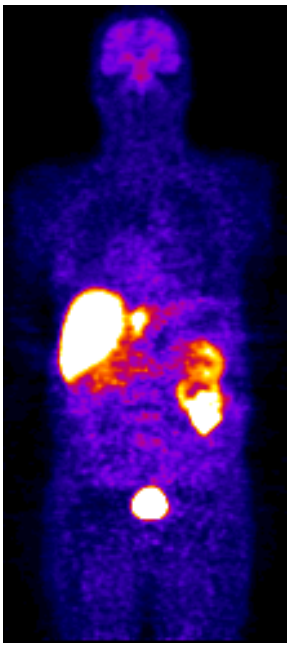

Figure 4.2: Coronal view of the cmulated acitivity map obtained with SRTRATOS for PA6.

4.2.2 Comparison of average absorbed doses

Because of the differences between the ORNL model and patient geometry, the comparison will be restricted to the absorbed doses obtained for 6 organs (liver, brain, kidneys, lungs, thyroid and spleen) whose geometry matched in the 2 datasets. Results obtained with Gate were arbitrarily chosen as a term of comparison for the other approaches; the absorbed doses obtained with OLINDA and STRATOS will be presented as ratios with respect to Gate absorbed doses (Gate absorbed dose/OLINDA absorbed dose and Gate absorbed dose/STRATOS absorbed dose).

In the vertical bar chart of figure 4.3a, the ratios between the Gate and OLINDA absorbed doses are reported for the 6 patients and the 6 organs considered. These results were obtained using the organ masses from OLINDA. The histogram does not show a clear tendency, with some of the organs receiving a higher absorbed dose according to Gate and others according to OLINDA. The average Gate/OLINDA ratio considering all organs is

	Residence times (h)					
Organs	PA1	PA2	PA3	PA4	PA5	PA6
UB Cont	0.153	0.125	0.138	0.056	0.226	0.231
Brain	0.102	0.121	0.077	0.059	0.079	0.098
GB Cont	0.242	-	0.246	0.014	0.133	0.364
Heart Cont	0.010	0.012	0.010	0.006	0.003	0.013
Heart wall	0.007	0.008	0.007	0.004	0.002	0.009
LLI Cont	0.073	0.117	0.076	0.101	0.128	0.061
SI Cont	0.560	0.898	0.584	0.773	0.981	0.472
Stom Cont	0.132	0.212	0.138	0.183	0.232	0.112
ULI cont	0.118	0.189	0.123	0.163	0.207	0.100
Kidney	0.113	0.090	0.072	0.057	0.050	0.055
Liver	0.922	1.278	0.783	0.366	0.536	0.860
Lungs	0.121	0.119	0.128	0.067	0.112	0.123
Spleen	0.018	0.011	0.010	0.007	0.022	0.020
Thyroid	0.0008	0.0008	0.0003	0.0008	0.0003	0.0125
Rem Body	0.111	0.154	0.114	0.068	0.157	0.108

Table 4.2: Residence times for the source organs considered in this study as enetered in the OLINDA/EXM software (UB= Urinary Bladder, GB = GallBladder, LLI = Lower Large Intestine, SI = Small Intestine, ULI = Upper Large Intestine). For PA2, the GallBladder was not segmented in the GE dataset.

1.23 ± 0.59 σ, ranging from 0.81 to 4.1: data were averaged over the 6 patients and all the organs.

When considering the actual organ masses in OLINDA calculation (figure 4.3b), absorbed doses calculated with Gate are higher than those calculated with OLINDA for all organs, with the exception of the lungs in one patient. The spread of the ratios in the cohort is also reduced; the average Gate/OLINDA ratio considering all organs is 1.38 ± 0.34 σ, ranging from 0.93 to 2.23. Even in this case data were averaged over the 6 patients and all the organs. The higher Gate/OLINDA ratios obtained when performing mass correction suggests that dosimetric differences between OLINDA and Gate do not depend on organ mass differences between the MIRD phantom and the actual patients. If considering the ratios of OLINDA absorbed doses averaged over the 6 patients and calculated with and without mass scaling (figure 4.4a), the mass scaling approach increases the differences between the two datasets. This tendency is confirmed by the lack of correlation between Gate/OLINDA ratios (without mass scaling for OLINDA) and the ratios between actual and ORNL's organ masses. In figure 4.4b, in fact, a twofold difference on mass may corresponds to absorbed dose ratios close to one. In general, the differences between OLINDA and Gate are rather pronounced only when the actual organ mass is smaller than MIRD's.

The Gate/OLINDA ratios averaged over the 6 patients for each organ are summarized in table 4.3. The discrepancies between OLINDA and Gate are particularly high for the thyroid, with an average Gate/OLINDA ratio of 1.97 ± 0.83 σ for the 6 patients. This disagreement is confirmed by $S_{thyroid \leftarrow liver}$ values calculated for the six patients of the cohort. The average thyroid-liver distance (measured at the barycentre of the organs) for the cohort was 23.6 cm ± 2.8 cm (σ), while in the ORNL model it is 56% larger (36.9 cm). The average ratio of the OLINDA and Gate S values for the 6 patients is 8.57 ± 2.72 σ (ranging from 5.12 to 11.75), confirming the significant impact of anatomy on the absorbed dose for target organs located far from the source.

In figure 4.5, the ratios between Gate and STRATOS absorbed doses are presented for the STRATOS calculation performed with the 7 × 7 × 7 voxels DVK matrix. The Gate/STRATOS ratios averaged over the 6 patients and all the organs considered is 2.51 ± 1.21 σ, ranging from 1.09 to 6.06. The larger discrepancy is found for the lungs: the average ratio for the 6 subjects is 4.76 ± 2.13 σ. The Gate/STRATOS ratios averaged for each organ over the patients from the cohort are summarized in table 4.3.

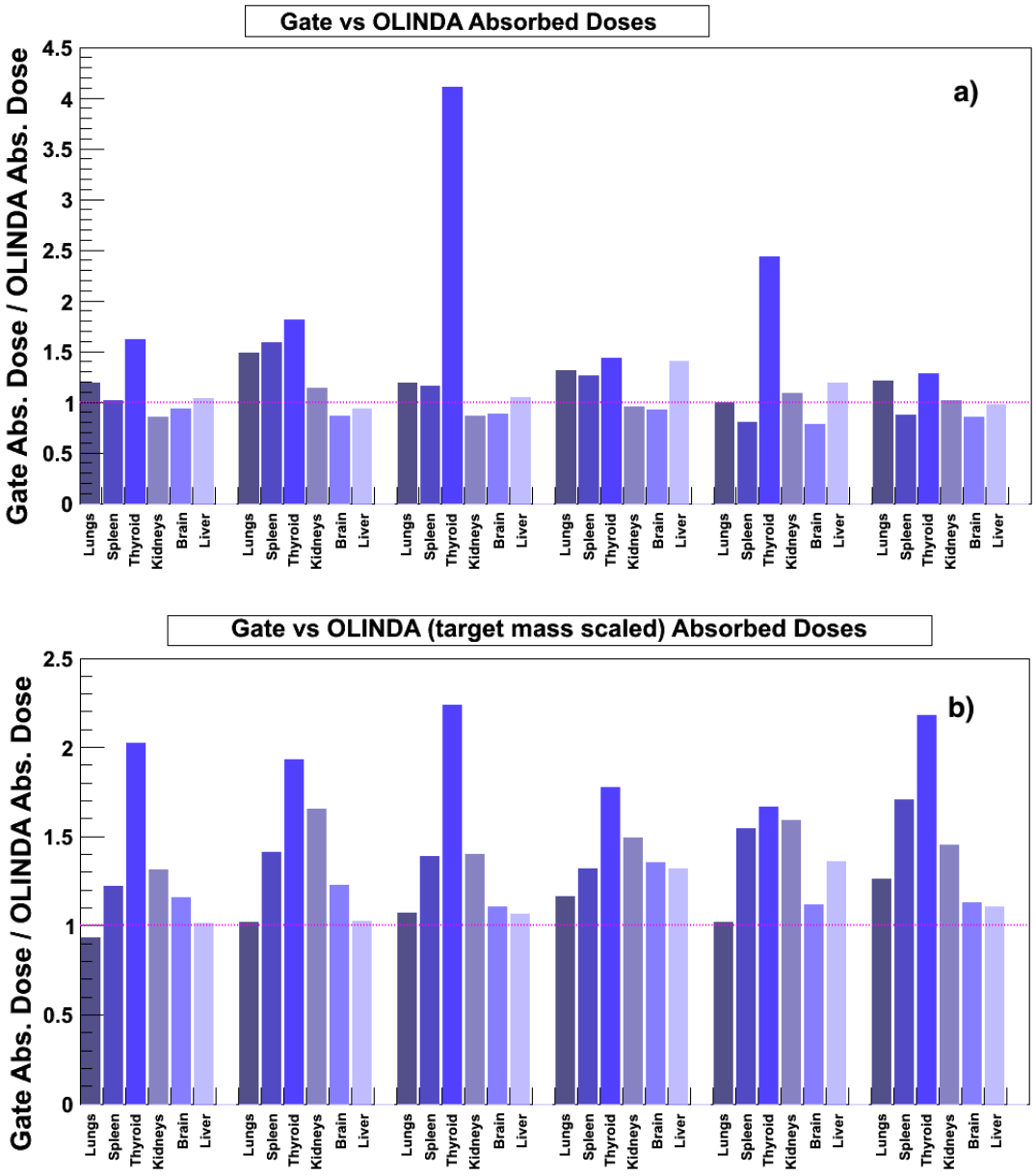

Figure 4.3: Ratios between Gate and OLINDA absorbed doses for the 6 patients (from PA1 to PA6 going from left to right) of the cohort and the 6 organs considered. In a), OLINDA dosimetry is performed using the ORNL phantom organ masses, while in b) actual patient organ masses are used

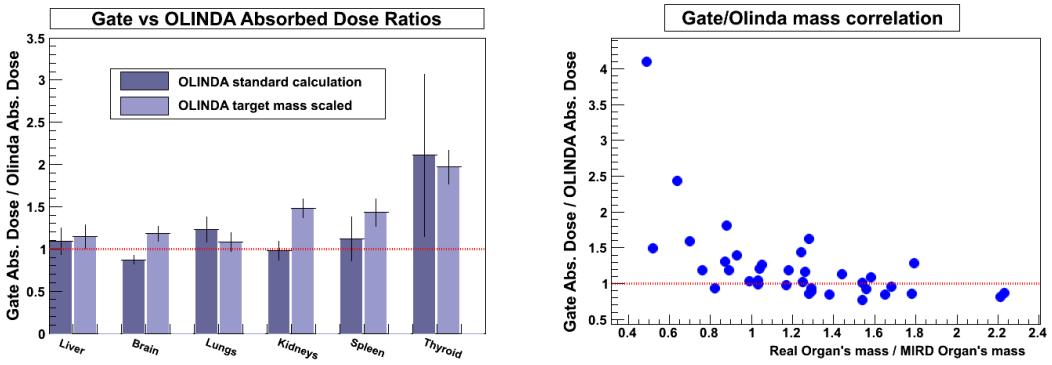

Figure 4.4: Left: Ratios between Gate and OLINDA absorbed doses averaged over the 6 patients with and without mass scaling in OLINDA calculation. Results are reported for the 6 organs considered in this study. Right: Lack of correlation between Gate/OLINDA ratios (OLINDA calculation performed without mass correction) and the ratios of actual and ORNL phantom organ mass.

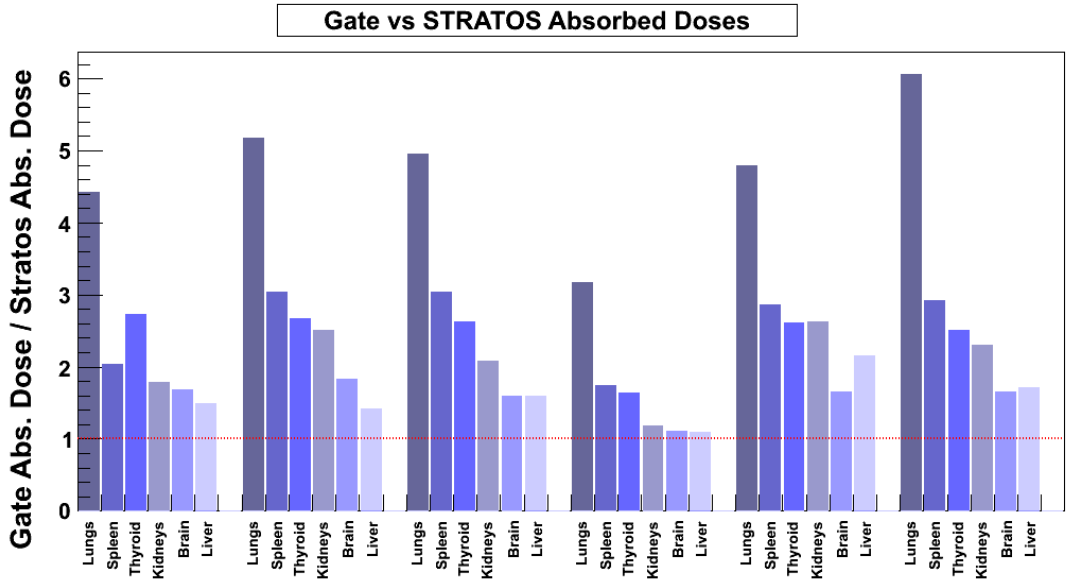

Figure 4.5: Ratios between Gate and STRATOS absorbed doses for the 6 patients (from PA1 to PA6 going from left to right) of the cohort and the 6 organs considered.

	Gate/OLINDA		Gate/OLINDA MS		Gate/STRATOS	
	Mean	St Dev	Mean	St Dev	Mean	St Dev
Brain	0.87	0.36	1.18	0.49	1.59	0.69
Kidneys	0.98	0.41	1.48	0.61	2.08	0.97
Liver	1.09	0.47	1.15	0.49	1.58	0.72
Lungs	1.23	0.52	1.08	0.45	4.76	2.13
Spleen	1.12	0.52	1.43	0.60	2.61	1.16
Thyroid	2.11	1.28	1.97	0.83	2.46	1.07
Mean	1.23	0.67	1.38	0.59	2.51	1.22

Table 4.3: Average absorbed dose ratios in the cohort and corresponding standard deviations for the 6 organs considered in this study. In the second column the ratios between Gate and OLINDA absorbed doses are obtained using ORNL organ masses, while in the fourth column OLINDA absorbed doses are scaled to the actual target organ masses (MS = Mass Scaled). In the sixth column the ratios between Gate and STRATOS absorbed doses is presented.

4.2.3 Impact of kernel size on DVK dosimetry

One patient (PA6) dataset was analysed using both the $7 \times 7 \times 7$ voxels kernel matrix provided by Philips and the generated in-house $15 \times 15 \times 15$ matrix. The results are compared in figure 4.6a in which Gate/STRATOS ratios are reported for the two kernel sizes. The ratio between Gate and STRATOS absorbed doses goes from an average of 2.44 $\pm$ 0.66 σ obtained with the $7 \times 7 \times 7$ DVKs to an average of 1.38 $\pm$ 0.37 σ obtained with the $15 \times 15 \times 15$ kernel: both values are obtained averaging the absorbed doses over all organs for the patient considered. The reduction of the differences between STRATOS and Gate when using the largest DVK matrix is more obvious in the case of brain, kidneys and liver, considered as source organs in the GE dataset. Conversely, for target organs such as lungs, spleen and thyroid, the use of a $15 \times 15 \times 15$ kernel is not sufficient to achieve an absorbed dose ratio close to 1. This behaviour suggests that the high Gate/STRATOS ratios obtained with the $7 \times 7 \times 7$ kernel is related to the 511 keV gamma absorbed dose.

In order to confirm this hypothesis, and to exclude at the same time that STRATOS and GATE differences come from tissue heterogeneity that are neglected in the DVK approach, two additional simulations were performed for PA6 under the following assumptions: a) patient body was only composed by soft tissue; b) patient body was

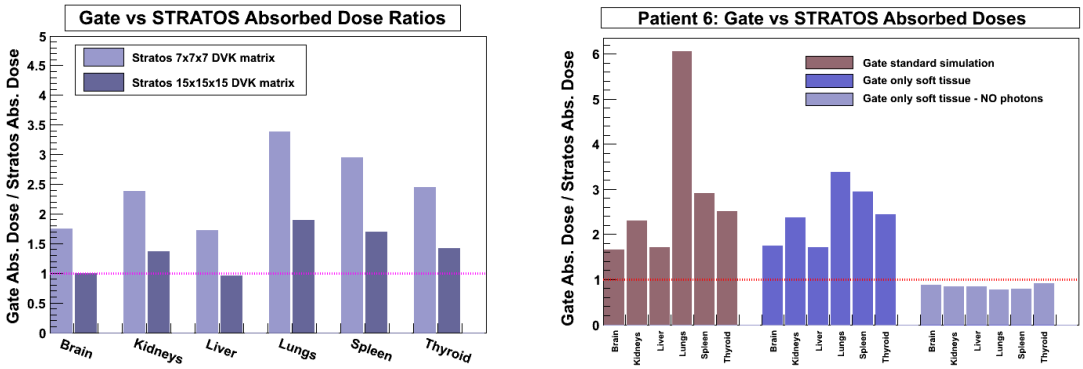

Figure 4.6: Left: Comparison of Gate/STRATOS absorbed dose ratios obtained with the 7 × 7 × 7 and the 15 × 15 × 15 kernel matrices for PA6. Right: Gate/STRATOS absorbed dose comparison for a standard Gate simulation (left) and assuming an homogeneous medium (centre) without photon generation (right). In all cases STRATOS absorbed doses were calculated with the 7 × 7 × 7 kernel.

only composed by soft tissue and photons were not generated. Indeed, while it was not feasible to take into account all photons deposited energy in STRATOS (the generation of large size DVK for STRATOS was beyond the scope of this work), it was possible to suppress their contribution in Gate for comparison purposes. Computed absorbed doses were compared to those obtained from 7 × 7 × 7 DVKs and reported in the histogram of figure 4.6b. The assumption of tissue homogeneity only impacts lungs absorbed dose (as expected). However, when photon generation is suppressed in Gate, absorbed dose ratios are much closer to 1. The average ratio between Gate and STRATOS is, in this case, 0.84 for the 6 organs considered; the ratio is obviously lower than 1, since in the Gate simulation no photons were generated, while in STRATOS a small fraction of the photon energy is deposited anyway.

4.2.4 Voxel dosimetry

While OLINDA results are limited to average organ absorbed doses, STRATOS and Gate dosimetry offer the additional possibility of obtaining absorbed dose distributions. In figure 4.7 the Dose Volume Histograms (DVHs) obtained for PA6 with Gate (b) and STRATOS implementing the 7 × 7 × 7 (c) and the 15 × 15 × 15 DVKs (d) are reported. The shift towards low absorbed doses in STRATOS 7 × 7 × 7 DVHs reflects the STRATOS underestimation of the average absorbed dose as reported in the previous section. DVHs obtained with the 15 × 15 × 15 kernels are in closer agreement to those obtained with

Gate; in this case, the liver absorbed dose is slightly higher for the STRATOS calculation, in accordance with the values reported in the histogram of figure 4.6a.

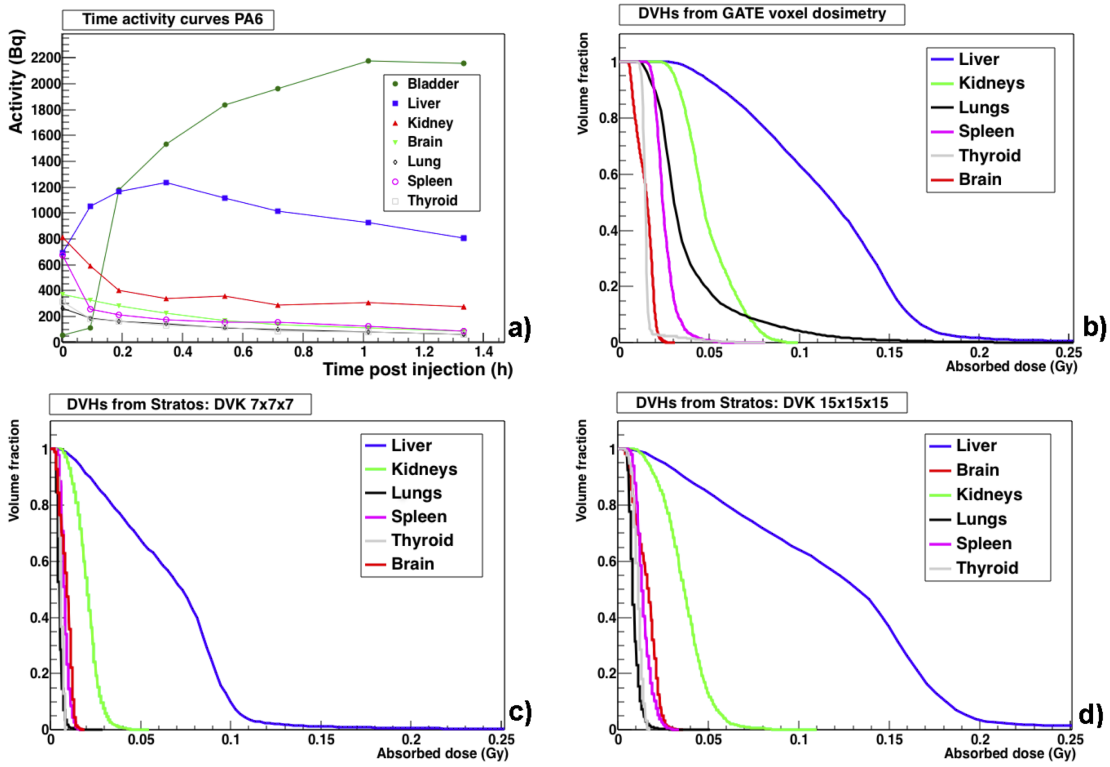

Figure 4.7: Time activity curves (a) for a selection of source organs in PA6, as obtained from STRATOS software. Dose volume histograms for PA6 and the 6 organs considered in this study calculated with Gate (b), STRATOS using the $7 \times 7 \times 7$DVKs (c) and the $15 \times 15 \times 15$ DVKs (d)

4.3 Critical aspects

One of the most critical feature of the GE dataset consisted in the approximate nature of the provided organ contours. Organ segmentation was manually performed by GE collaborators on the coronal projections of the first acquired PET scan. This approach is in many ways questionable. First, PET spatial resolution is about ten times worse than CT spatial resolution. Therefore, organ delineation is usually carried out on CT images (or morphological images in general) when those are available. In addition, the spatial sampling of tomographic images is typically larger along patient axis than in the trans-

verse plane. As a result, a coronal segmentation is by nature, far from being optimal. A direct consequence of the reduced spatial resolution, is that PET images are more prone to partial volume effect, which makes a precise delineation of organ boundaries more difficult. Besides, the determination "by eye"of organ edges on a PET image is known to depend on the contrast parameters selected in the visualisation software used. In general, when the average absorbed dose to an organ is demanded, the impact of inadequate organ segmentation is minimal: few voxels may be erroneously neglected or included in the Region Of Interest (ROI), only slightly shifting the average absorbed dose value. Conversely, when performing voxel dosimetry, results could be biased, and therefore they should be interpreted with care.

GE organ segmentation was particularly poor in the case of brain and liver. In figure 4.8 the worst case segmentation of the brain (occurring for PA1) is shown, superposed, from left to right, to the patient CT scan, his cumulated activity map, and the absorbed dose distributions obtained from Gate and STRATOS. In all cases the skull is clearly included in the ROI, resulting in an underestimation of the average absorbed dose in the brain for the two dosimetric techniques. For both STRATOS and Gate dosimetry in fact, the extra voxels lie in a region of lower cumulated activity with respect to actual brain, and therefore they contribute considerably less to the locally absorbed dose. In addition, Gate absorbed dose is even further underestimated, since it is scored in the actual tissue (bone in this case), while STRATOS considers a uniform propagating medium made by soft tissue. If the only difference between the two dosimetric methods was in the way they handle tissue heterogeneity, one would expect lower average absorbed dose for Gate. However, the comparison performed in this work demonstrated that STRATOS absorbed doses are systematically lower than Gate's, suggesting that organ segmentation erros only minimally impact on the dosimetric results.

A more accurate brain segmentation performed by applying a threshold on PA1 CT image (region growing technique) revealed that approximately 10388 additional voxels (on a total of 41657) were included in the ROI from GE, when applying the segmentation to the absorbed dose maps (voxels size of $4.42 \times 4.42 \times 4.42$ mm^3). In terms of differential absorbed dose volume histograms (see picture 4.9), this error could be approximately corrected by applying a cut to the 10388 lowest entries in both Gate and STRATOS histograms. The generation of dDVHs (differential DVHs) with the custom ROI evidenced

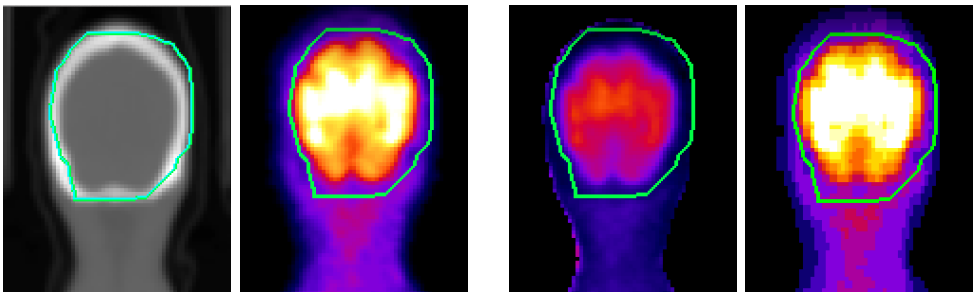

Figure 4.8: From left to right, an example of GE brain segmentation superposed to the patient CT image, to the cumulated activity map obtained from STRATOS, and to the absorbed dose maps calculated by direct Monte Carlo simulation and with STRATOS. Absorbed doses are reported in arbitrary scales.

a shift on the average absorbed dose: from the 1.60 10^{-2} mGy/MBq obtained with GE ROI to 1.83 10^{-2} mGy/MBq in the case of Gate dosimetry (14%); and from 0.93 10^{-2} mGy/MBq to 1.13 10^{-2} mGy/MBq in the case of STRATOS dosimetry (21%). Indeed, with a more accurate segmentation, the Gate/STRATOS ratio for the Brain in PA1 would have been about 5% lower (from 1.71 to 1.62). It should also be noted that in figure 4.9, Gate and STRATOS dDVHs are presented with a very different bin size. This is a direct consequence of the discrete absorbed dose levels generated by STRATOS: this discretisation is clearly visible form the absorbed dose maps (i.e. figure 4.8. first from the right). A possible explanation for this issue is a bad internal handling of data types by STRATOS, that determines a loss of resolution.

Another example of a possibly problematic segmentation in the GE dataset, is the liver. In figure 4.10, the worst case liver segmentation (occurring for PA4) is shown superposed to PA4 CT image and to the corresponding cumulated activity map (first and second images from left respectively). On the right, absorbed doses obtained with Gate and STRATOS are also presented. In this case, the liver ROI included extra voxels from the lung, resulting in an overestimation of the average liver absorbed dose calculated with Gate. In the direct MC simulation, in fact, the absorbed dose in the extra voxels is scored in a lower density material (lung tissue) instead of soft tissue. As a result, the absorbed dose is artificially high, even for voxels with a low cumulated activity.

This effect directly depends on patient breathing and movement during acquisition and it is typically encountered in the calculation of voxel absorbed dose via direct MC

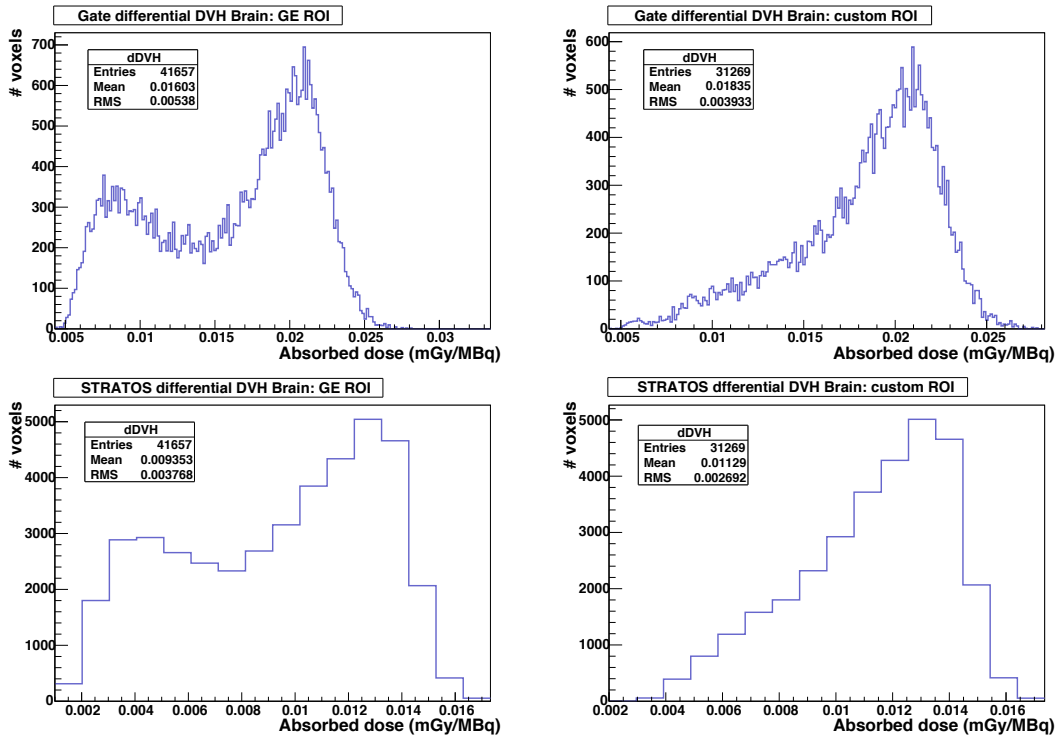

Figure 4.9: Top: brain dDVHs obtained with Gate implementing the GE ROI (left) and a custom ROI (right). Bottom: brain dDVHs obtained with STRATOS implementing the GE ROI (left) and a custom ROI (right).

simulation. A whole body CT scan, in fact, only last few second, and generally reflects patient anatomy corresponding to a single respiratory cycle (at least for what concerns the thorax). The PET acquisition, on the other hand, is considerably longer, and it thus registers internalised radioactivity through many respiratory cycles. Patient-specific dosimetry at liver/lung interface is particularly sensible to breathing artefacts: in the absence of a gated PET acquisition, it is impossible to avoid the spill out of liver activity in the lung. In the Gate absorbed dose distribution (figure 4.10), this effect is clearly visible at liver/lung interface. Nevertheless, an adequate organ segmentation could avoid including the artefacted voxels in the determination of the average organ absorbed dose and the organ dDVH. In this specific case, the dDVH obtained with Gate presents an artificial tail at high absorbed doses (figure 4.11) that is not present in STRATOS data. Cutting of the contribution of these voxels, the liver average absorbed is shifted from 7.00 10^{-2} mGy/MBq to 6.94 10^{-2} mGy/MBq (0.8%).

In contrast, STRATOS absorbed dose is slightly lowered by patient breathing and movement. Since the spilled out liver cumulated activity is scored in soft tissue, the

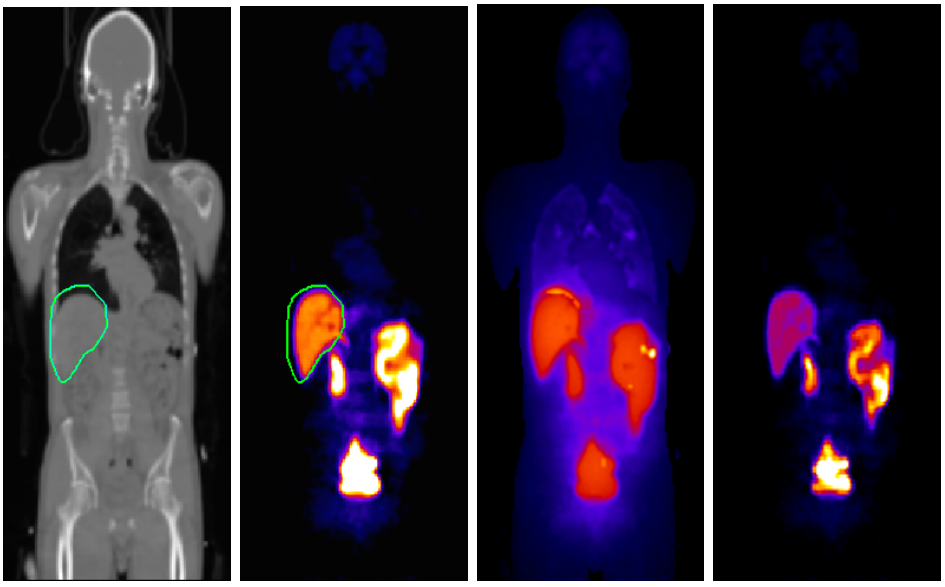

Figure 4.10: From left to right, an example of GE liver segmentation superposed to the patient CT image and to the cumulated activity map obtained from STRATOS. The absorbed dose maps calculated by direct Monte Carlo simulation and with STRATOS are also shown for the same patient. Absorbed doses are reported in arbitrary scales.

absorbed dose in the extra voxels is very low (because the cumulated activity is also very low). As a results, the additional voxels contribute increasing histogram counts in the lower absorbed dose region (figure 4.11b).

4.4 Discussion

Previous works demonstrated that OLINDA and the DVK approach can produce reliable absorbed doses in specific therapeutic scenarios (Grassi et al. 2014, Divoli et al. 2009, Dieudonné et al. 2013). Some of them focus on the calculation of the absorbed dose to limited regions of the body; in this case, even if a gamma emitter is taken into consideration, the calculation of the absorbed dose is limited to source organs (self-absorbed dose) or to organs in their proximity. Other works consider pure β-emitters such as ^{90}Y; in this case only source organs receive a measurable absorbed dose because of β-particles short range. Hence, in these studies, the effect of photon cross-irradiation for distant organs, relevant in a diagnostic scenario, is not investigated. Consequently, in both contexts, model- and the DVK-based approaches are capable to provide sound dosimetric results.

A completely different conclusion should be drawn in the case of photon absorbed

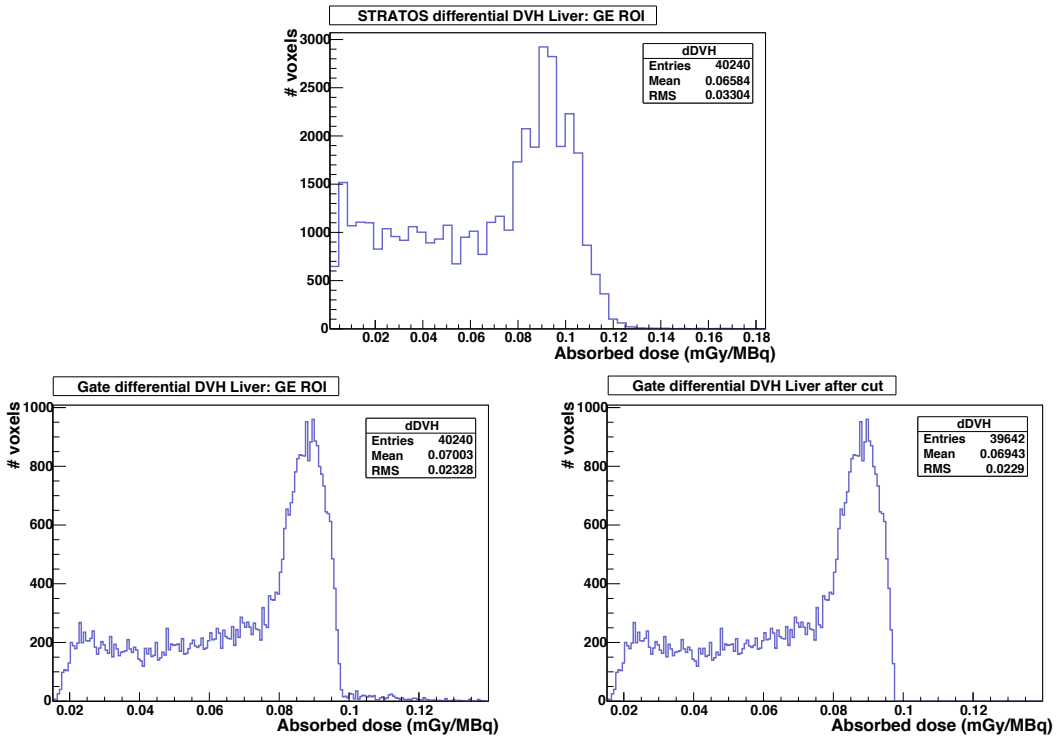

Figure 4.11: Top: liver dDVH obtained with STRATOS. Bottom: liver dDVHs obtained with Gate before (left) and after (right) cutting of the voxel contribution at lung/liver interface.

doses in non-source organs. This work demonstrates that the choice of the absorbed dose calculation algorithm is critical for non-source organs when gamma emitters are considered; average absorbed doses to target organs can be underestimated by up to a factor 3 (i.e the Gate/STRATOS ratios for the spleen) according to the algorithm.

The comparison between OLINDA and Gate dosimetry shows average Gate/OLINDA absorbed dose ratios of 1.23 $\pm$ 0.67 σ and 1.38 $\pm$ 0.59 σ when the model and the actual patient masses are considered respectively. The mass scaling procedure, instead, shifts OLINDA absorbed doses by 12% on average, while reducing the standard deviation of the average absorbed dose ratios within the cohort.

The mass scaled data also exhibit a clear trend, with OLINDA absorbed doses lower than Gate's for all organs. This trend is somehow expected considering the geometry of the ORNL model whose inter-organ distances are in general overestimated (Lamart et al. 2011, Zankl et al. 2003). The use of an approximate geometry for energy scoring during the MC simulation may have a major impact on photon ballistics. The number of photons generated in a source organ and reaching a certain target, strictly depends on the relative organ position. For large source-to-target distances, the relative number

of photons reaching the target decreases because of the reduced solid angle. This is confirmed, for example, by the fact that on average, the OLINDA $S_{thyroid \leftarrow liver}$ value is underestimated by 86% for male patients, while the liver–thyroid distance is 56% lower in the actual patients than in the ORNL model. As a result, thyroid absorbed dose calculated with Gate is on average two times that computed by OLINDA. It must be pointed out, however, that a factor 2 in absorbed dose only translates in a factor 0.05 $\times$ 2 (according to ICRP 60 tissue weighting factor) or 0.04 x $\times$ (according to ICRP 103) when calculating the effective dose.

Most of the issues arising from an approximate anatomical representation of the patient could be overcome in the future by adopting new models as a standard. With this aim, the ICRP has proposed two voxel-based computational models (adult male and female) whose anatomy is representative of the average man and woman (ICRP 2009, ICRP 2002). At this stage, however, pre-calculated absorbed dose factors for the ICRP 110 models are not available, and the implementation of ICRP recommendations would require an extensive preliminary work for the MC generation of S values for the radionuclides of interest. In order to overcome this issue, in our institution we are planning to compute absorbed doses for different radionuclides according to ICRP 103, implementing direct radiation transport on the ICRP 110 model.

Different comments should be made on DVK dosimetry. The comparison between STRATOS and Gate resulted in a mean Gate/STRATOS absorbed dose ratio of 2.51 $\pm$ 1.22 σ. Clearly, the absorbed dose to the lungs should be considered apart, since in standard DVK convolution (and STRATOS) specific tissue densities are not accounted for. However, the Gate/ STRATOS ratio remains high (2.06) even if lungs are not included in the sample. For other organs, the STRATOS assumption of unit density propagation medium is expected to produce discrepancies of less than 20% (Divoli et al. 2009) on the absorbed dose. On the other hand, increasing the DVK matrix has a major impact on the dosimetry in a diagnostic scenario, as was demonstrated for a patient of the cohort. When the DVK matrix size is doubled, the average Gate/STRATOS ratio for the 6 organs considered, goes from 2.44 $\pm$ 0.66 σ obtained with the 7 $\times$ 7 $\times$ 7 matrix to 1.38 $\pm$ 0.37 σ, suggesting that the lower absorbed doses found in STRATOS most likely depend on the limited kernel matrix size implemented. Also, the improvement in the results is higher for brain, kidneys and liver (source organs in the GE dataset) whose absorbed dose less

depends on cross irradiation.

Grassi et al. (2014) found an agreement within few percents between ^{177}Lu absorbed doses calculated for physical-phantoms with STRATOS and a home-made DVK software (VoxelMed). Their results are not in disagreement with ours as ^{177}Lu has a significantly lower gamma contribution (∼16%) and energies (112.9 and 208.4 keV) with respect to ^{18}F (∼80% of gamma emissions). Moreover, the DVKs implemented in VoxelMed have an overall size comparable to those implemented in Stratos (between $2.4 \times 2.4 \times 2.4$ cm^3 and $4.3 \times 4.3 \times 4.3$ cm^3 according to the voxel sizes used in their study).

The use of small kernel matrix is not an inherent limitation of STRATOS and the DVK approach. DVK matrices modelling energy deposition in larger volumes could be generated to appropriately score photon energy in the whole body. Nevertheless, the implementation of larger DVKs matrices is recommendable in diagnostic dosimetry, especially for radioisotopes having a higher fraction of gamma emissions. In the lack of an appropriate kernel size, the higher the gamma contribution (as in ^{18}F and ^{131}I), the more would the current DVK underestimate absorbed doses with respect to a full MC method. In analogy, radionuclides presenting higher gamma energies (as ^{131}I, ^{18}F and ^{124}I) result in a higher photon absorbed dose, due to the increased energy of the Compton recoil electron, and should be treated with DVKs of relevant size.

On the other hand, differences between Gate and OLINDA/EXM are mostly due to geometry and ballistics. Since OLINDA/EXM already considers photon contribution to the absorbed dose, these differences are expected to increase for radionuclides having higher gamma contributions.

In this work, the dosimetry performed with Gate is arbitrarily considered as the reference as it tries to explicitly consider morphological changes within patients and it implements detailed radiation transport in heterogeneous media (Marcatili et al. 2013, Hobbs et al. 2009, Dewaraja et al. 2010). In addition, Gate has already been validated for internal dosimetry (Mauxion et al. 2013, Papadimitroulas et al. 2012, Maigne et al. 2011) against data from the literature, and other MC codes. However, even the full MC approach is not free from limitations. As long as the input data (the 3D cumulated activity map in this case) used for the MC simulation are accurate, the user will obtain reliable results. The main issue arises when input data are not adequate, thereby introducing errors that are propagated in the MC calculation.

In this study the calculation of cumulated activity was not considered, as any error

introduced at this stage would impact the three techniques investigated approximately at the same level. However, it should be mentioned that the calculation of cumulated activity at the voxel level might indeed be critical, since it strictly depends on the accuracy of functional images co-registration. On the contrary, the assessment of an average cumulated activity in each organ is less prone to error, but this comes at the price of neglecting activity heterogeneities and therefore absorbed dose gradients. In this study, the co-registration errors have been minimized by acquiring the first 8 PET scans dynamically, and then accurately repositioning the patients for the last 2 scans.

Another major element to consider, concerns the time required to perform the dosimetric calculation with each approach. A great advantage of DVK and model based methods is that absorbed doses to various organ can be obtained very quickly (few seconds for OLINDA and less than 1 minute for STRATOS) while a whole body MC simulation may require many hours without adequate computer resources. Depending on the application and on the radionuclide, the user should evaluate which dosimetric approach is the most appropriate in terms of benefits and effort. For example, when photon contribution to the absorbed dose is of importance, MC calculation, even if longer, may be warranted.

All these comments generally stand for the intrinsic comparison of the computational approaches here considered. The availability of a complete dataset as the GE one, provided the opportunity to assess the inherent differences between these three dosimetric methods in the case of a radionuclide including both short and long range emissions. The conclusions drawn are therefore pertinent to other isotopes and applications (i.e. therapy with ^{131}I). However, in the specific case of diagnostic dosimetry, they must be further contextualised. Since the aim of diagnostic dosimety is to obtain an order of magnitude of the effective dose to infer population-based information and ensure safe level of patient irradiation, accuracy is not its main objective. Using a model to perform dosimetry is in this case accepted as it allows ensuring traceability of the dosimetric procedure. Even when approximate phantom geometry produces imprecise absorbed dose estimations, the impact on the effective dose may be significantly reduced depending on the tissue weighting factor for the organ considered. Nevertheless, the absorbed dose computation should in principle be performed with the best available tools. In the lack of absorbed dose factors for more accurate digital models (i.e. ICRP 110), the possibility of performing patient

specific absorbed dose computations for the patient enrolled in the trial was explored; the dosimetric results obtained could in principle be averaged to infer population-based effective doses.

4.5 Conclusions

The comparison of full MC dosimetry to those obtained using two commercially available software applications has illustrated how the choice of the absorbed dose calculation algorithm may introduce a bias when gamma radiations are of importance. Considering the full MC dosimetry as a term of comparison, it was observed that absorbed doses obtained with OLINDA could be underestimated up to a factor 2, while those obtained with STRATOS could be even smaller.

This study suggests that, when cross-organ irradiation is predominant, an exhaustive approach as MC may provide more reliable dosimetric results.

Chapter 5

Multi-resolution hybrid models for targeted radionuclide therapy dosimetry

5.1 Introduction

In recent years several models were developed for radiopharmaceutical dosimetry in clinical and preclinical settings. Currently, computational phantoms are available in three different formats: stylized, voxel and hybrid models. For a more detailed review on digital models please refer to chapter 1 and to Xu and Eckerman 2010.

Stylized phantoms (Cristy 1980, Snyder et al. 1975) are based on 3D surface mathematical equations and, despite they are widely employed for reference dosimetry, they offer limited realism.

Voxel based phantoms (Kramer et al. 2006, ICRP 2009, Zubal et al. 1994) were developed to reach a level of realism that could not be achieved by mathematical models. They are generally based on segmented tomographic images for which each voxel is tagged in order to univocally identify an organ, and thus they reflect the spatial sampling of the original image. Even though CT or MRI in-plane resolutions may be sufficient to show detailed organ boundaries, the sampling along the z axis for these techniques is typically quite coarse (few millimetres) resulting in the appearance of stair-stepped artifacts on the organ contours that compromise the realism of the model.

Finally, "hybrid" phantoms (Segars et al. 2010b, Lee et al. 2010 , Xu et al. 2007,

Na et al. 2010, Cassola et al. 2010), based on polygonal mesh geometry and/or NURBS (Non Uniform Rational Basis-Splines) representation, allow the highest level of realism as well as a further degree of versatility by offering the possibility to finely tune each model according to various parameters. Unfortunately, the direct implementation of such models in a Monte Carlo (MC) code is not currently envisaged since the time necessary to navigate the many facets of a polygonal mesh linearly scales with their number. For example, in the case of very detailed geometries typical of human phantoms, it has been demonstrated that the simulation of a tessellated solid in Geant4 can be up to two order of magnitudes slower than the simulation of the equivalent Constructed Solid Geometry (CSG) (Kim et al. 2011, Poole et al. 2012). Even if specific classes have been recently developed to allow faster simulation in polygonal mesh geometries (Han et al. 2013), these techniques may not be practical when the absorbed dose distribution inside the mesh organ is requested. In this case, in fact, the definition of a fine scoring grid reproducing as precisely as possible the polygonal mesh contours is required if the model realism is not to be lost. However, the implementation of a very thin scoring grid could in turn affect significantly simulation performances. Therefore, even hybrid models usually require the generation of a voxel version for MC simulation of radiation transport. Nevertheless, their implementation in MC simulations imposes strict constraints in terms of geometry definition. Since absorbed dose simulation time is strictly related to spatial sampling, a compromise should be made between model realism and simulation speed. In particular, the total number of voxels employed in a MC model is limited by the amount of memory needed to store the geometry before simulation. This trade-off between accuracy and calculation feasibility, leads on one side, in an overestimation of the size of small radiosensitive structures such as the skin or hollow organs' walls and, on the other, to unnecessarily detailed voxelization of large, homogeneous structures.

While reference models are valuable for defining idealised exposures conditions and for developing dose coefficients for radiological protection purposes, a completely different approach to radiopharmaceutical MC dosimetry in a therapeutic context, consists in directly employing 3D anatomical patient images for the computation of the absorbed dose (Marcatili et al. 2013, Dewaraja et al. 2010, Hobbs et al. 2009, Chiavassa et al. 2006). While this strategy offers the clear advantage of being more patient-specific than using models, it is prone to the same lack of anatomical realism of voxel phantoms when structures of small size need to be considered.

Since the simulation of very highly-sampled whole body absorbed dose distributions does not seem feasible using currently available computational resources, an alternative approach to MC dosimetry is proposed. This approach is built on the observation that, in most clinical applications, the degree of spatial accuracy required depends on the anatomical region. Typically, in radiotherapy applications, only the absorbed dose to a few organs (organs at risk) is of clinical interest. While in external beam radiotherapy, all these organs are grouped in the anatomical volume intersecting the collimated radiation beam, in Targeted Radionuclide Therapy (TRT) they are distributed all over patient's body. Therefore, for the MC computation of radiopharmaceutical absorbed dose, the whole patient body must be taken into consideration, meaning that a huge number of elements are needed to describe the simulation geometry.

The aim of this work is to develop flexible computational tools to implement multi-resolution models for Geant4 in order to better characterise energy deposition in selected anatomical structures, while preserving reasonable computation times. Some efforts have already been made by other groups (Kumada et al. 2011, Taschereau et al. 2008, Hubert-Tremblay et al. 2006) to reduce the trade-off between spatial accuracy and calculation speed using multi-resolution approaches. Here, the use of different voxel sizes to describe different anatomical areas is proposed. A fine voxelization can be used to describe small structures, organ walls and to achieve realistic organ's shape, while a coarser voxellization can be employed to describe organs whose anatomical structure is not of interest for the selected application. In this work, the tools developed are presented and validated through the implementation of a proof of principle example involving a limited number of organs. The ultimate goal is to apply the same strategy to whole body absorbed dose simulations merging 3D patient data and accurate organ models obtained with the proposed approach.

5.2 Material and Methods

The realisation of the multi-scale hybrid Monte Carlo model involved two main development stages: the construction of a multi-resolution digital model using the Visualization ToolKit (VTK) (Schroeder et al. 2006) and the effective implementation of multi-scale geometries in Geant4 (Agostinelli et al. 2003). The working principles behind these two pieces of software are described in details in the following sections and through a practical example.

5.2.1 Multi-scale digital model

The Python module of the Visualization ToolKit (VTK) was used to develop a pipeline for the construction of multi-resolution geometries on the basis of CT images or reference voxel models. The pipeline allows to extrapolate a polygonal mesh representation of each organ and to choose different sampling to build the corresponding voxel model. The software has been conceived with a modular structure allowing the user to select the optimal sequence of operations to built a realistic organ model for a given clinical application.

The first mandatory step of this process consists in the creation of a polygonal mesh starting from a segmented 3D medical image or a digital phantom (*Image2Mesh* module). Initially, the standard "discrete marching cubes"algorithm (Lorensen and Cline 1987) is applied to the 3D image matrix, then the resulting polygonal mesh is smoothed (*Smoothing* module) in order to minimise the stair-step artefacts commonly associated to the low spatial sampling of the original image. The effect of the smoothing process is to "relax"the mesh, making the cells better shaped and the vertices more evenly distributed.

The optional *VolumeDeformation* module allows to adjust the polygonal mesh volume to match the user-established value. Volume deformation is performed through uniform erosion or dilation along the mesh normals; each deformation operation is an iterative process in which acceptance criteria of relative error (typically 0.5%) in the adjusted organ volume is used. The main function of this module is to reproduce the organ size of a specific patient or to generate organ models complying to standards (i.e. ICRP 2002). In any case it can also be used to compensate for the volume shrinking naturally induced by the smoothing process.

When multiple organs are considered, the *MeshIntersection* module permits to handle mesh organ intersections applying boolean filters (Quammen et al. 2011) and selecting which organ the intersecting voxels must be assigned to.

The *OrganWall* module allows the user to build walls in the presence of hollow organs. Starting from the whole organ (wall plus internal part) polygonal mesh, the wall is created performing a uniform erosion along the mesh normals: the stopping criterion is given by the wall thickness or volume selected by the user. Two separate polygonal meshes, the organ wall and the inner organ, are thus generated.

The second mandatory module (*Voxelization* module) generates a High Resolution (HR) voxel model starting from the organ polygonal mesh previously processed according to user requirements. At this stage the user may opt for a standard voxelization imple-

menting a single voxel size, or for a multi-scale voxelization involving voxels of two different sizes. In the second case, voxels dimensions can be chosen arbitrarily but they should be one the multiple of the other. This multi-scale approach allows maintaining a realistic organ shape even after the voxelization process, while keeping the total number of voxels necessary to describe the organ low. Typically, each organ will be modelled by definying two geometrical elements. First, as many "big voxels"as possible are used to reproduce the internal part of the organ; then, "small voxels"are used to fill the organ volume up to its surface, thereby maintaining a realistic shape. The model built is then supposedly free from the typical artefacts introduced by the poor spatial sampling of the original images, and can be used to achieve a more accurate dosimetry.

In the case where multiple organs are considered, intersecting voxels are assigned to a single organ using a dedicated module (*VoxelIntersection* module), before generating a Geant4 input file for each organ. In the Geant4 input file, the voxel sizes implemented and the list of voxel coordinates are specified.

Most of the modules here described are fully automated with the exception of the *Mesh-* and *Voxel-Intersection* modules that require the user feedback for an optimal result.

5.2.2 Multi-scale geometry in Geant4

The use of the Monte Carlo technique in radiotherapy applications is usually limited by the lack of adequate computational resources. When dealing with the MC simulation of anatomical data extracted from medical images or digital models, two main aspects should be considered in order to make the simulation feasible: memory consumption to store the geometry and simulation time.

The most general way of representing voxel geometries in Geant4 is through the definition of an independent volume (through the *G4Box* class) to model each voxel, and to assign this volume a specific position and material composition. Since the definition of a single volume in Geant4 may require almost 200 bytes (Hubert-Tremblay et al. 2006), it is easy to understand why the use of this approach in geometries involving a huge number of voxels (typically $\sim 10^7$ in medical images), would not be feasible in terms of memory consumption. On the other hand, timing performances in this scenario are quite satisfactory, since the application only needs a simple access to the vector storing volumes information (position, size and material) in order to establish the particle position during tracking.

In order to improve the navigation speed in constructed solid geometries, Geant4 uses

by default an optimisation technique called *SmartVoxels* (Schümann et al. 2012). The simulation space is sliced along one or three axes creating virtual voxels (smart voxels) containing only a limited number of volumes each. Smart voxels are then used at simulation time to efficiently locate the next hit voxel through a hierarchical search on the virtual grid. The granularity of the voxelization is defined by the "smartless"parameter: the smaller the value, the coarser the optimisation. The use of *SmartVoxels* requires the allocation of additional memory to store the geometry; the amount of memory needed increases as the virtual grid becomes thinner.

Because of the large use of the MC technique in medical imaging and dosimetry applications, many MC toolkits offer specific tools for the implementation of voxelized geometries. In order to improve navigation speed and memory usage, Geant4 supports the use of parametrized volumes: with this feature only a volume is created in memory but, at simulation time, it appears to have different positions and material compositions. For a more detailed description of Geant4 parametrization options please refer to Schümann et al. 2012.

G4PhantomParametrization is one of the two parametrizations recommended by Geant4 for use in tightly packed 3D voxel geometries completely filling a parallelepiped space. The primary advantage of this class is that it has its own navigator (*G4RegularNavigation*) which allows faster voxel navigation using knowledge of a voxel's position within the 3D matrix in order to predict the next voxel to be hit. The voxel search is done through the *ComputeMaterial* method invoked at each step. The option of skipping voxel frontiers between equal materials can be selected to further reduce simulation time (Arce et al. 2008). This approach is expected to dramatically improve memory usage since it requires the placement of a single voxel volume instead of the several millions needed to describe a typical CT image. In any case, simulation time is strictly related to the the spatial sampling chosen for the geometry. On one hand, in fact, navigation time increases with the number of voxels, on the other, smaller voxels require the simulation of more primary events in order to achieve adequate statistical uncertainties at the voxel level. Therefore, in specific scenarios, *G4PhantomParametrisation* may not be the most performant approach.

Since a specific technique for handling multi-resolution voxel geometries in Geant4 does not yet exist, a dedicated approach based on the use of the *G4Box* and *G4AssemblyVolume* classes is proposed. It is based on the hypothesis that the reduced number of voxels needed

to describe the multi-resolution organ model may in part overcome memory issues arising from the implementation of independent voxel volumes. This hypothesis confirmed, the use of the *G4Box* class would intrinsically imply faster particle tracking performances with respect to phantom parametrization approach. Indeed, while in *G4PhantomParametrization* a specific method should be called at each step to locate the particle, with standard volume placements, the application only needs to access the vector storing volumes information.

Reading the Geant4 input files generated for each organ by the VTK application, a template voxel volume (*LogicalVolume*) of the right size and material composition was defined in the form of a *G4Box*. Then, as many logical volumes as indicated in the input file are added to a *G4AssemblyVolume* allowing for all the voxels to be positioned as a single entity (including translation, rotation and reflection operations) according to the coordinates listed in the file. A different assembly volume is generated for each organ included in the simulation. In terms of memory consumption, for each organ the definition of one *G4Box* volume (48 byte), one material composition (92 byte) and many physical volumes (56 bytes each) placed in different positions is required. Reasonable memory usage is expected based on the fact that *i)* the multi-scale organ model intrinsically uses less voxels than the corresponding high resolution parametrized volume, and that *ii)* with this approach only voxels actually belonging to the organ are defined, while in parametrized volumes, surrounding voxels should be considered as well. In order to reduce simulation time, voxel navigation is optimised activating the *SmartVoxel* option (typically using the default smartless value of 2). To further improve simulation performances, a specific *G4Region* is defined to bundle together voxels of the same dimensions, allowing for optimal definition of production cuts for particle tracking.

5.2.3 Multi-scale voxel sources in Geant4

The simulation of multiple voxels sources confined inside a specific organ is a typical scenario in radiopharmaceutical dosimetry applications. Generally the source distribution is either uniform within the organ volume, or derived from functional images (PET or SPECT) whose sampling pitch varies between few millimetres to about one centimetre. In both cases, the definition of a voxel source is necessary to reproduce the contours of the voxelized organ and hence, the same sampling as for the geometry should be used. While for low sampling models the definition of a voxel source does not present particular issues, with high resolution models memory and time performances problems may be

encountered due to the huge number of voxel sources implemented. For this reason, the multi-resolution approach is applied to the source definition as well. Therefore, when a radioactive distribution is associated to an organ modelled using two voxel sizes, two independent sources are generated, each including only voxels of a single size. Two separate simulations are run in this case, and the results are merged *a posteriori*, weighting for the relative contribution of each source in terms of total activity.

5.2.4 Proof of principle example

Model generation. In this work the potential advantages of implementing multi-resolution MC simulations is investigated through the use of a practical example. The digital female phantom provided within the ICRP 110 report (ICRP 2009) was chosen for convenience as a starting dataset, since it is already segmented and organ masses comply with reference values listed in the ICRP 89 report (ICRP 2002). Specifically the female model was considered because it presents a finer spatial sampling (voxels of 1.775 x 1.775 x 4.84 mm^3) than the male model (see figure 1.5 in chapter 1). The choice of modelling the bladder (wall and interior) and the uterus was made to test the different features of the VTK and Geant4 applications developed. In this example, the bladder wall represents the clinically interesting anatomical structure for which an accurate dosimetry is required. With an average thickness of 3.2 mm (Hakenberg et al. 2000), the bladder wall is typically very badly represented in digital models and cannot be identified in patient CT images. In the ICRP female model, the spatial sampling along the z axis is so coarse that the bladder wall is not even a closed structure (figure 5.2a. The bladder wall, in the coronal plane, is indicated in light blue). However, uniformly improving the spatial sampling of the entire bladder would produce a very detailed description of the inner bladder (in pink) which has no clinical interest. For these reasons, the bladder was considered a relevant organ to evaluate the multi-scale approach developed. In addition, being the bladder a hollow organ its allows validating validate the *OrganWall* module developed in VTK. The uterus (in red) has been added to the model in order to test the *Mesh-* and the *Voxel-Intersection* modules.

Using the software tools described in section 5.2.1, a realistic polygonal mesh model was generated for the three structures selected as illustrated in figure 5.1. Since in the ICRP 110 report only the mass/volumes of the organs are indicated and bladder wall thickness is not specified, first, a polygonal mesh describing the whole bladder was gen-

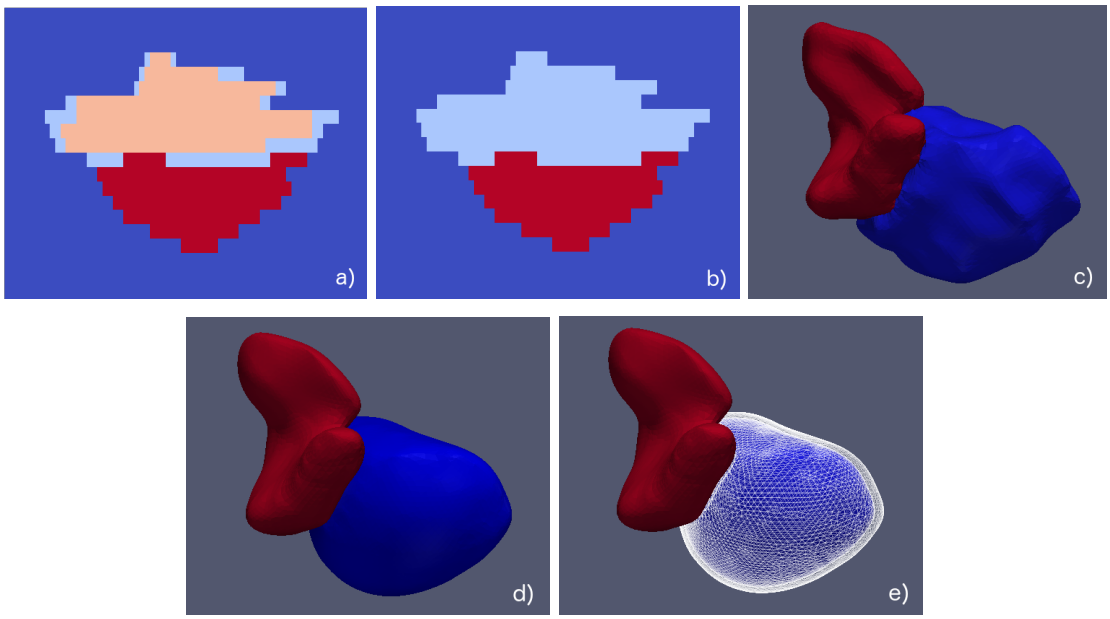

Figure 5.1: VTK pipeline for the generation of bladder and uterus polygonal meshes. From left to right and from top to bottom: coronal projection of ICRP 110 model with and without bladder wall explicitly segmented; uterus and bladder polygonal meshes as obtained from marching cube algorithm and after smoothing and mass scaling implementation; polygonal meshes including bladder wall.

erated using the *Image2Mesh* module (figure 5.1, a). Then, using the *Smoothing* and the *VolumeDeformation* modules the whole bladder mesh was recursively eroded until the resulting mesh volume was equal to the inner bladder volume (figure 5.1, d): the bladder wall mesh was obtained by subtraction of the whole bladder and the inner bladder meshes (5.1, e). The final polygonal mesh volumes for the three structures considered, are compatible to the volumes listed in the ICRP report within 5% after smoothing and correcting for organ intersections (*MeshIntersection* and *VoxelIntersection* modules). In fig. 5.2b, a 3D representation of the three polygonal meshes obtained is shown: the uterus is represented in red, the inner bladder in blue, and the bladder wall in white wireframe.

In order to implement this realistic model into a Geant4 simulation two high resolution voxel models were generated using cubic voxels of a single size (0.2 mm) and of two different sizes (0.2 mm and 2.0 mm). From here on, the first will be designated as High Resolution Single-Scale (HR–SS) model (shown in figure 5.2c) and the second as High Resolution Multi-Scale (HR–MS) model (shown in figure 5.2d). In the HR–MS model, the need of maintaining realistic organ shapes during the voxelization process resulted in

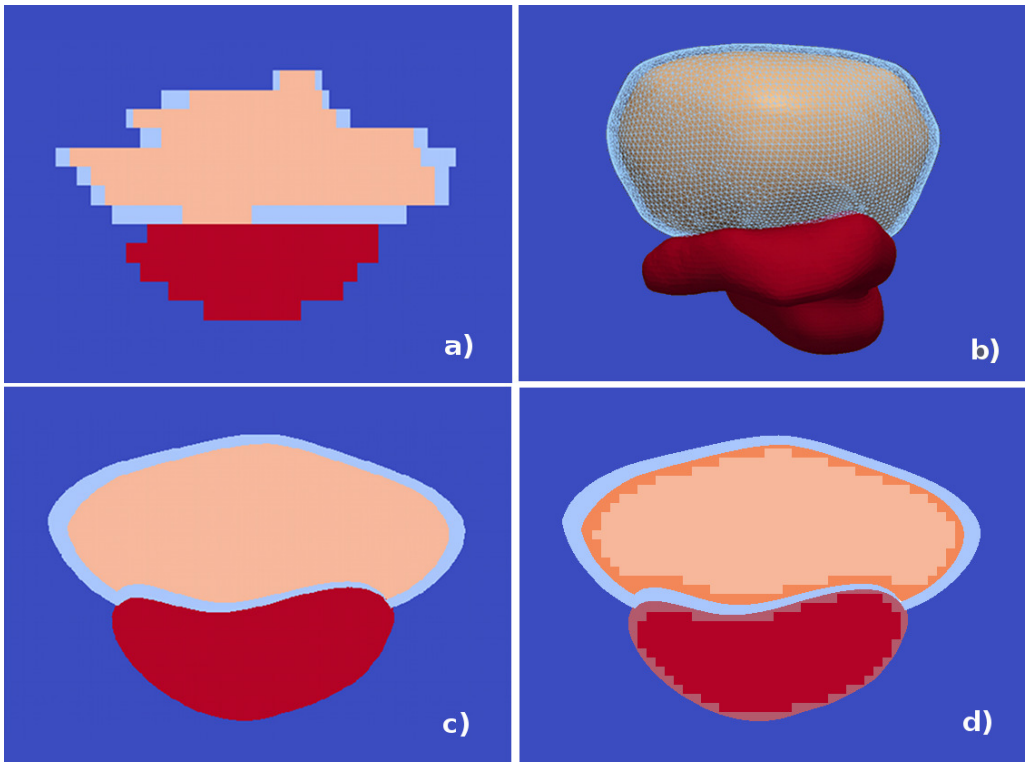

Figure 5.2: Coronal projections of the three selected organs (bladder, bladder wall and uterus) from a) the ICRP 110 female phantom (LR–MS model), b) the polygonal mesh model, c) the HR–SS and d) the HR–MS models.

the generation of five different structures. The bladder wall (in light blue in figure 5.2d) was sampled using 0.2 mm voxels while the inner bladder and the uterus were split in two regions each: the edge voxels having a size of 0.2 mm, and the internal voxels, having a size of 2.0 mm. In figure 5.2d, the inner bladder "big voxels"are represented in pink, and the "small voxels"in orange; the uterus "big voxels"are represented in red and "small voxels"in light red. The HR–MS model is composed of about 4 times less voxels than the HR–SS model (8386424 voxels against 28862039 voxels).

Geant4 simulations. Three separate simulations have been set-up on Geant4.9.6-patch01, for the calculation of the absorbed dose in the two high resolution models (HR–MS and HR–SS models) and in the original ICRP 110 bladder-uterus model (from now on indicated as Low Resolution Single-Scale — LR–SS — model). All organs are considered made of soft tissue according to Cristy and Eckerman (1987) material definition and surrounded by water. For each simulation, a uniform radioactive source inside the inner bladder is

defined, and the absorbed dose to the bladder, the bladder wall and the uterus is scored. The source spatial distribution in the LR–SS model coincided with the bladder voxels. For both high resolution models, the source optimisation procedure described in section 5.2.3 was implemented in order to achieve reasonable simulation times for the HR–SS model. For this proof of principle example two different radionuclides sources (^{90}Y and ^{131}I) were implemented as they provide beta emissions of very different endpoint energies (2.28 MeV for ^{90}Y and 606.31 keV for ^{131}I) well covering the range of beta energies typically used in TRT. These sources also offer the possibility of comparing the dosimetric impact of a pure β-emitter as ^{90}Y, and a beta/gamma emitter as ^{131}I (main gamma emission at 364.49 keV). Sources were generated using the *General Particle Source* module in Geant4 and the *G4Ion* class (Marcatili S. et al. 2013). For the three geometries the same physics list (*G4EmStandardPhysics_option4*) was used, implementing Livermore models (Chauvie et al. 2004) for the simulation of electromagnetic interactions down to 250 eV. These models have already been validated by several authors for Targeted Radionuclide Therapy applications (Amato et al. 2013, Mauxion et al. 2013, Papadimitroulas et al. 2012, Maigne et al. 2011), and they are based on the evaluated tables from LLNL (Lawrence Livermore National Laboratory): EPDL97 (Cullen et al. 1997), EEDL (Perkins et al. 1991a) and EADL (Perkins et al. 1991b). Specific cuts, consistent with the voxel size implemented have been applied. The voxel statistical uncertainty (standard deviation of the mean) was calculated at simulation time by considering the actual number of particles releasing their energy in the voxel (N_v) and it scales as $1/\sqrt{N_v(N_v-1)}$ (Visvikis et al. 2006).

The only difference between the three simulations consisted in the approach adopted to define the voxel geometry in Geant4. For the LR–SS (voxels of 1.775 × 1.775 × 4.84 mm^3) and the HR–SS (voxels of 2 × 2 × 2 mm^3) models a *G4PhantomParametrization* was implemented with production cuts of 0.1 and 0.01 mm respectively, for electrons and photons. The dedicated *G4RegularNavigation* algorithm was used, with the option of skipping voxels of equal materials enabled. The implementation of the HR–SS model as a parametrized volume required the definition of 560 × 570 × 360 voxels including the water voxels surrounding the actual organs.

On the other hand, the five structures generated for the HR–MS model were implemented in Geant4 in the form of five independent *G4AssemblyVolumes*. A total of 9791981 voxels were used to describe the three organs. Voxels of 2 mm size were added to the "big voxels" *G4Region* and production cuts of 0.1 mm were defined for electrons and photons;

voxels of 0.2 mm size were added to the "small voxels" *G4Region* were refined production cuts of 0.01 mm were set. The *SmartVoxel* optimisation along a single axis was used with a default smartless value of 2. Different smartless values were tested without significant improvement in computation speed. A three-dimensional optimisation was excluded to avoid excessive memory usage at simulation set-up. For each source 2.94 10^8 radionuclide decays were simulated in the case of high resolution models, and 7.50 10^7 events for the LR–SS model.

5.2.5 Tests performed

5.2.5.1 Validation of multi-scale geometry in Geant4.

Absorbed dose distributions were calculated for the three organs selected in this example and the three models implemented. The comparison between the two high resolution dosimetries allowed the validation of the proposed multi-scale approach in Geant4 with respect to the well established phantom parametrization method. The comparison of high and low resolution models, on the other hand, permitted to investigate the possible benefits of high resolution dosimetry.

5.2.5.2 Simulation performances

Simulation times for the two high resolutions models were evaluated in the case of a cubic source of $2 \times 2 \times 2$ mm^3 placed inside the bladder. Mono-energetic electrons (energy from 0.1 to 2.5 MeV) and photons (from 10 keV to 2 MeV) of different energies were employed in order to distinguish the effect of particle type on simulation speed. 10^5 primary events were simulated for each particle energy.

The memory and time needed to store the geometry for the three models was also estimated simulating a 300 keV geantino (the Geant4 non-interacting particle) cubic source ($2 \times 2 \times 2$ mm^3) at the center of the inner bladder, and generating a single primary event.

5.3 Results and Discussions

The proof of principle example described in this work was selected to investigate the possible advantages of implementing a multi-scale approach in the detailed MC simulation of small anatomical structures. In this perspective, results concerning the bladder wall (the selected target organ) are discussed more in details as they served as a validation

benchmark for the multi-scale approach. Uterus absorbed dose distributions are also presented to discuss the different statistical convergences of HR–SS and HR–MS models.

5.3.1 Validation of multi-scale geometry in Geant4: bladder wall dosimetry

Absorbed dose distributions were generated for the three organs considered and the three models selected. In figure 5.3 the transverse distributions obtained for the bladder wall are shown as an example. Absorbed dose maps corresponding to ^{90}Y sources are displayed on top, while those corresponding to ^{131}I sources are shown at the bottom. From left to right, absorbed dose distributions were obtained through MC simulation of the LR–SS, the HR–SS and the HR–MS models respectively. The pronounced visual similarity between absorbed dose distributions obtained with the two high resolution models offers a first level of validation for the *G4AssemblyVolume* approach with respect to the well acknowledged *G4PhantomParametrization* technique. On the other hand, the inaccuracy of the Low Resolution (LR) absorbed dose distributions confirms the need for more detailed organ modelling.

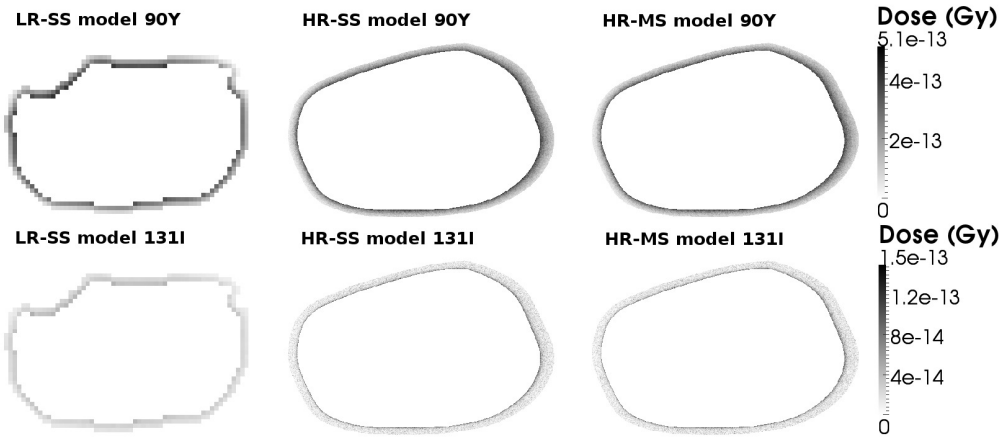

Figure 5.3: Bladder wall transverse absorbed dose distributions for the three models simulated (LR–SS, HR–SS and HR–MS from left to right) and the two sources considered (^{90}Y on top and ^{131}I below). The same vertical scale is used for the three distributions corresponding to each source.

In figure 5.4 absorbed dose profiles along the bladder wall thickness are shown for the two high resolution models, in the case of a ^{90}Y (left) and a ^{131}I (right) source. The

standard deviation associated to the average absorbed dose is smaller than the point size and hence it is not visible in the plot. These profiles are generated considering expanding shells (of 0.2 mm thickness) along the bladder surface normals, and by averaging absorbed doses in these regions. The shells were created through dilation of the bladder voxel model using the Visualization Toolkit. The vertical scales in the two plots were set to the same y_{max}/y_{min} ratio in order to highlight the differences in absorbed dose delivery for the two radionuclides. From the ^{131}I profile, the different contributions of the β-particle ($E^{\beta}_{EndPoint} = 606.31$ keV) and the main photon ($E_{\gamma} = 364.49$ keV) can be distinguished. The first produces a steep slope next to the source edge (corresponding to X axis origin in the plot) extending up to about 1 mm, which is compatible to the Continuous Slowing Down Approximation (CSDA) range of 2.3 mm (Lanconelli et al. 2012) expected for ^{131}I. The latter, is responsible for the slowly decreasing tail. On the contrary, ^{90}Y, being a pure β-emitter ($E^{\beta}_{EndPoint} = 2.28$ MeV, maximum beta CSDA range of 10.1 mm (Lanconelli et al. 2012)) produces a more continuous absorbed dose profile. As a general trend, the ^{131}I profile shows a faster absorbed dose decrease as the radiation penetrates in the tissues.

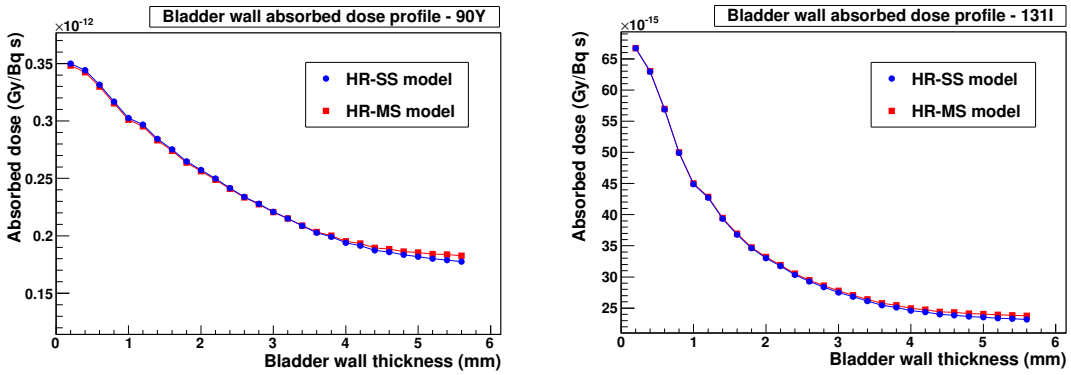

Figure 5.4: Bladder wall 3D absorbed dose profiles for the two high resolution models and the two sources simulated. ^{90}Y profiles are shown on the left and ^{131}I on the right.

In order to further validate the multi-scale approach, the average absorbed dose and the average statistical percentage error for the bladder wall were derived for the three models. The errors were calculated averaging the statistical percentage errors (standard deviation of the mean) over the voxels composing the organ. The results, reported in table 5.1 for both ^{90}Y and ^{131}I sources, show a high level of agreement between the two high resolution

models. The percentage differences ((HR–SS – HR–MS)/HR–SS) between the average absorbed doses are in this case below 1% for both radionuclides considered. The average absorbed dose percentage differences between the HR–SS model and the LR–SS model ((HR–SS – LR–SS)/HR–SS) are higher (7.70 % and 6.38% for ^{90}Y and ^{131}I respectively) but not huge, suggesting that the use of a low resolution model may be adequate if only the average absorbed dose to the organ is needed. The advantage of using the LR–SS model, in this specific case, lies in its faster statistical convergence. The statistical errors listed in the table correspond to 2.94 10^8 events run for the MC simulation of high resolution models, and to 7.50 10^7 primary events in the case of the LR–SS model. Hence, despite the simulation of about 4 time less events, the low resolution model generates much smaller statistical uncertainties.

	^{90}Y		^{131}I	
Model	AADose	% Error	AADose	% Error
HR–SS	1.82 10^{-13}	0.69	2.35 10^{-14}	5.13
HR–MS	1.81 10^{-13}	0.70	2.36 10^{-14}	5.26
LR–SS	1.68 10^{-13}	2.81 10^{-4}	2.21 10^{-14}	3.07 10^{-3}
	AADose percentage differences			
HR–MS vs. HR–SS	0.55		-0.43	
LR–SS vs. HR–SS	7.70		6.38	

Table 5.1: On top, average absorbed doses (AADose) in Gy/Bq s, and average statistical errors (in percentage) in the bladder wall in the case of ^{90}Y and ^{131}I sources. Below, AADose percentage differences between the two high resolution models (HR–MS vs. HR–SS), and between the LR–SS and HR–SS models, for ^{90}Y and ^{131}I.

On the other hand, the choice of a high resolution approach presents clear advantages when an accurate absorbed dose distribution is required. In order to highlight the differences between the absorbed dose distributions obtained with the three models, the bladder wall differential Dose Volume Histograms (DVH) was generated for each of them. For both ^{90}Y and ^{131}I sources (figure 5.5) the histograms for the two high resolution methods, in blue and red, appear perfectly superposed and present a well-defined shape reflecting the

non-uniform energy deposition along the bladder wall thickness. On the contrary, LR–SS model histograms (here normalised to the integral of the other two histograms) are quite coarse and, if in the case of ^{90}Y source the overall trend is in agreement with the high resolution models, for ^{131}I source the low resolution histogram appears "compressed"causing a remarkable miscalculation of the minimum and maximum absorbed dose delivered to the organ. Even though an appreciable discrepancy between the low and the high resolution DVHs was expected, this "shrinking"effect is mainly induced by the low spatial sampling of the LR–SS model rather than the geometry itself. It is in fact acknowledged that increasing the thickness of the absorbed dose scoring grid produces an averaging effect resulting in the compression of the differential DVH around the average absorbed dose value (Taschereau et al. 2008). In order to appreciate the sole effect of unrealistic organ modelling on the LR–SS DVH, a similar voxel size should be used to score the absorbed dose in the HR–MS and the LR–SS models: reducing the voxel linear dimension of the LR–SS model by a factor 8 in all directions, voxel dimensions of $0.219 \times 0.219 \times 0.60$ mm^3 are achieved, comparable to those of the HR-MS model in the transverse plane. In figure 5.6 LR–SS model DVHs obtained with the original sampling, and with a finer scoring grid (LR–SS/8) are reported for ^{90}Y and ^{131}I respectively. The HR–MS model DVH is also reported as a term of comparison. As can be observed from these plots, if the absorbed dose is scored on a finer voxel grid, the LR–SS and the HR-MS histograms for ^{131}I shows a more similar shape than the corresponding histograms for ^{90}Y. This qualitative observation highlights that the consequences of using low resolution organ models may be different for different sources. In order to better understand figures 5.6 and the bladder wall thickness in the HR–MS and the LR–SS models should considered. While the first presents a uniformly thick wall of 5.6 mm, in the LR-SS model the bladder wall thickness is very irregular. If the transverse plane 3D image of the ICRP bladder is considered, the wall is always modelled using two voxels (hence it has an average thickness of about 3.55 mm); however, considering the coronal images, we discover that the wall is represented with a number of voxels varying between 0 and 4 (hence, between 0 and 19.36 mm). This "exceeding"thickness has clearly a negligible impact on ^{131}I absorbed dose distributions, since most of the energy emitted by this radionuclide is absorbed within the first 2 mm anyway. On the contrary, for a radionuclide as ^{90}Y, emitting energetic β-particles (with a CSDA range in water of 10.1 mm), it causes an excess of voxels receiving a low absorbed dose.

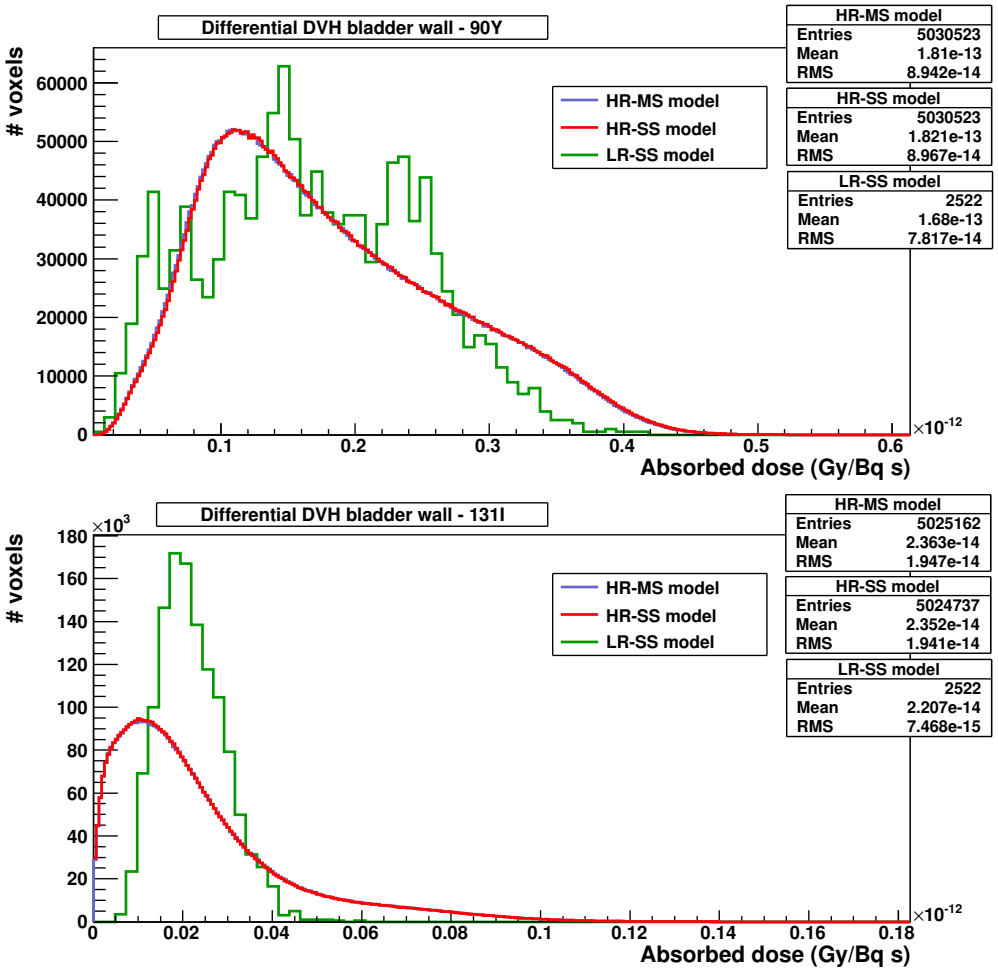

Figure 5.5: ^{90}Y (top) and ^{131}I (bottom) differential DVHs in the bladder wall for the LR–SS (in green), the HR–SS (in red) and the HR–MS (in blue) models, for a uniform source in the bladder. In the legend, the number of entries, the mean values and the Root Mean Square (RMS) values are reported for the three histograms. The number of entries matches the number of voxels implemented in the corresponding organ model.

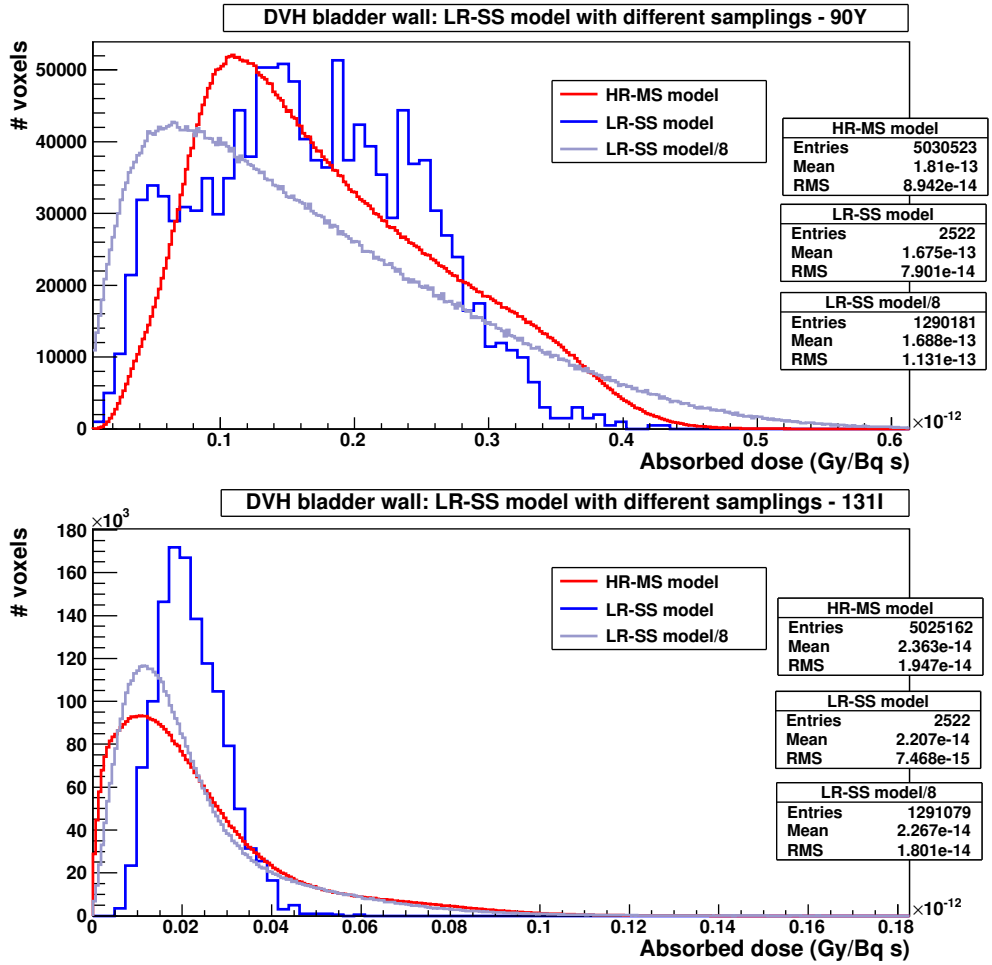

Figure 5.6: ^{90}Y (top) and ^{131}I (bottom) differential DVHs in the bladder wall generated from the LR–SS model with different scoring grids: one reproducing the original sampling (1.775 × 1.775 × 4.84 mm^3), the other having 8 times smaller voxels (0.219 × 0.219 × 0.605 mm^3). In red, the HR–MS model DVH is shown as a term of comparison. In the legend, the number of entries, the mean values and the Root Mean Square (RMS) values are reported for the three histograms. The number of entries matches the number of voxels implemented in the corresponding organ model.

5.3.2 Statistical uncertainty: uterus dosimetry

With a CSDA range in water of 10.1 mm, most of ^{90}Y β-particles emitted in the bladder deposit their energy in the 5.6 mm thick bladder wall. As a results, despite the large number of primary particles generated in the Monte Carlo simulation (2.94 10^8 events for the HR models), most of uterus voxels remain unfired by ^{90}Y radiation. In this context, the average organ absorbed dose is not necessarily a relevant parameter. Even the interpretation of the absorbed dose distribution (dDVH) is not straightforward; in particular, it is hard to say to which extent the heterogeneity depends on statistical uncertainty or on particle ballistics. A better understanding of this issues would therefore require a dedicated analysis which is beyond the scope of this work. For all these reasons, ^{90}Y dosimetry for the uterus will not be discussed here. Nevertheless, the ^{90}Y absorbed dose distribution obtained with the HR-SS model is shown in figure 5.7, left for reference. Here, the absorbed dose map is resampled to 2.0 $\times$ 2.0 $\times$ 2.0 mm^3 voxels in order to reduce statistical fluctuations and highlight the effect of limited particle range.

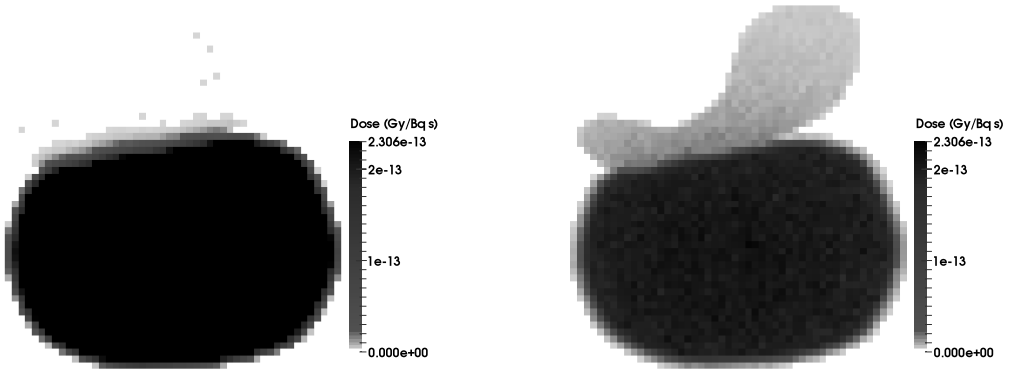

Figure 5.7: ^{90}Y (left) and ^{131}I (right) absorbed dose distribution obtained with the HR–SS model resampled to a voxel size of 2.0 x 2.0 x 2.0 mm^3.

In contrast, photons emitted by ^{131}I could, in principle, produce a measurable energy deposition in any voxels of the uterus model. However, depending on the voxel size chosen for the uterus representation, a partial irradiation may be achieved within the

simulation, regardless of the huge number of primary particle generated. In the case of the HR-SS model, for example, about 8% of the voxels are not hit by any radiation. As a consequence, the average statistical error for the voxel absorbed dose is quite high (18.26%) limiting the reliability of the absorbed dose distribution. In figure 5.8 the uterus absorbed dose map (left) obtained with the HR–SS model is shown together with the correspondant distribution of statistical percentage error (right). For the latter, the peak at 100% corresponds to the voxels not fired, and the peak at about 50% corresponds to the voxels receiving a single hit. As expected, the LR–SS and the HR-MS models performed much better in terms of statistical convergence. For the first, a 0.02% average statistical error was obtained with a limited number of simulated events (7.50 10^7). For the multi-scale model, a 0.04% average statistical error was obtained for the inner part of the uterus (representing about 80% of the total volume) and a 19.06% for the edge voxels.

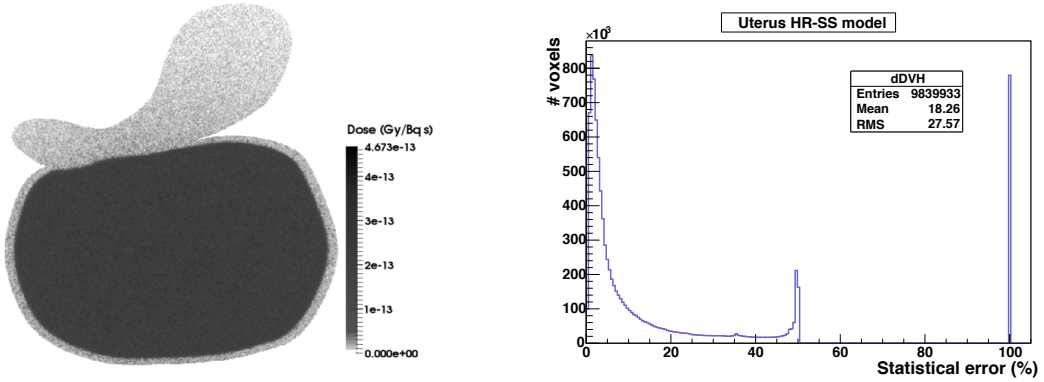

Figure 5.8: ^{131}I absorbed dose map (left) obtained with the HR–SS model, and the corresponding statistical error distribution in the uterus (right).

Also for what concerns the uterus dDVHs, the LR and the HR approach led to quite different results. In figure 5.9 (top), the ^{131}I dDVHs are presented for the three models, and normalised by the area of the HR–SS model to account for the different number of voxels fired by radiation. In this case, the HR–MS dDVH is much closer to the LR–SS dDVH than to the HR–SS model, while, again, the average absorbed doses (listed in the legend of figure 5.9 as "mean") to the organs are in good agreement: the differences between the HR–SS model and the HR–MS and the LR-SS models are 4.6% and 6.3% respectively: the difference between the HR–MS and the LR–SS models is, instead, of only 1.8%.

Considering the higher statistical uncertainty afflicting the HR–SS data, one might attribute the different shape of the HR–SS dDVH to the lack of convergence of the Monte Carlo simulation. However, a simple comparison of the dDVHs obtained from the HR–SS model with the 0.2 × 0.2 × 0.2 mm^3 voxel size, and from the same model resampled to 2.0 × 2.0 × 2.0 mm^3 voxels, demonstrates that the difference actually depends on sampling (see figure 5.9, bottom). Here, the same input data produce totally different absorbed dose distributions simply using different voxel sizes. As a reference, in figure 5.7 (left), the ^{131}I absorbed dose map is shown for the HR–SS model resampled to 2.0 × 2.0 × 2.0 mm^3 voxels in order to reduce statistical fluctuations due to sampling. The two absorbed dose distributions in figure 5.7 are presented using the same intensity scale to further highlight the differences between ^{90}Y and ^{131}I.

All the considerations made regarding the statistical convergence of the Monte Carlo simulation at the voxel level should not be applied to the interpretation of the average absorbed doses obtained. The convergence of the mean absorbed dose value, in fact, is much faster. According to conventional error propagation rules, the error on the mean absorbed dose is calculated as the squared sum of the voxel errors (e_i), divided by the number of voxels composing the organ model (N). Under the hypothesis that all voxel errors are the same, the error on the mean absorbed dose is given by the voxel error divided by N, and it is hence much smaller than e_i. As a consequence, the average absorbed dose calculated for the uterus remains relevant for the three models implemented.

5.3.3 Simulation performances

All the simulations for this study could be run on a 3.1 GHz Intel Core i5 computer with 12 GB of RAM without using the SWAP memory. As expected, the *G4AssemblyVolume* presented a higher memory consumption for geometry storage (see table 5.2). However, in this example, a 3.6 times increase in memory usage is not critical as it leaves the total memory consumption for the HR–MS model at 3.21 GB, a value that can be easily handled by any modern desktop computer.

The times needed to simulate a single geantino (the non-interacting Geant4 virtual particle used to test transportation processes) in both high resolution models are reported in table 5.2. Since the geantino navigation takes less than 0.01 seconds in both simulations, these values can be interpreted as the times necessary to build and store Geant4 geometry. No significant difference is found for the set-up time of the HR–MS and the HR–SS models.

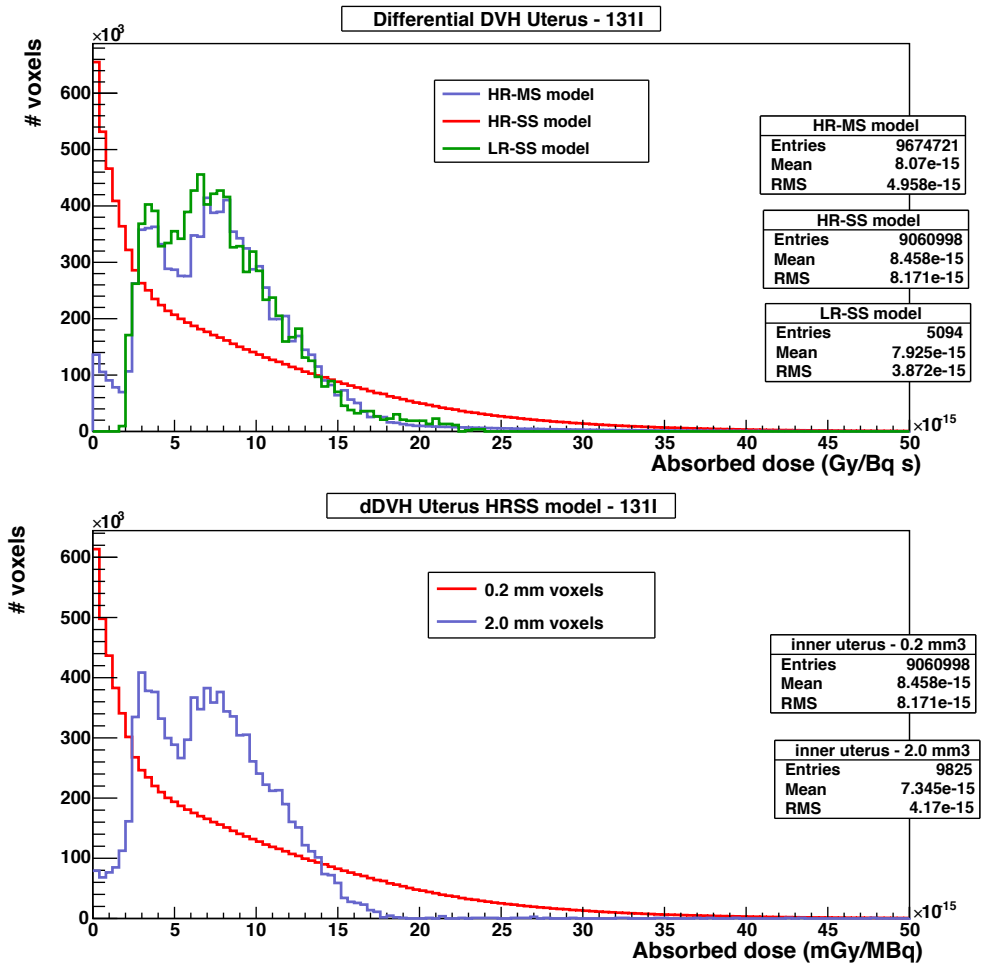

Figure 5.9: Top: ^{131}I uterus dDVHs obtained with the three models. Bottom: ^{131}I uterus dDVHs obtained from the HR–SS model with the 0.2 x 0.2 x 0.2 mm^3 voxel size (red line), and from the same model resampled to 2.0 x 2.0 x 2.0 mm^3 voxels (blue line).

In both cases these times seem negligible considering, for example, that the simulation of a few millions of ^{90}Y decays in the same geometry would take about 1 hour on a standard desktop computer.

	HR–MS	HR–SS
Time for geometry definition (s)	48	53
Memory to store geometry (GB)	3.21	0.88

Table 5.2: Geant4 time and memory performances at geometry set-up, for the HR–MS and the HR–SS models.

The evaluation of MC simulation times for the two high resolution models indicates that the simulation of multi-scale geometries in Geant4 according to the proposed method, is faster for both electrons and photons sources (see figure 5.10). For mono-energetic electrons the *G4AssemblyVolume* approach allows to speed up the simulation by a factor 2.1 on average with respect to the *G4PhantomParametrization* technique. In this case, the speed-up factor does not depend on particle energy because the number of voxels seen by electrons (energy from 0.1 to 2.5 MeV) during navigation is limited to few surrounding elements at any energy. Since for this test the source is placed at the centre of the bladder, the faster navigation in the HR–MS model is directly correlated to the larger voxel size in the HR–MS bladder. On the other hand, the speed-up factor in case of photon sources strictly depends on photon energy, with time ratios ($\text{Time}_{HR-SS}/\text{Time}_{HR-MS}$) going from 1.5 to 4.9 in the selected energy range (from 10 keV to 2 MeV). This behaviour reflects the dramatically increasing number of voxels seen at navigation by a gamma ray as its energy increases: since the total number of voxels in the HR–MS model is 3.9 times lower (excluding surrounding voxels) there is a gain in simulation time of the same order of magnitude.

Even considering more realistic simulations implementing extended radionuclide sources, the multi-resolution approach remains the fastest. For the simulation set-up described in section 5.2.3 (*Geant4 simulations*), a speed-up factor of 2.27 was obtained for ^{90}Y and of 1.90 for ^{131}I when comparing the HR–MS model to the HR–SS.

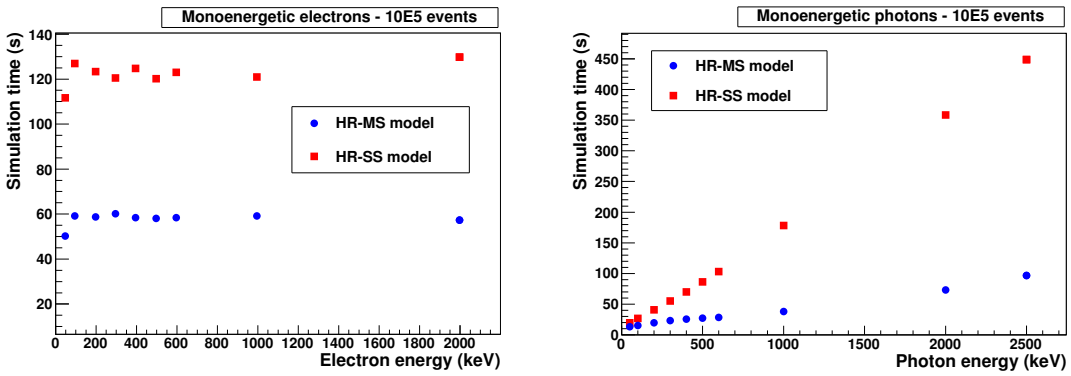

Figure 5.10: Simulation times for 10^5 electrons (on the left) and photons (on the right) of different energies, in the case of HR–MS and HR–SS models.

5.4 Conclusions

The accuracy of radiopharmaceutical absorbed dose distributions computed through MC simulations, is limited by the low spatial resolution of the 3D imaging techniques used to define the simulation geometry. This issue also persists with the implementation of realistic digital models, as they require to be simulated in their voxel form in order to reduce computation times. While for most organs the typical spatial sampling adopted to build the MC voxel geometry (few millimetres at best) is adequate, for small anatomical structures, the low sampling results in unrealistic organ shapes which may produce inaccurate dosimetry.

In this work a novel approach is proposed to adapt the spatial sampling of MC absorbed dose maps in different organs to the level of accuracy required by a specific clinical application, while maintaining the simulation time low. The software tools developed will eventually allow merging 3D patient images and accurate voxel models of selected organs, to perform multi-scale absorbed dose simulations with Geant4. Here the proposed approach is validate towards the recommended Geant4 technique to simulate 3D voxel geometries, using organ models of different spatial resolutions.

The comparison of two high resolution bladder models showed no significant differences in the dosimetry, both at the voxel and at the organ level, providing a validation of the multi-scale approach. At the same time, the comparison of high and low resolution dosimetries supported the need for high resolution models of small anatomical structures when an accurate knowledge of the absorbed dose distribution is required. In this case, in fact, the shape of resulting DVHs strictly depends on the model spatial resolution

as well as on the average range of the main emissions of the radionuclide considered. Here, for example, it was observed a significant bias in ^{90}Y dDVH shape caused by the unrealistic bladder thickness in the LR–SS model, which is not substantial in ^{131}I dDVH. Significant differences were also found in the shape of uterus dDVHs obtained with fine (HR–SS model) and coarse sampling (LR–SS and HR–MS models). The high statistical uncertainty associated to small size voxels suggests that a low resolution or a multi-scale approach is recommended for dosimetry of target organs far from the source (with respect to particle range). All these effects clearly indicate that spatial sampling of the anatomical model should be chosen with great care, not only to match the suited spatial resolution, but also accordingly to the radiation source selected.

On the other hand, relative differences between the average absorbed doses for the HR and the LR models were of the order of few percent. This discrepancy is not remarkable and suggests that a high resolution approach may not be necessary when only the average organ absorbed dose is needed. As a matter of fact, simply using a different MC toolkit implementing different physics models, or changing the binning of the radionuclide spectrum for the simulation of the source, would probably result in similar percentage differences for the average absorbed dose (Lanconelli et al. 2012).

It was also demonstrated that the proposed approach based on *G4AssemblyVolumes* allows reducing simulation times for the simplified geometry here discussed. The speed-up factor, of the order of 2 in this example, depends on the radionuclide emissions considered and on the relative number of voxels needed to describe the HR–SS and the HR–MS models. For the simulation of whole body geometries including selected HR organ models, even better time performances are anticipated with respect to the standard *G4PhantomParametrization* approach. As expected, the Geant4 memory usage to store the multi-scale model was higher than the memory needed for the single scale model. However, for limited size geometries, the reduced number of voxels necessary to describe the same anatomical area contributes to keep its amount to values that can be handled by standard desktop computers. In future works, memory consumption will be maintained low enough even in the case of whole body simulations using parallel worlds in Geant4 (Enger et al. 2012). In this scenario, the 3D whole body image of a patient could be modeled using *G4PhantomParametrization* in the main world, while the detailed multi-scale model could be implemented as a *G4AssemblyVolume* in the parallel world.

Conclusions and future perspectives

The MIRD formalism is by essence valid at any scale (from cellular to clinical studies) as long as the mean absorbed dose is the relevant parameter to assess. However, key factors need to be considered, as spatial resolution conditions (and sometimes limits) the relevance of a given dosimetric approach. In the past decades, limitation in computing power has led to the generation of dosimetric models of limited accuracy. Human and animal anatomy were represented using simple volume shapes as spheres, ellipsoides and so on. The advent of modern computers and the development of medical imaging techniques allowed the digital sampling of the volumes of interest, resulting in a refinement of geometry definition. This led to the generation of voxel-based and BREP models for both man and small animals. The implications of an improved geometry definition seems obvious at first sight: if the model geometry better matches the *in-vivo* or *in-vitro* biological system considered, a more realistic computation of the S factor can be implemented, and the dosimetric approach will be more accurate.

However, this is only one aspect of the problem. The overall accuracy of a given dosimetric approach depends on the accuracy of both parameters in the MIRD equation. Increasing the precision in the determination of the S value is fruitful only if the cumulated activity can be determined with the same level of accuracy. It is hence crucial to take into account spatial distribution of radioactivity, as it may vary even at the intra-cellular scale. This heterogeneity, combined with the range of radiations, induces absorbed dose gradients that directly impact the biological efficacy of the treatment. This is true for all particles involved in TRT (alpha, beta, Augers), depending on the size of the biological system they interact with. An important parameter to consider are the relative dimensions of particle range and propagation medium. In this sense, the spatial resolution

at which the activity should be quantified depends on the experimental context. In the presence of short-range emitters, dosimetry should consider events occurring at the tissue and even at the cellular scale. Conversely, for beta emitters, the assessment of activity variability within the organ volume is considered appropriate for most applications. Thus, while sometimes the use of the most refined imaging technologies is required to obtain dosimetric results of adequate accuracy, in other cases an approximate, but simpler approach may be implemented. In this work, examples of dosimetric calculations performed with different levels of detail have been discussed at the cellular, animal and clinical scales.

In chapter 2, the development of dedicated software tools has allowed the creation of virtual cell colonies on the basis of experimentally determined parameters. The generation of a realistic multi-cellular model was indeed necessary for the establishment of the absorbed dose-effect relationship in the case of ^{177}Lu labelled antibodies. Typical β-particles range in tissue can cover hundreds of cell radii; this means that the absorbed dose to a given cell in the culture is affected by the internalisation properties and actual spatial positions of thousands of cells. For the experimental conditions considered in this study, the cross-irradiation contribution was, in many cases, higher than self-absorption. This result strictly depends on how the experiment was conceived: cross-irradiation was relevant only before cells were seeded in different dishes for the formation of colonies (0 - 18 hours), while cell self-irradiation was continuos over the whole experiment time (0 - 336 hours). Hence, for *in-vivo* applications, as for example tissue dosimetry investigated at the cellular level, the cross-absorbed dose is in principle expected to contribute considerably more to the average cell absorbed dose. As a consequence, the implementation of realistic distributions and randomised cell properties is inevitable to obtain sound dosimetric results. This thesis is also supported by the high standard deviations ($\sim$24% on average) found for the cell average cross-absorbed dose, that reflects the high level of heterogeneity of the various parameters characterising the colony. In this perspective, performing a single dosimetric calculation for a given geometrical configuration and for a given average cell cumulated activity, could have resulted in absorbed dose values considerably distant from the mean.

All these considerations stand on the assumption that the cellular model developed is correct and appropriate. Even if there are no ground-truth data to benchmark the proposed approach, the establishment of an absorbed dose-effect correlation for Ramos cells may be considered indirect proof of its consistency. In particular, the similar surviv-

als achieved for the two specific (^{177}Lu-HH1 and ^{177}Lu-Rituximab) and the non-specific (^{177}Lu-Erbitux) mAbs is encouraging. For the latter, the absorbed dose is almost only due to non-specific irradiation from radioactivity in the culture medium. This makes the associated dosimetric model very simple and hence less prone to errors, as it depends on fewer parameters and assumptions. On the other hand, the lack of absorbed dose-effect correlation found for DOHH2 cells is most probably due to bystander effect (as observed in experiments performed at IRCM and not discussed in this thesis).

In chapter 3, the average tumour absorbed dose was shown not to correlate with treatment efficacy, in the case of α-RIT of small volume carcinomatosis. This study originated from a previous work carried out at IRCM with the aim of comparing the efficacy and toxicity of two different radiopharmaceuticals. In their work, Boudousq and colleagues established mice survival in relation to the treatment with two internalising (^{212}Pb-Trastuzumab) and non-internalising (^{212}Pb-35A7) mAbs. The internalising mAb showed significantly increased mice survival, however, the average absorbed dose was higher for tumours treated with the non-internalising mAb. In a second experiment, the acquisition of DAR images of tumour cryosections demonstrated that the non-internalising (at the cellular level) antibody, presented a very heterogeneous uptake at the tumour level. On the basis of these images, it was possible to assess the absorbed dose distribution with a spatial resolution of few micrometers. The resulting dose volume histograms evidenced that, despite the higher average absorbed dose found, a large part of tumours treated with the non-internalising mAb received a null absorbed dose. Tumour cells in these areas could hence freely proliferate, which explains the low efficacy of ^{212}Pb-35A7 treatment, and restores a correlation between absorbed dose delivered and therapeutic effect.

A more general conclusion regarding this study, concerns the pertinency of methods currently employed for the assessment of absorbed dose in small-animal experiments. The standard approach, based on organ/tumour biopsy and subsequent counting, only provides a measure of the average activity, neglecting sub-organ uptake heterogeneities. So, while this strategy has been proven reasonable for short range β-emitter dosimetry, for which particle range produces a smoothing effect on the absorbed dose distribution, it is a priori inappropriate for α-particles. A further demonstration that dosimetry may be unreliable when it is not carried out at the relevant scale (with respect to particle range and biological phenomena involved).

However, the implementation of the most refined dosimetric techniques is not always required, as seen in chapters 4 and 5 for two different clinical applications. In chapter 4, three different dosimetric approaches have been compared for the analysis of the same dataset acquired in the framework of a previous study. The aim of the original work, was to assess the effective dose for a novel PET radiotracer, ^{18}F-Flutemetamol. In the context of this thesis, the same dataset was used to derive more general conclusions regarding the accuracy of phantom-based, DVK and personalised MC dosimetry. Absorbed dose values for a sub-sample of organs was significantly different for the three methods. Values obtained with the phantom-based approach were up to two times lower than those obtained with Monte Carlo; DVKs (as implemented in STRATOS) absorbed doses were up to 3 times lower. Certainly, in a therapeutic context, these differences would not be acceptable, especially if regarding organs that are considered at risk for the treatment. However, the same conclusion does not hold in the context of diagnostic dosimetry. In this case, in fact, the aim is to obtain an order of magnitude for the effective dose to ensure safe levels of irradiation to the general population. Dosimetry does not need to be patient-specific and hence accuracy is not its main objective. Indeed, even a two- or threefold error in the determination of the absorbed dose, only slightly shifts the corresponding effective dose, because of the very low values of tissue-specific weighting factors (ICRP 1991, 2007). Still, this study has contributed to highlight how the choice of the computational method can impact patient dosimetry.

Even within the same treatment planning, the accuracy needed may vary for different anatomical structures. In chapter 5, a method to perform Monte Carlo based, multi-resolution dosimetry is proposed. It allows increasing the dosimetric accuracy for selected structures while keeping simulation time low.

As for EBRT, predictive dosimetry in TRT requires establishing the absorbed dose to a few organs that are considered at risk for the treatment. In EBRT, where radiation beams are collimated, these organs are included in a limited region of the body. For this reason, the dosimetric calculation is rather fast, even for MC methods (Sarrut et al. 2014). On the contrary, organs at risk in a TRT treatment may be very distant from one to another, since the irradiation is diffuse and isotropic. As a result, the dosimetric calculation may be considerable time-consuming as it should cover, in principle, the whole

body. In this sense, increasing the spatial resolution of the modelled geometry (in order to increase the accuracy of the absorbed dose distribution) seems unfeasible, as it would further compromise the calculation timing performances. A possible solution, however, is to improve the spatial sampling for the organ(s) of interest, while maintaining a coarse sampling for the rest of the body. Following this approach and through a proof of principle example, it was demonstrated that model spatial resolution may significantly affect the dosimetric endpoints obtained, and the shape of the absorbed dose distributions. The case discussed involved the dosimetry of the bladder wall for homogeneous ^{90}Y or ^{131}I sources in the bladder. For this configuration, for example, the maximum ^{131}I absorbed dose to the bladder wall predicted by the high resolution model was about four times higher than the value predicted by the low resolution one; a difference that is not certainly negligible for the determination of the activity to administer. On the other hand, however, using a fine voxellization was proven counterproductive for uterus dosimetry. In this example, in fact, the uterus was only partially irradiated by β-particles (and photons in the case of ^{131}I) generated in the bladder and, as a consequence, the MC convergence was very slow. In the specific case of ^{90}Y, most of uterus voxels remained unfired for both low and high resolution models, because of limited particle range. Nevertheless, in the case of ^{131}I source, the low- and the multi-resolution approaches (that used a coarse sampling for most of uterus voxels) performed much better than the high resolution single scale model, due to the larger volume of voxels implemented.

Another important aspect to consider for TRT optimisation, concerns the absolute quantification of radioactivity both *in vivo* and *ex vivo*. Being able to assess uptake heterogeneity, does not guarantee alone, achieving more accurate dosimetry. It is in fact crucial to establish the absolute value of cumulated activity with the highest possible precision. In chapter 3, for example, the choice of using DAR to quantify ^{212}Pb activity before transient equilibrium was achieved, may have partially biased the absolute absorbed doses obtained for tumours of the three groups (but the relative comparison of the three radiopharmaceutical still holds). At the same time, in the work discussed in chapter 2, a finer temporal sampling of the time-activity curves, would have resulted in smaller absorbed dose errors. A more accurate determination of activity was, in principle, possible for some of the dosimetric studies performed in the framework of this thesis. However, the optimisation of activity quantification procedures was beyond the scope of this work

that focused, instead, on the computational aspect of the dosimetric assessment process.

Through four practical examples, this thesis provided hints for the optimisation of absorbed dose calculation at different scales, separately. This multi-scale approach was felt necessary as a better determination of the absorbed dose-effect correlation in preclinical experiments, ultimately participates to the improvement of TRT treatments efficacy. In perspective, the integration of the dosimetric knowledge obtained at different scales may also contribute establishing more accurate predictive dosimetry for therapy. In a clinical setting, in fact, the scale at which biological information can be accessed is limited by the spatial resolution of currently available medical imaging scanners (from 1 to 10 mm depending on the technique). However, the biological efficacy of a given radiopharmaceutical ultimately depends on microscopic processes. Present-day clinical dosimetry simply neglects the complexity and heterogeneity that characterise living tissues at the cellular or multi-cellular level.

In principle, information obtained at a smaller scale can be used as a template for larger scale dosimetric calculations. This concept can be applied at different levels. For example, if the activity distribution pattern is assessed *ex vivo* (via autoradiography or using an alpha camera, with a spatial resolution of 10-50 um), the goal could be to inject this knowledge in the absorbed dose determination performed in vivo on animals (even if, at that scale, activity is determined with a spatial resolution of about 1 mm). Another application could consist in establishing radiobiological parameters via clonogenic survival assays and use this information to model DNA damages within the Monte Carlo computations of patient absorbed dose. This strategy could also be applied to the calculation of bone marrow absorbed dose, taking into account microscopic parameters. Patient images can be combined with macroscopic and microscopic representations of bone marrow merging voxel and analytical models, and then used to perform direct radiation transport as seen in chapter 5.

The application of this multi-scale approach requires the development of specific software tools that is currently on going at CRCT (Centre de Recherche en Cancérologie de Toulouse).

Conclusions et perspectives futures

Le formalisme du MIRD est, par définition, valide à toute les échelles, des études cellulaires aux études cliniques, tant que la dose absorbée moyenne est le paramètre d'intérêt. D'autres facteurs clés sont cependant à prendre en compte dans la mesure où la résolution spatiale conditionne (et parfois même limite) la pertinence de la méthode dosimétrique choisie. Jusqu'à une époque très récente, la puissance de calcul à disposition était le facteur limitant de la précision des modèles dosimétriques. L'anatomie humaine et de l'animal était donc représentée par une combinaison de volumes simples, comme des cubes, des sphères ou des ellipsoïdes. Les progrès récents en informatique et en imagerie médicale ont permis l'échantillonnage digital à haute précision des volumes mesurés, et donc l'obtention de modèles géométriques raffinés. Ces avancées ont menées au développement des modèles géométriques voxelisés et des modèles hybrides (BREP), tant pour l'homme que pour le petit animal. Les avantages d'une définition plus précise de la géométrie peuvent sembler évidents à première vue : si le modèle géométrique correspond mieux à la réalité du système biologique étudié, que ce soit *in vivo* ou *in vitro*, le calcul du facteur S sera mieux implémenté, et l'approche dosimétrique plus précise.

Cependant, ceci n'est que l'un des aspects du problème. En effet, améliorer le calcul du facteur S n'est utile que si l'activité cumulée peut être déterminée avec un niveau de précision similaire. La prise en compte de la distribution spatiale de la radioactivité est cruciale car celle-ci peut-être très hétérogène même à l'échelle intracellulaire. Cette hétérogénéité, combinée à la longueur d'interaction de la radiation, induit des gradients dans la distribution de la dose absorbée, qui impactent directement l'efficacité biologique du traitement. Ce phénomène est observé pour tous les types de particules rencontrés en RIV (alpha, beta, électrons Auger), selon les dimensions caractéristiques du système

biologique considéré. Le paramètre important est en fait la dimension relative du libre parcours moyen de la particule par rapport aux dimensions caractéristiques du milieu de propagation. La résolution spatiale à laquelle l'activité doit être quantifiée dépend donc du contexte expérimental. En présence d'émetteurs à courte longueur d'interaction, la dosimétrie doit être réalisée à l'échelle du tissu, voir même de la cellule. En revanche, pour les émetteurs beta, qui ont une plus grande longueur d'interaction, l'échelle de l'organe est suffisante pour obtenir une dosimétrie correcte dans la plupart des cas. En résumé, si l'utilisation de techniques d'imagerie avancées est parfois indispensable pour obtenir des résultats dosimétriques fiables, dans d'autres cas, l'implémentation d'une géométrie approximative dans le cadre d'une approche plus simple peut être suffisant. Dans cette thèse, divers exemples de calcul dosimétrique, réalisés à différents niveaux de détails, ont été présentés et analysés aux échelles cellulaire, animale et clinique.

Le chapitre 2 a présenté le travail réalisé pour le développement d'un outil informatique dédié à la création de colonies cellulaires virtuelles dont les paramètres correspondent aux mesures expérimentales fournies en entrée. La génération d'un modèle multi-cellulaire réaliste a en effet été nécessaire pour établir la relation dose absorbée-effet dans le cas d'anticorps marqués au lutétium 177 (^{177}Lu). La longueur d'interaction des particules β dans le tissu biologique couvre typiquement plusieurs centaines de rayons cellulaires, ce qui implique que la dose absorbée par une cellule donnée dans la culture dépend des capacités d'internalisation et de la distribution spatiale des milliers de cellules environnantes. Dans les conditions expérimentales étudiées dans ce travail, la contribution de l'irradiation par tirs croisés était, dans un grand nombre de cas, plus importante que celle de l'auto-absorption. Cependant, ce résultat dépend de manière stricte des conditions expérimentales choisies : l'irradiation par tirs croisés n'était importante que dans la phase initiale, avant que les cellules ne soient déposées dans les boîtes pour la formation des colonies (0 – 18 heures), alors que l'irradiation par auto-absorption a été continue pendant toute la durée de l'expérience (0 – 336 heures). Ainsi, dans le cas des applications *in vivo*, par exemple pour la dosimétrie d'un tissu étudié au niveau cellulaire, on s'attend à ce que l'irradiation par tirs croisés ait une contribution significative à la dose absorbée moyenne par cellule. L'implémentation de distributions réalistes, pour l'étalement spatial et les propriétés des cellules, est donc indispensable pour obtenir des résultats dosimétriques acceptables. Cette thèse est aussi supportée par la grande valeur observée de la déviation

standard (∼24%) de la dose absorbée par irradiation par tirs croisés, reflet du haut niveau d'hétérogénéité des divers paramètres caractérisant les colonies. Pour ce type d'étude, une dosimétrie réalisée en utilisant une unique instanciation de la géométrie, et pour une valeur donnée de l'activité moyenne par cellule, aurait fournie des doses absorbées éloignées de la moyenne réelle.

Ces considérations ne restent évidemment valides que sous la condition que le modèle de colonie cellulaire développé soit correct et adapté. Bien qu'il n'y ait pas de données de référence pour valider cette nouvelle approche, le fait de trouver une corrélation dose absorbée-effet pour les cellules Ramos peut être considéré comme un preuve indirect de sa consistance. En particulier, des courbes de survie très similaires sont obtenues pour les anticorps monoclonaux spécifiques (^{177}Lu-HH1 et ^{177}Lu-Rituximab) et non spécifiques (^{177}Lu-Erbitux) étudiés, ce qui est très encourageant. Pour ce dernier, la dose absorbée est presque uniquement due à l'irradiation non spécifique liée à la radioactivité dans le milieu de culture. Le modèle dosimétrique associé ne dépend donc que d'un nombre limité de paramètres et d'hypothèses, ce qui le rend relativement simple et limite le risque d'erreur. Par ailleurs, l'absence de corrélation dose absorbée-effet obtenue pour les cellules DOHH1 est très probablement due à l'effet *bystander*, comme observé lors d'expériences réalisées à l'IRCM et non présentées dans cette thèse.

Dans le chapitre 3, il a été démontré que la valeur moyenne de la dose absorbée par la tumeur n'est pas forcement corrélée à l'efficacité du traitement dans le cas de la radioimmunothérapie α des carcinoses de volume réduit. Cette étude prend son origine dans un travail précédemment réalisé à l'IRCM et ayant pour but la comparaison de l'efficacité et de la toxicité de deux radiopharmaceutiques différents. Dans leur travail, Boudousq et ses collègues ont établi les courbes de survie de souris traitées par deux anticorps différents, l'un internalisant (^{212}Pb-Trastuzumab) et l'autre non internalisant (^{212}Pb-35A7). L'anticorps internalisant donnait des taux de survie significativement plus élevés, alors que la dose absorbée moyenne à la tumeur était pourtant plus élevée pour l'anticorps non internalisant. Lors d'une seconde expérience, les images de coupes cryogéniques de la tumeur, obtenues par autoradiographie digitale, ont montré que l'anticorps non internalisant (au niveau cellulaire) était absorbé de manière très hétérogène au niveau de la tumeur. Ces images ont en outre permis d'extraire la distribution de la dose absorbée avec une résolution spatiale de quelques micromètres. Les histogrammes dose volume dérivés

ont mis en évidence le fait que, malgré la grande valeur moyenne de la dose absorbée, une grande partie de la tumeur traitée avec l'anticorps non internalisant recevait en fait une dose quasiment nulle. Les cellules tumorales de ces zones non traitées pouvaient donc proliférer librement ; ce qui explique la faible efficacité du traitement au ^{212}Pb-35A7, et permet aussi de restaurer la corrélation dose absorbée-effet thérapeutique.

D'un point de vue plus général, cette étude apporte un nouveau regard sur la pertinence des méthodes utilisées actuellement pour déterminer la dose absorbée dans les expériences sur le petit animal. La procédure standard, basée sur la biopsie de l'organe ou de la tumeur suivie du comptage des photons gamma, ne procure qu'une mesure moyenne de l'activité, et ne donne aucune information sur l'hétérogénéité de la radioactivité à l'intérieur de l'organe même. Alors que cette stratégie est tout à fait raisonnable pour faire de la dosimétrie avec des émetteurs β, pour lesquels la longueur d'interaction non négligeable produit un effet de lissage de la distribution de la dose absorbée, elle est a priori inadaptée en présence de particules α. Ceci est une autre démonstration du fait que la dosimétrie ne peut pas être fiable si elle n'est pas établie à la bonne échelle, soit, celle considérant la longueur d'interaction des particules en rapport aux dimensions caractéristiques des phénomènes biologiques étudiés.

L'implémentation d'un modèle dosimétrique très raffiné n'est cependant pas toujours utile, comme cela est démontré dans les chapitres 4 et 5, pour deux applications cliniques différentes. Dans le chapitre 4, trois approches dosimétriques différentes ont été comparées pour l'analyse d'un même jeu de données, obtenu dans le cadre d'une étude précédente. L'objectif du travail initial était d'établir la dose efficace pour un nouveau radiotraceur pour la TEP, le ^{18}F-Flutemetamol. Dans le contexte de cette thèse, ce même jeu de données a été utilisé pour dériver des conclusions plus générales sur la précision des différentes techniques dosimétriques : dosimétrie basée sur les fantômes, VDK et Monte-Carlo personnalisée. Les valeurs de dose absorbée obtenues pour un échantillon des organes se sont révélées être très différentes d'une méthode à l'autre. La dosimétrie basée sur les fantômes a fourni des valeurs de dose absorbée jusqu'à deux fois plus petites que celles obtenues par dosimétrie Monte-Carlo, alors que la dosimétrie VDK (via l'outil STRATOS) donnait des valeurs trois fois plus petites. Dans un contexte thérapeutique, ces différences ne seraient certainement pas acceptables, en particulier sur les organes considérés à risque pour le traitement. Cependant, dans le cadre d'une dosimétrie à visée diagnostique, elles

ne sont plus vraiment problématiques. En effet, dans ce cas, l'objectif est de dériver l'ordre de grandeur de la dose efficace permettant d'assurer un niveau d'irradiation acceptable pour une population de patients. La dosimétrie n'a alors pas besoin d'être spécifique à un patient donné, et la précision n'est plus l'objectif principal. En réalité, même une erreur d'un facteur deux ou trois sur la valeur de la dose absorbée n'est plus un problème car cela ne correspond qu'à une différence minimale sur la dose efficace, en raison des valeurs très faibles des facteurs de pondération des tissus (ICRP 1991, 2007). L'étude présentée ici a tout de même le mérite de contribuer à souligner l'importance de l'impact du choix de la méthode de calcul sur la dosimétrie personnalisée.

Même pour pour un plan de traitement donné, la précision dosimétrique nécessaire sera a priori différente pour chaque structure anatomique. Dans le chapitre 5, une méthode s'appuyant sur des simulations Monte-Carlo est proposée pour réaliser une dosimétrie multi-résolution. Cette méthode permet d'améliorer la précision de la dosimétrie pour les structures choisies, tout en contenant les temps de calcul.

Tout comme pour la radiothérapie externe, la dosimétrie prédictive en RIV requiert l'estimation de la dose absorbée pour les organes considérés à risque dans le cadre du traitement. En radiothérapie externe, où le faisceau de radiation est collimaté, ces organes sont compris dans une zone anatomique limitée. C'est pour cette raison que les calculs dosimétriques sont relativement rapides même si l'on utilise une méthode Monte-Carlo (Sarrut et al. 2014). En revanche, en RIV, les organes à risque peuvent être très distants les uns des autres, car la source de radiation est diffuse et isotrope. Les calculs dosimétriques peuvent alors prendre un temps considérable car ils doivent en principe prendre en compte le corps entier. L'augmentation de l'échantillonnage spatiale du modèle géométrique (pour améliorer la précision sur la distribution de la dose absorbée) semble complètement irréaliste, à cause de l'allongement des temps de calcul induit. Une solution possible est d'améliorer la résolution spatiale pour les organes d'intérêt, tout en maintenant un échantillonnage grossier du reste du corps. Cette approche a été implémentée sur un exemple particulier servant de preuve de principe, afin de démontrer que la résolution du modèle spatial peut impacter significativement les résultats de la dosimétrie, ainsi que la forme de la distribution de la dose absorbée. L'exemple choisi consiste à réaliser la dosimétrie de la paroi d'une vessie contenant une source homogène d'yttrium 90 (^{90}Y) ou d'iode 131 (^{131}I). Dans cette configuration, pour l'iode 131, le dose maximale absorbée

à la paroi de la vessie est quatre fois plus grande pour le modèle haute résolution, que pour le modèle basse résolution. C'est une différence certainement non négligeable pour la détermination de la valeur de l'activité à administrer. En revanche, pour la dosimétrie de l'utérus, la voxélisation fine de la géométrie s'est révélée être contre-productive. Dans l'exemple implémenté, l'utérus n'était en effet que partiellement irradié par les particules β (et des photons pour l'iode 131) provenant de la vessie, ce qui rendait la convergence de la simulation Monte-Carlo très lente. Pour le cas spécifique de l'yttrium 90, la plupart des voxels de l'utérus ne recevait aucun coup tant pour les modèles haute résolution que pour le modèle basse résolution, à cause de la faible longueur d'interaction des particules. Néanmoins, pour l'iode 131, les approches à basse résolution et multi-résolutions (entraînant un échantillonnage grossier de l'utérus) ont donné de meilleurs résultats que le modèle à très haute résolution, en raison du volume plus important des voxels qui a permis d'obtenir une meilleur statistique en terme de coups.

Un autre aspect important à considérer pour l'optimisation de la RIV, concerne la quantification absolue de la radioactivité, à la fois *in vivo* et *ex vivo*. Déterminer correctement l'hétérogénéité de l'absorption de la radioactivité n'est pas suffisant pour garantir l'obtention d'une dosimétrie plus précise. Il est en effet aussi crucial de déterminer avec autant de précision que nécessaire la valeur absolue de l'activité cumulée. Dans le chapitre 3 par exemple, le choix d'utiliser des images acquises par autoradiographie digitale, pour quantifier l'activité du plomb 212 (^{212}Pb), avant même que l'équilibre séculaire ne soit atteint, a peut être partiellement biaisé la valeur absolue des doses obtenues pour les tumeurs des trois groupes (mais la comparaison relative des trois radiopharmaceutiques reste elle correcte). Dans le même ordre d'idée, pour le travail présenté au chapitre 2, un meilleur échantillonnage temporel des courbes d'activité aurait permis de réduire significativement l'erreur finale sur la dose absorbée. En fait, certaines études dosimétriques menées durant cette thèse auraient pu, en principe, bénéficier d'une mesure plus précise de l'activité cumulée. Cependant, les procédures pour l'optimisation de la quantification de l'activité étaient trop éloignées du cadre de ce travaille, plutôt focalisé sur les aspects computationnels du process dosimétrique.

Ce travail de thèse présente plusieurs pistes pour l'optimisation du calcul de la dose absorbée à différentes échelles, et ceci à travers quatre cas pratiques. Cette approche

multi-échelle est apparue nécessaire car une meilleure détermination de la corrélation dose absorbée-effet dans les expériences précliniques, peut contribuer in fine à l'amélioration de l'efficacité des traitements RIV. De plus, l'intégration du calcul dosimétrique obtenu à différentes échelles pourrait aussi aider à établir une dosimétrie prédictive plus précise pour la thérapie. En effet, dans un contexte clinique, l'échelle à laquelle on peut accéder à l'information biologique est limitée par la résolution spatiale des scanners pour l'imagerie médicale actuellement disponibles (entre 1 et 10 mm selon les techniques). Hors, l'efficacité biologique d'un radiopharmaceutique donné dépend pourtant de processus microscopiques. La dosimétrie clinique pratiquée aujourd'hui néglige malheureusement la complexité et l'hétérogénéité qui caractérisent le tissu biologique vivant aux échelles cellulaire et multi-cellulaire.

En principe, les informations obtenues à petite échelle peuvent servir de modèle pour les calculs dosimétriques à plus grande échelle. Ce concept peut en fait être appliqué à différents niveaux. Par exemple, si le pattern de la distribution de l'activité est déterminé *ex vivo* (par autoradiographie ou en utilisant une caméra alpha ayant une résolution spatiale de 10 à 50 μm), cette information pourrait être utilisée pour la détermination de la dose absorbée aux animaux *in vivo* (bien qu'à cette échelle, l'activité ne puisse-t-être mesurée qu'avec une résolution spatiale de 1 mm). Une autre application pourrait être de dériver des paramètres radiobiologiques via des expériences de survie clonogénique, afin d'exploiter ces résultats pour mieux modéliser les dommages à l'ADN dans les calculs Monte-Carlo de dosimétrie personnalisée. Cette stratégie pourrait aussi permettre d'améliorer le calcul de la dose absorbée à la moelle osseuse en prenant en compte les paramètres microscopiques. Les images du patient peuvent être associées avec des représentations micro et macroscopiques de la moelle osseuse en combinant des modèles analytiques et voxelisés, et ensuite utilisées pour réaliser un transport direct de la radiation comme cela a été vu au chapitre 5.

L'application de cette méthode multi-échelle requiert le développement d'outils informatiques spécifiques, travail qui est actuellement mené au sein du CRCT (Centre de Recherche en Cancérologie de Toulouse).

Bibliography

[Aarts et al. 2007] Aarts F, Hendriks T, Boerman OC, Koppe MJ, Oyen WJG and Bleichrodt RP 2007 *A comparison between radioimmunotherapy and hyperthermic intraperitoneal chemotherapy for the treatment of peritoneal carcinomatosis of colonic origin in rats* Ann. Surg. Oncol. 14 3274-3282

[Agostinelli et al. 2003] Agostinelli S, Allison J, Amako K, Apostolakis J, Araujo H, Arce P, Asai M, Axen D, Banerjee S, Barrand G, Behner F, Bellagamba L, Boudreau J, Broglia L, Brunengo A, Burkhardt H, Chauvie S, Chuma J, Chytracek R, Cooperman G, Cosmo G, Degtyarenko P, Dell'Acqua A, Depaola G, Dietrich D, Enami R, Feliciello A, Ferguson C, Fesefeldt H, Folger G, Foppiano F, Forti A, Garelli S, Giani S, Giannitrapani R, Gibin G, Gómez Cadenas JJ, González I, Gracia Abril G, Greeniaus G, Greiner W, Grichine V, Grossheim A, Guatelli S, Gumplinger P, Hamatsu R, Hashimoto K, Hasui H, Heikkinen A, Howard A, Ivanchenko V, Johnson A, Jones FW, Kallenbach J, Kanaya N, Kawabata M, Kawabata Y, Kawaguti M, Kelner S, Kent P, Kimura A, Kodama T, Kokoulin R, Kossov M, Kurashige H, Lamanna E, Lampén T, Lara V, Lefebure V, Lei F, Liendl M, Lockman W, Longo F, Magni S, Maire M, Medernach E, Minamimoto K, Mora de Freitas P, MoritaY, Murakami K, Nagamatu M, Nartallo R, Nieminen P, Nishimura T, Ohtsubo K, Okamura M, O'Neale S, Oohata Y, Paech K, Perl J, Pfeiffer A, Pia MG, Ranjard F, Rybin A, Sadilov S, Di Salvo E, Santin G, Sasaki T, Savvas N, Sawada Y, Scherer S, Sei S, Sirotenko V, Smith D, Starkov N, Stoecker H, Sulkimo J, Takahata M, Tanaka S, Tcherniaev E, Safai Tehrani E, Tropeano M, Truscott P, Uno H, Urban L, Urban P, Verderi M, Walkden A, Wander W, Weber H, Wellisch JP, Wenaus T, Williams DC, Wright D, Yamada T, Yoshida H, and Zschiesche D 2003 *G4–a simulation toolkit* Nucl. Instr. Meth. Phys. Res. Sect. A 506 250-303

[Amato et al. 2011] Amato E, Lizio D and Baldari S 2011 *Absorbed fractions for electrons in ellipsoidal volumes* Phys. Med. Biol. 56 357-365

[Amato et al. 2012] Amato E, Minutoli F, Pacilio M, Campennì A and Baldari S 2012 *An analytical method for computing voxel S values for electrons and photons* Med. Phys. 39 6808-6817

[Amato et al. 2013] Amato E, Italiano A, Minutoli F and Baldari S 2013 *Use of the GEANT4 Monte Carlo to determine three-dimensional dose factors for radionuclide dosimetry* Nucl. Instr. Meth. Phys. Res. A 708 15–18

[Arce et al. 2008] Arce P, Apostolakis J and Cosmo G 2008 *A technique for optimised navigation in regular geometries* IEEE Nuclear Science Symp. Conf. Record 857-859

[Arnaud 2013] Arnaud FX 2013 *Etude pluridisciplinaire de la dosimétrie des électrons Auger dans un contexte de radioimmunothérapie à l'iode 125* PhD Dissertation University of Toulouse III, in French

[Baidoo et al. 2013] Baidoo KE, Milenic DE and Brechbiel MW 2013 *Methodology for Labeling Proteins and Peptides with Lead-212* Nucl. Med. Biol. 40 592-599

[Bardiès et al. 1990] Bardiès M, Lamé J, Myers MJ and Simoen JP 1990 *A simplified approach to beta dosimetry for small spheres labelled on the surface* Phys. Med. Biol. 35 1039-1050

[Bardiès and Chatal 1994] Bardiès M and Chatal JF 1994 *Absorbed doses for internal radiotherapyfrom 22 beta-emittingradionuclides: beta dosimetry of small spheres* Phys. Med. Biol. 39 961-981

[Bardiès and Pihet 2000] Bardiès M and Pihet P 2000 *Dosimetry and Microdosimetry of Targeted Radiotherapy* Curr. Pharm. Des. 6 1469-1502

[Bardiès et al. 2003] Bardies M, Kwok C and Sgouros G 2003 Dose point-kernels for radionuclide dosimetry. In: Zaidi H and Sgouros G *Therapeutic Applications of Monte Carlo calculations in nuclear medicine* IOP publishing Ltd, Bristol and Philadelphia

[Barone et al. 2005] Barone R, Borson-Chazot F, Valkema, R Walrand S, Chauvin F, Gogou L, Kvols LK, Krenning EP, Jamar F and Pauwels S 2005 *Patient-specific dosimetry in predicting renal toxicity with (90)Y-DOTATOC: relevance of kidney volume and dose rate in finding a dose-effect relationship* J. Nucl. Med. 46 99S-106S

[Baselga et al. 1998] Baselga J, Norton L, Albanell J, Kim YM and Mendelsohn J 1998 *Recombinant humanized anti-HER2 antibody (Herceptin) enhances the antitumor activity of paclitaxel and doxorubicin against HER2/neu overexpressing human breast cancer xenografts* Cancer. Res. 58 2825-2831

[Becker et al. 2007] Becker J, Zankl M and Petoussi-Henss N 2007 *A software tool for modification of human voxel models used for application in radiation protection* Phys. Med. Biol. 52 N195-205

[Behr et al. 2000] Behr TM, Blumenthal RD, Memtsoudis S, Sharkey RM, Gratz S, Becker W and Goldenberg DM 2000 *Cure of Metastatic Human Colonic Cancer in Mice with Radiolabeled Monoclonal Antibody Fragments* Clin. Cancer. Res. 6 4900-4907

[Berger 1971] Berger MJ 1971 *MIRD Pamphlet no 7 - Distribution of absorbed dose around point sources of electrons and beta particles in water and other media* J. Nucl. Med. 12 5-23

[Berger 1973] Berger MJ 1973 *Improved point kernel for electrons and beta-ray dosimetry* U.S. Atomic Energy Commission

[Berger et al. 2009] Berger MJ, Coursey J S, Zucker MA and Chang J 2009 *Stopping-power and range tables for electrons, protons, and Helium ions* NIST, Physical Measurement Laboratory

[Bitar et al. 2007] Bitar A, Lisbona A, Thedrez P, Sai Maurel C, Le Forestier D, Barbet J and Bardiès M 2007 *A voxel-based mouse for internal dose calculations using Monte Carlo simulations (MCNP)* Phys. Med. Biol. 52 1013-1025

[Bolch et al. 1999] Bolch WE, Bouchet LG, Robertson JS, Wessels BW, Siegel JA, Howell RW, Erdi AK, Aydogan B, Costes S and Watson EE 1999 *MIRD Pamphlet No. 17: The dosimetry of nonuniform activity distributions – radionuclide S values at the voxel level* J. Nucl. Med. 40 118-368

[Bolch et al. 2009] Bolch WE, Eckerman KF, Sgouros G and Thomas SR 2009 *MIRD Pamphlet No. 21: A generalized schema for radiopharmaceutical dosimetry—standardization of nomenclature* J. Nucl. Med. 50 477-484

[Bolch et al. 2010] Bolch W, Lee C, Wayson M, Johnson P 2010 *Hybrid computational phantoms for medical dose reconstruction* Radiat. Environ. Biophys. 49 155-168

[Botta et al. 2011] Botta F, Mairani A, Battistoni G, Cremonesi M, Di Dia A, Fassò A, Ferrari A, Ferrari M, Paganelli G, Pedroli G and Valente M 2011 *Calculation of electron and isotopes dose point kernels with FLUKA Monte Carlo code for dosimetry in nuclear medicine therapy* Med. Phys. 38 3944-3954

[Boudousq et al. 2010] Boudousq V, Ricaud S, Garambois V, Bascoul-Mollevi C, Boutaleb S, Busson M, Quenet F, Colombo PE, Bardiès M, Kotzki PO, Navarro-Teulon I, Pèlegrin A and Pouget JP 2010 *Brief intraperitoneal radioimmunotherapy of small peritoneal carcinomatosis using high activities of noninternalizing* ^{125}*I-labeled monoclonal antibodies* J. Nucl. Med. 51 1748-1755

[Boudousq et al. 2013] Boudousq V, Bobyk L, Busson M, Garambois V, Jarlier M, Charalambatou P, Pèlegrin A, Paillas S, Chouin N, Quenet F, Maquaire P, Torgue J, Navarro-Teulon I and Pouget PJ 2013 *Comparison between internalizing anti-HER2 mAbs and non-internalizing anti-CEA mAbs in alpha-radioimmunotherapy of small volume peritoneal carcinomatosis using* ^{212}*Pb* Plos One 8 e69613

[Bousis et al. 2010] Bousis C, Emfietzoglou D, Hadjidoukas P and Nikjoo H 2010 *Monte Carlo single-cell dosimetry of Auger-electron emitting radionuclides* Phys. Med. Biol. 55 2555-2572

[Boutaleb et al. 2009] Boutaleb S, Pouget JP, Hindorf C, Pèlegrin A, Barbet J, Kotzki PO and Bardiès M 2009 *Impact of mouse model on pre-clinical dosimetry in Targeted Radionuclide Therapy* Proc. of IEEE 97 2076-2085

[Breedveld 2000] Breedveld, F. C. 2000 *Therapeutic monoclonal antibodies* Lancet 355 735-740

[Briesmeister 2000] Briesmeister J F 2000 *MCNPTM—a general Monte Carlo N-particle transport code, version 4C* Report LA–13709–M, Los Alamos National Laboratory, Los Alamos, NM

[Brolin et al. 2015] Brolin G, Gustafsson J, Ljungberg M and Sjögreen Gleisner K 2015 *Pharmacokinetic digital phantoms for accuracy assessment of image-based dosimetry in 177Lu-DOTATATE peptide receptor radionuclide therapy* Phys. Med. Biol. 60 6131-6149

[Browne and Firestone 1986] Browne E and Firestone RB 1986 *Table of Radioactive Isotopes* New York, NY, John Wiley & Sons

[Brun and Rademakers 1997] Brun R and Rademakers F 1997 *ROOT–an object oriented data analysis framework* Nucl. Instrum. Methods Phys. Res. A 389 81–86

[Buckley et al. 2009] Buckley SE, Chittenden SJ, Saran FH, Meller ST and Flux GD 2009 *Whole-body dosimetry for individualized treatment planning of 131I-MIBG radionuclide therapy for neuroblastoma* J. Nucl. Med. 50 1518-1524

[Cai et al. 2010] Cai Z, Pignol JP, Chan C and Reilly RM 2010 *Cellular Dosimetry of 111In Using Monte Carlo N-Particle computer code: comparison with analytic methods and correlation with in vitro cytotoxicity* J. Nucl. Med. 51 462-470

[Cassola et al. 2010] Cassola V F, de Melo Lima V J, Kramer R and Khoury H J 2010 *FASH and MASH: female and male adult human phantoms based on polygon mesh surfaces: I. Development of the anatomy* Phys. Med. Biol. 55 133-162

[Chatal et al. 1999] Chatal JF1 and Hoefnagel CA. 1999 *Radionuclide therapy* Lancet. 354 931-935

[Chauvie et al. 2006] Chauvie S, Francis Z, Guatelli S, Incerti S, Mascialino B, Montarou G, Moretto P, Nieminen P and Pia MG 2006 *Monte Carlo simulation of interactions of radiation with biological systems at the cellular and DNA levels : The Geant4-DNA Project* Rad. Res. Vol. 166 652-689

[Chauvie et al. 2004] Chauvie S, Guatelli S, Ivanchenko V, Longo F, Mantero A, Mascialino B, Nieminen P, Pandola L, Parlati S, Peralta L, Pia MG, Piergentili M, Rodrigues P, Saliceti S and Tnndade, A 2004 *Geant4 low energy electromagnetic physics* IEEE Nuclear Science Symp. Conf. Record 3 1881-1885

[Chiavassa et al. 2006] Chiavassa S, Aubineau-Lanice I, Bitar A, Lisbona A, Barbet J, Franck D, Jourdain JR and Bardiès M 2006 *Validation of a personalized dosimetric evaluation tool (Oedipe) for targeted radiotherapy based on the Monte Carlo MCNPX code* Phys. Med. Biol. 51 601-616

[Chouin et al. 2009] Chouin N, Bernardeau K, Bardiès M, Faivre-Chauvet A, Bourgeois M, Apostolidis C, Morgenstern A, Lisbona A, Chérel M, Davodeau F. 2009 *Evidence of extra-nuclear cell sensitivity to alpha irradiation using a new microdosimetric model II. Application of the new microdosimetric model to experimental results* Rad. Research 171 664-673

[Cole 1969] Cole A 1969 *Absorption of 20 eV to 50,000 eV electron beams in air and plastic* Radiat. Res. 38 7-33

[Cousins 2010] Cousins B 2010 *Probability density functions for positive nuisance parameters, internal note of the CMS statistic committee* 2010 available at available online at: http://www.physics.ucla.edu/c̃ousins/stats/cousins_lognormal_prior.pdf

[Couturier et al. 2005] Couturier O, Supiot S, Degraef-Mougin M, Faivre-Chauvet A, Carlier T, Chatal JF, Davodeau F, Cherel M 2005 *Cancer radioimmunotherapy with alpha-emitting nuclides* Eur. J. Nucl. Med. Mol. Imaging 32 601-614

[Cristy 1980] Cristy M 1980 *Matemathical phantoms representing children of various ages for use in estimates of internal dose* Report ORNL/NUREG/TM-367, Oak Ridge National Laboratory, Oak Ridge, TN

[Cristy and Eckerman 1987] Cristy M and Eckerman KF 1987 *Specific absorbed fractions of energy at various ages from internal photon sources volumes I-VII* Report ORNL/TM-8381, Oak Ridge National Laboratory, Oak Ridge, TN

[Cross et al. 1982] Cross WG, Ing H, Freedman NO and Mainville J 1982 *Tables of beta ray dose distributions in water, air and other media* Report AECL-7617, Atomic Energy of Canada Ltd., Chalk River Nuclear Laboratories, Ontario

[Cullen et al. 1997] Cullen D, Hubbell JH and Kissel L 1997 *The Evaluated Photon Data Library* Technical Report UCRL-50400 vol 6, Lawrence Livermore National Laboratory, Livermore, CA

[Dale 1985] Dale RG 1985 *The application of the linear-quadratic dose-effect equation to fractionated and protracted radiotherapy* Br. J. Radiol. 58 515-28

[Dash et al. 2013] Dash A, Knapp FF and Pillai MRA 2013 *Targeted Radionuclide Therapy – an overview* Curr. Radiopharm. 6 000-000

[Defrise et al. 1997] Defrise M, PE Kinahan, DW Townsend, C Michel, M Sibomana and DF Newport 1997 *Exact and approximate rebinnig algorithms for 3D PET data* IEEE T. Med. Imaging 16 145-158

[Dewaraja et al. 2005] Dewaraja YK, Wilderman SJ, Ljungberg M, Koral KF, Zasadny K and Kaminiski MS 2005 *Accurate dosimetry in ^{131}I radionuclide therapy using patient-*

specific, 3-dimensional methods for SPECT reconstruction and absorbed dose calculation J. Nucl. Med. 46 840-849

[Dewaraja et al. 2010] Dewaraja YK, Schipper MJ, Roberson PL, Wilderman SJ, Amro H, Regan DD, Koral KF, Kaminski MS and Avram AM 2010 ^{131}*I-Tositumomab radioimmunotherapy: initial tumor dose response results using 3-dimensional dosimetry including radiobiologic modeling* J. Nucl. Med. 51 1155-1162

[Dieudonné et al. 2010] Dieudonné A, Hobbs RF, Bolch WE, Sgouros G and Gardin I 2010 *Fine-resolution voxel S values for constructing absorbed dose distributions at variable voxel size* J. Nucl. Med. 51 1600-1607

[Dieudonné et al. 2013] Dieudonné A, Hobbs RF, Lebtahi R, Maurel F, Baechler S, Wahl RL, Boubaker A, Le Guludec D, Sgouros G and Gardin I 2013 *Study of the impact of tissue density heterogeneities on 3-Dimensional abdominal dosimetry: comparison between dose kernel convolution and direct Monte Carlo methods* J. Nucl. Med. 54 236-243

[Divoli et al. 2009] Divoli A, Chiavassa S, Ferrer L, Barbet J, Flux GD and Bardiès M 2009 *Effect of patient morphology on dosimetric calculations for internal irradiation as assessed by comparisons of Monte Carlo versus conventional methodologies* J. Nucl. Med. 50 316-323

[Dogdas et al. 2007] Dogdas B, Stout D, Chatziioannou AF and Leahy RM 2007 *Digimouse: a 3D whole body mouse atlas from CT and cryosection data* Phys. Med. Biol. 52 577-587

[Eckerman and Endo 2008] Eckerman KF and Endo A 2008 *MIRD radionuclide data and decay schemes, 2nd edition* The Society of Nuclear Medicine, Reston, VA, SNM.

[Ehrlich 1899] Ehrlich P 1899 *On immunity with special reference to cell life* In the collected papers of Paul Ehrlich, volume II. London U.K., Pergamon Press edition.

[Emfietzoglou et al. 2008] Emfietzoglou D, Kostarelos K, Hadjidoukas P, Bousis C, Fotopoulos A, Pathak A and Nikjoo H 2008 *Subcellular S-factors for low-energy electrons: a comparison of Monte Carlo simulations and continuous-slowing-down calculations* Int. J. Radiat. Biol. 84 1034-1044

[Enger et al. 2012] Enger S A, Landry G, D'Amours M, Verhaegen F, Beaulieu L, Asai M and Perl J 2012 *Layered mass geometry: a novel technique to overlay seeds and applicators onto patient geometry in Geant4 brachytherapy simulations* Phys. Med. Biol. 57 6269-6277

[Ersahin et al. 2011] Ersahin D, Doddamane I and David Cheng 2011 *Targeted Radionuclide Therapy* Cancers 3 3838-3855

[Faraggi et al. 1998] Faraggi M, Gardin I, Stievenart JL, Bok BD and Le Guludec D 1998 *Comparison of cellular and conventional dosimetry in assessing self-dose and cross-dose delivered to the cell nucleus by electron emissions of* ^{99m}Tc, ^{123}I, ^{111}In, ^{67}Ga *and* ^{201}Tl Eur. J. Nucl. Med. 25 205-214

[Fernández et al. 2013] Fernández M, Hänscheid H, Mauxion T, Bardiès M, Kletting P, Glatting G and Lassmann M 2013 *A fast method for rescaling voxel S values for arbitrary voxel sizes in targeted radionuclide therapy from a single Monte Carlo calculation* Med. Phys. 40 082502-1-8

[Ferrer et al. 2012] Ferrer L, Malek E, Bodet-Milin C, Legouill S, Prangère T, Robu D, Jeans S, Tipping J, Huglo D, Carpentier P, Illidge T, Kraeber-Boderé F, Morschhauser F and Bardiès M 2012 *Comparisons of dosimetric approaches for fractionated radioimmunotherapy of non-Hodgkin lymphoma* Q. J. Nucl. Med. Mol. Imaging 56 529-537

[Fill et al. 2004] Fill U A, Zankl M, Petoussi-Henss N, Siebert M and Regulla D 2004 *Adult female voxel models of different stature and photon conversion coefficients for radiation protection* Health. Phys. 86 253-272

[Fisher and Snyder 1966] Fisher HLJ and Snyder WS 1966 *Variation of dose delivered by* ^{137}Cs *as a function of body size from infancy to adulthood* Report ORNL-4007, Oak Ridge National Laboratory, Oak Ridge

[Fisher and Snyder 1967] Fisher HLJ and Snyder WS 1967 *Distribution of dose in the body from a source of gamma rays distributed uniformly in an organ* Health Physics Division Annual Progress Report for Period Ending July 31, Report ORNL-4168 (Oak Ridge, TN: Oak Ridge National Laboratory)

[Flux et al. 2010] Flux GD, Haq M, Chittenden SJ, Buckley S, Hindorf C, Newbold K and Harmer CL 2010 *A dose-effect correlation for radioiodine ablation in differentiated thyroid cancer* Eur. J. Nucl. Med. Mol. Imaging 37 270-275

[Flynn et al. 2001] Flynn AA, Green AJ, Pedley RB, Boxer GM, Boden R and Begent RHJ 2001 *A mouse model for calculating the absorbed beta-particle dose from* ^{131}I- *and* ^{90}Y-

labeled immunoconjugates, including a method for dealing with heterogeneity in kidney and tumor Radiat. Res. 156 28-35

[Freudenberg et al. 2011] Freudenberg R, Wendisch M and Kotzerke J 2011 *Geant4-Simulations for cellular dosimetry in nuclear medicine* Z. Med. Phys. 21 281-289

[Furhang et al. 1996] Furhang EE, Sgouros G and Chui C 1996 *Radionuclide photon dose kernels for internal emitter dosimetry* Med. Phys. 23 759-764

[Garin et al. 2012] Garin E, Lenoir L, Rolland, Y Edeline J, Mesbah H, Laffont S, Porée P, Clément B, Raoul JL and Boucher E 2012 *Dosimetry based on 99mTc-macroaggregated albumin SPECT/CT accurately predicts tumor response and survival in hepatocellular carcinoma patients treated with* ^{90}*Y-loaded glass microspheres: preliminary results* J. Nucl. Med. 53 255-263

[Glatting et al. 2013] Glatting G, Bardiès M and Lassmann M 2013 *Treatment planning in molecular radiotherapy* Zeitschrift für Medizinische Physik 23 262-269

[Goddu et al. 1994a] Goddu SM, Howell RW and Rao DV 1994 *Cellular dosimetry: absorbed fractions for monoenergetic electron and alpha particle sources and S-values for radionuclides uniformly distributed in different cell compartments* J. Nucl. Med. 35 303-316

[Goddu et al. 1994b] Goddu SM, Rao DV and Howell RW 1994 *Multicellular dosimetry for micrometastases: dependence of self-dose versus cross-dose to cell nuclei on type and energy of radiation and subcellular distribution of radionuclides* J. Nucl. Med. 35 521-530

[Goddu et al. 1997] Goddu SM, Howell RW, Bouchet LG, Bolch WE and Rao DV 1997 *MIRD cellular S values* SNM MIRD Committee. Society of Nuclear Medicine edition

[Goel et al. 2010] Goel MK, Khanna P and Kishore J 2010 *Understanding survival analysis: Kaplan-Meier estimate* Int. J. Ayurveda Res. 1 274-278

[Goldsmith 2010] Goldsmith SJ 2010 *Radioimmunotherapy of lymphoma: Bexxar and Zevalin* Semin. Nucl. Med. 40 122-135

[Grassi et al. 2014] Grassi E, Fioroni F, Ferri V, Mezzenga E, Sarti MA, Paulus T, Lanconelli N, Filice A, Versari A and Iori M 2014 *Quantitative comparison between the commercial software STRATOS by Philips and a homemade software for voxel-dosimetry in radiopeptide therapy* Phys. Medica 31 72-79

[Hakenberg et al. 2000] Hakenberg O W, Linne C, Manseck A and Wirth M P 2000 *Bladder wall thickness in normal adults and men with mild lower urinary tract symptoms and benign prostatic enlargement* Neurourology and Urodynamics 19 585-593

[Hammarstrom et al. 1989] Hammarstrom S, Shively JE, Paxton RJ, Beatty BG, Larsson A, Ghosh R, Bormer O, Buchegger F, Mach JP, Burtin P, Seguin P, Darbouret B, Degorce F, Sertour J, Jolu JP, Fuks A, Kalthoff H, Schmiegel W, Arndt R, Kloppel G, von Kleist S, Grunert F, Schwarz K, Matsuoka Y, Kuroki M, Wagener C, Weber T, Yachi A, Imai K, Hishikawa N and Tsujisaki M 1989 *Antigenic sites in carcinoembryonic antigen* Cancer. Res. 49 4852-4858

[Han et al. 2013] Han M C, Kim C H, Jeong J H, Yeom Y S, Kim S, Wilson P P H and Apostolakis J 2013 *DagSolid: a new Geant4 solid class for fast simulation in polygon-mesh geometry* Phys. Med. Biol. 58 4595-4609

[Hartman et al. 2000] Hartman TRN, Lundqvist H, Westlin JE and Carlsson J 2000 *Radiation doses to the cell nucleus in single cells and cells in micrometastases in targeted therapy with* ^{131}I *labeled ligands or antibodies* Int. J. Radiation Oncology Biol. Phys. 46 1025-1036

[Hindorf et al. 2004] Hindorf C, Ljungberg M, Strand SE 2004 *Evaluation of parameters influencing S-values in mouse dosimetry* J. Nucl. Med. 45 1960-1965

[Hobbs et al. 2009] Hobbs RF, Wahl RL, Lodge MA, Javadi MS, Cho SY, Chien DT, Ewertz ME, Esaias CE, Ladenson PW and Sgouros G 2009 ^{124}I *PET-based 3D-RD dosimetry for a pediatric thyroid cancer patient: real-time treatment planning and methodologic comparison* J. Nucl. Med. 50 1844-1847

[Horak et al. 1997] Horak E, Hartmann F, Garmestani K, Wu C, Brechbiel M, Gansow OA, Landolfi NF and Waldmann TA 1997 *Radioimmunotherapy targeting of HER2/neu oncoprotein on ovarian tumor using lead-212-DOTA-AE1* J. Nucl. Med. 38 1944-1950

[Howell et al. 1989] Howell RW, Rao DV and Sastry KSR 1989 *Macroscopic dosimetry for radioimmunotherapy: Nonuniform activity distributions in solid tumors* Med. Phys. 16 66-74

[Howell et al. 1990] Howell RW, Rao DV and Haydock C 1990 *Dosimetry techniques for therapeutic applications of incorporated radionuclides.* In: Adelstein SJ, Kassis AI, Burt

RW *Dosimetry of administered radionuclides* American College of Nuclear Physicians, Washington DC

[Howell et al. 1994] Howell RW, Azure MT, Narra VR and Rao DV 1994 *Relative biological effectiveness of alpha-particle emitters in vivo at low doses* Radiat. Res. 137 352-360

[Howell et al. 2012] Howell RW, Rajon D and Bolch WE 2012 *Monte Carlo simulation of irradiation and killing in three dimensional cell populations with lognormal cellular uptake of radioactivity* Int. J. Rad. Biol. 88 115-122

[Hubert-Tremblay et al. 2006] Hubert-Tremblay V, Archambault L, Tubic D, Roy R and Beaulieu L 2006 *Octree indexing of DICOM images for voxel number reduction and improvement of Monte Carlo simulation computing efficiency* Med. Phys. 33 2819-2831

[Hudis et al. 2007] Hudis CA 2007 *Trastuzumab–mechanism of action and use in clinical practice* N. Engl. J. Med. 357 39-51

[Hui et al. 1994] Hui TE, Fisher DR, Kuhn JA, Williams LE, Nourigat C, Badger CC, Beatty BG and Beatty JD 1994 *A mouse model for calculating cross-organ beta doses from yttrium-90-labeled immunoconjugates* Cancer 73 951-957

[Humm et al. 1994] Humm JL, Howell RW and Rao DV 1994 *Dosimetry of Auger-electron-emitting radionuclides: report No. 3 of AAPM Nuclear Medicine Task Group No. 6.* Med. Phys. 21 1901-1915

[ICRU 1993] ICRU 1993 *Stopping powers and ranges for protons and alpha particles. Report 49* International Commission on Radiation Units and Measurements, Bethesda, MD

[ICRP 1960] ICRP 1960 *Report of committee II on permissible dose for internal radiation* Ann. ICRP 2 1-233

[ICRP 1975] ICRP 1975 *Report of the task group on reference man. ICRP Publication 23* Ann. ICRP 23 1-480

[ICRP 1991] ICRP 1991 *Recommendations of the International Commission on Radiological Protection. ICRP Publication 60.* Ann. ICRP 21 1-201

[ICRP 2002] ICRP 2002 *Basic anatomical and physiological data for use in radiological protection: reference values. ICRP Publication 89* Ann. ICRP 32 1-277

[ICRP 2007] ICRP 2007 *The 2007 Recommendations of the International Commission on Radiological Protection. ICRP Publication 103* Ann. ICRP 37 1-332

[ICRP 2009] ICRP 2009 *Adult reference computational phantoms. ICRP Publication 110* Ann. ICRP 39 1-166

[Jan et al. 2004] Jan S, Santin G, Strul D, Staelens S, Assié K, Autret D, Avner S, Barbier R, Bardiès M, Bloomfield PM, Brasse D, Breton V, Bruyndonckx P, Buvat I, Chatziioannou AF, Choi Y, Chung YH, Comtat C, Donnarieix D, Ferrer L, Glick SJ, Groiselle CJ, Guez D, Honore PF, Kerhoas-Cavata S, Kirov AS, Kohli V, Koole M, Krieguer M, van der Laan DJ, Lamare F, Largeron G, Lartizien C, Lazaro D, Maas MC, Maigne L, Mayet F, Melot F, Merheb C, Pennacchio E, Perez J, Pietrzyk U, Rannou FR, Rey M, Schaart DR, Schmidtlein CR, Simon L, Song TY, Vieira JM, Visvikis D, Van de Walle R, Wieërs E and Morel C 2004 *GATE: a simulation toolkit for PET and SPECT* Phys. Med. Biol. 49 4543-4561

[Jan et al. 2011] Jan S, Benoit D, Becheva E, Carlier T, Cassol F, Descourt P, Frisson T, Grevillot L, Guigues L, Maigne L, Morel C, Perrot Y, Rehfeld N, Sarrut D, Schaart DR, Stute S, Pietrzyk U, Visvikis D, Zahra N and Buvat I 2011 *GATE V6: a major enhancement of the GATE simulation platform enabling modelling of CT and radiotherapy* Phys. Med. Biol. 56 881-901

[Kawrakow and Rogers 2003] Kawrakow I and Rogers DWO 2003 *The EGSnrc code system: Monte Carlo simulation of electron and photon transport* Report PIRS-701, National Research Council of Canada

[Keenan et al. 2010] Keenan MA, Stabin MG, Segars WP and Fernald MJ 2010 *RADAR realistic animal model series for dose assessment* J. Nucl. Med. 51 471-476

[Kim et al. 2011] Kim C H, Jeong J H, Bolch W E, Cho K W and Hwang S B 2011 *A polygon-surface reference Korean male phantom (PSRK-Man) and its direct implementation in Geant4 Monte Carlo simulation* Phys. Med. Biol. 56 3137-3161

[Kohler et al. 1976] Kohler G, Howe SC and Milstein C 1976 *Fusion between immunoglobulin-secreting and nonsecreting myeloma cell lines* Eur. J. Immunol. 6 292-295

[Konijnenberg et al. 2007] Konijnenberg MW, Melis M, Valkema R, Krenning E and de Jong

M 2007 *Radiation dose distribution in human kidneys by octreotides in Peptide Receptor Radionuclide Therapy* J. Nucl. Med. 48 134-142

[Konijnenberg et al. 2011] Konijnenberg MW and de Jong M 2011 *Preclinical animal research on therapy dosimetry with dual isotopes* Eur. J. Nucl. Mol. Imaging 38 19-27

[Koppe et al. 2005] Koppe MJ, Bleichrodt RP, Oyen WJG and Boerman OC 2005 *Radioimmunotherapy and colorectal cancer* Br. J. Surg. 92 264-276

[Kramer et al. 2003] Kramer R, Vieira JW, Khoury HJ, Lima FRA and Fuelle D 2003 All about MAX: a Male Adult voXel phantom for Monte Carlo calculations in radiation protection dosimetry Phys. Med. Biol. 48 1239-1262

[Kramer et al. 2004] Kramer R, Khoury HJ, Vieira JW, Loureiro ECM, Lima VJM, Lima FRA and Hoff G 2004 All about FAX: a Female Adult voXel phantom for Monte Carlo calculation in radiation protection dosimetry Phys. Med. Biol. 49 5203-5216

[Kramer et al. 2006] Kramer R, Khoury HJ, Vieira JW and Lima VJM 2006 *MAX06 and FAX06: update of two adult human phantoms for radiation protection dosimetry* Phys. Med. Biol. 51 3331-3346

[Kumada et al. 2011] Kumada H, Saito K, Nakamura T, Sakae T, Sakurai H, Matsumura A and Ono K 2011 *Multistep Lattice-Voxel method utilizing lattice function for Monte-Carlo treatment planning with pixel based voxel model* Appl. Radiat. Isot. 69 1866-1869

[Lamart et al. 2011] Lamart S, Bouville A, Simon SL, Eckerman KF, Melo D and Lee C 2011 *Comparison of internal dosimetry factors for three classes of adult computational phantoms with emphasis on I-131 in the thyroid* Phys. Med. Biol. 56 7317-7335

[Lanconelli et al. 2012] Lanconelli N, Pacilio M, Lo Meo S, Botta F, Di Dia A, Torres Aroche LA, Pérez MAC and Cremonesi M 2012 *A free database of radionuclide voxel S values for the dosimetry of nonuniform activity distributions* Phys. Med. Biol. 57 517-533

[LarssonmE et al. 2007] LarssonmE, Strand SE, Ljungberg M and Jönsson BA 2007 *Mouse S-factors based on Monte Carlo simulations in the anatomical realistic Moby phantom for internal dosimetry* Cancer Biother. Radiopharm. 22 438-442

[Larsson et al. 2011] Larsson E, Ljungberg M, Strand SE and Jönsson BA 2011 *Monte Carlo calculations of absorbed doses in tumours using a modified MOBY mouse phantom for pre-clinical dosimetry studies* Acta Oncol. 50 973-980

[Lassmann et al. 2011] Lassmann M, Chiesa C, Flux G and Bardiès M 2011 *EANM dosimetry committee guidance document: good practice of clinical dosimetry reporting* Eur. J. Nucl. Med. Mol. Imaging 38 192-200

[Lee et al. 2007] Lee C, Lodwick D, Hasenauer D, Williams JL, Lee C and Bolch WE 2007 *Hybrid computational phantoms of the male and female newborn patient: NURBS-based whole-body models* Phys. Med. Biol. 52 3309-3333

[Lee et al. 2008] Lee C, Lodwick D, Williams JL and Bolch WE 2008 *Hybrid computational phantoms of the 15-year male and female adolescent: applications to CT organ dosimetry for patients of variable morphometry* Med. Phys. 35 2366-2382

[Lee et al. 2010] Lee C, Lodwick D, Hurtado J, Pafundi D, Williams JL and Bolch WE 2010 *The UF family of reference hybrid phantoms for computational radiation dosimetry* Phys. Med. Biol. 55 339-363

[Lehmann et al. 2005] Lehmann , Hartmann Siantar C, Wessol DE, Wemple CA, Nigg D, Cogliati J, Daly T, Descalle MA, Flickinger T, Pletcher D and Denardo GJ 2005 *Monte Carlo treatment planning for molecular targeted radiotherapy within the MINERVA system* Phys. Med. Biol. 50 947–958

[Leyton et al. 2001] Leyton M 2001 *A generative theory of shape* (Berlin: Springer)

[Limpert et al. 2001] Limpert E, Stahel WA and Abbt M 2001 *Log-normal distributions across the sciences: keys and clues* BioScience 51 341-352

[Loevinger et al. 1991] Loevinger R, Budinger TF and Watson EE 1991 *MIRD primer for absorbed dose calculations* Revised ed. New York, NY, The Society of Nuclear Medicine

[Lorensen and Cline 1987] Lorensen W E and Cline H E 1987 *Marching cubes: a high resolution 3D surface construction algorithm* Computer Graphics 21 163-169

[Maiello and Hoover 2010] Maiello ML and Hoover MD 2010 *Radioactive air sampling methods* CRC Press

[Maigne et al. 2011] Maigne L, Perrot Y, Schaart DR, Donnarieix D and Breton V 2011 *Comparison of GATE/GEANT4 with EGSnrc and MCNP for electron dose calculations at energies between 15 keV and 20 MeV* Phys. Med. Biol. 56 811-827

[Makrigiorgos et al. 1990] Makrigiorgos GM, Ito S, Baranowska-Kortylewicz J, Vinter DW, Iqbal A, Van den Abbeele AD, Adelstein SJ and Kassis AI 1990 *Inhomogeneous deposition of radiopharmaceuticals at the cellular level: Experimental evidence and dosimetric implications* J. Nucl. Med. 31 1358-1363

[Malaroda et al. 2003] Malaroda A, Flux GD, Buffa FM and Ott RJ 2003 *Multicellular dosimetry in voxel geometry for Targeted Radionuclide Therapy* Cancer Biother. Radiopharm. 18 451-461

[Marcatili et al. 2013] Marcatili S, Pettinato C, Daniels S, Lewis G, Edwards P, Fanti S and Spezi E 2013 *Development and validation of RAYDOSE: a Geant4-based application for molecular radiotherapy* Phys. Med. Biol. 58 2491-2508

[Marcatili et al. 2014] Marcatili S, Villoing D, Garcia MP and Bardies M 2014 *Multi-scale hybrid models for radiopharmaceutical dosimetry with Geant4* Phys. Med. Biol. 59 7625-7641

[Marcatili et al. 2015] Marcatili S, Villoing D, Mauxion T, McParland BJ, and Bardiès M 2015 *Model-based versus specific dosimetry in diagnostic context: Comparison of three dosimetric approaches* Med. Phys. 42 1288-1296

[Mauxion et al. 2013] Mauxion T, Barbet J, Suhard J, Pouget J, Poirot M and Bardiès M 2013 *Improved realism of hybrid mouse models may not be sufficient to generate reference dosimetric data* Med. Phys. 40 052501-1-11

[Maynard et al. 2011] Maynard MR, Geyer JW, Aris JP, Shifrin RY and Bolch WE 2011 *The UF family of hybrid phantoms of the developing human fetus for computational radiation dosimetry* Phys. Med. Biol. 56 4839-4879

[McParland 2010] McParland BJ 2010 *Nuclear medicine radiation dosimetry. Advanced theoretical principles* Springer–Verlag London Limited.

[Milenic et al. 2005] Milenic DE, Garmestani K, Brady ED, Albert PS, Ma D, Abdulla A and Brechbiel MW 2005 *Alpha-particle radioimmunotherapy of disseminated peritoneal disease using a (212)Pb-labeled radioimmunoconjugate targeting HER2* Cancer Biother. Radiopharm. 20 557-568

[Milenic et al. 2007] Milenic DE, Garmestani K, Brady ED, Albert PS, Abdulla A, Flynn J and Brechbiel MW 2007 *Potentiation of high-LET radiation by gemcitabine: targeting*

HER2 with trastuzumab to treat disseminated peritoneal disease Clin. Cancer. Res. 13 1926-1935

[Milenic et al. 2008] Milenic DE, Garmestani K, Brady ED, Baidoo KE, Albert PS, Wong KJ, Flynn J and Brechbiel MW 2008 *Multimodality therapy: potentiation of high linear energy transfer radiation with paclitaxel for the treatment of disseminated peritoneal disease* Clin. Cancer. Res. 14 5108–5115

[Motulsky and Christopoulos 2005] Motulsky HJ and Christopoulos A 2005 *Fitting models to biological data using linear and nonlinear regression. A practical guide to curve fitting* GraphPad Software Inc. San Diego, CA

[Na et al. 2010] Na Y H, Zhang B, Zhang J, Caracappa P F and Xu X G 2010 *Deformable adult phantoms for radiation protection dosiemtry: anthropometric data representing size distributions of adult worker populations and software algorithms* Phys. Med. Biol. 55 3789-3811

[Oei et al. 2007] Oei AL, Verheijen RH, Seiden MV, Benigno BB, Lopes A, Soper JT, Epenetos AA and Massuger LF 2007 *Decreased intraperitoneal disease recurrence in epithelial ovarian cancer patients receiving intraperitoneal consolidation treatment with yttrium-90-labeled murine HMFG1 without improvement in overall survival* Int. J. Cancer 120 2710-2714

[Papadimitroulas et al. 2012] Papadimitroulas P, Loudos G, Nikiforidis GC and Kagadis GC 2012 *A dose point kernel database using GATE Monte Carlo simulation toolkit for nuclear medicine applications: Comparison with other Monte Carlo codes* Med. Phys. 39 5238-5247

[Parker et al. 2013] Parker C, Nilsson S, Heinrich D, Helle SI, O'Sullivan JM, Fossa SD, Chodacki A, Wiechno P, Logue J, Seke M, Widmark A, Johannessen DC, Hoskin P, Bottomley D, James ND, Solberg A, Syndikus I, Kliment J, Wedel S, Boehmer S, Dall'Oglio M, Franzén L, Coleman R, Vogelzang NJ, O'Bryan-Tear CG, Staudacher K, Garcia-Vargas J, Shan M, Bruland OS and Sartor O for the ALSYMPCA Investigators 2013 *Alpha Emitter Radium-223 and Survival in Metastatic Prostate Cancer* N. Engl. J. Med. 369 213-223

[Pérez et al. 2011] Pérez P, Botta F, Pedroli G and Valente M 2011 *Dosimetry for beta-emitter radionuclides by means of Monte Carlo simulations* InTech. Chap. 11 265–286

[Perkins et al. 1991a] Perkins ST, Cullen DE and Seltzer SM 1991 *Tables and graphs of electron-interaction cross-sections from 10 eV to 100 GeV derived from the LLNL Evaluated Electron Data Library (EEDL), Z = 1–100* Report UCRL-50400 vol 31, Lawrence Livermore National Laboratory, Livermore, CA

[Perkins et al. 1991b] Perkins ST, Cullen DE and Seltzer SM 1991 *Tables and graphs of atomic subshell and relaxation data derived from the LLNL Evaluated Atomic Data Library (EADL), Z = 1–100* Report UCRL-50400 vol 30, Lawrence Livermore National Laboratory, Livermore, CA

[Petoussi-Henss et al. 2002] Petoussi-Henss N, Zankl M, Fill U and Regulla D 2002 *The GSF family of voxel phantoms* Phys. Med. Biol. 47 89-106

[Poole et al. 2012] Poole C M, Cornelius I, Trapp J V and Langton C M 2012 Fast tessellated solid navigation in Geant4 IEEE Trans. Nucl. Sci. 59 1695-1701

[Pouget et al. 2008] Pouget JP, Santoro L, Raymond L, Chouin N, Bardiès M, Bascoul-Mollevi C, Huguet H, Azria D, Kotzki PO, Pèlegrin M, Vivès E and Pèlegrin A 2008 *Cell membrane is a more sensitive target than cytoplasm to dense ionization produced by Auger electrons* Radiat. Res. 170 192-200

[Pouget et al. 2011] Pouget JP, Navarro-Teulon I, Bardiès M, Chouin N, Cartron G, Pèlegrin A and Azria D 2011 *Clinical radioimmunotherapy – the role of radiobiology* Nat. Rev. Clin. Oncol. 8 720-734

[Prestwich et al. 1989a] Prestwich WV, Nunes J and Kwok CS 1989 *Beta dose point kernels for radionuclides of potential use in radioimmunotherapy* J. Nucl. Med. 30 1036-1046

[Prestwich et al. 1989b] Prestwich WV, Nunes J and Kwok C S 1989 *Tables of beta ray dose distributions in water, air and other media* J. Nucl. Med. 30 1036-1046

[Quammen et al. 2011] Quammen C, Weigle C and Taylor R M 2011 *Boolean operations on surfaces in VTK without external libraries* available online at: http://www.vtkjournal.org/browse/publication/797

[Rajon et al. 2011] Rajon D, Bolch WE and Howell RW 2011 *Lognormal distribution of cellular uptake of radioactivity: Monte Carlo simulation of irradiation and cell killing in 3-dimensional populations in carbon scaffolds* J. Nucl. Med. 52 926-933

[Robert et al. 1996] Robert B, Mach JP, Mani JC, Ychou M, Folli S, Artus JC and Pèlegrin A 1996 *Cytokine targeting in tumors using a bispecific antibody directed against carcinoembryonic antigen and tumor necrosis factor alpha* Cancer. Res. 56 4758-4765

[Roeske et al. 2008] Roeske JC, Aydogan B, Bardiès M and Humm JL 2008 *Small-scale dosimetry: challenges and future directions* Semin. Nucl. Med. 38 367-383

[Santoro et al. 2009] Santoro L, Boutaleb S, Garambois V, Bascoul-Mollevi C, Boudousq V, Kotzki PO, Pèlegrin M, Navarro-Teulon I, Pèlegrin A and JP Pouget 2009 *Non internalising monoclonal antibodies are suitable candidates for 125I radioimmunotherapy of small-volume peritoneal carcinomatosis* J. Nucl. Med. 50 2033-2041

[Santos et al. 2012] Santos S, Torcato I and Castanho MA 2012 *Biomedical applications of dipeptides and tripeptides* Biopolymers. 98 288-393

[Sarrut et al. 2014] Sarrut D, Bardiès M, Boussion N, Freud N, Jan S, Letang JM, Loudos G, Maigne L, Marcatili S, Mauxion T, Papadimitroulas P, Perrot Y, Pietrzyk U, Robert C, Schaart DR, Visvikis D and Buvat I 2014 *A review of the use and potential of the GATE Monte Carlo simulation code for radiation therapy and dosimetry applications.* Med. Phys. 41 64301-1-14

[Schroeder et al. 2006] Schroeder W, Martin K, Lorensen B 2006 *The visualization toolkit: an object-oriented approach to 3D graphics, 4th Edition* US: Kitware, Inc. publishers

[Schümann et al. 2012] Schümann J, Paganetti H, Shin J, Faddegon B and Perl J 2012 *Efficient voxel navigation for proton therapy dose calculation in TOPAS and Geant4* Phys. Med. Biol. 57 3281-3293

[Segars 2001] Segars W P 2001 *Development and application of the new dynamic NURBS-based cardiac-torso (NCAT) phantom* PhD Dissertation University of North Carolina

[Segars et al. 2004] Segars WP, Tsui BMW, Frey EC, Johnson GA and Berr SS 2004 *Development of a 4D Digital Mouse Phantom for Molecular Imaging Research* Mol. Imaging Biol. 6 149-159

[Segars and Tsui 2007] Segars WP and Tsui B 2007 *4D MOBY and NCAT phantoms for medical imaging simulation of mice and men* J. Nucl. Med. 48 203P

[Segars et al. 2009] Segars WP, Lalush DS, Frey EC, Manocha D, King M and Tsui BMW 2009 *Improved dynamic cardiac phantom based on 4D NURBS and tagged MRI* IEEE Trans. Nucl. Sci. 56 2728-2738

[Segars et al. 2010a] Segars WP and Tsui BMW 2010 *The MCAT, NCAT, XCAT, and MOBY computational human and mouse phantoms Handbook of Anatomical Models for Radiation Dosimetry* (Boca Raton, FL: Taylor & Francis) 105-134

[Segars et al. 2010b] Segars W P, Sturgeon G, Mendonca S, Grimes J and Tsui BMW 2010 *4D XCAT phantom for multimodality imaging research* Med. Phys. 37, 4902-4915

[Smith et al. 2000] Smith TJ, Petouissi N and Zankl M 2000 *Comparison of internal radiation doses estimated by MIRD and voxel techniques for a family of phantoms* Eur. J. Nucl. Med. 27 1387-1398

[Snyder et al. 1969] Snyder W S, Fisher HL, Ford MR and Warner GG 1969 *Estimates of absorbed fractions for monoenergetic photon sources uniformly distributed in various organs of a heterogeneous phantom* J. Nucl. Med. 10 5-52

[Snyder et al. 1975] Snyder W S, Ford M R and Warner GG 1975 *Estimates of specific absorbed fractions for photon sources uniformly distributed in a heterogeneous phantom, MIRD Pamphlet No. 5* Society of Nuclear Medicine

[Snyder et al. 1978] Snyder WS, Ford MR and Warner GG 1978 *Estimates of specific absorbed fractions for monoenergetic photon sources uniformly distributed in various organs of a heterogeneous phantom* MIRD Pamphlet 5, Revised, Oak Ridge National Laboratory, Oak Ridge, TN

[Sofou 2008] Sofou S 2008 *Radionuclides carriers for targeting of cancer* Int. J. Nanomedicine 3 181-199

[Song et al. 2006] Song H, He B, Prideaux A, Du Y, Frey E, Kasecamp W, Ladenson P W, Wahl RW and Sgouros G 2006 *Lung dosimetry for radioiodine treatment planning in the case of diffuse lung metastases* J. Nucl. Med. 47 1985-1994

[Stabin et al. 1994] Stabin MG, Eckerman KF, Ryman JC and Williams LE 1994 *Bremsstrahlung radiation dose in yttrium-90 therapy applications* J. Nucl. Med. 35 1377-1380

[Stabin et al. 1995] Stabin M, Watson E, Cristy M, Ryman JC, Eckerman KF, Davis JL, Marshall D and Gehlen MK 1995 *Mathematical models and specific absorbed fractions of photon energy in the nonpregnant adult female and at the end of each trimester of pregnancy*, Oak Ridge, TN: ORNL; Report ORNL/TM-12907

[Stabin and Yoriyaz 2001] Stabin M and Yoriyaz H 2001 *Photon specific absorbed fractions calculated in the trunk of an adult male voxel-based phantom* Health. Phys. 82 21-44

[Stabin et al. 2005] Stabin MG, Sparks RB and Crowe E 2005 *OLINDA/EXM: the second-generation personal computer software for internal dose assessment in Nuclear Medicine* J. Nucl. Med. 46 1023-1027

[Stabin et al. 2006] Stabin MG, Peterson TE, Holburn GE, and Emmons MA 2006 *Voxel-based mouse and rat models for internal dose calculations* J. Nucl. Med. 47 655-659

[Strigari et al. 2014] Strigari L, Konijnenberg M, Chiesa C, Bardiès M, Du Y, Sjögreen Gleisner K, Lassmann M and Flux G 2014 *The evidence base for the use of internal dosimetry in the clinical practice of molecular radiotherapy* Eur. J. Nucl. Med. Mol. Imaging 41 1976-88

[Stroud 2006] Stroud I 2006 *Boundary representation modeling techniques* (London: Springer)

[Tan et al. 2012] Tan Z, Chen P, Schneider N, Glover S, Cui L, Torgue J, Rixe O, Spitz HB and Dong Z 2012 *Significant systemic therapeutic effects of high-LET immunoradiation by ^{212}Pb-trastuzumab against prostatic tumors of androgen-independent human prostate cancer in mice* Int. J. Oncol. 40 1881-1888

[Taschereau and Chatziioannou 2008] Taschereau R and Chatziioannou A F 2008 *Compressed voxels for high-resolution phantom simulations* Mol. Imaging. Biol. 10 40-47

[Uusijarvi et al. 2008] Uusijarvi H, Bernhardt P and Forssell-Aronsson E 2008 *Tumor control probability (TCP) for non-uniform activity distribution in radionuclide therapy* Phys. Med. Biol. 53 4369-4381.

[Vaziri et al. 2014] Vaziri B, Wu H, Dhawan AP, Du P and Howell RW 2014 *MIRD Pamphlet No. 25: MIRDcell V2.0 software tool for dosimetric analysis of biologic response of multicellular populations* J. Nucl. Med. 55 1557-1564

[Verheijen et al. 2006] Verheijen RH, Massuger LF, Benigno BB, Epenetos AA, Lopes A, Soper JT, Markowska J, Vyzula R, Jobling T, Stamp G, Spiegel G, Thurston D, Falke T, Lambert J and Seiden MV 2006 *Phase III trial of intraperitoneal therapy with yttrium-90-labeled HMFG1 murine monoclonal antibody in patients with epithelial ovarian cancer after a surgically defined complete remission* J. Clin. Oncol. 24 571-578

[Wheldon and O'Donoghue 1990] Wheldon TE and O'Donoghue JA 1990 *The radiobiology of Targeted Radiotherapy* Int. J. Rad. Biol. 58 1-21

[Williams et al. 1986] Williams G, Zankl M, Abmayr W, Veit R and Drexler G 1986 *The calculation of dose from external photon exposures using reference and realistic human phantoms and Monte Carlo methods* Phys. Med. Biol. 31 449-452

[Williams et al. 1989] Williams L, Wong J, Findley D and Forell B 1989 *Measurement and estimation of organ bremsstrahlung radiation dose* J. Nucl. Med. 30 1373-1377

[Worden 2014] Worden F 2014 *Treatment strategies for radioactive iodine-refractory differentiated thyroid cancer* Ther. Adv. Med. Oncol. 6 267-279

[Visvikis et al. 2006] Visvikis D, Bardiès M, Chiavassa S, Danford C, Kirov A, Lamare F, Maigne L, Staelens S and Taschereau R 2006 *Use of the GATE Monte Carlo package for dosimetry applications* Nucl. Instrum. Meth. A 569 335-340

[Xie et al. 2013] Xie T, Bolch WE, Lee C and Zaidi H 2013 *Pediatric radiation dosimetry for positron-emitting radionuclides using anthropomorphic phantoms* Med. Phys. 40 102502-1-14

[Xie and Zaidi 2013] Xie T and Zaidi H 2013 *Monte Carlo-based evaluation of S-values in mouse models for positron-emitting radionuclides* Phys. Med. Biol. 58 169-182

[Xie and Zaidi 2014] Xie T and Zaidi H 2014 *Evaluation of radiation dose to anthropomorphic paediatric models from positron-emitting labelled tracers* Phys. Med. Biol. 59 1165-1187

[Xu et al. 2000] Xu XG, Chao TC and Bozkurt A 2000 *VIP-MAN: An image-based whole-body adult male model constructed from color photographs of the visible human project for multi-particle Monte Carlo calculations* Health. Phys. 78 476-486

[Xu et al. 2007] Xu XG, Taranenko V, Zhang J and Shi C 2007 *A boundary-representation method for designing whole-body radiation dosimetry models: pregnant females at the ends of three gestational periods—RPI-P3, -P6 and -P9* Phys. Med. Biol. 52 7023-7044

[Xu et al. 2010] Xu X G and Eckerman K F 2010 *Handbook of anatomical models for radiation dosimetry* (Boca Raton, FL: Taylor & Francis Group)

[Xu et al. 2014] Xu XG 2014 *An exponential growth of computational phantom research in radiation protection, imaging, and radiotherapy: a review of the fifty-year history* Phys. Med. Biol. 59 R233-R302

[Yoriyaz et al. 2000] Yoriyaz H, dos Santos A, Stabin M, Cabezas R 2000 *Absorbed fractions in a voxel-based phantom calculated with the MCNP-4B code* Med. Phys. 27 1555-1562

[Yoriyaz et al. 2001] Yoriyaz H, Stabin MG and dos Santos A 2001 *Monte Carlo MCNP-4B-based absorbed dose distribution estimates for patient-specific dosimetry* J. Nucl. Med. 42 662-669

[Zankl et al. 1988] Zankl M, Veit R, Williams G, Schneider K, Fendel H, Petoussi N and Drexler G 1988 *The construction of computer tomographic phantoms and their application in radiology and radiation protection* Radiat. Environ. Biophys. 27 153-164

[Zankl et al. 2002] Zankl M, Fill U, Petoussi-Henss N and Regulla D 2002 *Organ dose conversion coefficients for external photon irradiation of male and female voxel models* Phys. Med. Biol. 47 2367-2385

[Zankl et al. 2003] Zankl M, Petoussi-Henss N, Fill U and Regulla D. 2003 *The application of voxel phantoms to the internal dosimetry of radionuclides* Rad. Prot. Dos. 105 539-548

[Zankl et al. 2005] Zankl M, Becker J, Fill U, Petoussi-Henss N and Eckerman KF 2005 *GSF male and female adult voxel models representing ICRP Reference Man—the present status. The Monte Carlo method: versatility unbounded in a dynamic computing* World Proc. of the Monte Carlo 2005 Topical Meeting on CD-ROM (Chattanooga, TN, 17–21 April 2005) (LaGrange, Park IL: American Nuclear Society)

[Zhang et al. 2009] Zhang J, Na YH, Caracappa PF and Xu XG 2009 *RPI-AM and RPI-AF, a pair of mesh-based, size-adjustable adult male and female computational phantoms using ICRP-89 parameters and their calculations for organ doses from monoenergetic photon beams* Phys. Med. Biol. 54 5885-5908

[Zubal et al. 1994] Zubal IG, Harrell CR, Smith EO, Rattner Z, Gindi G and Hoffer PB 1994 *Computerized three-dimensional segmented human anatomy* Med. Phys. 21 299-302

Scientific production

Journal papers

Marcatili S, Villoing D, Mauxion T, McParland BJ, Bardiès M. *Model-based versus specific dosimetry in diagnostic context: comparison of three dosimetric approaches.* Medical Physics 2015;42(3):1288-96.

Marcatili S, Villoing D, Garcia MP, Bardiès M. *Multi-scale hybrid models for radiopharmaceutical dosimetry with Geant4.* Physics in Medicine and Biology. 2014;59(24):7625-41.

Sarrut D, Bardiès M, Boussion N, Freud N, Jan S, Letang J-M, Loudos G, Maigne L, Marcatili S, Mauxion T, Papadimitroulas P, Perrot Y, Pietrzyk U, Robert C, Schaart DR, Visvikis D, Buvat I. *A review of the use and potential of the GATE Monte Carlo simulation code for radiation therapy and dosimetry applications.* Medical Physics. 2014;41(6):064301-1-14.

International conferences

Marcatili S, Pichard A, Courteau A, Ladjohounlou R,Navarro-Teulon I, Repetto-Llamazares A, Heyerdahl H, Dahle J, Pouget JP, Bardiès M. European Association of Nuclear Medicine congress 2015. *Multi-cellular dosimetry for ^{177}Lu labelled antibodies: model and application.* October 10-14 2015. Hamburg, Germany. Poster presentation.

Marcatili S. European Association of Nuclear Medicine congress 2014. *Introduction to the GATE Monte Carlo Code.* October 18-22 2014. Gothenburg, Sweden. Invited talk.

Marcatili S, Villoing D, Garcia MP, Poirot M, Bardiès M. European Association of Nuclear

Medicine congress 2013. *Development of a hybrid multi-scale phantom for Monte Carlo based internal dosimetry.* October 19-23 2013, Lyon, France. Oral presentation.

Marcatili S, Mauxion T, Villoing D, McParland B, Bardiès M. European Association of Nuclear Medicine congress 2013. *Absorbed dose in Molecular Radiotherapy: a comparison study of Monte Carlo, Dose Voxel Kernels and phantom based dosimetry.* October 19-23 2013, Lyon, France. Oral presentation.

Marcatili S, Villoing D, Garcia MP, Poirot M, Bardiès M. Geant4 2013 International User Conference. *Multi-scale hybrid models for radiopharmaceutical dosimetry with Geant4.* October 7-9 2013, Bordeaux, France. Oral presentation.

Marcatili S, Mauxion T, Villoing D, McParland B, Bardiès M. GSO Young scientist workshop: Radiobiology applied to oncology. *Absorbed dose in Molecular Radiotherapy: a comparison study of Monte Carlo, Dose Voxel Kernels and phantom based dosimetry.* April 3-6 2013, Vallée de Lesponne, France. Oral presentation.

MULTI-SCALE DOSIMETRY FOR TARGETED RADIONUCLIDE THERAPY OPTIMISATION

Author : Sara MARCATILI

Abstract

Targeted Radionuclide Therapy (TRT) consists in killing tumour targets by using radiolabeled vectors (radiopharmaceuticals) that selectively bind to tumour cells. In a context of TRT optimization, a better determination of energy deposition within biologic material is a prerequisite to the definition of the absorbed dose-effect relationship and the improvement of future cancer treatment. This requires being able to quantitatively assess activity distribution (with the most appropriate molecular imaging technique) and perform radiation transport at the scale at which biologically relevant phenomena occur. The methodologies that should be applied and the problematic to be faced strictly depend on the scale (cell, tissue, body) of the application considered, and on the type of radiation involved (photons, electrons, alpha). This research work consisted in developing dedicated dosimetric techniques (single-scale dosimetry) capable of taking into account the peculiarity of different experimental scenarios (cellular, pre-clinical, clinical TRT).

Keywords: Targeted radionuclide therapy – Cellular dosimetry – Preclinical dosimetry – Clinical dosimetry – Monte Carlo modelling – Multi-scale dosimetry.

DOSIMETRIE MULTI-ECHELLE POUR L'OPTIMISATION DE LA RADIOTHERAPIE INTERNE VECTORISEE

Auteure : Sara MARCATILI
Directeur de thèse : Manuel BARDIES
Lieu et date de Soutenance : Toulouse, 20 Octobre 2015

Résumé

La Radiothérapie Interne Vectorisée (RIV) consiste à détruire des cibles tumorales en utilisant des vecteurs radiomarqués (radiopharmaceutiques) qui se lient sélectivement à des cellules tumorales. Dans un contexte d'optimisation de la RIV, une meilleure détermination du dépôt d'énergie dans les tissues biologiques est primordiale pour la définition d'une relation dose absorbée - effet biologique et pour l'optimisation des traitement du cancer. Cela nécessite une évaluation quantitative de la distribution de l'activité (avec la technique d'imagerie moléculaire la plus appropriée) et d'effectuer le transport du rayonnement à l'échelle à laquelle se produisent les phénomènes biologiques pertinents. Les méthodologies à appliquer et les problématiques à établir dépendent strictement de l'échelle (cellule, tissu, organe) de l'application considérée, et du type de rayonnement en cause (photons, électrons, particules alpha). Mon travail de recherche a consisté à développer des techniques dosimétriques dédiées (dosimétrie mono-échelle) et innovantes, capables de prendre en compte la particularité de différents scénarios expérimentaux (cellulaire, pré-clinique, RIV clinique).

Mots-clés : Radiothérapie interne vectorisée - dosimétrie cellulaire - dosimétrie préclinique - dosimétrie clinique - modélisation Monte Carlo - dosimétrie multi-échelle.

Discipline administrative : Radio-physique et Imagerie Médicale

---

Laboratoire :
UMR 1037 INSERM-UPS
Centre de Recherche en Cancérologie de Toulouse (CRCT)
Faculté de Médecine de Toulouse-Rangueil – Bâtiment A3
133 route de Narbonne, 31062 TOULOUSE